

**EXTRACTING THE STRAIN-SOFTENING RESPONSE OF
COMPOSITES USING FULL-FIELD DISPLACEMENT
MEASUREMENT**

by

Navid Zobeiry

B.Sc., University of Tehran, 2002

M.A.Sc., University of British Columbia, 2005

A THESIS SUBMITTED IN PARTIAL FULFILMENT OF
THE REQUIREMENTS FOR THE DEGREE OF

DOCTOR OF PHILOSOPHY

in

The Faculty of Graduate Studies

(Civil Engineering)

THE UNIVERSITY OF BRITISH COLUMBIA
(Vancouver)

June 2010

© Navid Zobeiry, 2010

ABSTRACT

From both numerical and experimental standpoints, it is very desirable to develop a general methodology that can be used to determine the strain-softening response and characteristic damage properties (e.g. fracture energy, damage height) of quasi-brittle materials. In the absence of a direct methodology, one has to conduct multiple experiments combined with trial-and-error procedures and/or simplifying assumptions regarding the damaging behaviour of the material in order to construct a strain-softening curve.

In this study, a new methodology is developed that directly identifies the damaging constitutive response of composite materials using full-field measurements of kinematic variables. Using this methodology, the damage related properties can be extracted and the strain-softening response of composite materials under Mode I loading can be obtained directly. Compared to other available indirect approaches, this method invokes fewer assumptions about the behaviour of the material and does not require any prior assumption regarding the shape of the constitutive response, as is required in other approaches.

A series of compact compression and over-height compact tension tests are conducted on IM7/8552 quasi-isotropic laminates. Using the digital image correlation technique, full-field displacement vectors of the specimen surface are measured in each test. Based on the acquired data and using the basic principles of mechanics (equilibrium and compatibility), a family of approximate stress-strain curves are obtained. These approximate curves are then used in an iterative process to determine the optimized strain-softening response of the laminate.

To validate the capability of the method to capture the local damaging behaviour of the composite laminate, a series of destructive tests such as deplying and sectioning are performed on the damaged specimens. The tested laminates are also simulated using

finite element analyses of the specimens that employ the extracted strain-softening curve as input to a damage mechanics based material model. The proposed methodology provides insight into the details of damage propagation in composite materials and is a promising tool for characterizing the strain-softening behaviour of composite laminates in a relatively easy and direct manner.

TABLE OF CONTENTS

| | |
|---|-------------|
| Abstract..... | ii |
| Table of Contents | iv |
| List of Tables | viii |
| List of Figures..... | x |
| Nomenclature | xxi |
| Acknowledgments | xxiv |
| Chapter 1 : Introduction | 1 |
| Chapter 2 : Literature Review..... | 4 |
| 2.1. Background..... | 4 |
| 2.2. Field Measurements | 9 |
| 2.2.1. Selective versus Full-field Measurement | 9 |
| 2.2.2. Selective Line Measurement: Line Analysis | 10 |
| 2.2.3. Full-field Optical Measurement | 12 |
| 2.3. Inverse Identification of Constitutive Response | 13 |
| 2.3.1. Finite Element Model Updating Method | 14 |
| 2.3.2. Constitutive Equation Gap Method | 15 |
| 2.3.3. Virtual Fields Method..... | 15 |
| 2.3.4. Equilibrium Gap Method | 16 |
| 2.3.5. Reciprocity Gap Method..... | 17 |
| 2.4. Comparison of Various Methods | 17 |

| | |
|--|-----------|
| Chapter 3 : Development of A New Methodology to Extract The Strain-Softening Response..... | 21 |
| 3.1. Introduction | 21 |
| 3.1.1. Full-field Measurement Using DIC Technique..... | 22 |
| 3.2. Step I: Construction of an Approximate Constitutive Response | 25 |
| 3.2.1. Introduction..... | 25 |
| 3.2.2. Strain Calculation | 26 |
| 3.2.3. Damage Detection | 28 |
| 3.2.4. Construction of an Approximate Stress-Strain Curve..... | 35 |
| 3.3. Step II: Optimization of the Approximate Constitutive Response | 46 |
| 3.3.1. Introduction..... | 46 |
| 3.3.2. Possible Shapes of the Constitutive Response | 46 |
| 3.3.3. Optimized Constitutive Response..... | 50 |
| 3.3.3.1. Global Criterion for Optimization: Fracture Energy | 50 |
| 3.3.3.2. Local Criterion for Optimization: Equilibrium | 53 |
| 3.4. Limits of Applicability and Sources of Error | 58 |
| 3.5. Description of the Developed Code-CrackPro..... | 59 |
| 3.6. Summary | 62 |
| | |
| Chapter 4 : Application to OCT Tests and Validation Using FE Simulation and Destructive Testing | 64 |
| 4.1. Introduction | 64 |
| 4.2. Over-height Compact Tension Tests..... | 64 |
| 4.2.1. Material and Lay-up..... | 64 |
| 4.2.2. OCT Test Setup and Equipment | 67 |
| 4.2.3. Test Results..... | 69 |
| 4.2.4. Application of the Proposed Method | 75 |
| 4.2.5. Finite Element Simulation | 95 |
| 4.2.6. Sensitivity Analysis of the Optimized Response | 100 |

| | |
|---|------------|
| 4.3. Non-destructive and Destructive Investigation of Damaged Specimens | 109 |
| 4.3.1. Non-destructive Tests using CT Scans | 109 |
| 4.3.2. Destructive Tests: Cross-sectional Cuts..... | 110 |
| 4.3.3. Destructive Testing: Deploying | 120 |
| 4.4. Summary and Conclusions | 123 |
| | |
| Chapter 5 : Application to CC Tests and Validation Using FE Simulation and Destructive Testing | 125 |
| 5.1. Introduction | 125 |
| 5.2. Compressive Testing Jig | 125 |
| 5.3. Compact Compression Tests | 130 |
| 5.3.1. Tests..... | 130 |
| 5.3.2. Application of the Proposed Method | 132 |
| 5.3.3. Finite Element Simulation | 138 |
| 5.3.4. Deploying | 139 |
| 5.3.5. Sectioning | 144 |
| 5.4. Compressive Damage Length | 148 |
| 5.5. Summary and Conclusions | 152 |
| | |
| Chapter 6 : Conclusions and Contributions..... | 154 |
| 6.1. Notable Findings of Current Study..... | 155 |
| 6.2. Limitations and Applicability of Current Approach | 156 |
| 6.3. Contributions | 157 |
| | |
| References | 159 |
| | |
| Appendix A: CrackPro Code..... | 166 |
| A.1. Step I: Importing | 166 |

A.2. Step I: Assembling..... 168

A.3. Step I: Pre-processing 169

A.4. Step I: Damage Detection..... 174

A.5. Step I: Response Construction 177

A.6. Step II: Optimization..... 180

Appendix B: Sensitivity Analysis of the Center-Notched Specimen to Parameters of the Strain-Softening Curve 187

Appendix C: Comparison with Line Analysis..... 192

C.1. Compact Tension Test..... 192

C.2. Application of the New Method..... 193

C.3. Application of the Line Analysis Method 194

C.4. Comparison of the Two Methods 199

LIST OF TABLES

| | | |
|------------|---|-----|
| Table 2-1 | Summary of notable methods to identify constitutive parameters using full-field measurement techniques..... | 19 |
| Table 2-2 | Comparison of current available methods with the proposed method I this study..... | 20 |
| Table 4-1 | Lamina properties for an IM7/8552 lamina with a resin volume fraction of 34% (Hexcel)..... | 66 |
| Table 4-2 | Initial elastic properties of the IM7/8552 quasi-isotropic laminate obtained using laminate plate theory..... | 66 |
| Table 4-3 | Tensile properties of the IM7/8552 quasi-isotropic laminate used in this study..... | 67 |
| Table 4-4 | Specifications of OCT specimens tested in this study..... | 69 |
| Table 4-5 | Calculating the fracture energy for CTA1 based on the area below the load-POD curve confined by the unloading path..... | 90 |
| Table 4-6 | Calculating the fracture energy for CTA2 based on the area below the load-POD curve and confined by the unloading path..... | 90 |
| Table 4-7 | Summary of the properties obtained for the composite laminate..... | 94 |
| Table 4-8 | Coordinates of the optimized response curves obtained using the proposed method..... | 94 |
| Table 4-9 | Comparison of the experimental results and FE results obtained using the optimized linear, bilinear and trilinear softening curves..... | 98 |
| Table 4-10 | Sensitivity analysis of various parameters of the optimized trilinear softening curve..... | 109 |
| Table 4-11 | Damage zone and saturated zone identified from the schematics of damage in cross-sections..... | 118 |
| Table 5-1 | Specification of CC specimens tested in this study..... | 131 |
| Table 5-2 | Key values in the optimized constitutive response obtained using the proposed methodology applied to CC tests..... | 136 |

| | | |
|-----------|---|-----|
| Table 5-3 | Comparison of experimental and numerical results for CC tests. | 139 |
| Table 5-4 | Section cuts in front of the notch tip for CCA2 specimen and the maximum strain in each section..... | 145 |
| Table B-1 | Specifications of center-notched specimens. | 188 |
| Table B-2 | Sensitivity of the strength to various parameters of the trilinear softening response for different sizes of the center-notched specimen (Table B-1). . | 190 |
| Table C-1 | Finding damage initiation based on different criteria in line analysis. | 197 |

LIST OF FIGURES

| | | |
|------------|--|----|
| Figure 2-1 | Simplified strain-softening responses proposed for quasi-brittle materials, (a) linear softening, (b) bilinear softening, (c) exponential softening and (d) multi-quadratic softening curves. | 6 |
| Figure 2-2 | Constructing a linear softening response using three sets of experiments, (a) compact tension test to determine fracture energy, G_f , (b) sectioning the damaged specimen to measure characteristic damage height, h_c , (c) tensile test to determine the peak stress, σ_{peak} and (d) constructed constitutive response. | 8 |
| Figure 2-3 | Comparison of data recording during an OCT test: (a) strain measurement at selective points using strain gauges, (b) average strain measurement between selective lines using line analysis method (Kongshavn and Poursartip, 1999) and (c) full-field measurement using Digital Image Correlation (DIC) technique. | 10 |
| Figure 2-4 | (a) OCT specimen geometry and (b) OCT experimental setup. | 11 |
| Figure 3-1 | (a) DIC experimental setup and (b) treated specimen surface with black and white spray paints. | 23 |
| Figure 3-2 | Obtaining deformation vector field by measuring displacements of virtual nodes on the specimen surface. | 23 |
| Figure 3-3 | The masked area and virtual nodes generated by DaVis to calculate deformation vector field for a compact compression test. | 24 |
| Figure 3-4 | An example of specimen surface images and load-displacement curve recorded by DaVis during a test. Displacement vectors are exported for the virtual nodes generated by DaVis. | 25 |
| Figure 3-5 | An assumed 4-noded element based on the generated nodes in DaVis software. | 26 |
| Figure 3-6 | Satisfying equilibrium at each node by calculating nodal forces in each element. | 31 |

| | | |
|-------------|---|----|
| Figure 3-7 | Detecting damage zone by checking equilibrium at each node. | 31 |
| Figure 3-8 | Checking strains on the boundary of the damage zone to calculate an average damage initiation strain. ϵ_d and ϵ_{ud} denote strains in the damaged and undamaged elements. | 34 |
| Figure 3-9 | Identifying known parameters in a 2D damaged body: σ_{ud} and ϵ_{ud} in the undamaged region, Ω_{ud} and ϵ_d in the damaged region, Ω_d | 35 |
| Figure 3-10 | (a) Satisfying equilibrium at the tip of the damage zone, node “a” and (b) nodal forces for elements at the damage tip. | 36 |
| Figure 3-11 | Illustration of in-plane failure modes: (a) model I (opening mode), (b) Mode II (sliding mode) and (c) mixed Mode I/Mode II. | 38 |
| Figure 3-12 | (a) Damage zone identified using the proposed method and (b) stress distribution in the damage zone. | 38 |
| Figure 3-13 | Stress distribution along the y direction in a single-edge-notched specimen. | 40 |
| Figure 3-14 | (a) Finite element mesh to simulate the Mode I failure in a SEN specimen and (b) stresses along the y direction, σ_y , around the damage zone. | 41 |
| Figure 3-15 | (a) Stress distribution around the damage zone in OCT test and (b) approximating the stress inside the damage zone using a representative strip of elements. | 42 |
| Figure 3-16 | An example of the stress-strain response for the composite laminate strip shown in Figure 3-15 constructed from all images. | 43 |
| Figure 3-17 | (a) Schematic showing the state of stress and strain in the elements within and around the damage zone and (b) FE mesh of OCT test geometry. | 44 |
| Figure 3-18 | Stress-strain curve used as input (linear softening - dashed line) in the FE simulation of the OCT test shown together with the approximate stress-strain curve obtained using the same assumptions as in the proposed method (i.e. stress in the undamaged element versus the strain in the damaged element). | 44 |
| Figure 3-19 | Stress-strain curve used as input (bilinear softening - dashed line) in the FE simulation of the OCT test shown together with the approximate stress-strain curve obtained using the same assumptions as in the proposed | |

| | | |
|-------------|---|----|
| | method (i.e. stress in the undamaged element versus the strain in the damaged element). | 45 |
| Figure 3-20 | Stress-strain curve used as input (trilinear softening - dashed line) in the FE simulation of the OCT test shown together with the approximate stress-strain curve obtained using the same assumptions as in the proposed method (i.e. stress in the undamaged element versus the strain in the damaged element). | 45 |
| Figure 3-21 | Example of an approximate family of curves and identified bounds for an OCT test on an IM7/8552 quasi-isotropic laminate. | 47 |
| Figure 3-22 | Example of an approximate family of curves and identified bounds for a compact compression test on an IM7/8552 quasi-isotropic laminate. | 47 |
| Figure 3-23 | Example of an approximate family of curves and optimized linear, bilinear and trilinear softening curves for an OCT test on an IM7/8552 quasi-isotropic laminate. | 49 |
| Figure 3-24 | Schematic showing the damage area in an OCT test. | 51 |
| Figure 3-25 | (a) Total dissipated energy calculated from the area below the load-displacement curve and (b) fracture energy density calculated from the softening response of the material. | 52 |
| Figure 3-26 | Example of a selected family of curves with equal specific energy densities and within the regions specified in the first step of the optimization. | 52 |
| Figure 3-27 | Calculating energy from the stress-strain response of an element. | 53 |
| Figure 3-28 | (a) An assumed bilinear softening response, (b) dividing the bilinear curve into two linear softening curves, (c) the damage parameter as a function of strain, and (d) the modulus reduction factor as a function of strain for the bilinear softening curve. | 55 |
| Figure 3-29 | Schematic representation of steps and calculations in CrackPro code. | 60 |
| Figure 4-1 | An OCT test with [45/0/-45/90] _{4S} layup which shows large splitting areas on the surface. | 65 |
| Figure 4-2 | Cutting panels at 45 degree angles to make [90/45/0/-45] _{4S} specimens. .. | 66 |
| Figure 4-3 | (a) OCT test setup, (b) OCT specimen geometry. | 68 |

| | | |
|-------------|--|----|
| Figure 4-4 | Schematic representation of test setup and equipment. | 69 |
| Figure 4-5 | Load-POD curves for the OCT tests conducted in this study. | 70 |
| Figure 4-6 | Load-Pod curve of CTA1 test showing some of the associated image numbers. | 71 |
| Figure 4-7 | Image #490 for CTA1 test showing the painted area in front of the notch... | 71 |
| Figure 4-8 | Image #534 for CTA1 test showing the painted area in front of the notch... | 72 |
| Figure 4-9 | Image #734 for CTA1 test showing the painted area in front of the notch... | 72 |
| Figure 4-10 | Load-Pod curve of CTA2 test showing some of the image numbers on the curve. | 73 |
| Figure 4-11 | Image #1276 for CTA2 test showing the painted area in front of the notch. | 73 |
| Figure 4-12 | Image #1887 for CTA2 test showing the painted area in front of the notch. | 74 |
| Figure 4-13 | Image #2913 for CTA2 test showing the painted area in front of the notch. | 74 |
| Figure 4-14 | Mesh generated by DaVis on the surface of CTA1 specimen with element sizes equal to 2.036 mm. | 75 |
| Figure 4-15 | Mesh generated by DaVis on the surface of CTA2 specimen with element sizes equal to 2.054 mm. | 76 |
| Figure 4-16 | Measuring vertical strains along the line 1 on the CTA1 specimen surface. | 76 |
| Figure 4-17 | Y-Strains (vertical or loading direction) along the line 1 in CTA1 for 5 images: #500, #680, #730, #740 and #770 (Figure 4-16). | 77 |
| Figure 4-18 | Finding the average damage initiation strain from the strains of the damage boundary elements in CTA1. | 78 |
| Figure 4-19 | Damaged area for CTA1 specimen based on the mesh generated by DaVis (Figure 4-16), in Image #730 (Figure 4-6). Damage is identified as the | |

| | | |
|-------------|---|----|
| | zone in which strains are higher than the damage initiation strain equal to 1.1% in this study..... | 78 |
| Figure 4-20 | Damaged area for CTA1 specimen based on the mesh generated by DaVis (Figure 4-16), in Image #740 (Figure 4-6)..... | 79 |
| Figure 4-21 | Approximate stress-strain response of the composite laminate extracted from CTA1 specimen, 6 mm ahead of the notch tip. | 80 |
| Figure 4-22 | Approximate family of stress-strain responses of the composite laminate obtained from CTA1 specimen. | 80 |
| Figure 4-23 | Approximate stress-strain response of composite laminate extracted from CTA2 specimen, 5 mm ahead of the notch tip..... | 81 |
| Figure 4-24 | Approximate family of stress-strain responses of the composite laminate obtained from CTA2 specimen. | 81 |
| Figure 4-25 | Specifying some of the load drops (A, B and C) in the load-POD curve of the CTA2 specimen..... | 83 |
| Figure 4-26 | Surface images of the CTA2 specimen before and after the sudden load drops specified in Figure 4-25. (a) and (b) before and after the load drop “A”. (c) and (d) before and after the load drop “B”. (e) and (f) before and after the load drop “C”. | 84 |
| Figure 4-27 | Stress-strain response, 5 mm ahead of the notch tip in the CTA2 specimen. Sudden jumps in the response curve (A, B and C) correlate to load drops in the global load-POD curve (Figure 4-25). | 85 |
| Figure 4-28 | Stress-strain response, 7 mm ahead of the notch tip in the CTA2 specimen. Sudden jumps in the response curve (A, B and C) correlate to load drops in the global load-POD curve (Figure 4-25). | 85 |
| Figure 4-29 | Calculated damage length-POD in the CTA2 specimen using the proposed method. Sudden damage growth (e.g. A, B and C) correlates to the load drops in the global load-POD curve (Figure 4-25). | 86 |
| Figure 4-30 | Specifying some of the load drops (D and E) in the load-POD curve of the CTA1 specimen..... | 86 |

| | | |
|-------------|---|----|
| Figure 4-31 | Stress-strain response, 4 mm ahead of the notch tip in the CTA1 specimen. Sudden jumps in the response curve (D and E) correlate to load drops in the global load-POD curve (Figure 4-30). | 87 |
| Figure 4-32 | Stress-strain response, 6 mm ahead of the notch tip in the CTA1 specimen. Sudden jumps in the response curve (D and E) correlate to load drops in the global load-POD curve (Figure 4-30). | 87 |
| Figure 4-33 | Calculated damage length-POD in the CTA1 specimen using the proposed method. Sudden damage growth (e.g. D and E) correlates to the load drops in the global load-POD curve (Figure 4-30) | 88 |
| Figure 4-34 | Upper-bound and lower-bound responses based on the family of approximate stress-strain curves. Linear, bilinear and trilinear softening responses considered for the optimization process are also shown here. . | 89 |
| Figure 4-35 | Measuring fracture energy for the area below the load-POD curve and limited to the unloading path for CTA1..... | 91 |
| Figure 4-36 | Measuring fracture energy for the area below the load-POD curve and limited to the unloading path for CTA2..... | 91 |
| Figure 4-37 | Finding the average fracture energy from OCT tests..... | 92 |
| Figure 4-38 | Stress-strain curves obtained from the satisfaction of global energy criterion based on a bilinear response shape. | 92 |
| Figure 4-39 | Optimized softening curves obtained using the proposed method. | 94 |
| Figure 4-40 | Part of the finite element mesh used to simulate the response of OCT specimens with 0.25 mm elements at the notch tip..... | 95 |
| Figure 4-41 | Applying the Bazant's crack band scaling law to adjust the energy density of elements (Bazant and Oh, 1983)..... | 96 |
| Figure 4-42 | (a) Original stress-strain curve, (b) Scaling the original stress-strain curve based on the Bazant's crack band scaling law (Bazant and Oh, 1983, and (c) modifying the scaled stress-strain curve to consider the effect of large deformation calculation in FE codes..... | 97 |
| Figure 4-43 | Comparison of load-POD curves obtained using optimized linear, bilinear and trilinear softening responses with experimental results. | 99 |

| | | |
|-------------|--|-----|
| Figure 4-44 | Equivalent damage length-POD curves for the CTA1 and CTA2 experiments and FE results obtained using the optimized softening curves. | 99 |
| Figure 4-45 | Sensitivity analysis of the various parameters of the trilinear softening curve..... | 100 |
| Figure 4-46 | Changing the first slope after the peak of the optimized trilinear softening curve to study its effect on the load-POD response of OCT specimens. | 103 |
| Figure 4-47 | FE results for effect of increasing the first slope of the trilinear softening curve (Figure 4-46) on the load-POD response of the OCT test. | 103 |
| Figure 4-48 | Changing the second slope of the optimized trilinear softening curve to study its effect on the load-POD response of OCT specimens. | 104 |
| Figure 4-49 | FE results for effect of increasing the second slope of the trilinear softening curve (Figure 4-48) on the load-POD response of the OCT test... | 104 |
| Figure 4-50 | Changing the third slope of the optimized trilinear softening curve to study its effect on the load-POD response of OCT specimens..... | 105 |
| Figure 4-51 | FE results for effect of increasing the third slope of the trilinear softening curve (Figure 4-50) on the load-POD response of the OCT test. | 105 |
| Figure 4-52 | Changing the damage initiation strain of the optimized trilinear softening curve to study its effect on the load-POD response of OCT specimens. | 106 |
| Figure 4-53 | FE results for effect of increasing the damage initiation strain of the trilinear softening curve (Figure 4-52) on the load-POD response of the OCT test. | 106 |
| Figure 4-54 | Changing the plateau stress of the optimized trilinear softening curve to study its effect on the load-POD response of OCT specimens. | 107 |
| Figure 4-55 | FE results for effect of increasing the plateau stress of the trilinear softening curve (Figure 4-54) on the load-POD response of the OCT test... | 107 |
| Figure 4-56 | Changing the energy density of the optimized trilinear softening curve to study its effect on the load-POD response of OCT specimens. | 108 |

| | | |
|-------------|---|-----|
| Figure 4-57 | FE results for effect of increasing the energy density of the trilinear softening curve (Figure 4-56) on the load-POD response of the OCT test... | 108 |
| Figure 4-58 | Damage height obtained using (a) CT scanning at a cross-section 1 mm ahead of the notch tip and (b) the proposed method. | 110 |
| Figure 4-59 | Sections cut from CTA1 specimen. Sections 4 to 16 are shown in this figure. | 112 |
| Figure 4-60 | An image of section #12 obtained using a 10x microscope. | 112 |
| Figure 4-61 | An image of section #12 obtained using an optical microscope. | 113 |
| Figure 4-62 | An image obtained for section #12 using SEM showing fibre breakage (A), matrix cracking (B) and delamination (C). | 113 |
| Figure 4-63 | SEM image of cross-section #12 of CTA1 specimen. | 114 |
| Figure 4-64 | SEM image of cross-section #13 of CTA1 specimen. | 114 |
| Figure 4-65 | Schematic representation of damage in cross-sections #7 to #11 in CTA1. 0 mm indicates the notch tip vertical position. | 115 |
| Figure 4-66 | Schematic representation of damage in cross-sections #12 to #16 in CTA1. 0 mm is the notch tip vertical coordinate. | 115 |
| Figure 4-67 | Identifying saturated damage zone and saturation strain from the schematic of damage and also strain distribution in cross-section #12. | 118 |
| Figure 4-68 | Identified damage zone and damage saturated zone from the cross-sections of the CTA1 specimen. | 119 |
| Figure 4-69 | Comparison of damage zone and damage saturated zone measured using the sectioning method and calculated using the proposed methodology in CTA1. | 119 |
| Figure 4-70 | CTA2 specimen surface at the end of the experiment. An area of interest was cut out to be analyzed using the deplying technique. | 120 |
| Figure 4-71 | Ply # 3 of CTA2 specimen with 0° fibre direction. | 121 |
| Figure 4-72 | Ply # 10 of CTA2 specimen with +45 ° fibre direction. | 121 |
| Figure 4-73 | Ply # 21 of CTA2 specimen with -45 ° fibre direction. | 121 |
| Figure 4-74 | Fibre breakage traces in some of the plies of CTA2 specimen. | 122 |

| | | |
|-------------|--|-----|
| Figure 4-75 | Comparing the calculated damage zone for CTA2 specimen using the proposed methodology and the fibre breakage zone obtained using the deplying technique. | 123 |
| Figure 5-1 | Compact compression test fixture. | 128 |
| Figure 5-2 | Schematic of compact compression test fixture. | 128 |
| Figure 5-3 | Compact compression specimen geometry. | 129 |
| Figure 5-4 | Comparing the elastic strains on the surface of a CC specimen with the strains obtained from FE simulation. (a) Location of comparison line and (b) Strains in Y direction along line A at POD = -0.7 mm. | 129 |
| Figure 5-5 | Load-POD curves for CC tests. | 131 |
| Figure 5-6 | Surface image of CCB1 specimen at the end of the experiment. | 132 |
| Figure 5-7 | The mesh generated by DaVis on the surface of CCB1 specimen with element sizes equal to 2.452 mm. | 133 |
| Figure 5-8 | The mesh generated by DaVis on the surface of CCA2 specimen with element sizes equal to 2.801 mm. | 133 |
| Figure 5-9 | Approximate compressive stress-strain response obtained from CCB1, 1.2 mm ahead of the initial notch tip. | 134 |
| Figure 5-10 | Approximate compressive stress-strain response obtained from CCB1, 11 mm ahead of the initial notch tip. | 135 |
| Figure 5-11 | Approximate stress-strain responses along with the optimized response shape obtained from the optimization process. | 135 |
| Figure 5-12 | Optimized compressive response obtained using the proposed methodology. | 137 |
| Figure 5-13 | Damaged area in CCB1 specimen just before final unloading. Damage height grows to about 12 mm after band broadening stage. | 137 |
| Figure 5-14 | Part of the mesh used for simulating CC tests in LS-DYNA. | 138 |
| Figure 5-15 | Comparison of load-POD curve obtained from LS-DYNA and experimental results. | 139 |
| Figure 5-16 | Fibre breakage/bending trace in ply #4 of CCB1 specimen with -45° fibre direction for a 43x32 mm cut. | 141 |

| | | |
|-------------|--|-----|
| Figure 5-17 | Fibre breakage/bending trace in ply #6 of CCB1 specimen with +45° fibre direction for a 43x32 mm cut..... | 141 |
| Figure 5-18 | Fibre breakage/bending trace in ply #7 of CCB1 specimen with 0° fibre direction for a 43x32 mm cut..... | 141 |
| Figure 5-19 | Fibre breakage/bending traces in various plies of CCB1 specimen. Each cut is 43x32 mm..... | 142 |
| Figure 5-20 | (a) Fibre breakage/bending traces in layer #22 of CCB1 specimen with 0° fibre direction, (b) showing part of the damage tip, (c) part of the damage zone that still can transfer load under compression and (d) rubble formation leading to loss of load bearing capacity..... | 143 |
| Figure 5-21 | Overlaying fibre breakage/bending traces identified using deplying technique in all layers of CCB1 specimen..... | 144 |
| Figure 5-22 | Overview of damage zone in the composite laminate under compression obtained from cross-section #10 using SEM technique. Failure mechanisms are kinking (A), off axis matrix cracking and fibre breakage/bending (B) and delamination (C)..... | 145 |
| Figure 5-23 | Formation of slip surfaces in sections of CCA2 specimen: (a) cross-section #6 with maximum strain equal to -0.7%, (b) cross-section #7 with maximum strain equal to -0.9%, (c) cross-section #8 with maximum strain equal to -1.2%..... | 146 |
| Figure 5-24 | (a) and (b) Formation of slip surfaces in cross section # 8 of CCA2 specimen..... | 147 |
| Figure 5-25 | (a) Cross section #10 in CCA2 specimen and (b) Kink band formation. | 147 |
| Figure 5-26 | Formation of damage zones in composite laminates under compression..... | 149 |
| Figure 5-27 | Modified stress-strain response of the composite laminate under compression with pre-peak nonlinearity..... | 150 |
| Figure B-1 | Geometry of the center-notched specimen..... | 187 |
| Figure B-2 | Size effect observed in the center-notched specimens..... | 188 |
| Figure B-3 | (a) Stress-strain responses used to obtain the sensitivity of the center-notched specimens to the damage initiation value (curve 1: $\epsilon_i=1.1\%$ and | |

| | | |
|------------|---|-----|
| | curve 2: $\epsilon_i=1.3\%$) and (b) FE simulation results of the specimen #2 (Table B-1) using different damage initiation values..... | 189 |
| Figure B-4 | Sensitivity of the strength to various parameters of the trilinear softening response for different sizes of the center-notched specimen (Table B-1)..... | 190 |
| Figure B-5 | (a) Curve 1: softening response with $\epsilon_i=1.1\%$ and $G_f=110$ kJ/m ² , (b) Curve 2: softening response with $\epsilon_i=1.3\%$ and $G_f=110$ kJ/m ² and (c) Curve 3: softening response with $\epsilon_i=1.1\%$ and $G_f=50$ kJ/m ² | 191 |
| Figure B-6 | Simulation results in center notched specimens using three different softening response (Figure B-5)..... | 191 |
| Figure C-1 | Compact tension specimen specifications..... | 192 |
| Figure C-2 | Load-POD curve obtained for the CT test. | 193 |
| Figure C-3 | Mesh generated by DaVis software for the CT specimen. | 193 |
| Figure C-4 | Damage initiation strains for CT specimen obtained from various images. . | 194 |
| Figure C-5 | Virtual scribed lines on the surface of the CT specimen. | 195 |
| Figure C-6 | Displacement of line 1 as a function of position in front of the notch tip. Each curve represents the position of line 1 in a specific image. | 196 |
| Figure C-7 | Displacement of line 3 as a function of position in front of the notch tip. Each curve represents the position of line 3 in a specific image. | 196 |
| Figure C-8 | Line analysis for Line 1 based on different thresholds. | 198 |
| Figure C-9 | Crack length obtained using line analysis and various assumptions for crack onset..... | 198 |

NOMENCLATURE

Latin Symbols

| | |
|-------------------------|--|
| a | Crack length |
| B | Strain-displacement vector |
| D | Material stiffness matrix |
| e_d | Error in measured displacements |
| e_{energy} | Maximum error in energy calculation |
| $e_{equilibrium}$ | Maximum error in nodal equilibrium equation |
| $\bar{e}_{equilibrium}$ | Average error in nodal equilibrium |
| e_F | Maximum error in nodal forces |
| e_ϵ | Error in calculated strains |
| E_0 | Undamaged modulus |
| E | Young's modulus |
| F | Force |
| $F(\epsilon)$ | Effective strain |
| G | Shear modulus |
| G_f | Fracture energy |
| h_c | Characteristic damage height |
| h_e | Element height |
| K | Stiffness matrix |
| L | Length |
| m | Number of nodes inside the area of interest |
| n | Bazant's scale factor |
| N | Shape function |
| POD | Pin opening displacement |
| P_{ux} | Complete polynomial for displacements in x direction |
| R | Modulus reduction factor |

| | |
|-------------------|---|
| $R_{equilibrium}$ | Total equilibrium error |
| r_{ij} | Remaining equilibrium force in node i and image j |
| S | Sensitivity parameter |
| t | Thickness |
| U | Displacement |
| W | Total dissipated energy |

Greek Symbols

| | |
|---------------------------|--|
| γ | Fracture energy density |
| γ_i | Fracture energy density in element i |
| γ_s | Scaled fracture energy density |
| Δ | Increment |
| δ | Displacement |
| ε | Strain |
| ε_{avg} | Average strain |
| ε_d | Strain in the damaged region |
| ε_E | Engineering strain |
| ε_i | Damage initiation strain |
| ε_s | Damage saturation strain |
| ε_T | True strain |
| ε_u | Damage ultimate strain |
| ε_{ud} | Strain in the undamaged region |
| $\varepsilon_{unloading}$ | Unloading strain |
| θ | Slope of the strain-softening response |
| ν | Poisson's ratio |
| σ | Normal stress |
| σ_{avg} | Average stress |
| σ_d | Stress in the damaged region |

| | |
|--------------------|----------------------------------|
| σ_{error} | Error in the calculated stresses |
| $\sigma_{plateau}$ | Plateau stress |
| σ_{ud} | Stress in the undamaged region |
| σ_{peak} | Peak stress |
| τ | Shear stress |
| ω | Damage parameter |

ACKNOWLEDGMENTS

I would like to thank my family members for their unconditional love, encouragement and support. I would like to thank my dear parents, Tilla and Mohammad for providing me a life full of joy and inspiration. I would like to thank my dear brother and sister, Nima and Nazli, for supporting me all my life. I would like to thank my dearest Yalda who supported me and helped me to achieve my goals.

I would like to sincerely and especially thank my supervisors, Dr. Reza Vaziri and Dr. Anoush Poursartip, for their guidance, encouragement and constructive criticisms. Their valuable suggestions and constant support have made this thesis a better product.

Above all, I thank God for giving me the knowledge, vision, and ability to proceed and achieve. It is only through his grace that achievement can truly be accomplished.

Chapter 1: Introduction

Composite materials are being used in many industrial applications most notably in aerospace industry. This is mainly due to their high specific stiffness, light weight and energy absorbing properties. Their use also lowers the long term maintenance costs required for metal structures associated with fatigue and corrosion.

Defects and imperfections can deteriorate the strength of composite components. These components are likely to contain voids and defects introduced either intentionally, e.g. cut-outs and fastener holes, or unintentionally, e.g. fabrication defects and accidental damages. These defects can act as potential sites for development and propagation of damage.

In recent years, many studies have been dedicated to characterizing damage in composite materials. These studies range from identifying damage modes under various loading conditions to deriving damage related parameters such as fracture energy and damage initiation strain leading to construction of constitutive responses or calibration of existing constitutive models. Such models can be implemented in a finite element code to simulate the behaviour of large scale composite components and predict their failure strength thus minimizing the cost of experimental studies. Due to the increase use of composite materials in primary load bearing structures, developing a methodology to identify damage properties of composite materials becomes a desirable goal. Using these properties, one can calibrate existing strain-softening models and predict the response and load carrying capacity of composite structures with various geometries.

For example, currently, a series of experiments such as over-height compact tension tests can be performed in conjunction with analysis of local displacements of inscribed lines on the specimen surface to extract damage properties of composite laminates (Kongshavn and Poursartip, 1999). Data from these experiments can then be fed into a damage mechanics based constitutive model (Williams, 1998; Williams et al., 2003) to predict the

response of composite components. However, only a limited number of damage related parameters can be obtained using this method.

In recent years, non-contact measurement techniques, such as digital image correlation method (DIC), using low-cost CCD cameras and powerful PCs have advanced. One of the key application of such techniques is to identify elastic and damage properties of various materials using full-field measurement of kinematic field variables such as displacement or strain vectors (e.g. Pierron et al., 2007a, 2007b; Avril et al., 2008). Among notable approaches to identify material properties using full-field measurement techniques are the virtual field method (Chalal et al., 2004), equilibrium gap method (Claire et al., 2007), finite element updating technique (Meuwissen et al., 1998) and the constitutive equation gap method (Geymonat, 2002; Geymonat et al., 2003). However, almost all of these approaches are based on an initial assumption for the shape of the strain-softening curve to identify damage properties. Clearly, in all these methods, a biased assumption for the shape of the constitutive response may result in identifying incorrect damage properties.

In this study, a methodology is presented to identify constitutive response and damage properties of composite laminates under various loading conditions. The method has been successfully applied to specific geometries such as over-height compact tension (OCT) (Kongshavn and Poursartip, 1999) and also compact compression (CC) to identify strain-softening response of composite laminates.

In the method developed in this study, using high resolution cameras and image analysis software packages such as DaVis (LaVision, 2007), displacement vectors on the specimen surface are measured at different stages of the experiment. This data is then used to perform a two-step analysis to identify the damaged region and damage related parameters.

In the first step of this method, surface strains are calculated using the measured displacement vectors. Using the strain field and finite element equations, equilibrium is checked on the specimen surface to determine the damage zone at each stage of the test.

Afterward, using the elastic stress distribution on the damage zone boundary, an approximate stress distribution inside the damage zone is obtained.

The second step involves an updating approach in which iteration is used to minimize local and global cost functions in order to obtain an optimized form of the constitutive response of composite laminates. In this step, iteration is limited to the approximate response area and response shape obtained in the first step.

To validate the proposed methodology, a series of OCT and also CC tests are conducted. Full-field measurement data obtained during these tests are analyzed and constitutive response of the composite laminate is identified. The obtained constitutive response is then verified using FE simulations. In addition, the identified damage boundaries using the proposed method are also validated using destructive tests such as deplying and sectioning of damaged specimens.

The proposed method benefits from the advantages of both non-updating techniques that are computationally inexpensive and updating techniques that are insensitive to error and noise in the measured displacement data. Moreover, unlike other techniques, this method does not suffer from any prior assumption on the shape of the constitutive response. The methodology presented here is promising as a means of characterizing and constructing the strain-softening behaviour of composite materials in a relatively easy manner.

In this study, a literature review of the current available techniques capable of identifying constitutive parameters using full-field measurement of displacement is carried out and presented in Chapter 2. The proposed two-step method is then presented in detail in Chapter 3. In Chapter 4 and Chapter 5, OCT and CC tests conducted on IM7/8552 composite panels are presented. For each test, analysis results from the proposed method, FE simulation, deplying and sectioning results are presented and compared. It is concluded that the proposed method can successfully identify the constitutive response and damage related properties of IM7/8552 composite panels under both tensile and compressive loading.

Chapter 2: Literature Review

2.1. Background

In quasi-brittle materials such as fibre composites, concrete or wood particle board, localization of damage in the failure process zone (FPZ) results in load redistribution and consequently local softening behaviour. For example, in composite laminates, the softening behaviour is caused by localization of failure mechanisms such as fibre breakage, matrix cracking or interface failure in the FPZ. Usually in these materials, unlike true brittle materials, the size of the FPZ cannot be neglected compared to other dimensions of small notched specimens or structural components. As a result, characterizing the softening behaviour of quasi-brittle materials becomes a necessity to simulate their damaging behaviour and predict the load bearing capacity of their structural components.

In several studies, micromechanical stages and overall responses of composite components during the damage propagation under tension (e.g. Williams, 1998; Williams et al., 2003; Floyd, 2004) and compression (e.g. Moran et al. 1995; Sivashanker et al., 1996; Fleck, 1997; Sivashanker, 1998) have been investigated. For example, it has been pointed out that in notched quasi-isotropic laminates under tension, initially, matrix cracks start to grow in 90° layers in front of the notch (Floyd, 2004). This failure mechanism is usually followed by matrix cracking in off-axis layers due to the redistribution of stress followed by damage in 90° layers. Matrix cracking may also result in fibre and matrix interface failure, and delamination. Eventually fibre breakage in off-axis and 0° layers results in the damage saturation of the FPZ (Floyd, 2004). The sequence and evolution of these failure mechanisms may vary depending on various parameters, including the laminate stacking sequence or the lamina thickness. For example, in thick-ply laminates, other failure mechanisms such as splitting may also become operative.

Under compression, it is shown that the kink band formation process is the main failure mechanism in unidirectional composites and a combination of kinking, delamination and off-axis matrix cracking are the main failure mechanisms in multidirectional composites (Moran et al. 1995; Sivashanker et al., 1996; Fleck, 1997; Sivashanker, 1998; Zobeiry, 2004). All of these failure mechanisms under tension and compression contribute to the loss of material stiffness and subsequently loss of load bearing capacity.

The current approach of continuum damage mechanics is to consider the degradation of material properties in a smeared band based on a strain-softening law to simulate the damaging behaviour of quasi-brittle materials. Since strain-softening is a generalized continuum approach, it is compatible with FE models and can easily be incorporated into nonlinear FE codes. In composites, for example, this approach has been successfully applied and its predictive capability for global behaviour of notched specimens has been demonstrated (e.g. Walker et al., 1996; Kongshavn and Poursartip, 1999; Williams et al., 2003; Floyd, 2004; McClennan, 2004; Maimi et al., 2007a, 2007b; McGregor et al., 2007).

In principle, the most direct approach to measure the strain-softening response is to conduct stable uniaxial tensile or compressive tests. However, as it is noted in other studies (e.g. Elices et al., 2002), such an approach has some major drawbacks that makes it difficult, if not impossible, to apply. In uniaxial tests, multiple cracking may occur due to the material heterogeneity. On the other hand, in cases where the characteristic damage height is small (i.e. narrow damage band compared to the specimen size), these tests result in catastrophic failure before observing any softening behaviour. Due to difficulties associated with the direct measurement of strain-softening response, researchers have applied indirect methods (or inverse methods) based on parametric fitting of the experimental data. As a result, many solutions have been proposed for the shape of the strain-softening response in quasi-brittle materials. These solutions range from simple linear and bilinear softening responses (e.g. Bazant and Cedolin, 1991; Elices et al., 2002) to more complicated exponential (e.g. Jirasek and Patzak, 2002; Maimi et al., 2007a) and multi-quadratic softening responses (Williams et al., 2003; McGregor et al., 2008) as shown in Figure 2-1.

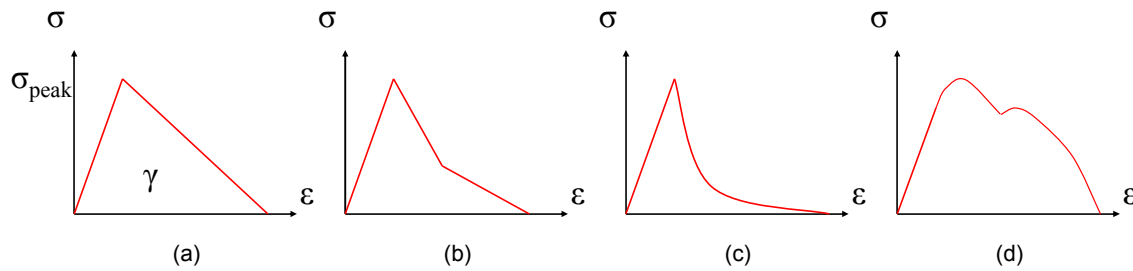


Figure 2-1 Simplified strain-softening responses proposed for quasi-brittle materials, (a) linear softening, (b) bilinear softening, (c) exponential softening and (d) multi-quadratic softening curves.

In composites, the shape of the strain-softening curve depends on various parameters such as material properties, lay-up, thickness or even loading condition (Walker et al., 1996; Zobeiry, 2004; Zobeiry et al., 2008). Therefore, a strain-softening law has to be identified and characterized for each different laminate and for each loading condition. This requires identifying the shape of the strain-softening curve, measuring damage related parameters such as fracture energy or strength to construct the constitutive response of the material.

In recent years many studies have been focused on characterizing the strain-softening behaviour of composite materials (e.g. Walker et al., 1996; McClennan, 2004; Zobeiry et al., 2008; McGregor et al., 2008). Usually the characterization of strain-softening laws involves a process of trial-and-error. For example, in the Boeing's program for Advanced Technology Composite Aircraft Structure (ATCAS) (Walker et al., 1991, 1992, 1993 and 1996; Ilcewicz et al., 1993), experimental results from characterization of the damage zone and also tensile coupons were used in a trial-and-error process until predictions matched results of small-notch tests. These responses were then successfully used for larger structures. Obviously, such an approach requires a large number of tests, is computationally intensive and does not provide a fundamental reasoning for the shape of the strain-softening curve that is linked to the damage properties.

Another approach, based on an assumed shape for the constitutive response, requires one to characterize the softening behaviour from relatively few tests. For example, based on an assumed linear softening shape (Figure 2-2d), one can obtain the required damage

properties by conducting three sets of experiments. From compact tension tests (Figure 2-2a), the fracture energy of the material, G_f , can be measured. By sectioning the damaged specimen and analyzing the FPZ, the characteristic damage height, h_c (Figure 2-2b), can be identified. By conducting uniaxial tensile tests (Figure 2-2c), the material strength, σ_{peak} , can also be measured. Using these values, one can construct a linear softening response for the behaviour of the material (Figure 2-2d). The main problem with such an approach is the initial assumption for the shape of the constitutive response. As noted before, the shape of the softening law depends on various parameters. A biased assumption for the shape of the constitutive response may introduce errors in the calculations and thus result in wrong predictions for the damaging behaviour of notched specimens and structural components.

The other issue with above approaches is the underlying assumption for the homogeneity of the material response. Any voids or defects, introduced in the manufacturing process, can inherently change the local behaviour of the material and consequently change its strain-softening response. As shown in other studies (e.g. Walker et al., 1993), the manufacturing method of producing a laminate, might introduce repeatable inhomogeneity at the scale of the fibre tows during automated placement processes. This results in heterogeneous fibre failure and consequently an inhomogeneous softening law. Obviously, in such cases, the proposed strain-softening law, should at least represent the average behaviour of the damaging material. This of course highlights the importance of conducting experiments to directly measure and characterize the strain-softening response of composites.

In recent years, full-field measurement techniques using high resolution cameras and powerful PCs have advanced. One of the main applications of such techniques is to identify material damage properties using measurement of kinematic field variables (strains or displacements). Compared to other indirect techniques in which constitutive parameters are inferred using global measured quantities and simplified assumptions such as homogeneity of strain, full-field measurements are more flexible and versatile methods based on much more measured quantities and fewer simplified assumptions.

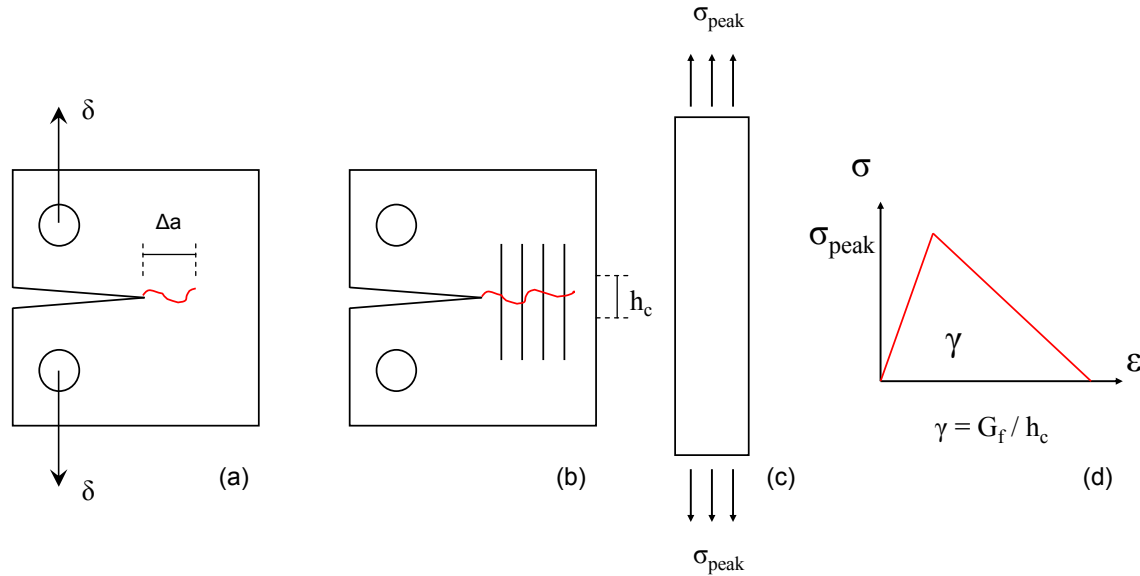


Figure 2-2 Constructing a linear softening response using three sets of experiments, (a) compact tension test to determine fracture energy, G_f , (b) sectioning the damaged specimen to measure characteristic damage height, h_c , (c) tensile test to determine the peak stress, σ_{peak} and (d) constructed constitutive response.

The traditional approach to measure kinematic field variables such as strain is to use strain gauges at selective points on the surface of a specimen during a test. Recent approaches such as line analysis (Kongshavn and Poursartip, 1999) provide more details by measuring average strains between various inscribed lines on the surface of the specimen using high resolution cameras. Full-field measurement techniques, on the other hand, measure surface strains at every point in a zone of interest on the surface of the specimen. The vast amount of data that is generated can be analyzed to obtain details of the material behaviour and its strain-softening response.

It should be noted that the identification process of material properties using full-field measurement data is limited to the cases where the surface strains represent, or at least relate, to the through-thickness strains. This is of course the case in plane strain or plane stress conditions or in the bending of thin plates. Here we review the notable techniques to indirectly measure the strain-softening response of quasi-brittle materials using full-field measurement of kinematic field variables. In the next chapter, a method is proposed that can directly identify the strain-softening response.

2.2. Field Measurements

2.2.1. Selective versus Full-field Measurement

Using Compact Tension (CT) or Over-height Compact Tension (OCT) (Kongshavn and Poursartip, 1999) geometry, damage properties of composites can be studied during progressive damage propagation. Some of these properties are fracture energy, damage initiation strain, damage length and damage height. Besides the global response of the laminate in terms of load versus pin opening displacement (POD), strain pattern around and in front of the damage zone is also needed to identify some of the above parameters.

To obtain surface strains during each test, strain gauges at selective points on the specimen surface can be mounted (Figure 2-3a). This method, which is referred to as *selective point measurement* in this study, can provide a limited data regarding the behaviour of the laminate. Using this technique, strains at selective points along a specific direction during the test are determined. Approximation and extrapolation are then needed to identify the damage front and hence measure the damage length.

In 1999, Kongshavn and Poursartip (Kongshavn and Poursartip, 1999) presented the line analysis method to monitor surface displacements during OCT tests. In this approach, using cameras, average strains between selective inscribed lines on the surface of the specimen were measured during each test (Figure 2-3b). Compared to selective point measurement, using this method which is referred to as *selective line measurement*, more data and hence more accurate damage properties are obtained.

More recently, the advancement of high resolution cameras and image processing techniques, gave rise to *full-field measurement* approaches. Using these techniques, surface displacement vectors and thus surface strains are measured during each test. For example in Digital Image Correlation technique (DIC), by treating the specimen surface with spray paints and using high resolution cameras and image processing software packages, surface strains are determined (Figure 2-3c).

By comparing above methods, it is obvious that full-field measurement approach provides us with much more data on the behaviour of the material and potentially can be

used to obtain more accurate damage properties. Various techniques to identify material constitutive parameters using full-field measurement approach have been developed and utilized in recent years. These techniques are explained in more details in this section.

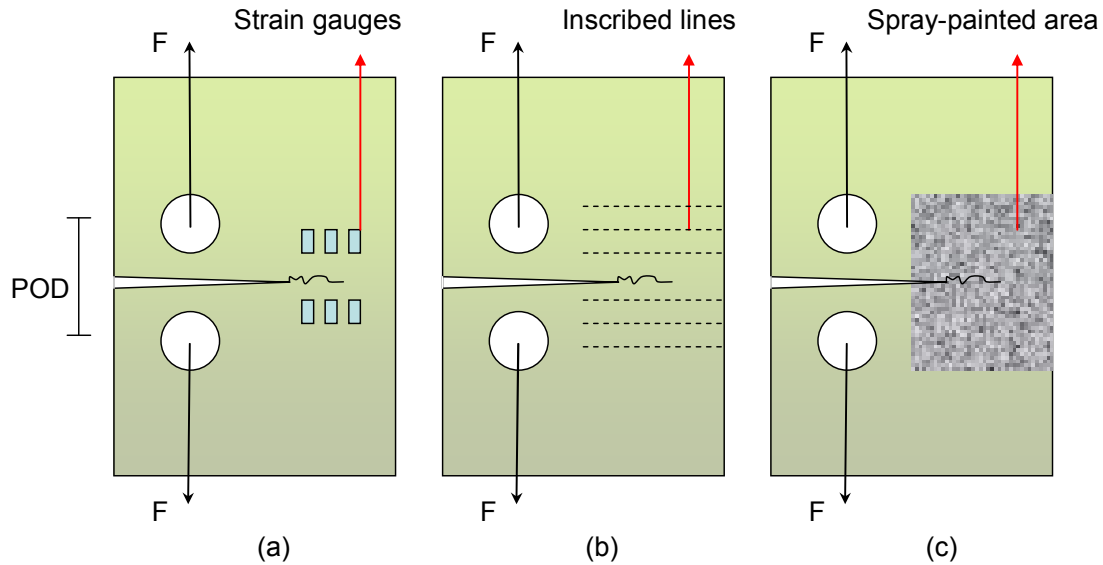


Figure 2-3 Comparison of data recording during an OCT test: (a) strain measurement at selective points using strain gauges, (b) average strain measurement between selective lines using line analysis method (Kongshavn and Poursartip, 1999) and (c) full-field measurement using Digital Image Correlation (DIC) technique.

2.2.2. Selective Line Measurement: Line Analysis

One of the early attempts to measure field kinematic quantities such as displacement vectors was the line analysis approach. The line analysis method was developed by Kongshavn and Poursartip (1999) and was used to determine damage characteristics such as crack length and fracture energy (Kongshavn and Poursartip, 1999; Mitchell, 2002; McClennan, 2004). In this approach, lines are inscribed on the surface of a specimen parallel to the crack growth direction. By taking images from the specimen surface during the test and studying the deformation of the inscribed lines, damage properties such as crack length are identified. By approximating the total dissipated energy from the area below the global load-displacement curve, the fracture energy as a function of crack length can be measured using this method.

A modified compact tension test specimen, the over-height compact tension (OCT) was developed and utilized in this approach. In an OCT specimen, the height is twice the width to prevent the influence of the boundaries on the crack propagation while producing a stable damage growth. This provides an opportunity to study and identify damage properties of composite laminates. A typical OCT specimen geometry and experimental setup is shown in Figure 2-4.

Since displacements are only measured along selective lines, compared to full-field measurements, this approach is faster and computationally inexpensive. On the other hand, the selective measurement technique, limits the capability of the line analysis method in identifying damage parameters and may also introduce errors in the identification process.

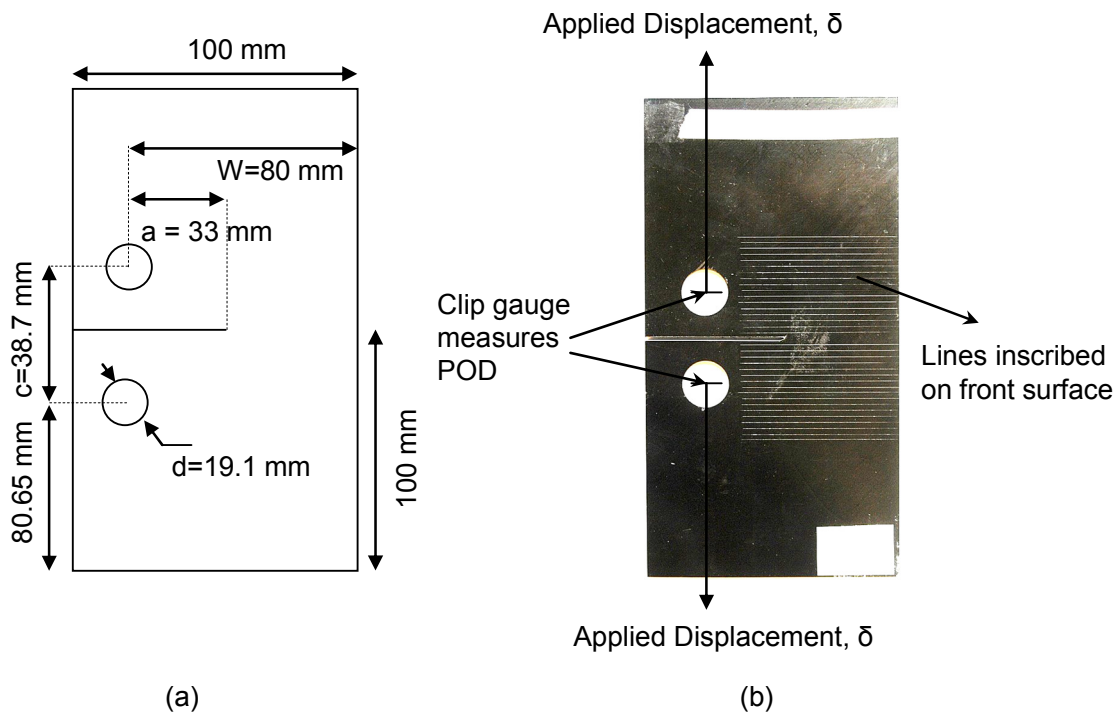


Figure 2-4 (a) OCT specimen geometry and (b) OCT experimental setup.

2.2.3. Full-field Optical Measurement

Compared to available selective measurement techniques, full-field measurements provide much more details on the behaviour of a material, hence can result in more accurate identification of damage properties. Among the notable full-field measurement techniques are *digital image correlation* (DIC) (LaVision, 2007), *Moiré and speckle interferometry* (Mollenhauer et al., 2006) and *grid method* (Avril et al., 2004; Pierron et al., 2007a and 2007b).

Moiré interferometry is an optical technique capable of measuring in-plane deformation vectors with high degree of accuracy. In this technique, the deformation is measured by exposing a diffraction grating on a specimen surface to two beams of laser lights and analyzing the changes of the return frequencies. As the specimen is deformed, a fringe pattern of the in-plane displacement is obtained. This method is very accurate but also difficult to adopt for identification of damage properties (Mollenhauer et al., 2006).

In the grid method, a grid pattern is deposited onto the specimen surface using special printers. Using high resolution cameras and image processing methods, a deformation pattern of the specimen surface during the test can be obtained. Although the grid method is not as accurate as the Moiré interferometry, it is easier to use for damage identification (Pierron et al., 2007a).

Digital image correlation (DIC) technique, adopted in this study, is based on comparing a pair of digital images obtained from a specimen surface before and after the deformation of the specimen. To obtain full-field measurement in each experiment, the surface of the specimen should be treated with a speckle pattern. Using black and white spray paints, a random pattern is applied on the surface of the specimen. Compared to the other two methods, this is the least accurate one but also the easiest to adopt.

Using the full-field displacement vectors, strain fields are calculated to be used for damage parameters identification. To obtain more accurate strain fields, polynomial fitting is used to reduce the noise and error in displacement data (Pierron et al., 2007a). In an approach that was adopted by Pierron et al. (2007a), a 17th order complete polynomial

fitting was used to reduce the noise in the displacement data. In this study, however, it was noted that in damaged areas, this method may increase the degree of noise. As a result, polynomial fitting was only used for elastic cases.

2.3. Inverse Identification of Constitutive Response

The usual problem in solid mechanics is to determine displacement, strain and stress fields by using constitutive equations and a well posed set of boundary conditions. This is called a direct problem. On the other hand, identifying the constitutive parameters is usually called an inverse problem. This can be better understood based on the following standard set of FEM equations:

$$\mathbf{K} \mathbf{U} = \mathbf{F} \quad (2-1)$$

In the above equation, \mathbf{K} is the stiffness matrix, \mathbf{U} is the displacement vector which contains the unknown degrees of freedom introduced by the FEM discretization, and \mathbf{F} is the generalized load vector. Using known constitutive parameters, the stiffness matrix can be constructed to calculate unknown displacements and loads. This is a direct problem compared to the inverse case where \mathbf{K} is unknown. In an inverse problem, constitutive parameters and hence stiffness matrix should be obtained not only based on the boundary conditions, but also measured strain or displacement fields. One way of dealing with inverse problems is to use closed form solutions which are only available for a few cases such as the uniaxial tensile test or 3-point bending test. However, usually we cannot construct a direct link between measured quantities, such as displacements, and constitutive parameters.

Using full-field measurement to implicitly identify constitutive parameters in inverse problems is a promising path that has been thoroughly explored in recent years. Here we review some of the notable proposed methods to identify constitutive parameters using full-field measurement techniques (Avril et al., 2008). These methods are listed here:

1. The finite element model updating method (FEMU)

2. The constitutive equation gap method (CEGM)
3. The virtual fields method (VFM)
4. The equilibrium gap method (EGM)
5. The reciprocity gap method (RGM)

2.3.1. Finite Element Model Updating Method

This method is based on performing finite element simulations iteratively and minimizing the error between measured and calculated values to identify constitutive parameters. In its simplest form, this method starts by assuming initial values for constitutive parameters. Using these values, one can calculate the discrepancy between known forces, F , and calculated forces, KU , in which the stiffness, K , is a function of the initial assumptions for constitutive parameters. This discrepancy is then minimized using an optimization algorithm such as the Gauss-Newton method. Iteration is continued until a pre-defined error criterion is satisfied.

Many variants of the above method have been proposed and utilized to extract parameters of both linear and nonlinear constitutive equations (Meuwissen et al., 1998; Le Magorou et al., 2002). The notable variants of this approach are FEMU-U and FEMU-F. FEMU-F is based on minimizing the discrepancy between the measured and calculated forces. The other variation, FEMU-U, is an iterative approach which minimizes discrepancy between measured and calculated displacements. In FEMU-F approach, usually a least square function, J , in the following form is minimized:

$$J = \frac{1}{2} (\bar{R} - \bar{K} \bar{U}) \bar{W} (\bar{R} - \bar{K} \bar{U}) \quad (2-2)$$

In above equation, R and U are known forces and displacements. W is a positive definite weighting matrix and K is a function of unknown constitutive parameters. In this approach, the loading distribution must be known to feed into the finite element model. In cases where only the resulting forces are measured, assumptions are made for loading distribution which inherently could introduce error in the calculations. The presence of

noise in the displacement data may also lead to an incorrect iterative result due to the accumulation of error.

Due to its ease of implementation this method is quite popular. On the other hand, iterations make this a time consuming approach. Moreover, for problems with damage propagation, the initial assumption for the damage parameters and the shape of the constitutive response may yield biased results.

2.3.2. Constitutive Equation Gap Method

This method minimizes a convex functional defined based on the distance between a given stress field and a computed stress field from an assumed constitutive response and measured displacement field in order to derive elastic properties (Geymonat, 2002; Geymonat et al., 2003). For a linearly elastic constitutive model with a given stress field, $\boldsymbol{\tau}$, and a given displacement field, \boldsymbol{v} , this gap is defined as:

$$\Delta = \frac{1}{2} \int (\boldsymbol{\tau} - \boldsymbol{A} \boldsymbol{\varepsilon}[\boldsymbol{v}]) \boldsymbol{A}^{-1} (\boldsymbol{\tau} - \boldsymbol{A} \boldsymbol{\varepsilon}[\boldsymbol{v}]) dV \quad (2-3)$$

In which \boldsymbol{A} is the elasticity tensor. This approach was initially utilized for identification of linear elastic properties and later extended to nonlinear constitutive responses (Latourte et al., 2008). This model may also be extended to determine the damage parameters for cracked specimens using the state coupling between elasticity and damage (Geymonat, 2003; Avril et al., 2008). This application, however, has not been fully exploited yet.

2.3.3. Virtual Fields Method

This approach relies on a weak form of equilibrium, the virtual work formulation, to obtain the constitutive parameters. First, based on an assumed constitutive response, the governing virtual work formula as a function of unknown constitutive parameters is derived. Next, based on well-chosen admissible virtual fields, the constitutive parameters are identified explicitly (Chalal et al., 2004; Grediac et al., 2006; Avril et al., 2008). Assuming that body forces are equal to zero, the principle of virtual work becomes:

$$-\int_{\Omega} \boldsymbol{\sigma} \boldsymbol{\varepsilon}[\mathbf{u}^*] dV + \int_S \mathbf{T} \mathbf{u}^* dV = \int_{\Omega} \rho \mathbf{u}'' \cdot \mathbf{u}^* dV \quad (2-4)$$

in which \mathbf{u}^* is an admissible virtual displacement field, \mathbf{T} is the boundary traction and \mathbf{u} is the measured displacement field. This method has been applied to a vast range of problems including linear anisotropic elasticity, nonlinear anisotropic elasticity, viscoelasticity, elastoplasticity and more recently, damage propagation (Grediac et al., 2006; Pierron et al., 2007a; Avril et al., 2008).

One of the drawbacks of the virtual fields method relates to its assumption for the constitutive model. To identify damage properties, this method relies on an assumed damage law. This assumption may lead to a biased identification of damage properties. Moreover, since this approach is based on a weak form of equilibrium, local equilibrium equations are not satisfied. This will lead to accumulation of error specially in presence of damage and may affect the accuracy of the identified constitutive parameters. In cases where the degree of noise in the measured displacement field is high, this method may not be able to identify constitutive parameters (Avril et al., 2008).

2.3.4. Equilibrium Gap Method

This method has been developed for the cases where the constitutive matrix takes the form of a scalar field:

$$\mathbf{A}(x) = C(x) \mathbf{A}_0 \quad (2-5)$$

in which \mathbf{A}_0 is known and the scalar variable $C(x)$ is used to represent 1D isotropic damage, $C(x)=1-D(x)$ (Claire et al., 2007; Avril et al., 2008).

In this approach, a FE mesh is set up based on the virtual nodes generated during full-field measurement process. The strain energy is then derived for each element. By satisfying equilibrium at each node, $C(x)$ is calculated. For damaged areas, the residual force at each node is used to calculate the 1D damage variable in each element.

This method is sensitive to the error in the displacement field measurement since the damage calculation is based on the raw displacement data. Also, the 1D assumption for damage and the scalar field assumption, limit the applicability of this approach.

2.3.5. Reciprocity Gap Method

This approach, which is based on the Maxwell-Betti reciprocity theorem, has been developed for the cases where full-field measurements are available on the boundary of the domain (Avril et al., 2008). From the Maxwell-Betti theorem, the reciprocity gap can be identified as a function of measured data on the boundary. This approach is considered as a variation of VFM for which kinematic variables are only measured on the boundary. Obviously this limits its applicability to cases where such information is available. Besides the elastic cases, this method has also been used for crack identification (Abda et al., 1999).

2.4. Comparison of Various Methods

The current available methods can be divided into two categories: Updating and Non-updating methods. Updating methods such as FEMU-U, CEGM and RGM are iterative approaches. Usually based on an initial assumption for constitutive parameters, the actual parameters are iteratively derived by minimizing a cost function. Due to the iteration process involved, these methods are usually slow and CPU-intensive. Furthermore, they may become sensitive to the noise in the displacement data (Avril et al., 2008).

Non-updating techniques such as FEMU-F, EGM and VFM, are based on an assumed constitutive response to implicitly identify constitutive parameters from the full-field measurement data. The non-updating methods are usually faster than updating methods since there is no iteration involved in the identification process. These methods, however, are more sensitive to the noise and error in the displacement data. In some cases they may fail to identify constitutive parameters due to the high degree of noise in the measured data (Avril et al., 2008).

It may be noted that in cases where these methods are utilized for damage identification (Claire et al., 2007; Pierron et al., 2007a), an assumption for the shape of the constitutive response is required. This assumption may lead to biased or incorrect estimation of damage parameters. The summary of all the current methods along with their applicability and limitations are presented in Table 2-1.

The proposed method in this study uses the advantages of both updating and non-updating techniques to identify damage parameters without invoking any prior assumption on the shape of the constitutive response. This method consists of two steps. The first step is a non-updating approach from which an approximate shape of the constitutive response can be constructed. In this step, the elastic properties of the material are needed and can be identified using any of the current available methods. The second step is an updating approach which optimizes the approximate response and consequently reduces the error sensitivity of the previous step. Since the iteration for the second step is limited to an obtained zone for the constitutive response, the optimization is much faster compared to current updating approaches. Moreover, this method doesn't suffer from any pre-assumption for the constitutive response. The advantages and disadvantages of various approaches to identify damage properties have been summarized in Table 2-2.

Table 2-1 Summary of notable methods to identify constitutive parameters using full-field measurement techniques.

| Model | Method | Application | Drawbacks |
|--------------|---|---|--|
| <i>FEMU</i> | Iterating to minimize discrepancy between measured and calculated parameters | <ul style="list-style-type: none"> - Linear elasticity - Viscoelasticity - Hyperelasticity - Elasto-plasticity | <ul style="list-style-type: none"> - Initial assumption for the loading distribution - Initial assumption for constitutive model - Computationally expensive |
| <i>CEGM</i> | Iterating to minimize a constitutive equation gap functional | <ul style="list-style-type: none"> - Linear elasticity - Elasto-plasticity | <ul style="list-style-type: none"> - Not fully developed for damage identification - Computationally expensive |
| <i>VFM</i> | Satisfying the virtual work equation based on admissible virtual fields and measured strains | <ul style="list-style-type: none"> - Linear anisotropic elasticity - Nonlinear anisotropic elasticity - Elasto-plasticity - Viscoelasticity - Damage - Dynamic Vibrations | <ul style="list-style-type: none"> - Initial assumption for constitutive model - Sensitive to the error in displacement data |
| <i>EGM</i> | Satisfying equilibrium in virtual nodes based on the calculation of strain energy in each element | <ul style="list-style-type: none"> - Scalar field elasticity - 1D damage | <ul style="list-style-type: none"> - Assumption for constitutive model in form of scalar field - 1D assumption for the damage law - Sensitive to the error in displacement data |
| <i>RGM</i> | Minimizing the reciprocity gap based on the Maxwell-Betti reciprocity theorem | <ul style="list-style-type: none"> - Linear elasticity - Crack identification | <ul style="list-style-type: none"> - Full-field measurement data on the boundary is required |

Table 2-2 Comparison of current available methods with the proposed method I this study.

| Damage identification | Advantages | Disadvantages |
|------------------------------|---|--|
| <i>Updating methods</i> | <ul style="list-style-type: none"> - Reducing noise sensitivity by using iteration. | <ul style="list-style-type: none"> - Slow and CPU-intense - Required assumption for the shape of the constitutive response |
| <i>Non-updating methods</i> | <ul style="list-style-type: none"> - Fast | <ul style="list-style-type: none"> - Noise sensitive - Required assumption for the shape of the constitutive response |
| <i>Proposed method</i> | <ul style="list-style-type: none"> - Fast - Reducing noise sensitivity by using iteration. - No assumption for the constitutive response | <ul style="list-style-type: none"> - Only applicable to pure loading modes (Mode I). |

Chapter 3: Development of A New Methodology to Extract The Strain-Softening Response

3.1. Introduction

The methodology proposed in this study uses full-field measurement of displacement to identify damage properties and strain softening response of composite laminates. Measurement of displacement vectors is performed using the DIC technique. During each test, high resolution cameras are used to capture images from the surface of the specimen while data is recorded using LaVision's DaVis software (LaVision, 2007) on a dedicated PC. Using image processing techniques, full-field displacement vectors are obtained and used in the first step of the proposed method.

The first step is a non-updating approach which uses local equilibrium equations to construct a family of approximate constitutive responses for the composite laminate. The second step involves an updating approach where iteration is used to minimize cost functions, defined based on global and also local criteria, within the limit range of the approximate constitutive responses obtained in the first step.

Since this method combines updating and non-updating techniques, it has the advantages of both approaches. For example, like other updating approaches, iteration reduces the sensitivity to noise and error in the raw displacement data. However, compared to other updating approaches, this method requires less CPU time since the iteration is limited to a region identified in the first step. Also, as noted previously, unlike other methods, no assumption is required for the shape of the constitutive response since an approximate shape of the stress-strain curve is obtained in the first step.

To identify damage parameters using the proposed method, a series of Visual Basic subroutines, referred to as CrackPro code in this study, have been developed. After importing full-field measurement data into CrackPro, a series of finite element

calculations are performed in order to construct a family of approximate constitutive responses. These approximate responses are then optimized to identify damage parameters and the strain softening response of the laminate.

In this section, the process of full-field measurement using DIC technique is first explained. Next, the two steps of the proposed method to construct constitutive response of composite laminates are described in detail. Finally an overview of the main subroutines of the CrackPro is presented.

3.1.1. Full-field Measurement Using DIC Technique

DIC technique works by comparing a pair of digital images obtained from a specimen surface before and after load application to determine a deformation vector field for each image.

Before conducting each experiment, the surface of the specimen should be treated with a speckle pattern. Using black and white spray paints, a random pattern is applied on the surface of the specimen. During the test, surface images are captured using high resolution cameras (Figure 3-1).

In this study, data from each test were recorded using LaVision's DaVis Software (LaVision, 2007) on a dedicated PC. DaVis is an acquisition software for imaging applications such as material surface imaging and deformation tracking. Using recorded images, DaVis analyzes the speckle pattern and constructs a deformation vector field. Before each analysis, a virtual mesh on the surface of the specimen is created (Figure 3-2). By comparing specimen surface patterns at time t and $t+\Delta t$, the deformation vectors for the center of the virtual elements are calculated (Figure 3-2).

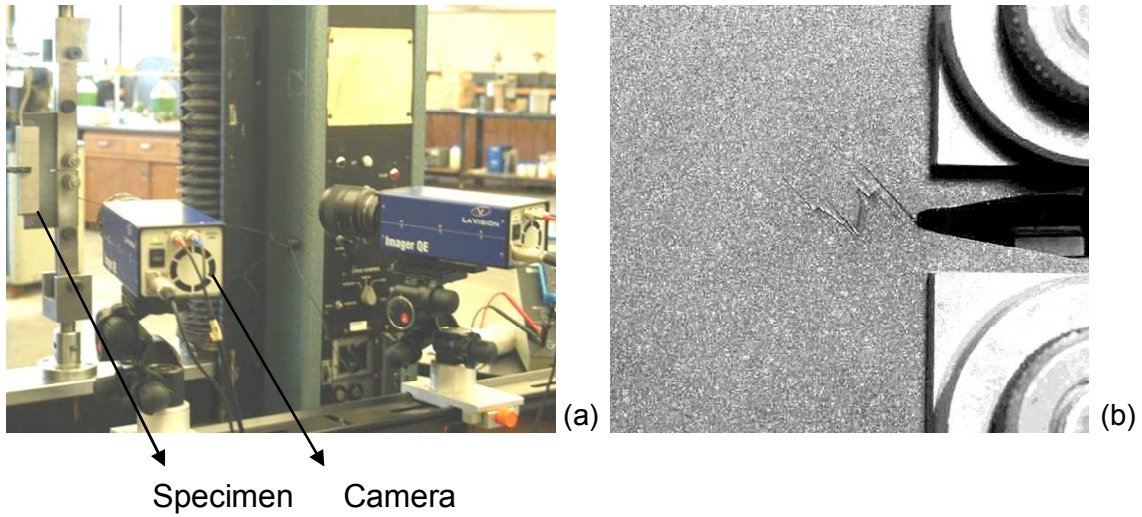


Figure 3-1 (a) DIC experimental setup and (b) treated specimen surface with black and white spray paints.

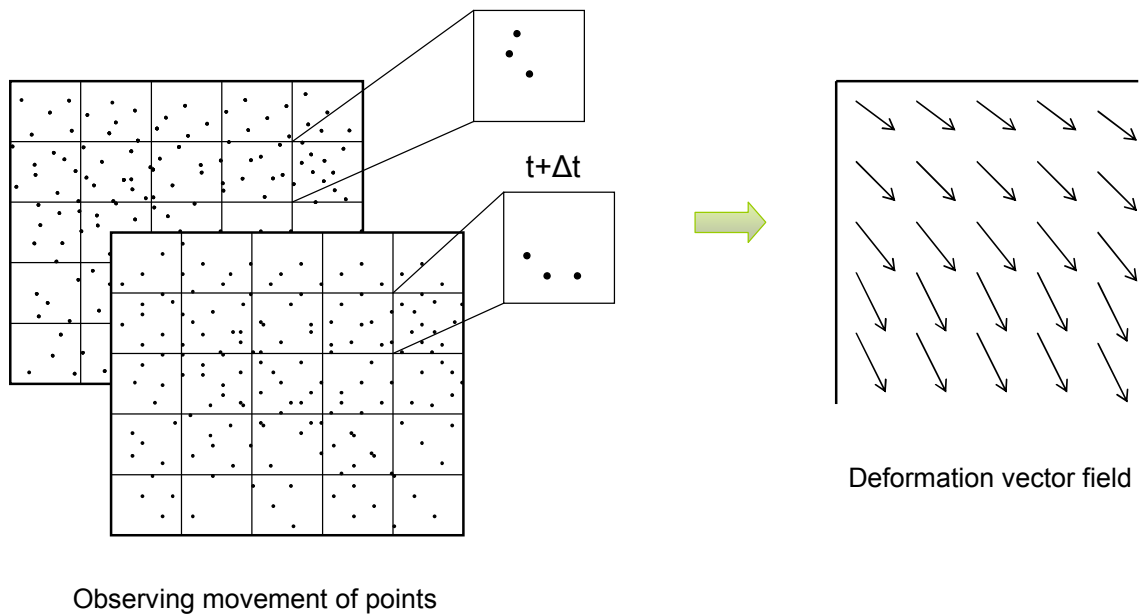


Figure 3-2 Obtaining deformation vector field by measuring displacements of virtual nodes on the specimen surface.

After measuring the full-field data, deformation vectors for an area of interest (masked area as shown in Figure 3-3), can be exported into text files. For each image, DaVis reports the deformation vector field at the virtual nodes inside the masked area.

The distance between these nodes or virtual element size is an important factor in the accuracy of calculated strains based on the exported displacement field. Important factors in determining this distance are maximum surface displacement, camera resolution, brightness and contrast on the surface of the specimen and distance between the camera and specimen. By decreasing this distance, the degree of noise in the displacement field increases. On the other hand, by increasing this distance, strain gradients on the surface of the specimen may not be captured. Based on a recommendation by the DaVis developers (Lavisio) to minimize the error in the displacement field, this distance should be larger than four times the maximum displacement on the surface of the specimen. For example, in this study, for an OCT test of a quasi-isotropic IM7/8552 composite laminate, this distance was approximately set to 2 mm based on this recommendation.

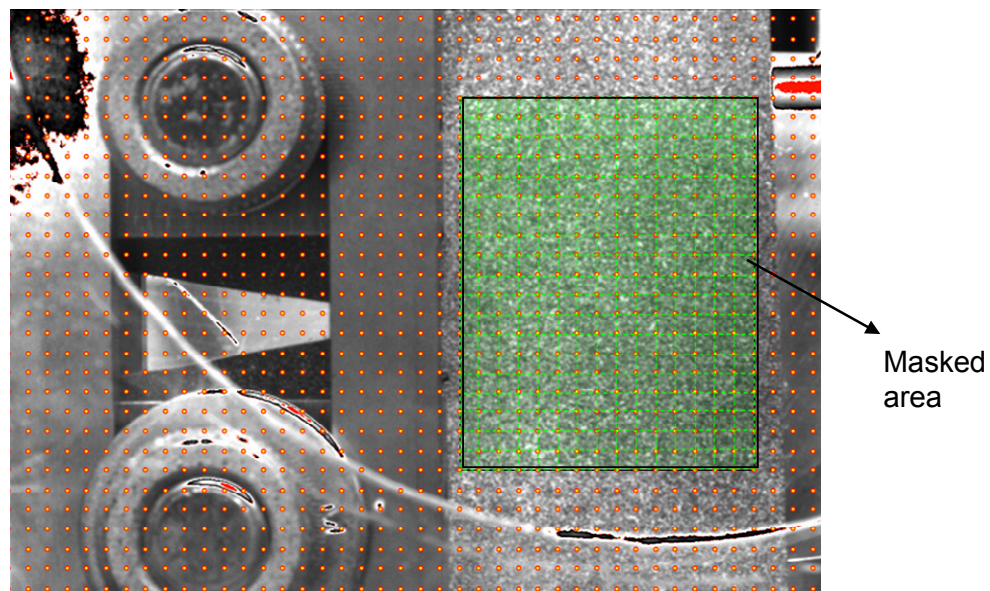


Figure 3-3 The masked area and virtual nodes generated by DaVis to calculate deformation vector field for a compact compression test.

For each test, in addition to the surface images, the applied load and pin opening displacement are also recorded. Therefore for each test, DaVis also reports a recorded load-displacement curve and surface images associated with points on this curve. This global load-displacement curve, along with the measured displacement vectors are used in the current study to identify composite damage parameters and construct an

appropriate constitutive response. An example of recorded data using DaVis software is shown in Figure 3-4.

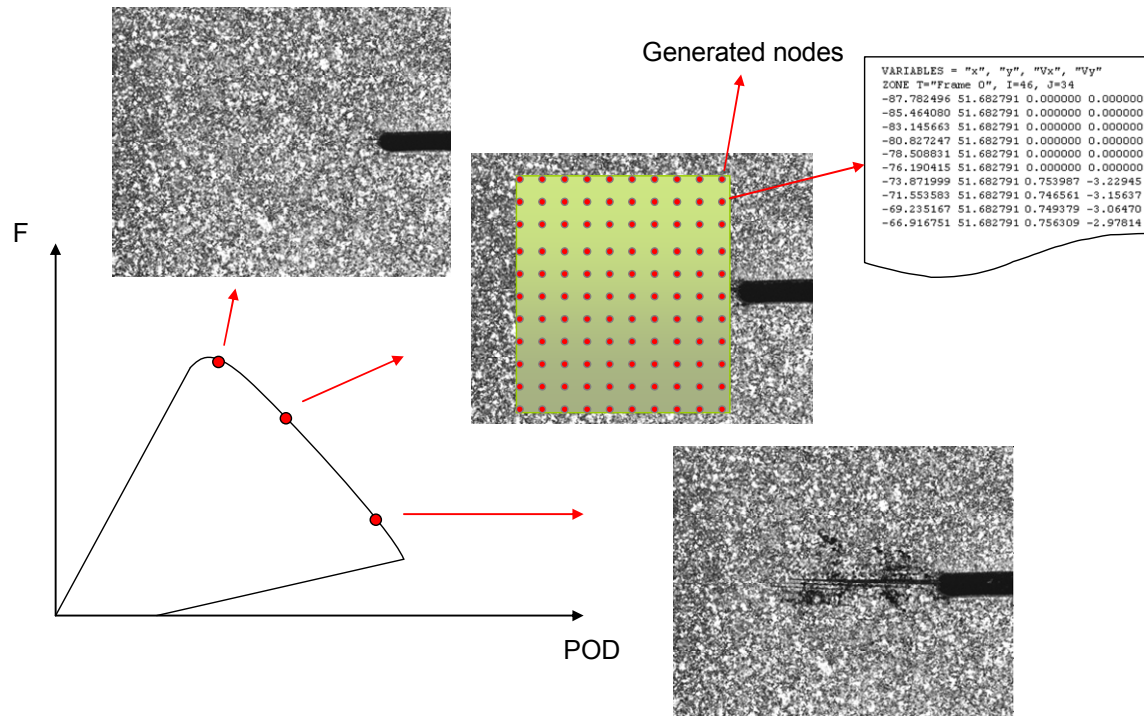


Figure 3-4 An example of specimen surface images and load-displacement curve recorded by DaVis during a test. Displacement vectors are exported for the virtual nodes generated by DaVis.

3.2. Step I: Construction of an Approximate Constitutive Response

3.2.1. Introduction

In this step, using displacement vectors reported by DaVis, strains in the whole domain and also stresses in the elastic zone are calculated. By checking the equilibrium condition at each node, the damaged area is identified as follows. If all the elements attached to one node are elastic, equilibrium will be satisfied at that node (i.e. the nodal forces contributed by all elements sharing that node sum up to zero or a value that is deemed to be within an acceptable tolerance). On the other hand, if equilibrium is not satisfied (i.e. sum of the internal forces exceed the tolerance limit), then one or more elements attached to that node are damaged. This method can be applied to the whole measured field to

detect the damage zone corresponding to each image. Afterward, based on some simplified assumptions, in a longitudinal strip of elements, the stress (σ_y for OCT and CC tests) in the damaged element(s) is taken to be the same as the stress in the undamaged element(s) within that strip under Mode I loading. Using the average strain of the damaged elements together with this approximate stress value, an approximate stress-strain response of the damaged material can be constructed. Under mixed Mode I/II loading, however, this approximate response cannot be constructed and only the damage region can be detected. These steps are explained in more details next.

3.2.2. Strain Calculation

The exported displacement field from DaVis software is used to calculate surface strains. Based on the generated nodes in DaVis, a 2D FE mesh using 4-noded elements is constructed (Figure 3-5).

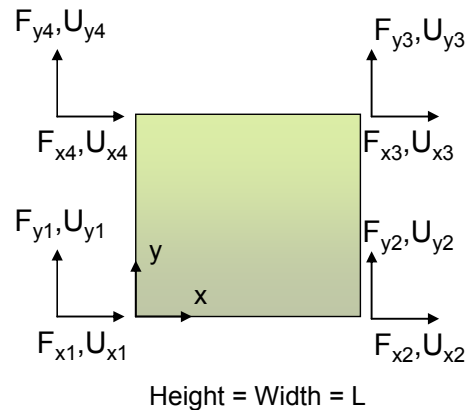


Figure 3-5 An assumed 4-noded element based on the generated nodes in DaVis software.

For the 4-noded element shown in Figure 3-5, the displacement shape functions, N_i , and also the strain-displacement matrix, \mathbf{B} , are given:

$$\begin{aligned}
 N_1 &= (1-x/L)(1-y/L) & N_3 &= (x/L)(y/L) \\
 N_2 &= (x/L)(1-y/L) & N_4 &= (1-x/L)(y/L)
 \end{aligned} \tag{3-1}$$

$$\mathbf{B} = \begin{bmatrix} \frac{dN_1}{dx} & 0 & \frac{dN_2}{dx} & 0 & \frac{dN_3}{dx} & 0 & \frac{dN_4}{dx} & 0 \\ 0 & \frac{dN_1}{dy} & 0 & \frac{dN_2}{dy} & 0 & \frac{dN_3}{dy} & 0 & \frac{dN_4}{dy} \\ \frac{dN_1}{dy} & \frac{dN_1}{dx} & \frac{dN_2}{dy} & \frac{dN_2}{dx} & \frac{dN_3}{dy} & \frac{dN_3}{dx} & \frac{dN_4}{dy} & \frac{dN_4}{dx} \end{bmatrix}$$

The element strain vector is calculated as :

$$\boldsymbol{\varepsilon} = \begin{Bmatrix} \varepsilon_x \\ \varepsilon_y \\ \gamma_{xy} \end{Bmatrix} = \mathbf{B} \mathbf{U} \tag{3-2}$$

Where \mathbf{U} is the measured nodal displacement vector. Therefore, the calculated strains at the center of the element are as follows:

$$\begin{aligned}
 \varepsilon_x &= \frac{U_{x2} + U_{x3} - U_{x1} - U_{x4}}{2L} \\
 \varepsilon_y &= \frac{U_{y3} + U_{y4} - U_{y1} - U_{y2}}{2L} \\
 \gamma_{xy} &= \frac{U_{y2} + U_{y3} - U_{y1} - U_{y4} + U_{x3} + U_{x4} - U_{x1} - U_{x2}}{4L}
 \end{aligned} \tag{3-3}$$

The accuracy of the above equations depends on the degree of noise and error in the raw displacement data. One way of reducing the error in calculated strains is to use data fitting for displacement vectors. In a study by Pierron et al. (2007a) the N^{th} order polynomial fitting was used to reduce the error in strain calculation. After some investigations, a 17th order complete polynomial was used in their study for data fitting. One might want to start with local differentiation which is the least square fitting to define the best plane through the deformation data set. To increase the accuracy of data

fitting technique, the degree of polynomial can be increased until satisfactory results are achieved.

To fit a N^{th} order polynomial to the displacement data, initially, a complete polynomial is assumed in the following form for the displacements in the x direction:

$$P_{ux} = \sum_{i=0}^N \sum_{j=0}^N a_{ij} x^i y^j \quad (3-4)$$

In this equation, x and y are coordinates and a 's are unknown coefficients. In the same manner, we can also define P_{uy} for the displacements in the y direction. To derive the values of these coefficients, a cost function, defined based on the measured and calculated displacement values, is minimized:

$$R = \sqrt{\sum_{i=0}^m (P_{ux} - U_x)^2} \quad (3-5)$$

In which U_x is the measured displacements in the x direction and m is the total number of nodes. To minimize this cost function, derivatives with respect to unknown coefficients are set to zero:

$$\frac{\partial R}{\partial a_{ij}} = 0 \quad (3-6)$$

For a complete N^{th} order polynomial, there are N^2 unknown coefficients and N^2 derivatives from which all the unknowns are calculated.

In this study, using polynomial data fitting, satisfactory results were obtained with a 10^{th} order complete polynomial. However, it was noted that by using this method, the degree of noise and error for strains in the damaged area increased. As a result, in this study, polynomial fitting was only used for the elastic cases.

3.2.3. Damage Detection

In this first step, it is assumed that elastic properties of the composite laminate such as Young's modulus and Poisson's ratio are known. Various approaches are available for obtaining these properties. One method is to conduct tensile tests on composite coupons to obtain these properties using readings of mounted strain gauges. The other method is

to use laminate plate theory. Knowing the lay-up of the laminate and also elastic properties of the lamina, we can derive the elastic properties of the laminate. In another approach, full-field measured data can be used to identify elastic properties using any of the current available techniques such as the virtual fields method (Chalal, 2004; Grediac et al., 2006).

Knowing the material properties of the laminate and assuming that the laminate is elastic and undamaged, stresses and consequently nodal forces in each element can be calculated using standard FE equations. For the assumed 4 noded element (Figure 3-5), the plane stress material stiffness matrix, \mathbf{D} , is given below:

$$\mathbf{D} = \begin{bmatrix} \frac{E_x}{1-\nu_{xy}\nu_{yx}} & \frac{\nu_{yx}E_x}{1-\nu_{xy}\nu_{yx}} & 0 \\ \frac{\nu_{xy}E_y}{1-\nu_{xy}\nu_{yx}} & \frac{E_y}{1-\nu_{xy}\nu_{yx}} & 0 \\ 0 & 0 & G_{xy} \end{bmatrix} \quad (3-7)$$

In which E_x , E_y and G_{xy} are elastic moduli and ν_{xy} and ν_{yx} are major and minor Poisson's ratios. To calculate nodal forces, we need to construct the element stiffness matrix using the material stiffness matrix and shape functions based on the standard formulation given below:

$$\mathbf{K} = \int_0^L \int_0^L \mathbf{B}^T \mathbf{D} \mathbf{B} t \, dx dy \quad (3-8)$$

In which t is the thickness of the element. Finally we can derive nodal forces of the assumed 4 noded elastic element (Figure 3-5) as presented here:

$$\begin{bmatrix} F_{x1} \\ F_{y1} \\ F_{x2} \\ F_{y2} \\ F_{x3} \\ F_{y3} \\ F_{x4} \\ F_{y4} \end{bmatrix} = \mathbf{K} \begin{bmatrix} U_{x1} \\ U_{y1} \\ U_{x2} \\ U_{y2} \\ U_{x3} \\ U_{y3} \\ U_{x4} \\ U_{y4} \end{bmatrix} \quad (3-9)$$

The elasticity assumption in these calculations will be violated when damage starts to propagate. The method presented here to identify the damage zone is to check the equilibrium at each node. Within the measured field, each node is shared by four elements as previously shown in Figure 3-3. If all the elements attached to a node remain elastic, the sum of all nodal forces will be within an acceptable tolerance. On the other hand, if the sum of the nodal forces exceeds the tolerance limit, one or more elements attached to that node are damaged. By checking equilibrium equations in all nodes, the damage zone corresponding to each image can be detected. This is explained in the following simple example. Assume that there are 9 elements, Elem₁-Elem₉, in a measured field as shown in Figure 3-6. There are 4 nodes within the measured domain, n₁-n₄, each of which is shared by four elements. Let's assume that equilibrium is satisfied in three of the nodes, n₂-n₄, but not in n₁. For these nodes, we can write:

$$\begin{cases} \sum F_x = 0 \\ \sum F_y = 0 \end{cases} \text{ in nodes } n_2, n_3 \text{ and } n_4 \quad (3-10)$$

$$\begin{cases} \sum F_x \neq 0 \\ \sum F_y \neq 0 \end{cases} \text{ in node } n_1 \quad (3-11)$$

Since elements 5, 6, 8 and 9 are connected to n₄ and equilibrium is satisfied at this node, it can be concluded that these elements are elastic and undamaged. The same argument can be applied to nodes n₂ and n₃ to identify elements 2, 3, 4 and 7 as undamaged. Since equilibrium is not satisfied in node n₁, nodal forces calculated from elastic properties for

one or more elements attached to this node are not correct. This means that one or more elements among Elem₁, Elem₂, Elem₄ and Elem₅ are damaged. Since from equilibrium in other nodes Elem₂, Elem₄ and Elem₅ were identified as undamaged, we can conclude that Elem₁ is damaged. This argument is schematically depicted in Figure 3-7.

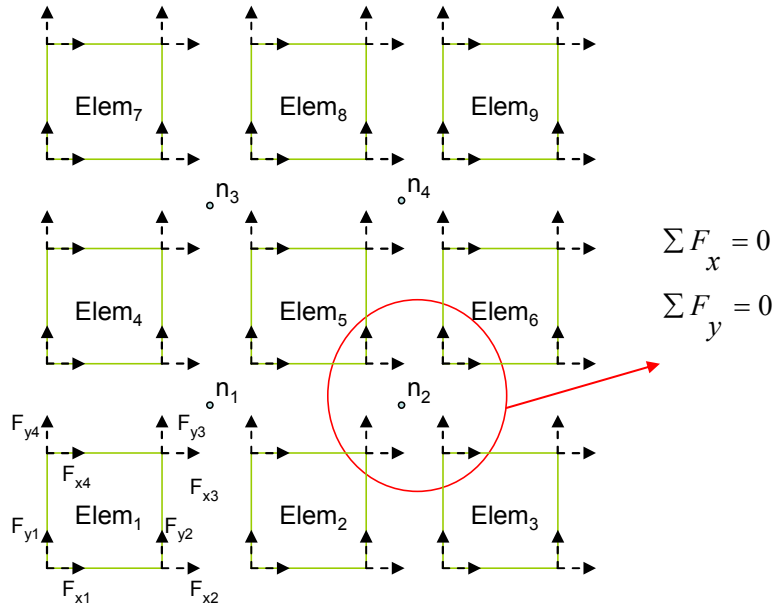


Figure 3-6 Satisfying equilibrium at each node by calculating nodal forces in each element.

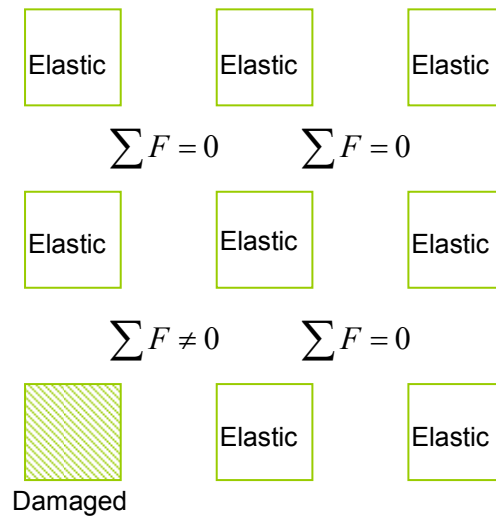


Figure 3-7 Detecting damage zone by checking equilibrium at each node.

As explained previously, accuracy of the calculated nodal forces depends on the degree of error in the measured displacement data. Due to the noise in displacement data and subsequently error in calculated nodal forces, we might not be able to satisfy equilibrium even for the undamaged parts of the composite laminate.

Assuming that the average error in the DIC process to measure displacement vectors is e_d , for the 4-noded element (Figure 3-5), the error in the calculated strains is:

$$e_\varepsilon = \frac{2e_d}{L} \quad (3-12)$$

As mentioned earlier, from this equation one can conclude that the error in the strain field decreases by increasing the element size. On the other hand by increasing the element size, any gradient in the strain field might be ignored. Maximum error in nodal forces can be obtained from multiplying the displacement error by the element stiffness matrix:

$$e_F = K e_d \quad (3-13)$$

Eventually, the maximum error in nodal equilibrium is obtained as follows:

$$e_{equilibrium} = 4 e_F \quad (3-14)$$

which is the maximum allowable tolerance for satisfying equilibrium equations at each node. This means that if the remaining force at each node is larger than this tolerance, it cannot be attributed to the error in the acquired displacement data. Therefore, to detect the damage zone, we should modify the criterion in satisfaction of equilibrium as follows:

$$\sum F < e_{equilibrium} \rightarrow \text{Equilibrium is satisfied} \quad (3-15)$$

A better approach to measuring the average tolerance is to calculate this value from remaining equilibrium forces in undamaged parts of the composite laminate. For example, in an OCT test, in the early stages of load application, the composite laminate is not damaged. Using the DIC technique, we can measure the displacement vectors on the surface of the laminate. Since this is an elastic body, following the above procedure to

calculate nodal forces, we should be able to satisfy equilibrium at all nodes. At this stage, any remaining forces from the equilibrium equations can be attributed to the error in the measured displacement vectors. Using this technique and averaging the remaining forces in all nodes, we can calculate an average value for the equilibrium tolerance as follows:

$$\bar{e}_{equilibrium} = \sqrt{\frac{\sum_{i=0}^m e_i^2}{m}} \quad (3-16)$$

where m is the number of nodes inside the area of interest. In order to further reduce the effect of noise and error on the detected damage zone, a strain averaging technique was utilized in this study. This technique is based on a common assumption that when an effective strain in an element reaches a critical value, damage propagates (e.g. Williams, 1998; Williams et al., 2003; Floyd, 2004; McGregor, 2005). Usually the effective strain or damage potential is defined as a function of all the strains in the element. For example, in a study by Williams et al. (2003) this function was defined as:

$$F(\varepsilon) = \sqrt{\left(\frac{\varepsilon_x}{K}\right)^2 - \left(\frac{\varepsilon_x}{K}\right)\left(\frac{\varepsilon_y}{L}\right) + \left(\frac{\varepsilon_y}{L}\right)^2 + \left(\frac{\gamma_{xy}}{S}\right)^2 + \left(\frac{\gamma_{yz}}{T}\right)^2 + \left(\frac{\gamma_{zx}}{U}\right)^2} \quad (3-17)$$

where K , L , S , T and U are constant values. In a test such as OCT in which ε_y dominates the other strains, this effective strain can be approximately set to ε_y .

In each element, when this potential function reaches a critical value, damage starts to grow. This function can be used to find an average critical strain value in each test based on the strains on the boundary of the detected damage zone. This average value approximately represents the critical strain which is also referred to as the damage initiation strain, ε_i . For example, in Figure 3-8, assuming that there are n elements on the boundary of the damage zone, the damage initiation strain is calculated as:

$$\varepsilon_i = \frac{\sum_{i=0}^n F(\varepsilon_i)}{n} \quad (3-18)$$

It should be noted that in the above equation, strains should be calculated on the boundary of the damage zone. In this study, this average critical strain value is used to reduce the effect of displacement error on the detected damaged area.

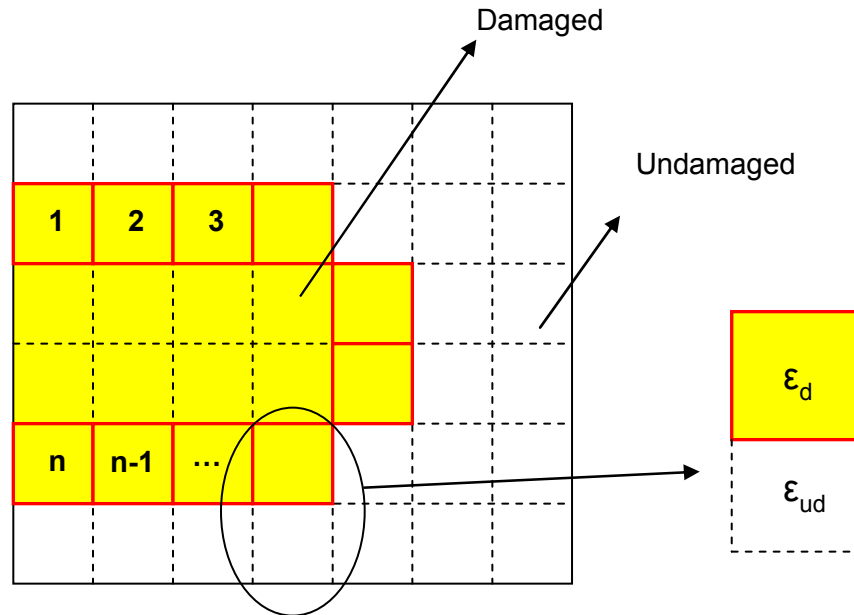


Figure 3-8 Checking strains on the boundary of the damage zone to calculate an average damage initiation strain. ϵ_d and ϵ_{ud} denote strains in the damaged and undamaged elements.

The steps involved in detecting the damage zone is now summarized here:

1. Use the DIC method for full-field measurement of displacement vectors.
2. Use polynomial fitting to reduce the noise in displacement data.
3. Calculate nodal forces using known elastic properties.
4. Measure an average allowable tolerance, $\bar{e}_{equilibrium}$, for satisfying equilibrium of nodal forces.
5. Compare the residual forces from equilibrium at each node to the tolerance, $\bar{e}_{equilibrium}$, to detect the damage zone.

6. Calculate strains.
7. Calculate an average critical strain value from the strains on the boundary of the damage zone.
8. Use the average critical strain value to reduce the effect of displacement error on the detected damaged area.

3.2.4. Construction of an Approximate Stress-Strain Curve

After identifying the damage zone, using a few simplified assumptions, a family of approximate stress-strain curves for the material is constructed. It should be noted that these approximate responses are simply used to provide a crude estimate of the cloud of points (or bounds) in the stress-strain space within which a more accurate representation of the stress-strain curve will be sought using an optimization technique to be discussed later.

Assume that kinematic variables such as displacement vectors are known in a 2D body, Ω , using a full-field measurement technique. Also assume that the undamaged region, Ω_{ud} , and the damaged region, Ω_d (Figure 3-9) have been identified in this body using the methodology presented in this study. The known quantities in this body are 2D strains and also stresses in the undamaged region ($\sigma_{ud} = \mathbf{D}\cdot\epsilon$). The unknown parameters are stresses inside the damage zone which are to be approximately determined in this section.

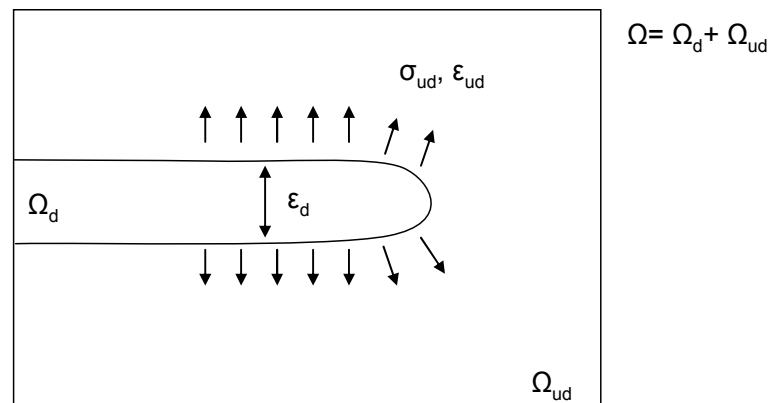


Figure 3-9 Identifying known parameters in a 2D damaged body: σ_{ud} and ϵ_{ud} in the undamaged region, Ω_{ud} and ϵ_d in the damaged region, Ω_d .

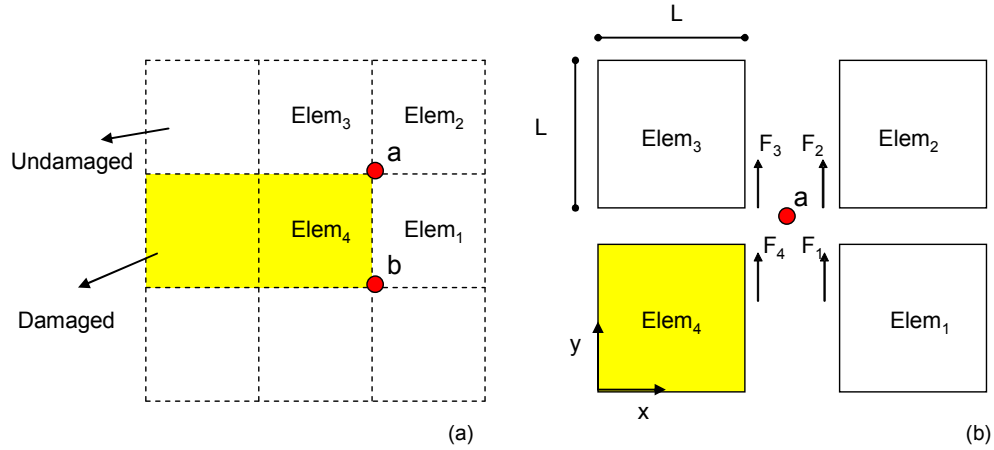


Figure 3-10 (a) Satisfying equilibrium at the tip of the damage zone, node “a” and (b) nodal forces for elements at the damage tip.

Assume that the FE mesh has been set such that only one row of elements fills the damage zone as shown in Figure 3-10a. By calculating nodal forces in the y direction for the elements connected to node a in Figure 3-10b, using one integration point to calculate stresses in the center of each element, we have:

$$\begin{aligned}
 F_1 &= \frac{tL}{2}(\sigma_{y_1} - \tau_1) \\
 F_2 &= \frac{-tL}{2}(\sigma_{y_2} + \tau_2) \\
 F_3 &= \frac{-tL}{2}(\sigma_{y_3} - \tau_3) \\
 F_4 &= \frac{tL}{2}(\sigma_{y_4} + \tau_4)
 \end{aligned}
 \tag{3-19}$$

In which L is the element size and t is the element thickness. σ_y and τ are nominal stress in the y direction and shear stress respectively. Similarly we can calculate nodal forces in the x direction. To satisfy the equilibrium condition at node a , we should have:

$$\begin{cases} \sum F_x = 0 \\ \sum F_y = 0 \end{cases}
 \tag{3-20}$$

The unknown parameters in the above equations are σ_x , σ_y and τ in element 4. By satisfying equilibrium at node b (Figure 3-10a), the total number of equilibrium equations

in front of the damage zone will be 4. Therefore there are enough equations to calculate all the unknowns. In a symmetric case, such as OCT geometry, where shear strain is equal to zero in element 4, there are 2 unknowns and 2 equations (equilibrium in node a and b results in the same set of equations). On the other hand, even for a case with two elements within the damage height, there are enough equations (6 equations: two at each node) to calculate all the unknown stresses inside the damage zone (6 stresses: 3 for each element). After finding the stresses in the damage front, the stress distribution inside the damage zone can be calculated following the same procedure.

Although in theory using this method the stresses inside the damage zone can be calculated, there are two main issues that limit the applicability of this approach. One issue is that when the number of elements in the damage height exceeds two elements, the number of equations will be less than unknown parameters and therefore it is not possible to calculate stresses inside the damage zone. One way of dealing with this problem is to remesh the surface area that the damage height is covered with only two elements.

The other issue is the presence of noise and error in the measured displacement data. As explained previously, this issue prevents the exact satisfaction of equilibrium equations and therefore the accuracy of the calculated stresses inside the damage zone will be affected.

The above issues prevent the exact calculation of stresses inside the damage zone and force us to seek an alternative approximate approach. As mentioned previously, all the approximations and assumptions at this stage are simply used to provide an estimate of the stress-strain response within the damage zone and an optimized representation of the softening response will be obtained later.

To proceed with the estimation of stresses, we assume that the damage zone is narrow enough (i.e. small damage height) such that the stress along the damage height can be considered constant (i.e. negligible stress gradient normal to the crack path). In a plane

strain or plane stress problem, possible failure modes are Mode I (opening mode), Mode II (sliding or shearing mode) and mixed Mode I/II as depicted in Figure 3-11.

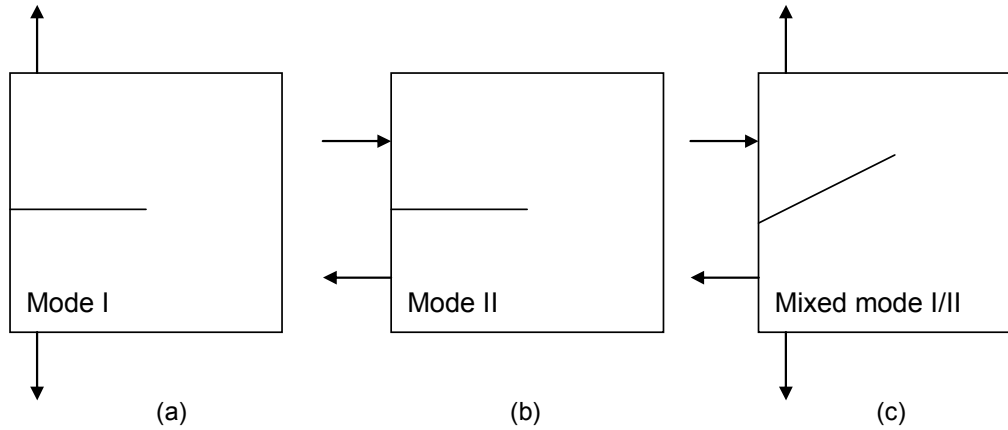


Figure 3-11 Illustration of in-plane failure modes: (a) model I (opening mode), (b) Mode II (sliding mode) and (c) mixed Mode I/Mode II.

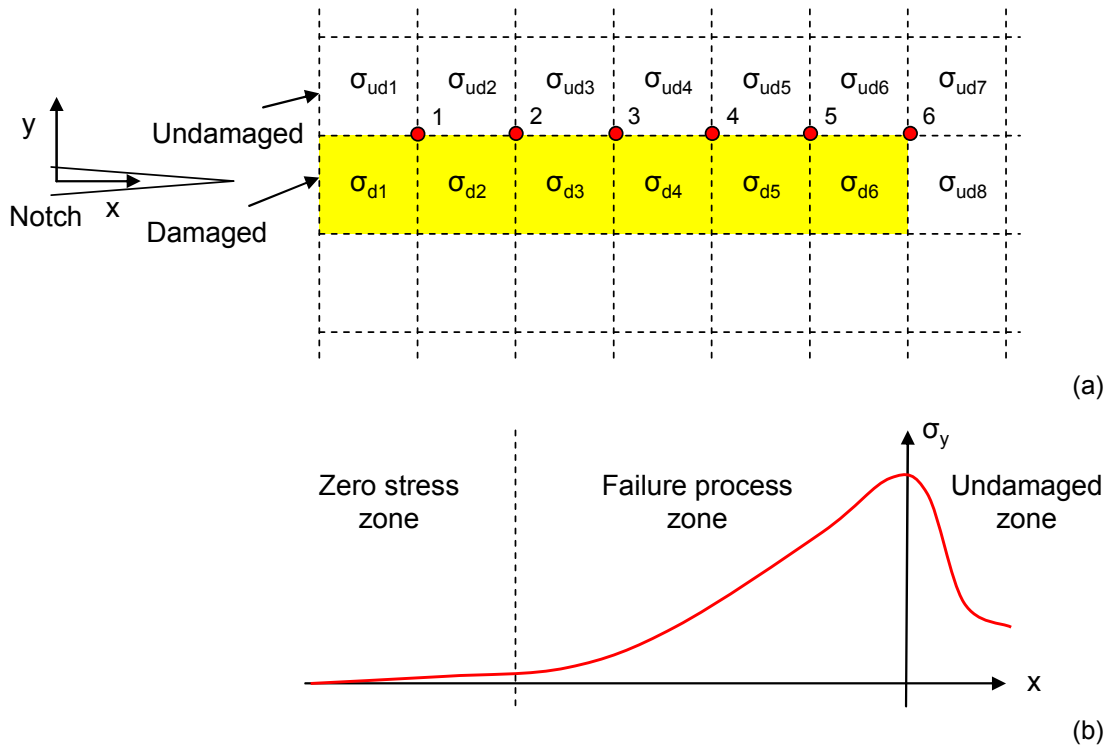


Figure 3-12 (a) Damage zone identified using the proposed method and (b) stress distribution in the damage zone.

Assume that for the Mode I of failure in a specimen (e.g. OCT or CC tests), the damage zone has been identified using the process explained in this chapter as shown in Figure

3-12a. Also assume that stress distribution in the damage zone along the opening direction (y direction in Figure 3-12) is known such that:

$$\begin{aligned}\sigma_{d1} &= \sigma_{d2} = 0 \\ \sigma_{d6} &> \sigma_{d5} > \sigma_{d4} > \sigma_{d3} > 0\end{aligned}\tag{3-21}$$

Also, for Mode I failure, due to symmetry of the geometry, loading conditions and boundary conditions, we can assume that the shear stress around the damage zone is negligible comparing to the stresses along the opening direction (i.e. $\tau \ll \sigma_d$ & σ_{ud}). Now by rewriting Equation 3-20 for node 1 we have:

$$\begin{cases} \sum F_y = 0 \\ \tau \ll \sigma_d \text{ \& } \sigma_{ud} \end{cases} \Rightarrow \sigma_{d1} + \sigma_{d2} = \sigma_{ud1} + \sigma_{ud2}\tag{3-22}$$

Therefore since $\sigma_{d1} = \sigma_{d2} = 0$ and the product of the two undamaged stresses $\sigma_{ud1} \cdot \sigma_{ud2} \geq 0$ (i.e. for tensile or compressive loadings, these two stresses are in the same direction), we have:

$$\sigma_{d1} = \sigma_{d2} = \sigma_{ud1} = \sigma_{ud2} = 0\tag{3-23}$$

By rewriting Equation 3-20 for nodes 2, 3, 4 and 5, we have:

$$\begin{aligned}\sigma_{d2} + \sigma_{d3} &= \sigma_{ud2} + \sigma_{ud3} \rightarrow \sigma_{d3} = \sigma_{ud3} \\ \sigma_{d4} &= \sigma_{ud4} \\ \sigma_{d5} &= \sigma_{ud5} \\ \sigma_{d6} &= \sigma_{ud6}\end{aligned}\tag{3-24}$$

These equations all imply that when shear stress around a narrow damage band is negligible (i.e. $\partial\tau_{xy}/\partial x = 0$), using the stress distribution on the boundary of the damage zone, we can approximately obtain stresses inside the damage zone. In fact, by writing the equilibrium equation along the y direction in Figure 3-12 and neglecting the shear stress around the damage zone, we have:

$$\begin{cases} \frac{\partial\sigma_y}{\partial y} + \frac{\partial\tau_{xy}}{\partial x} = 0 \\ \frac{\partial\tau_{xy}}{\partial x} \approx 0 \end{cases} \rightarrow \frac{\partial\sigma_y}{\partial y} = 0\tag{3-25}$$

Which implies that stresses along the y direction around the damage zone can be assumed constant. To investigate the accuracy of this approximation, FE simulation of the Mode I failure in a single-edge-notched (SEN) specimen was carried out in the commercial explicit FE code, LS-DYNA. A mesh consisting of 1x1 mm elements was generated for a 20x50 mm SEN specimen size. To simulate the strain-softening behaviour of the damaged material, the built-in material model, MAT_081 (MAT_PLASTICITY_WITH_DAMAGE) was used. Using this material model, a multi-linear strain softening response can be defined for the elements. Upon exceeding the damage initiation strain, damage starts to grow and continue to evolve until reaching a saturation strain. In this simulation, damage initiation and saturation strains were assumed to be equal to 1% and 10%, respectively, with a linear strain-softening response. Stress distribution along the opening direction (y) was obtained and is shown in Figure 3-13 and Figure 3-14.

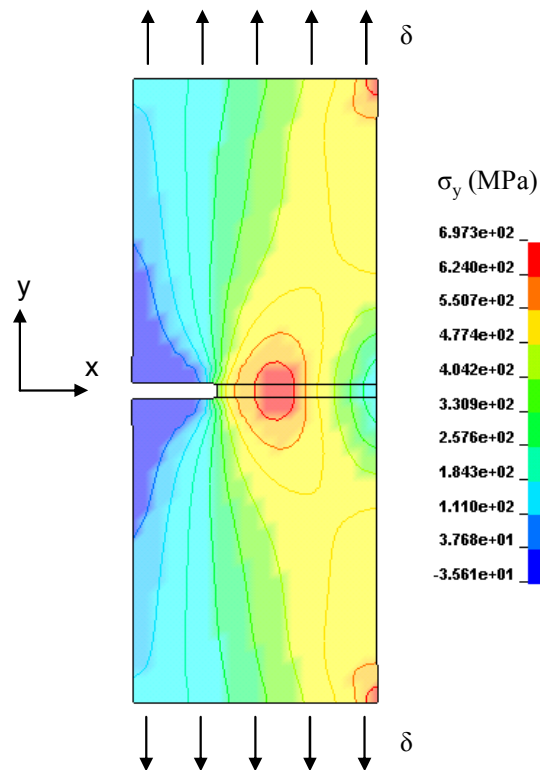


Figure 3-13 Stress distribution along the y direction in a single-edge-notched specimen.

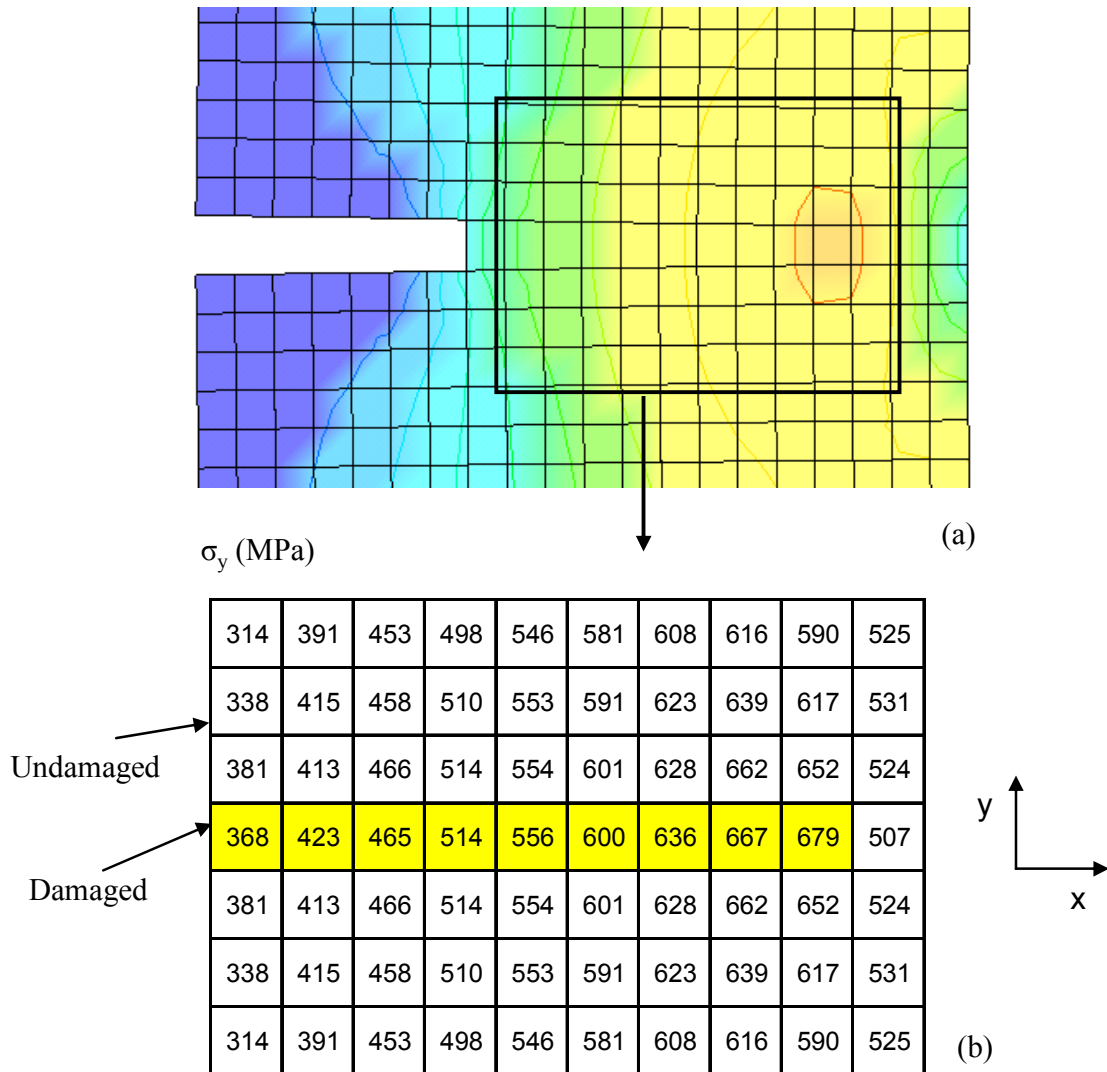


Figure 3-14 (a) Finite element mesh to simulate the Mode I failure in a SEN specimen and (b) stresses along the y direction, σ_y , around the damage zone.

From these figures, it can be observed that the stresses in the y direction along various longitudinal strips and in the vicinity of the damage zone are almost constant. In fact the average difference between stresses in the damaged elements and stresses in the undamaged surrounding elements is about 1.5% in Figure 3-14. This simulation validates the assumption that the stress distribution in the damage zone can be approximately inferred from the stresses on its boundary. It should be noted that, for the Mode II failure (Figure 3-11b), using the same procedure and neglecting normal stresses, in theory, one can obtain the approximate shear stress distribution in the damage zone. For the mixed mode failure (Figure 3-11c), however, no approximate response can be constructed. This

implies that the current approximation to obtain the stress-strain response of the material is only applicable to Mode I and Mode II failure. It should be noted that the damage detection process explained previously is not limited to pure failure modes and can be applied to mixed modes as well. The applicability of the proposed method to Mode II and mixed mode of failure, however, has not been studied here and is left for future work.

Based on the above verification study, for Mode I loading, in a longitudinal strip of elements, the stress, σ_y , in the undamaged element is assumed to be an approximate representation of the stress in the damaged element(s) within that strip, i.e. σ_{avg} (Figure 3-15b).

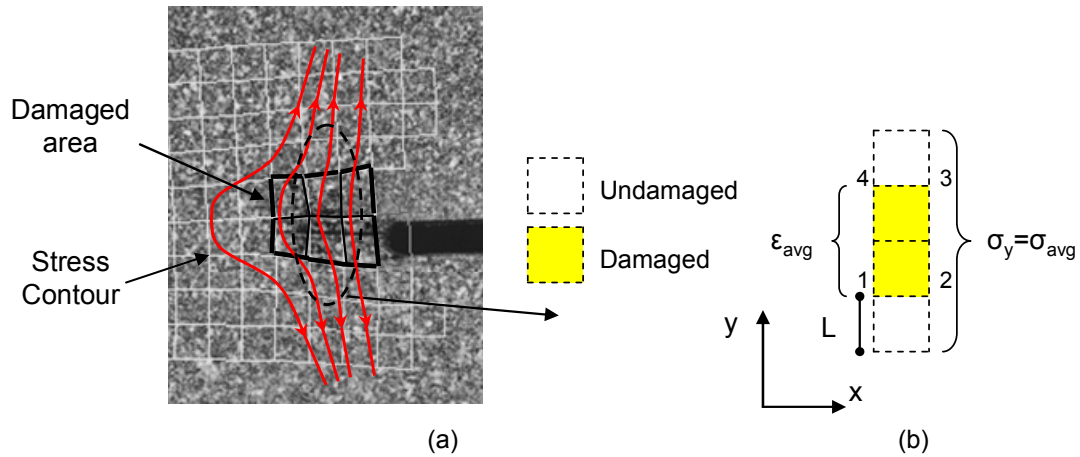


Figure 3-15 (a) Stress distribution around the damage zone in OCT test and (b) approximating the stress inside the damage zone using a representative strip of elements.

In this longitudinal strip of elements (Figure 3-15b), an average value for the strain in the damaged elements is calculated based on the displacement vectors as follows:

$$\epsilon_{avg} = \frac{U_{y3} + U_{y4} - U_{y1} - U_{y2}}{4L} \quad (3-26)$$

In which ϵ_{avg} is the average strain for the damaged elements and U is the displacement at the corners of that strip of elements. Using the average strain of the damaged elements together with the approximate average stress value, a stress-strain pair $(\sigma_{avg}, \epsilon_{avg})$ for a given strip of elements can be evaluated in a single image. By applying this procedure to all images, we can construct an approximate stress-strain response for each strip (e.g.

Figure 3-16). This approximation basically provides us with a tool to estimate the stress-strain response of the damage zone. Providing that: (1) the height of the damage zone is relatively small compared to other dimensions of the specimen, and (2) shear stresses are small and negligible around the damage zone, this approximation becomes an acceptable representation of the stress flow in the damage zone for Mode I failure.

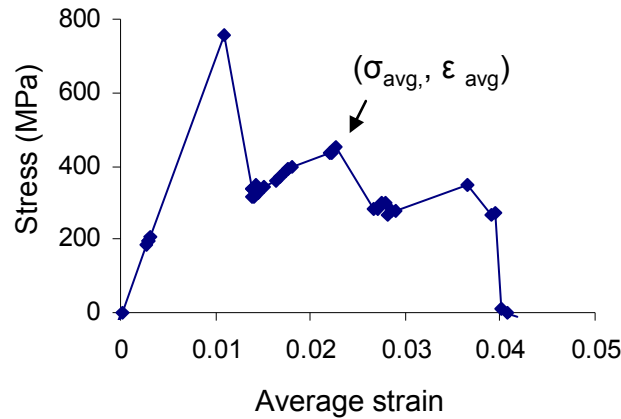


Figure 3-16 An example of the stress-strain response for the composite laminate strip shown in Figure 3-15 constructed from all images.

To investigate the accuracy of the above method, independent FE simulations of the OCT tests were carried out. Again, in these simulations, for the softening behaviour, the built in material model, MAT_081, was used in LS-DYNA. Quasi-static simulations of the OCT test were carried out using a 2 mm mesh size (Figure 3-17). Three different softening responses were assumed for the behaviour of the material: linear, bilinear and bilinear with a plateau stress. Using stress distribution around the damage zone, approximate constitutive responses were constructed for the strip of elements in front of the initial notch tip. These responses are shown in Figure 3-18, Figure 3-19 and Figure 3-20. In these curves, the approximate responses have been constructed using the stresses in the undamaged zone, σ_{ud} , and strains in the damaged zone, ε_d . It can be observed that by using the proposed methodology, the approximate shape of the softening response can be determined.

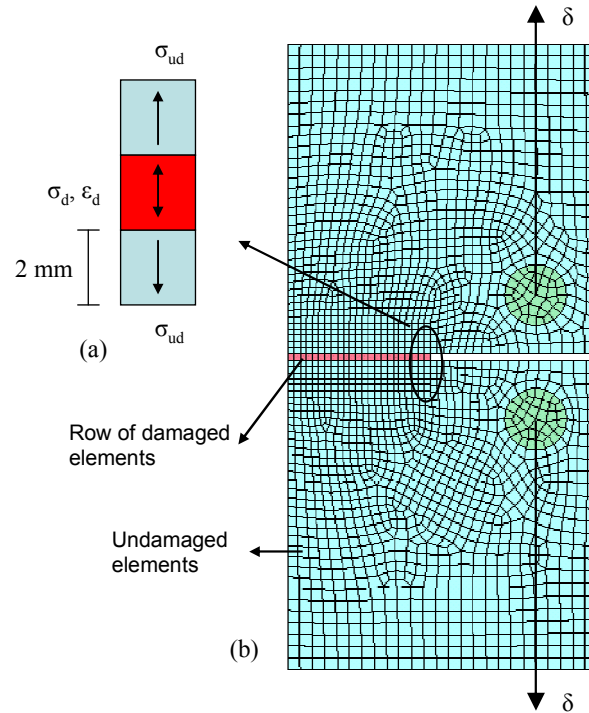


Figure 3-17 (a) Schematic showing the state of stress and strain in the elements within and around the damage zone and (b) FE mesh of OCT test geometry.

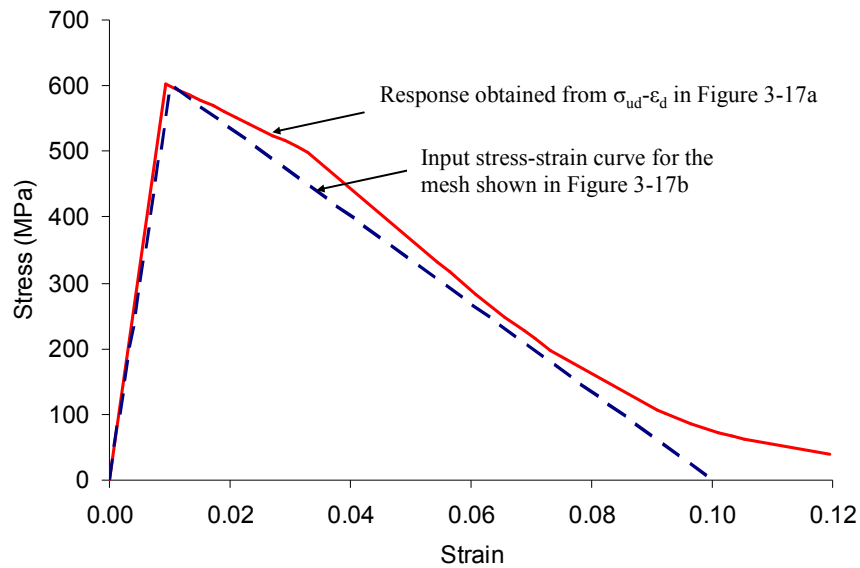


Figure 3-18 Stress-strain curve used as input (linear softening - dashed line) in the FE simulation of the OCT test shown together with the approximate stress-strain curve obtained using the same assumptions as in the proposed method (i.e. stress in the undamaged element versus the strain in the damaged element).

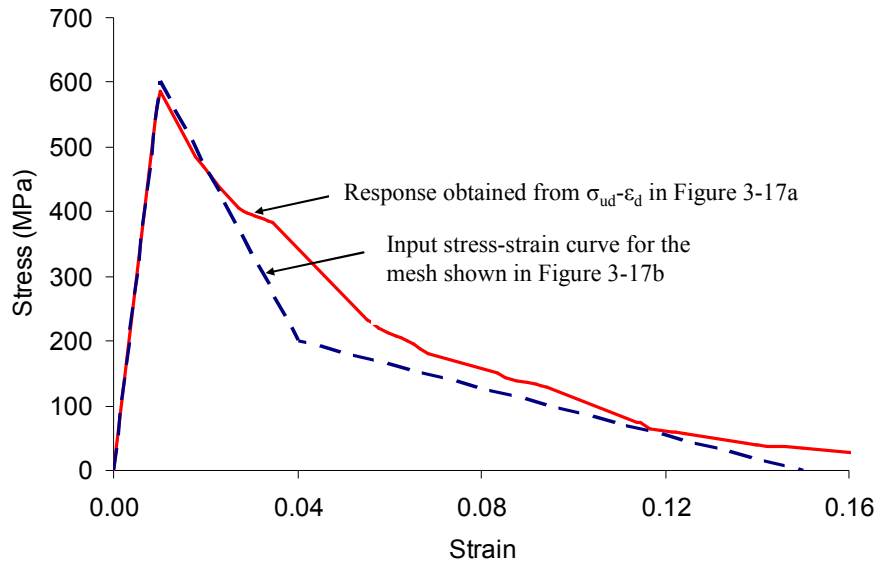


Figure 3-19 Stress-strain curve used as input (bilinear softening - dashed line) in the FE simulation of the OCT test shown together with the approximate stress-strain curve obtained using the same assumptions as in the proposed method (i.e. stress in the undamaged element versus the strain in the damaged element).

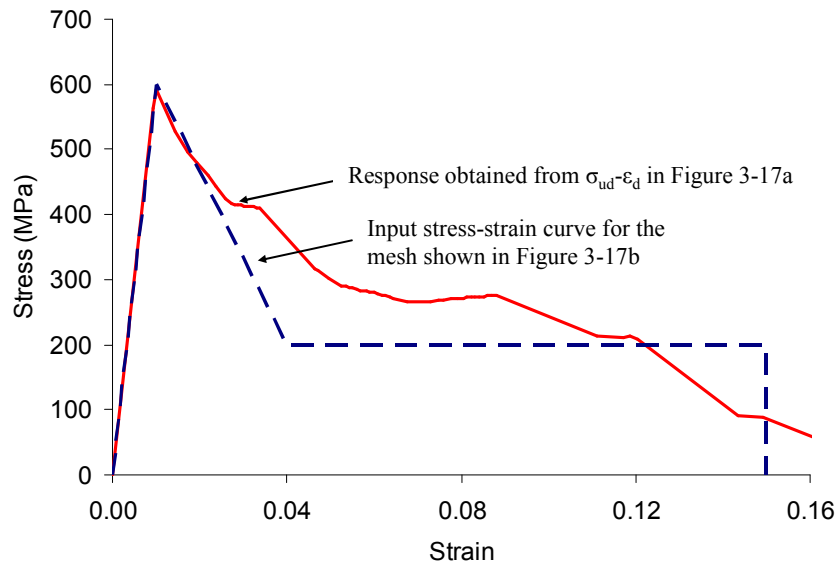


Figure 3-20 Stress-strain curve used as input (trilinear softening - dashed line) in the FE simulation of the OCT test shown together with the approximate stress-strain curve obtained using the same assumptions as in the proposed method (i.e. stress in the undamaged element versus the strain in the damaged element).

Following above procedure, we can derive similar response curves for other strips of elements along the damage band. One would expect that all of these curves overlap since they represent the behaviour of the same laminate. However, due to the presence of error in the measured local displacement field, inhomogeneous material behaviour, and also the approximations involved in arriving at these stress-strain curves, this is not the case. On a master plot consisting of stress-strain curves obtained from all the images, we can identify a region (band) within which the real stress-strain curve should lie. To find the best curve that represents the constitutive response of the laminate, an optimization technique is utilized in this study which not only minimizes the error in the equilibrium equations (local criterion) but also results in a fracture energy, G_f , that closely matches the experimentally measured value (global criterion). The optimization process is discussed in the next section.

3.3. Step II: Optimization of the Approximate Constitutive Response

3.3.1. Introduction

After constructing a family of approximate responses as discussed in the previous step, to find the best curve that represents the constitutive response of the laminate, an optimization technique is used to minimize a set of local and global cost functions defined based on the energy balance and equilibrium equations. Although any standard iteration technique such as Gauss-Newton method can be used to find an optimized curve, in this study, we use a simpler approach. Various strain-softening curves that fall within the identified region on the master stress-strain plot are chosen. The shape of these curves are such that they represent the approximate shape obtained in the previous step. After minimizing the local and global cost functions using these curves, the optimized response is obtained.

3.3.2. Possible Shapes of the Constitutive Response

From step I of this methodology, we can obtain a family of stress-strain curves that all represent the approximate behaviour of the damaged material. On a master plot

consisting of these curves, a region (band) can be identified within which the stress-strain response of the material should lie. In Figure 3-21 and Figure 3-22, examples of approximate family of curves obtained from over-height compact tension and compact compression tests on IM7/8552 quasi-isotropic laminates are shown, respectively.

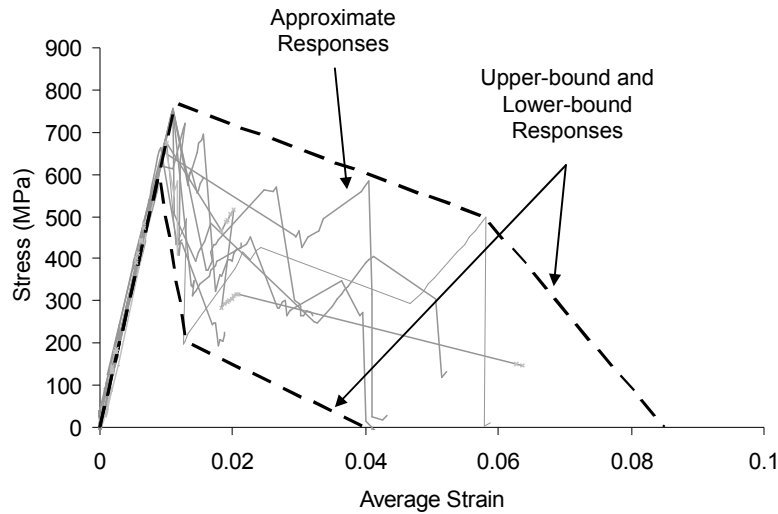


Figure 3-21 Example of an approximate family of curves and identified bounds for an OCT test on an IM7/8552 quasi-isotropic laminate.

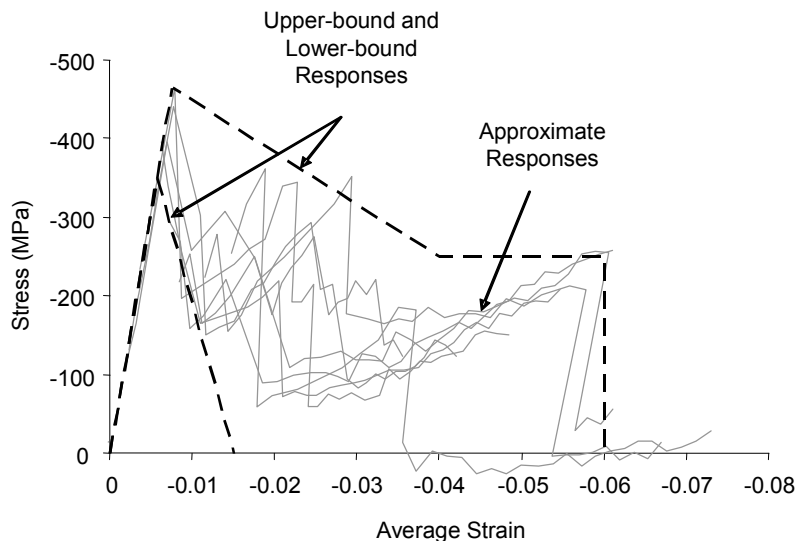


Figure 3-22 Example of an approximate family of curves and identified bounds for a compact compression test on an IM7/8552 quasi-isotropic laminate.

From these curves we can identify two important properties of the laminate strain-softening response:

1. The region (enclosed by upper-bound and lower-bound curves) within which the stress-strain curve is sought.
2. The shape of the stress-strain curve.

The size of the region, identified with upper-bound and lower bound curves in Figure 3-21 and Figure 3-22, is mainly a function of error and noise in displacement data, approximation involved in the process and also inhomogeneous behaviour of the material. In this step, the optimization process is limited to this region. This significantly decreases the iteration time compared to other updating techniques for which an initial region for the response of the material is not available.

The other property identified here is the shape of the constitutive response. For example by analyzing Figure 3-22, a plateau stress approximately equal to 200 MPa after the first softening response can be identified. This in fact confirms the previous studies on this subject (Moran et al., 1995; Sivashanker, 1998; Sivashanker, 2001; Sivashanker and Bag, 2001; Zobeiry, 2004; McGregor et al., 2008;) in which the existence of this plateau stress was confirmed for damage propagation in composites under compression.

In many of the current available approaches, to identify the constitutive parameters, a shape for the constitutive response is assumed. Usually this assumption consists of a simple linear softening response in which any complex shape of the constitutive response is avoided. As a consequence of this simplifying assumption, a biased constitutive response may be obtained.

On the other hand, from the family of approximate stress-strain curves shown in Figure 3-21 and Figure 3-22, it may seem that a more complex (multi-linear) shape should be considered for the purpose of optimization. However, as shown in other studies (e.g. Ilcewicz et al., 1993; Bazant and Planas, 1998; Planas et al., 1999), for relatively small notched specimen geometries such as OCT, only the initial part of the softening curve

together with the fracture energy influence the damaging behaviour and the global response of the structure. This is mainly due to the fact that specimen fails before the damaged material goes through the complete stress-strain curve. As a result, in this study the following curves have been considered in the optimization process of composite laminates:

1. Linear softening curve
2. Bilinear softening curve
3. Trilinear softening curve

Based on the shape of the approximate constitutive responses, one of the above curves is chosen and then optimized to obtain its parameters. An example of optimized softening curves for an OCT test are shown in Figure 3-23.

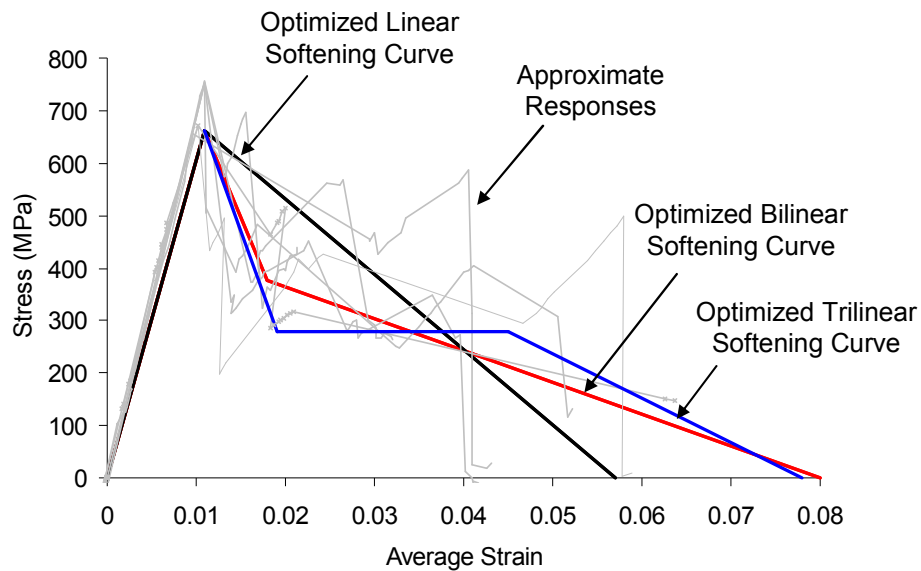


Figure 3-23 Example of an approximate family of curves and optimized linear, bilinear and trilinear softening curves for an OCT test on an IM7/8552 quasi-isotropic laminate.

3.3.3. Optimized Constitutive Response

To find the best constitutive response, two criteria need to be satisfied: a global criterion based on the fracture energy of the material and a local criterion based on local equilibrium equations. In the following we discuss these two criteria.

3.3.3.1. Global Criterion for Optimization: Fracture Energy

The global criterion is defined based on the dissipated energy calculated from the global load-displacement curve. Assume that the damage zone in an OCT test has been identified using the procedure explained in previous step. For this test, the damage height, h , and the crack length (assuming that the failure process zone is negligible), Δa have been measured (Figure 3-24). To measure the fracture energy from the OCT test, several load-unloading cycles have been conducted during the test. From the area below the global load-displacement curve limited to the unloading path (Figure 3-25a), the total dissipated energy, W , is calculated. Therefore, the fracture energy, G_f , can be calculated as follows:

$$G_f = \frac{W}{t \Delta a} \quad (3-27)$$

In which t is the thickness of the specimen and Δa is the crack length. On the other hand, the fracture energy can be calculated from the fracture energy density, γ , obtained from the stress-strain response of the material (Figure 3-25b) as follows:

$$G_f = \gamma h \quad (3-28)$$

In which h is the damage height. From the above two equations for fracture energy, it can be concluded that:

$$\gamma = \frac{W}{h t \Delta a} \quad (3-29)$$

Therefore the optimization process will be limited to the curves that lie between the upper-bound and lower-bound responses (Figure 3-21 and Figure 3-22) and yield the

fracture energy density equal to the value calculated in Equation 3-29. In other words, by generating a family of curves with specific fracture energy density and specific shape within the specified upper bound and lower bound, the global criterion limits the number of curves that will be analyzed in the optimization process. For example, for the approximate stress-strain curves presented in Figure 3-21, assuming that the shape of the optimized response is bilinear, the acceptable family of curves (that correspond to the same specific energy density from Equation 3-29) is obtained and shown in Figure 3-26. The minimum considered distance between selected strains to generate these curves was equal to 0.001. This value was chosen based on the measurement error in the DIC technique. The minimum considered distance in the stress range was also equal to 20 MPa. This results in a limited number of curves generated in this step.

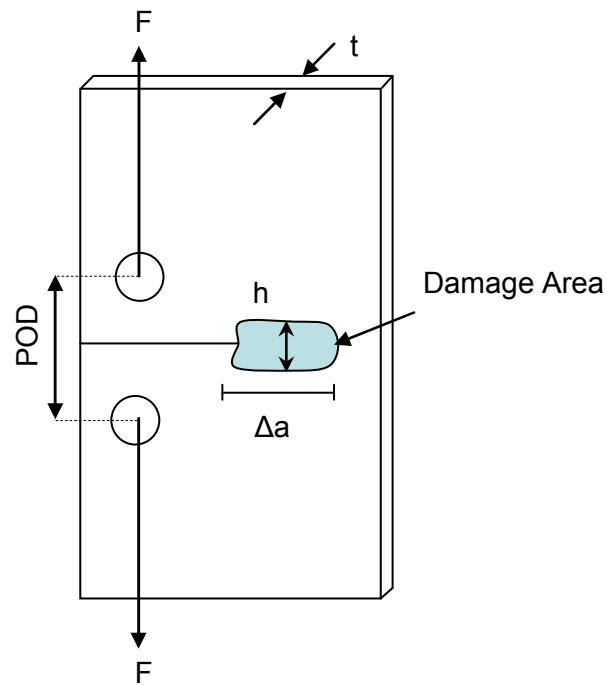


Figure 3-24 Schematic showing the damage area in an OCT test.

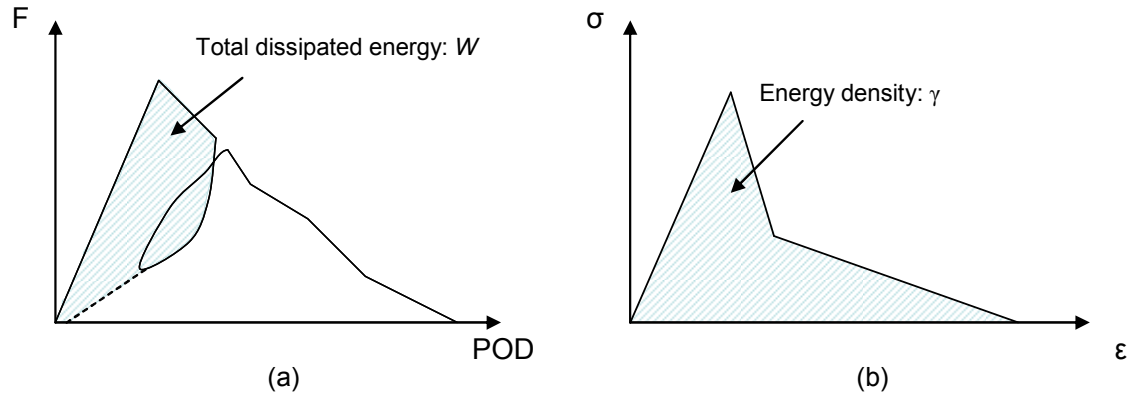


Figure 3-25 (a) Total dissipated energy calculated from the area below the load-displacement curve and (b) fracture energy density calculated from the softening response of the material.

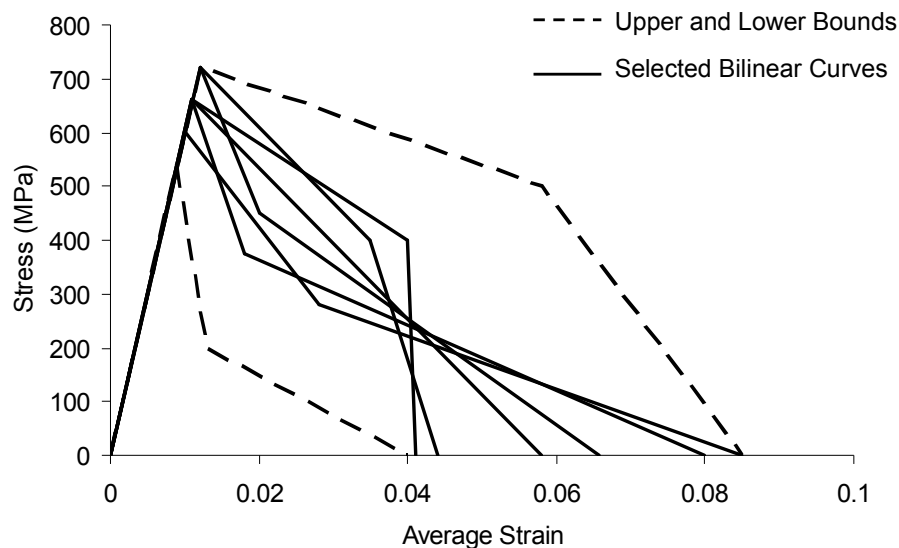


Figure 3-26 Example of a selected family of curves with equal specific energy densities and within the regions specified in the first step of the optimization.

In another approach to satisfy the global energy criterion, instead of satisfying energy dissipation using approximate damage height and damage length, (Figure 3-24), the total dissipated energy is calculated using finite element analysis. Assume that there are m damaged elements identified in the damage zone. Further assume that the constitutive response of an element is known as shown in Figure 3-27. The total dissipated energy in the element is calculated as:

$$w_i = (h_e)^2 t \gamma_i \quad (3-30)$$

In which t is the thickness of the element, h_e is the element size (assuming a square element) and γ_i is the energy density limited to the unloading path as shown in Figure 3-27.

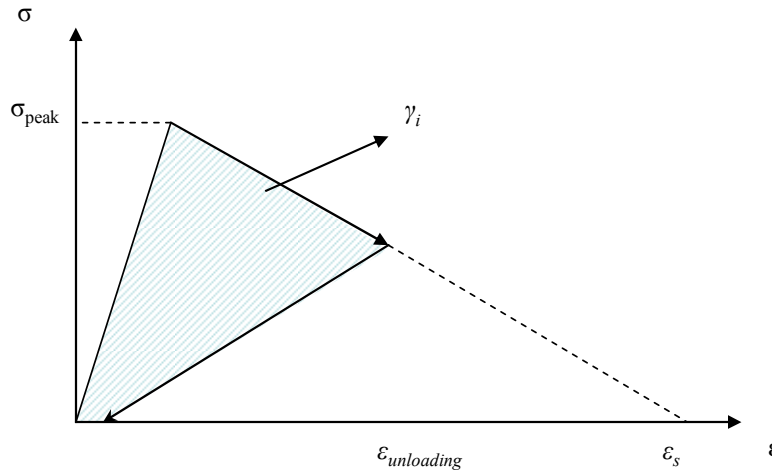


Figure 3-27 Calculating energy from the stress-strain response of an element.

Therefore, the total dissipated energy in the damaged area is calculated as:

$$W_e = \sum_{i=1}^m w_i \quad (3-31)$$

In which m is the total number of damaged elements. This energy should be equal to the total dissipated energy calculated from the area below the global load-displacement curve. Therefore, in the second approach to satisfy global energy criterion, constitutive responses with specific shape (e.g. bilinear softening response) within the identified bounds are chosen for which the calculated dissipated energy in the elements matches with the calculated dissipated energy from load-POD curve.

3.3.3.2. Local Criterion for Optimization: Equilibrium

The curves that are chosen in the global criterion step, satisfy the following conditions:

1. Their energy densities are equal to a global measured quantity obtained from the fracture energy calculation (Equation (3-29)).
2. Their shapes, represent the shape of the approximate stress-strain responses obtained in the damage identification process
3. They fall within the identified region on the master stress-strain plot (Figure 3-26).

In this step, by satisfying a local criterion, among all the above curves, a constitutive response is chosen that best represents the behaviour of the composite laminate. The local criterion is defined based on the satisfaction of equilibrium equations. The best response is defined as the curve that has the least amount of error in the nodal equilibrium forces. Here are the steps involved in the identification of the best curve:

1. A constitutive response from the family of curves obtained in the global criterion satisfaction process is chosen.
2. Using this response, the remaining equilibrium force (residual force) in each node in each image, r_{ij} , is calculated. Here i represents the node number and j represents the image number.
3. The total equilibrium error for a given curve is calculated:

$$R_{equilibrium} = \sqrt{\sum_i \sum_j (r_{ij} - \bar{e}_{equilibrium})^2} \quad (3-32)$$

In which $\bar{e}_{equilibrium}$ is the average equilibrium error calculated previously (Equation 3-16).

4. The constitutive response that has the minimum amount of R among all the curves is identified.

The final curve not only satisfies the energy dissipation criterion, but also has the least amount of nodal equilibrium error. Here, calculations for deriving the material stiffness matrix in the process of satisfying nodal equilibrium satisfaction process are presented. These equations are based on a bilinear softening response. However, they can be extended to a trilinear softening curve or rewritten for a linear softening curve as well.

Assume that a bilinear softening response is chosen from the family of curves obtained in satisfying the global criterion for fracture energy (Figure 3-28a). At each step of loading, using this response, the reduced stiffness matrix has to be constructed to calculate stresses and nodal forces.

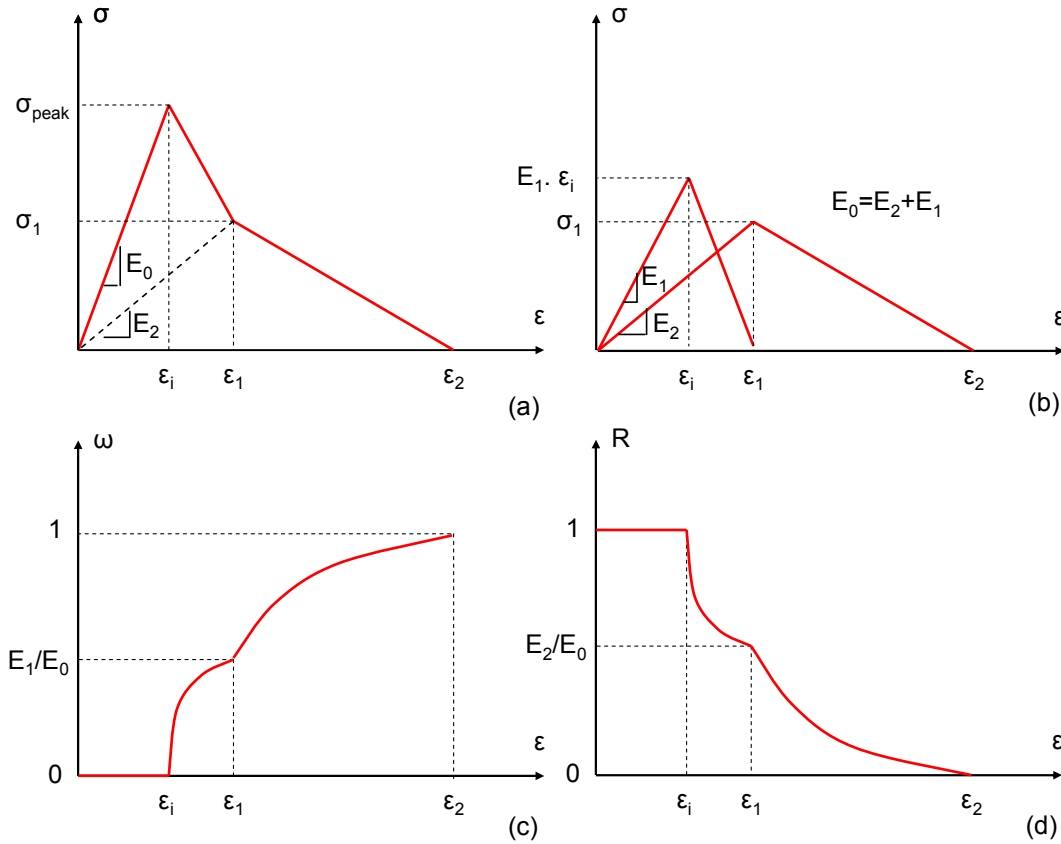


Figure 3-28 (a) An assumed bilinear softening response, (b) dividing the bilinear curve into two linear softening curves, (c) the damage parameter as a function of strain, and (d) the modulus reduction factor as a function of strain for the bilinear softening curve.

In the continuum approach, the 1D stress-strain relation can be written as follows:

$$\sigma = E \epsilon = (1 - \omega) E_0 \epsilon = R E_0 \epsilon \quad (3-33)$$

In which ω is the damage parameter defined as a scalar between 0 and 1 (undamaged to fully damaged states respectively), R is the modulus reduction factor, E is the damaged modulus, and E_0 is the undamaged modulus of the material. The bilinear softening curve in Figure 3-28a can be divided into two linear softening curves, as shown in Figure 3-28b, such that:

$$E_1 = E_0 - E_2 = \frac{\sigma_{peak}}{\varepsilon_i} - \frac{\sigma_1}{\varepsilon_1} \quad (3-34)$$

$$E_2 = \frac{\sigma_1}{\varepsilon_1}$$

For each of these curves, a separate damage parameter and consequently a separate reduction factor can be defined. Since, in these curves, stress is a linear function of strain, the reduction factors should be defined as follows:

$$R_1 = 1 - \omega_1 = \frac{\varepsilon_i}{\varepsilon} \frac{\varepsilon_1 - \varepsilon}{\varepsilon_1 - \varepsilon_i} \quad (3-35)$$

$$R_2 = 1 - \omega_2 = \frac{\varepsilon_1}{\varepsilon} \frac{\varepsilon_2 - \varepsilon}{\varepsilon_2 - \varepsilon_1}$$

Multiplying the above parameters by the total damage value for each curve, E_i/E_0 ($i= 1$ or 2), and adding together, we can calculate the total damage parameter and the total reduction factor (Williams et al., 2003). These values are given below and also schematically depicted in Figure 3-28c and Figure 3-28d, respectively.

$$\left\{ \begin{array}{ll} \omega = 0 & \varepsilon \leq \varepsilon_i \\ \omega = \frac{E_1}{E} \left(\frac{\varepsilon_1}{\varepsilon} \frac{\varepsilon - \varepsilon_i}{\varepsilon_1 - \varepsilon_i} \right) & \varepsilon_i < \varepsilon \leq \varepsilon_1 \\ \omega = \frac{E_1}{E} + \frac{E_2}{E} \left(\frac{\varepsilon_2}{\varepsilon} \frac{\varepsilon - \varepsilon_1}{\varepsilon_2 - \varepsilon_1} \right) & \varepsilon_1 < \varepsilon \leq \varepsilon_2 \\ \omega = 1 & \varepsilon_2 < \varepsilon \end{array} \right. \quad (3-36)$$

$$\begin{cases} R = 1 & \varepsilon \leq \varepsilon_i \\ R = \frac{E_2}{E} + \frac{E_1}{E} \left(\frac{\varepsilon_i}{\varepsilon} \frac{\varepsilon_1 - \varepsilon}{\varepsilon_1 - \varepsilon_i} \right) & \varepsilon_i < \varepsilon \leq \varepsilon_1 \\ R = \frac{E_2}{E} \left(\frac{\varepsilon_1}{\varepsilon} \frac{\varepsilon_2 - \varepsilon}{\varepsilon_2 - \varepsilon_1} \right) & \varepsilon_1 < \varepsilon \leq \varepsilon_2 \\ R = 0 & \varepsilon_2 < \varepsilon \end{cases} \quad (3-37)$$

In a 2D domain, three different reduction factors for x and y directions, R_x and R_y , and also for shear loading, R_{xy} , have to be calculated. In this study, for the current quasi-isotropic laminate, the same reduction function is assumed for x and y directions. However, since in OCT and CC tests, no damage is introduced in the x direction (parallel to the crack direction), R_x was equal to 1 in most cases. For an anisotropic material, separate reduction functions have to be defined for x and y directions. For the shear reduction factor, based on a study by Williams et al. (2003), the following relation was used:

$$\begin{aligned} \omega_{xy} &= \sqrt{\omega_x^2 + \omega_y^2 - \omega_x \omega_y} \rightarrow \\ R_{xy} &= 1 - \omega_{xy} = 1 - \sqrt{(1 - R_x)^2 + (1 - R_y)^2 - (1 - R_x)(1 - R_y)} \end{aligned} \quad (3-38)$$

In which ω_{xy} is the shear damage parameter. Finally, the plane stress material stiffness matrix (Equation 3-7), can be rewritten as (Williams et al., 2003):

$$\mathbf{D} = \begin{bmatrix} \frac{R_x E_x}{1 - R_x R_y \nu_{xy} \nu_{yx}} & \frac{R_x R_y \nu_{yx} E_x}{1 - R_x R_y \nu_{xy} \nu_{yx}} & 0 \\ \frac{R_x R_y \nu_{xy} E_y}{1 - R_x R_y \nu_{xy} \nu_{yx}} & \frac{R_y E_y}{1 - R_x R_y \nu_{xy} \nu_{yx}} & 0 \\ 0 & 0 & R_{xy} G_{xy} \end{bmatrix} \quad (3-39)$$

In satisfying the local criterion for equilibrium, this matrix has to be computed for each element at each step. Using this matrix, as described previously, stresses and nodal forces can be calculated and equilibrium can be checked at each node.

3.4. Limits of Applicability and Sources of Error

The family of approximate softening responses, can be obtained for Mode I failure. Although in theory, approximate responses can also be obtained for Mode II failure, it has not been studied here. For mixed Mode I/II, the approximation process is not applicable. The damage detection process based on equilibrium equations, however, is not limited to Mode I failure.

Here are various factors and assumptions that can affect the validity of the proposed methodology for determining the damaging constitutive response of composite laminates:

1. Error in the raw displacement data obtained using the DIC technique. As explained earlier, many factors in this technique such as camera resolution might introduce errors in the final measured data.
2. The procedure to obtain the upper and lower bounds for constitutive response and also the shape of the constitutive response involves various approximations (e.g. negligibility of the shear stress around the damage zone in Mode I failure).
3. The total dissipated energy which was used in the optimization technique was obtained using the area below the load-displacement curve. This calculation is affected by measurement errors.

To deal with the error in the raw displacement data, we have to define a tolerance limit and margin of error. Since the error in the displacement data affects the calculation of nodal forces, an acceptable error range for the equilibrium satisfaction process should be defined. As explained earlier, this tolerance value, $\bar{e}_{equilibrium}$, is used in the damage identification process.

To reduce the effect of error due to the assumptions in the identification process, an averaging technique was introduced. As explained in section 3.2.3., this averaging technique reduces the error effect on the damage detection process. Errors generated in this process are reduced during the optimization step.

To reduce the effect of error in the fracture energy calculation, we can introduce a tolerance, e_{energy} , for the global criterion satisfaction. Therefore, the global energy criterion, is changed to the following condition:

$$\left| \gamma - \frac{W}{ht \Delta a} \right| < e_{energy} \quad (3-40)$$

In which e_{energy} is obtained from the errors involved in the total dissipated energy calculation. Knowing the error in measured displacements and strains (e_ϵ), for an identified damage region, this value can be calculated:

$$e_{energy} = f(e_\epsilon, w, \Delta a) \quad (3-41)$$

For an assumed softening curve, this value is derived by integrating the energy density over the damaged region and measuring the energy error, introduced due to the error in stresses and strains (Equation 3-30 and Equation 3-31).

3.5. Description of the Developed Code-CrackPro

A series of subroutines in Visual Basic code, CrackPro, has been developed for the identification process of the strain-softening response of composite laminates. In each analysis, the measured local displacement vectors are imported into CrackPro. Using the local displacement data, this code computes the surface strains and then using elastic properties, calculates the nodal forces. Equilibrium at each node is checked and using the methodology described previously, the damage zone is detected. Afterward, average stresses and strains are computed which are then used to construct a family of approximate stress-strain responses for the laminate. CrackPro currently uses either a linear, bi-linear or tri-linear softening curve in order to arrive at an optimum shape that minimizes the local and global cost functions. The schematic representation of steps and calculations in CrackPro code is shown in Figure 3-29. The main subroutines of CrackPro are given in Appendix A. The following provides a summary of these subroutines:

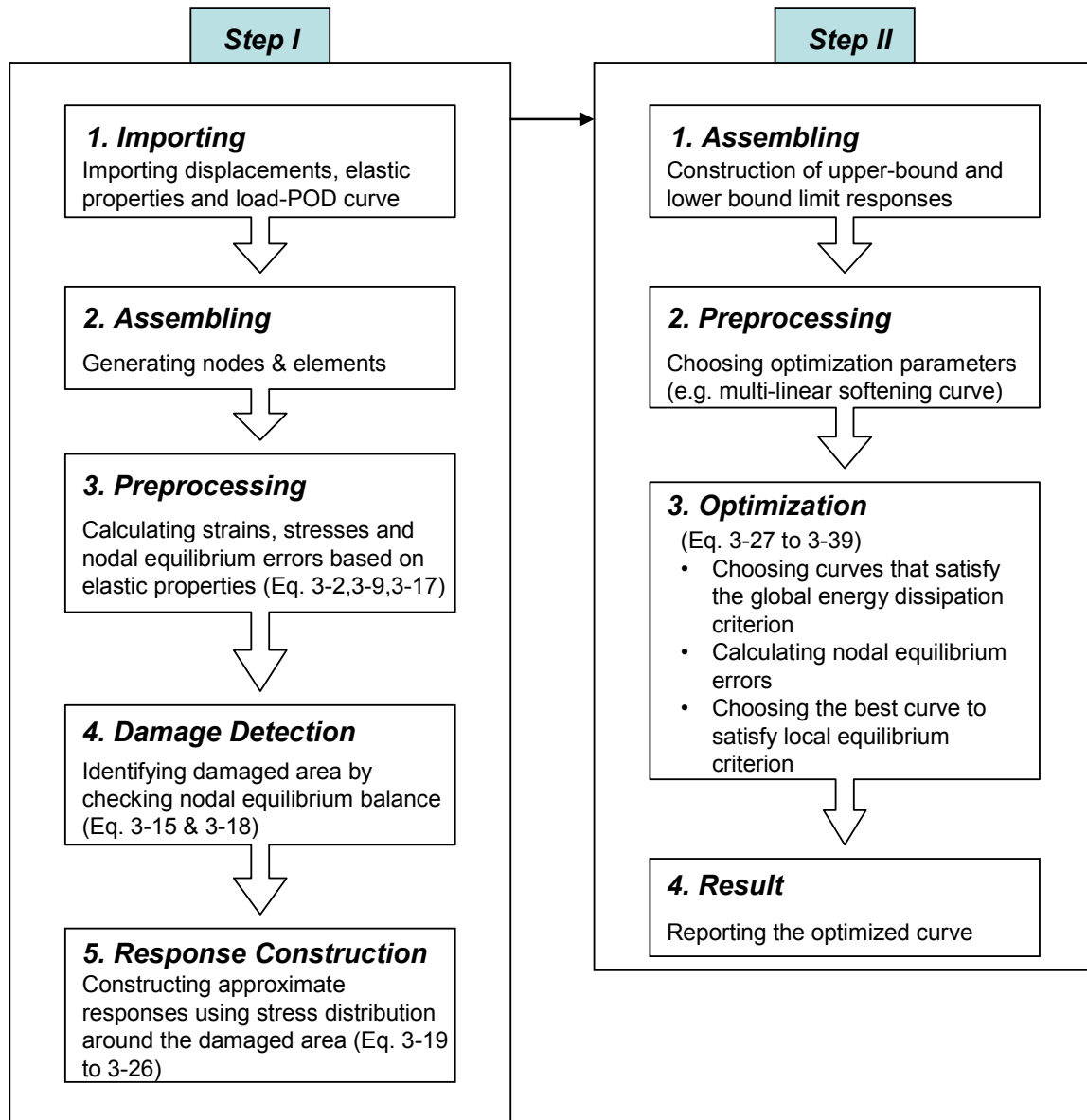


Figure 3-29 Schematic representation of steps and calculations in CrackPro code.

Step I

1. Importing (Appendix A.1): The displacement data is imported into CrackPro using this subroutine. As explained previously, for each image, DaVis generates a text file containing the coordinates of virtual nodes and also displacement vectors associated with these nodes. These files along with the material elastic properties and also load-POD curve are imported

into CrackPro. At this stage, CrackPro creates an Excel™ file and records displacement data in Excel™ sheets. It then calculates the size of the elements and the masked area (the area on the specimen surface for which displacement vectors are reported).

2. Assembling (Appendix A.2): The nodes and elements are generated based on the virtual nodes reported by DaVis. In this subroutine, node numbers and element numbers are created.
3. Pre-processing (Appendix A.3): Assuming that all the elements are elastic, the following parameters are calculated for all the elements in all the images: surface strains, effective strains, surface stresses, nodal forces and remaining equilibrium forces (Equations 3-2, 3-9 and 3-17).
4. Damage detection (Appendix A.4): Damaged elements are identified by checking equilibrium at each node. An average damage initiation strain is determined to minimize the error dependency of the process. (Equations 3-15 and 3-18).
5. Response construction (Appendix A.5): Elements on the boundary of the damaged area are identified. Using stresses in these elements and also the average strain value of the strip of damaged elements, approximate family of stress-strain responses of the damaged area is constructed (Equations 3-19 to 3-26).

Step II

1. Assembling: Based on the approximate family of curves, upper-bound and lower-bound limits for optimization process are identified.
2. Pre-processing: The parameters for the optimization process are identified. This also includes the shape of the stress-strain curve which could be linear softening, bilinear softening or trilinear softening response.

3. Optimization (Appendix A.6): Optimization is carried out based on the defined parameters. Both global energy dissipation criterion and local equilibrium criterion are checked (Equations 3-27 to 3-39).
4. Reporting: The optimized stress-strain response is reported.

3.6. Summary

In this chapter, a new methodology to identify the strain-softening response of composite laminates was introduced. The steps involved in this approach are summarized below:

1. During a test, full-field displacement vectors are measured using the DIC approach.
2. Surface strains are calculated based on the measured deformation and virtual nodes created during the DIC analysis.
3. Assuming that the material is undamaged, using the elastic properties and measured strains, surface stresses and nodal forces are calculated.
4. Equilibrium is checked at each node. If equilibrium is satisfied within a tolerance, it will be concluded that elements attached to that node are elastic. Otherwise, one or more elements attached to the node are identified as being damaged.
5. Using equilibrium, the damaged area on the surface of the specimen is identified. An averaging technique is used reduce the effect of error in displacement vectors.
6. For Mode I failure, assuming that shear stress is negligible around the damage zone, an approximate stress distribution inside the damage zone is obtained.
7. Using the approximate stress distribution and also average strain values, a family of approximate stress-strain responses is constructed.

8. Based on the family of curves, upper-bound and lower-bound of the real response of the material are identified. A constitutive response shape is also chosen based on the approximate responses.
9. Based on a global criterion (dissipated energy) and also a local criterion (equilibrium), an optimization technique has been developed. Using this technique and also the identified parameters for the shape of the constitutive response, the best curve that represents the constitutive response of the composite laminate is obtained.

Chapter 4: Application to OCT Tests and Validation Using FE Simulation and Destructive Testing

4.1. Introduction

In order to demonstrate the capability of the proposed methodology for identifying softening response and damage properties of composite laminates, a series of tensile and compressive tests were conducted. In the following two chapters, the results of the experimental studies along with the numerical simulations of the tests using the derived constitutive models are presented. In each chapter, initially, the experimental results are presented. These results are then compared with the numerical results obtained using the current proposed method. To further validate the proposed technique, results obtained from sectioning and depleting of the damaged specimens are also presented and compared with the numerical findings.

For tensile tests, over-height compact tension (OCT) test geometry, developed by Kongshavn and Poursartip (1999) and for compression tests, compact compression (CC) test geometry are used. In this chapter, experimental and numerical results for tensile tests are presented. The results of compression tests are presented in Chapter 5.

4.2. Over-height Compact Tension Tests

4.2.1. Material and Lay-up

Two 500x500 mm IM7/8552 carbon-epoxy composite panels with a quasi-isotropic lay-up of $[45/0/-45/90]_{4S}$ were used in this study. Both panels had a thickness of about 4 mm. OCT and CC specimens were cut out from these two panels. Initial tests for specimens with 45 degree lamina on the outer surface showed large splitting areas as shown in Figure 4-1. After splitting occurs, some parts of the specimen surface (i.e. outer lamina), separate from the inner layers. This means that strains on these parts, no longer represent

the through-thickness strains. Moreover, splitting suddenly changes the surface contrast by creating darker areas along the splitted zone as shown in Figure 4-1. This prevents the application of DIC method and consequently the application of the proposed method to obtain strain-softening behaviour of the laminate. To minimize surface splitting, the laminate lay-up was changed to $[90/45/0/-45]_{4S}$ with the 90 degree lamina on the two outer surfaces. To do this, specimens were cut at a 45 degree angle to the edges of the original panels as shown in Figure 4-2. Basically, 90 degree layers on the outer surfaces, confine the inner layers and by providing support for off-axis layers, prevent splitting. This results in self similar crack growth in the specimen and allows us to measure the surface displacements more accurately.

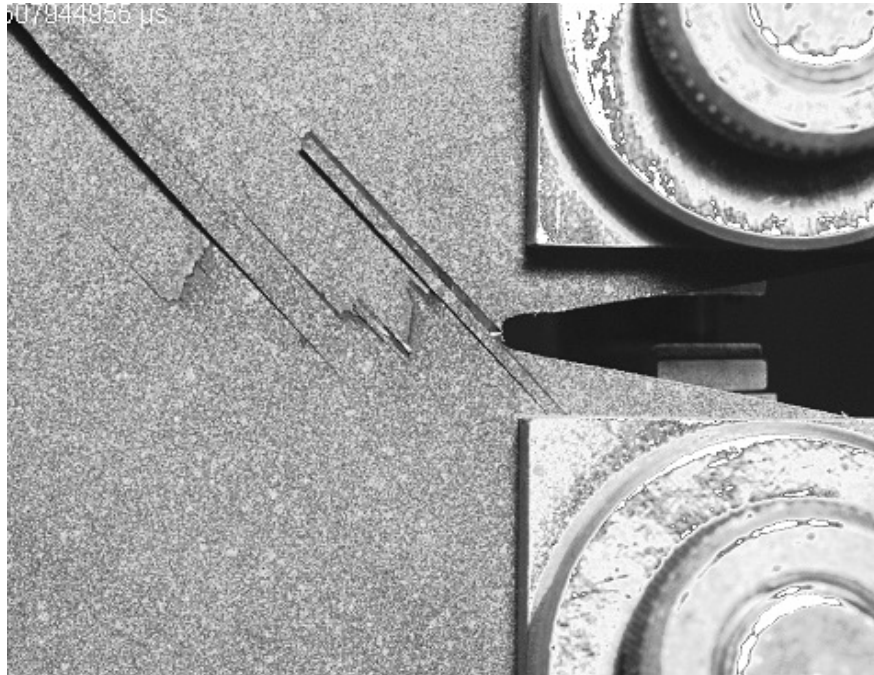


Figure 4-1 An OCT test with $[45/0/-45/90]_{4S}$ layup which shows large splitting areas on the surface.

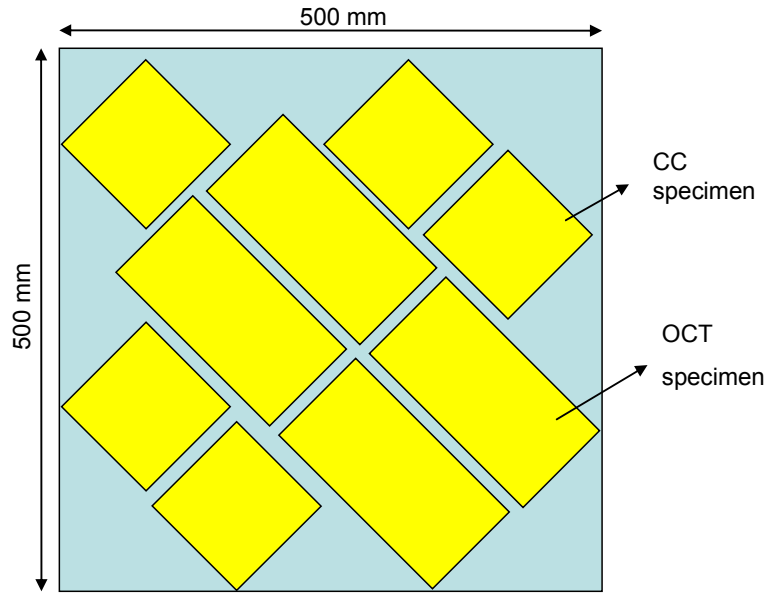


Figure 4-2 Cutting panels at 45 degree angles to make $[90/45/0/-45]_{4S}$ specimens.

The elastic properties reported for a unidirectional IM7/8552 lamina by the manufacturer, Hexcel Composites Ltd (Hexcel), are listed in Table 4-1.

Table 4-1 Lamina properties for an IM7/8552 lamina with a resin volume fraction of 34% (Hexcel).

| Resin V_r | Thickness | E_{11} | E_{22} | G_{12} | ν_{12} |
|-------------|-----------|----------|----------|----------|------------|
| 34% | 0.125 mm | 150 GPa | 11 GPa | 4.6 GPa | 0.3 |

To obtain the elastic properties of the quasi-isotropic laminate, initially, the laminate plate theory (LPT) was utilized based on the reported lamina properties listed in Table 4-1. The laminate properties obtained using LPT are listed in Table 4-2.

Table 4-2 Initial elastic properties of the IM7/8552 quasi-isotropic laminate obtained using laminate plate theory.

| Lay-up | E_x | E_y | G_{xy} | ν_{xy} |
|----------------------|-----------|-----------|-----------|------------|
| $[90/45/0/-45]_{4S}$ | 57.36 GPa | 57.36 GPa | 21.73 GPa | 0.32 |

These initial values were then updated using FE simulations. The average slopes of the elastic portion of the global load-displacement curves in OCT and CC tests were measured and matched with those obtained using elastic FE simulations. By approximating the Poisson's ratio to be equal to the value obtained from laminate plate theory (0.32), the Young's modulus and subsequently the shear modulus were updated (given the quasi-isotropic properties of the laminate). The updated tensile laminate properties are listed in Table 4-3.

Table 4-3 Tensile properties of the IM7/8552 quasi-isotropic laminate used in this study.

| Lay-up | E_x | E_y | G_{xy} | ν_{xy} |
|----------------------|-----------|-----------|-----------|------------|
| $[90/45/0/-45]_{4s}$ | 60.24 GPa | 60.24 GPa | 22.82 GPa | 0.32 |

To obtain a more accurate set of elastic properties, one can conduct ASTM standard tests (ASTM D 3039, 2000). Also as explained earlier, any of the current available full-field measurement techniques can be used to obtain the laminate elastic properties.

4.2.2. OCT Test Setup and Equipment

As described previously, the OCT test geometry was developed by Kongshvan and Poursartip (1999). They demonstrated that under displacement control, the OCT test geometry with a sharp notch is stable and also large enough so that its boundaries doesn't affect the damage propagation process. As shown in previous studies (Mitchell, 2002; McClennan, 2004; McGregor et al., 2005), using the OCT test geometry, a stable crack growth can be obtained in order to investigate the progressive damage behaviour of composite materials.

In this study, a sharp notch with a notch tip radius of about 1 mm was cut in all specimens. The OCT specimen geometry is shown in Figure 4-3. The laminate thickness was about 4 mm in all tests.

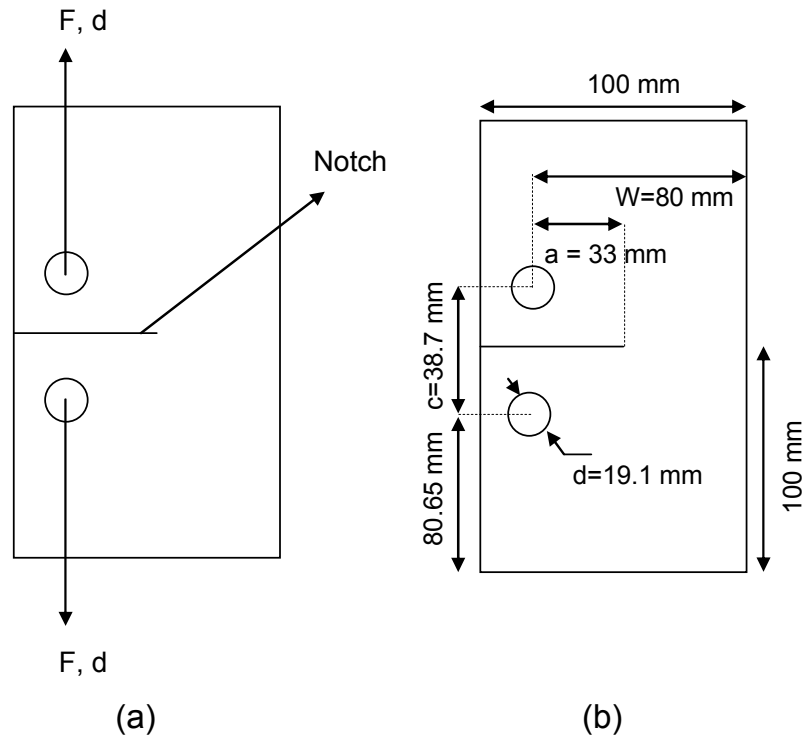


Figure 4-3 (a) OCT test setup, (b) OCT specimen geometry.

For OCT and CC tests, a screw-driven Instron uniaxial testing machine was used with an 89 kN (20,000 lb) MTS load cell. An Instron extensometer (model 2620-825 with ± 5 mm travel) was fixed between the upper and lower loading pins to measure the pin opening displacement (POD) during each test. An Instron controller was also used to output the extensometer signal and transfer the POD data to a dedicated PC with DaVis software installed on it. During each test, a 12 bit (4096 dynamic shades)-1.3 MegaPixel LaVision Imager QE camera with a 60 mm AF Micro Nikkor lens was used to capture images of the specimen surface. All specimens were loaded under displacement controlled condition with a loading rate of 0.25 mm/min. A schematic representation of test equipment and test setup is shown in Figure 4-4.

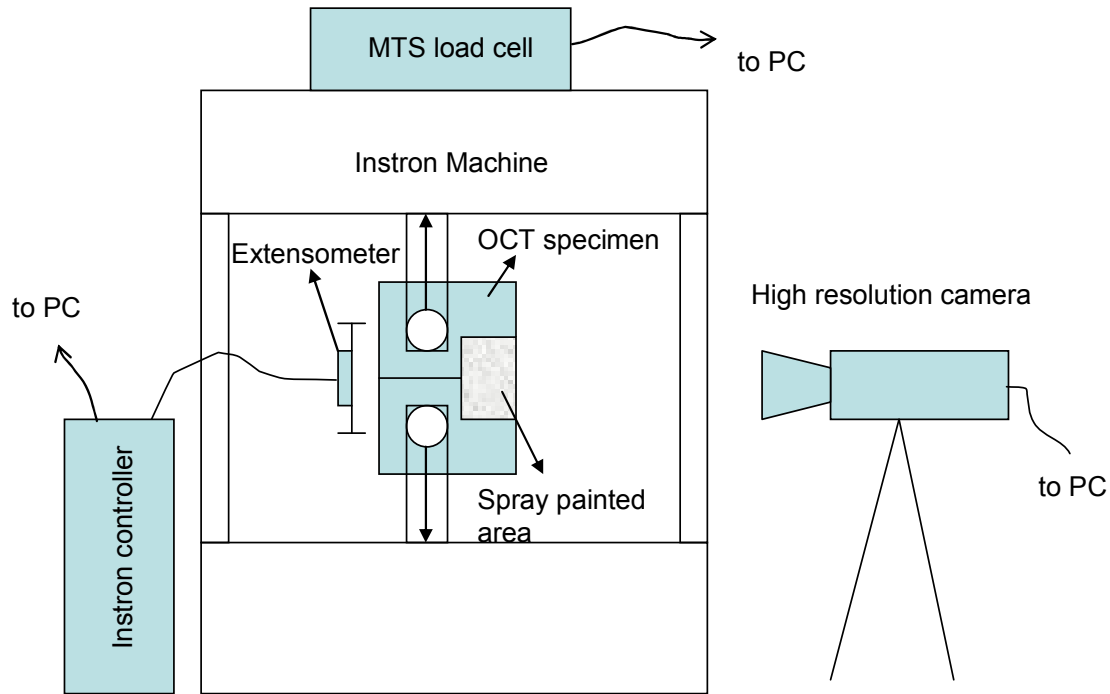


Figure 4-4 Schematic representation of test setup and equipment.

In all tests, images were recorded every second using DaVis StrainMaster software. For each image, an average value for the applied load and also an average value for the pin opening displacement over the period of one second were recorded. This means that for each point on the load-displacement curve, there is an associated recorded image.

4.2.3. Test Results

Three OCT tests were conducted in this study using specimens cut from panel A. These specimens are referred to as CTA1, CTA2 and CTA3 in this study. Specifications for OCT specimens are listed in Table 4-4.

Table 4-4 Specifications of OCT specimens tested in this study.

| Specimen | Height (mm) | Width (mm) | Thickness (mm) | Notch (mm) |
|----------|-------------|------------|----------------|------------|
| CTA1 | 200 | 100.2 | 4.06 | 53.4 |
| CTA2 | 200 | 100.1 | 4.09 | 53.3 |
| CTA3 | 200 | 100.4 | 4.06 | 53.4 |

In two of the tests, CTA1 and CTA2, multiple load-unload cycles were performed in order to measure the fracture energy more accurately. The load-POD curves of the three tests are shown in Figure 4-5.

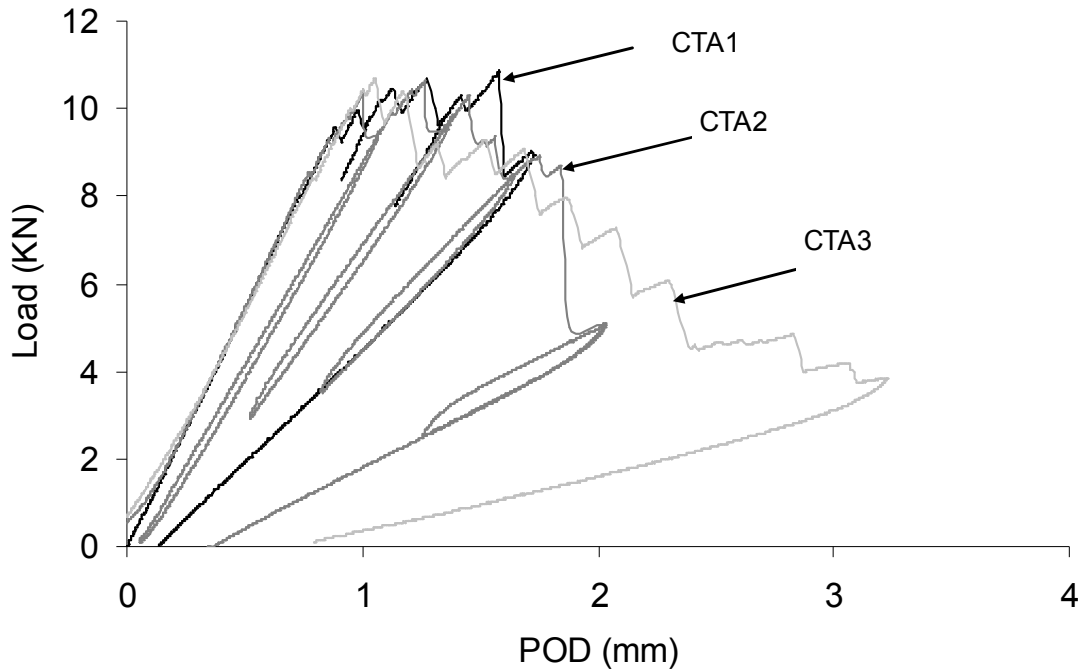


Figure 4-5 Load-POD curves for the OCT tests conducted in this study.

For CTA1, there were 770 images and 770 points on the load-POD curve before the final unloading as shown in Figure 4-6. For CTA1, images #490, #534 and #734 are shown in Figure 4-7, Figure 4-8 and Figure 4-9 respectively.

For CTA2, 2913 images were recorded before the final unloading as shown in Figure 4-10. For this test, images #1276, #1887 and #2468 are shown in Figure 4-11, Figure 4-12 and Figure 4-13, respectively.

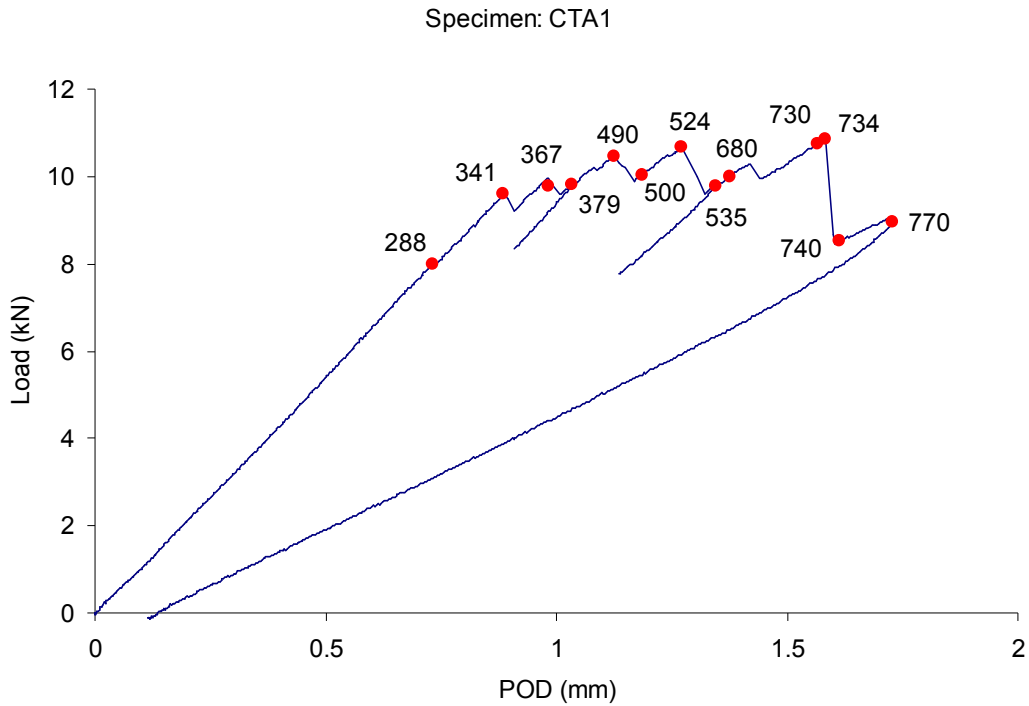


Figure 4-6 Load-Pod curve of CTA1 test showing some of the associated image numbers.

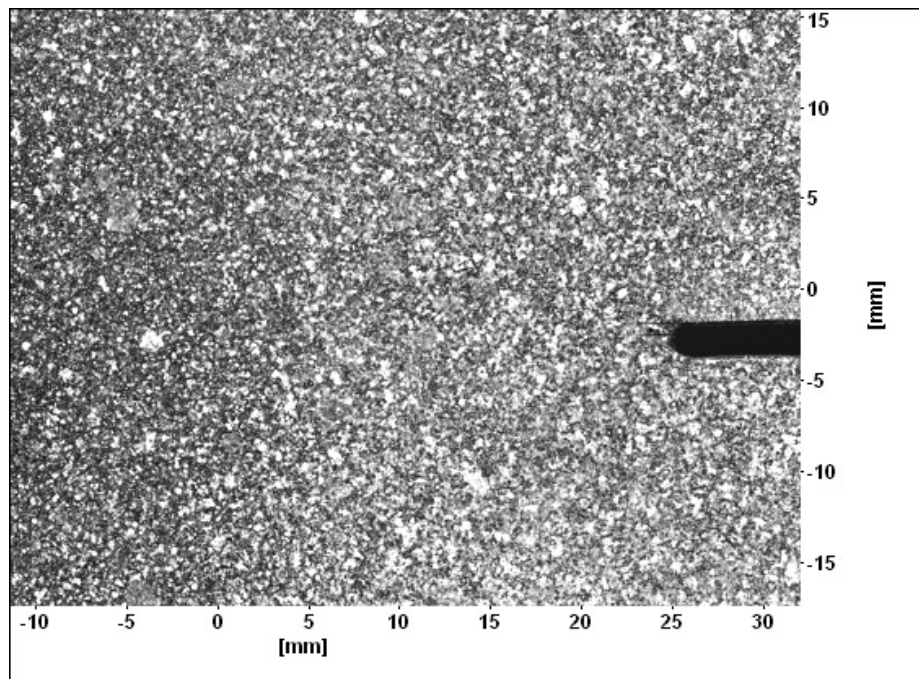


Figure 4-7 Image #490 for CTA1 test showing the painted area in front of the notch.

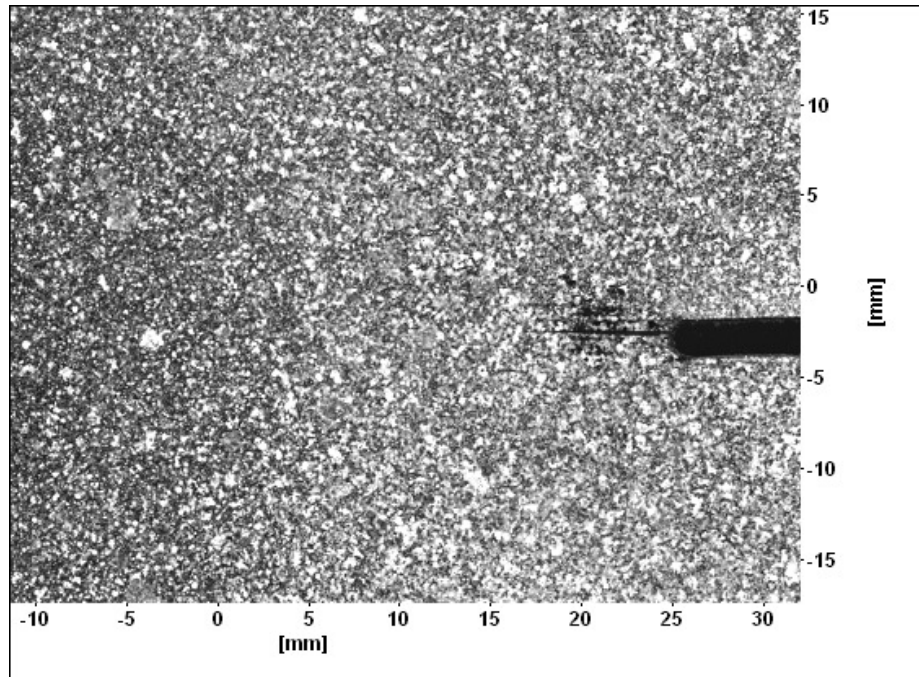


Figure 4-8 Image #534 for CTA1 test showing the painted area in front of the notch.

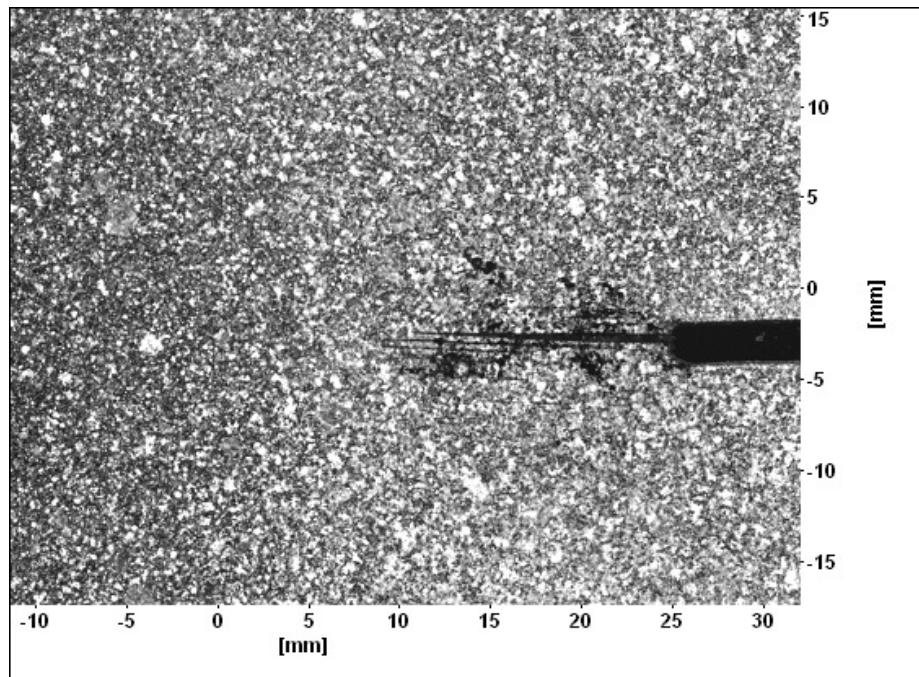


Figure 4-9 Image #734 for CTA1 test showing the painted area in front of the notch.

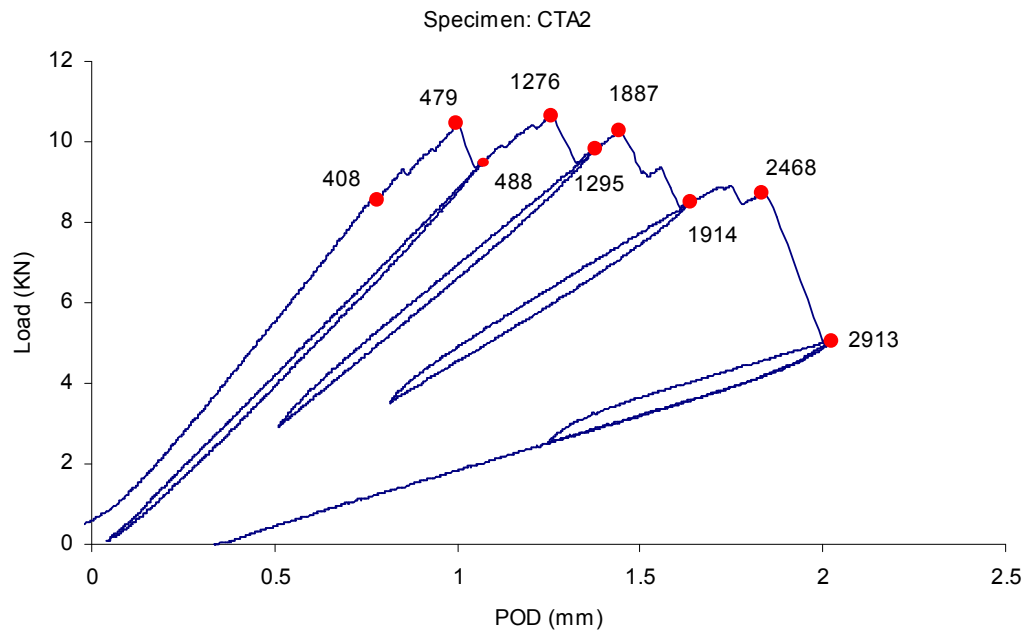


Figure 4-10 Load-Pod curve of CTA2 test showing some of the image numbers on the curve.

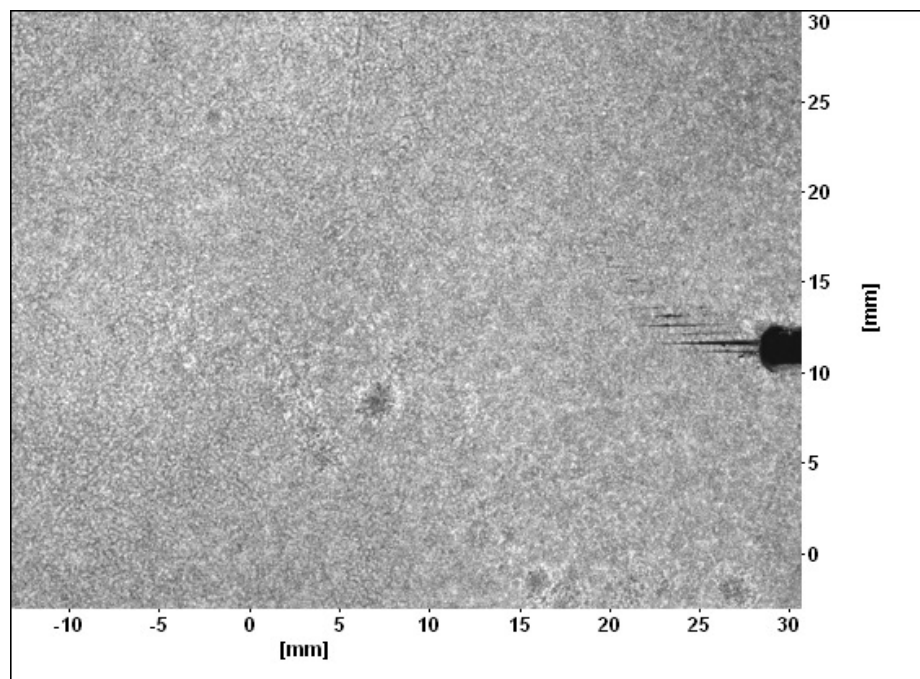


Figure 4-11 Image #1276 for CTA2 test showing the painted area in front of the notch.

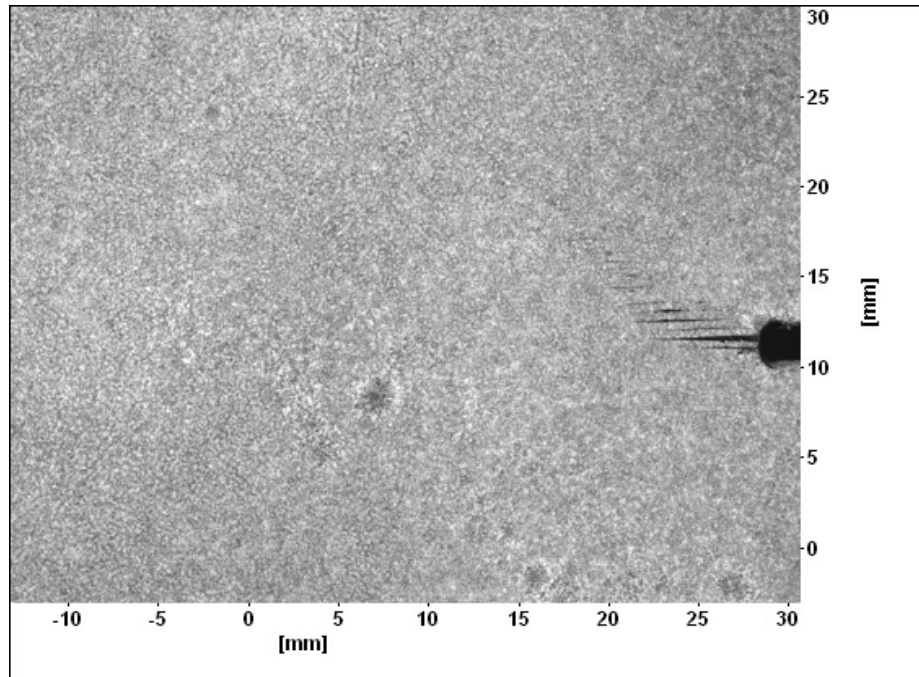


Figure 4-12 Image #1887 for CTA2 test showing the painted area in front of the notch.

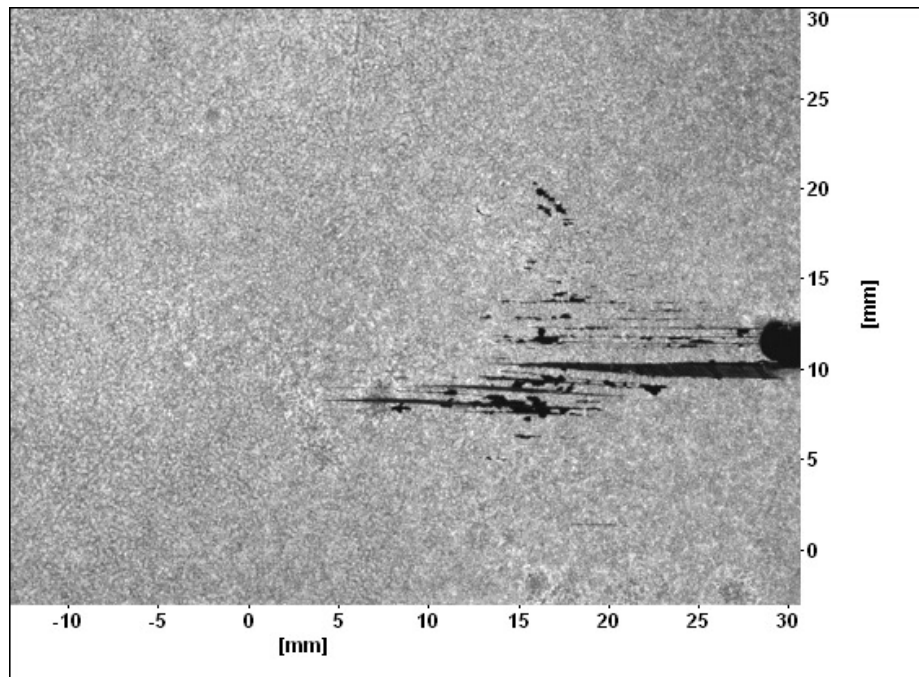


Figure 4-13 Image #2913 for CTA2 test showing the painted area in front of the notch.

4.2.4. Application of the Proposed Method

For CTA1, DaVis generated a virtual mesh with element sizes equal to 2.036 mm. For CTA2, element sizes were 2.054 mm. The mesh generated by DaVis for CTA1 and CTA2 are shown in Figure 4-14 and Figure 4-15 respectively. As shown in these figures, the area of interest in CTA1 is a 14 (horizontal direction) by 10 (vertical direction) elements area and in CTA2 is a 19 by 14 elements area.

For these three tests, the displacement data files were imported into CrackPro to calculate surface strains. As an example, in CTA1, the calculated vertical strains in the loading direction along the line 1 in Figure 4-16, are shown in Figure 4-17.

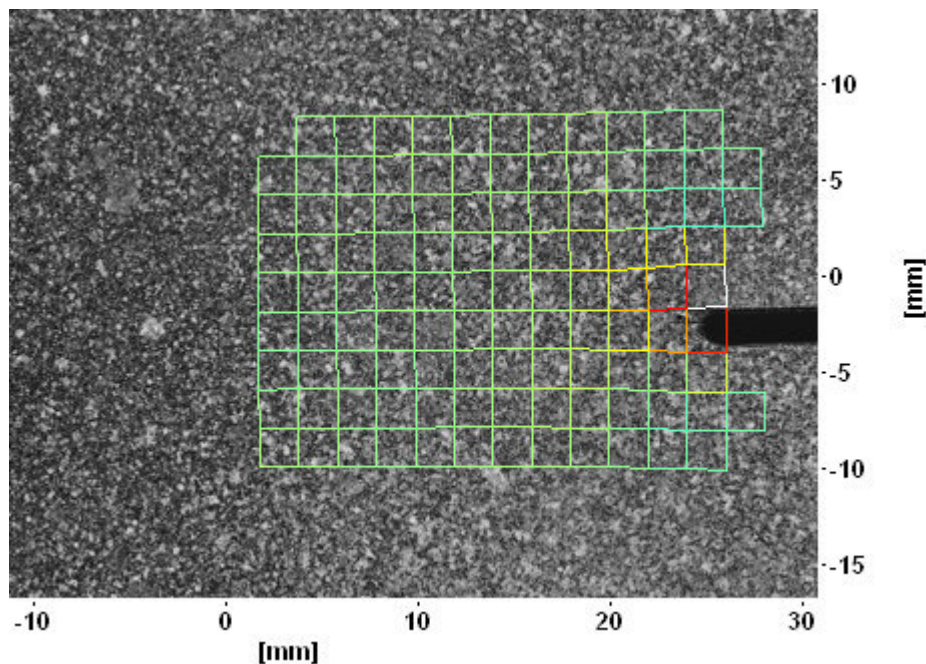


Figure 4-14 Mesh generated by DaVis on the surface of CTA1 specimen with element sizes equal to 2.036 mm.

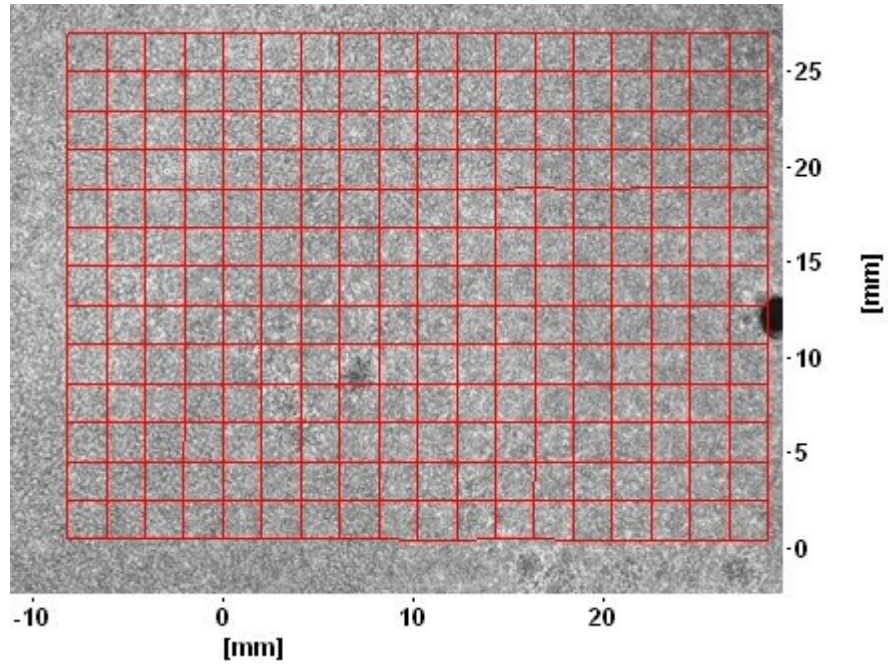


Figure 4-15 Mesh generated by DaVis on the surface of CTA2 specimen with element sizes equal to 2.054 mm.

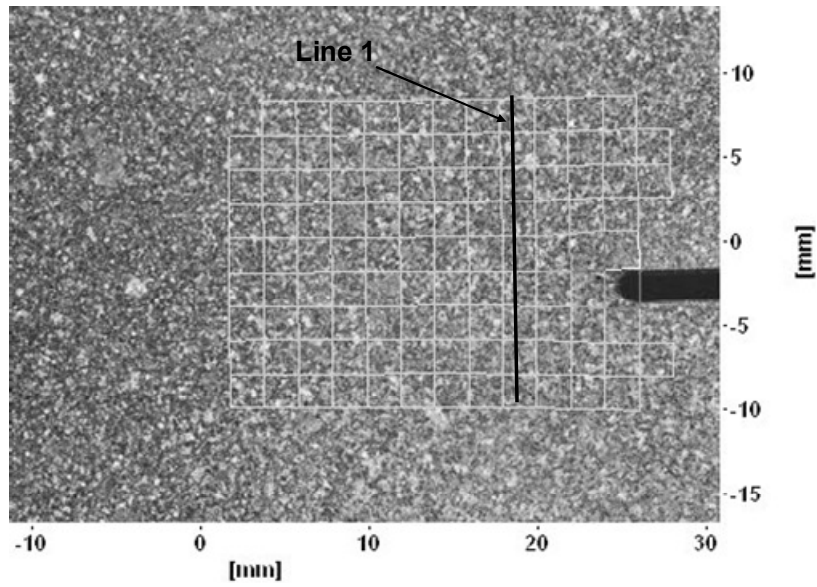


Figure 4-16 Measuring vertical strains along the line 1 on the CTA1 specimen surface.

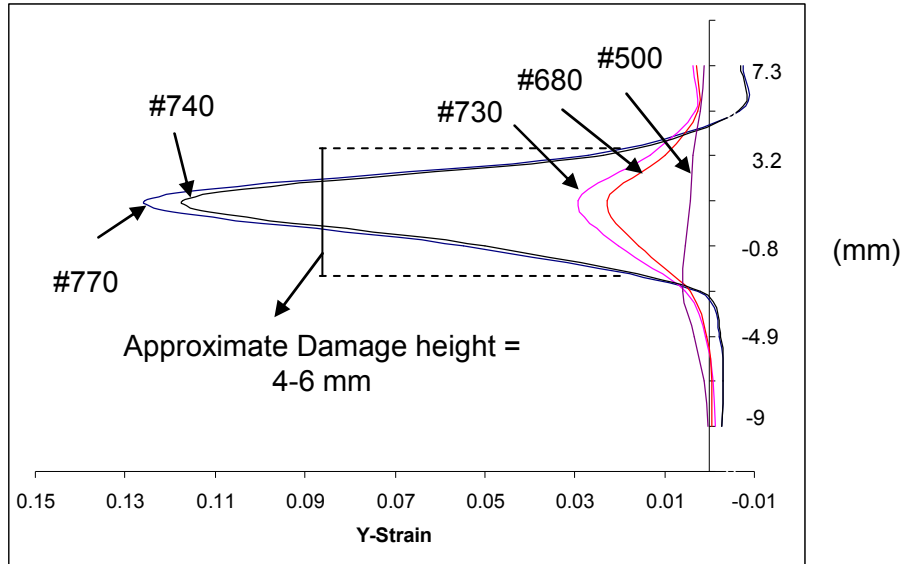


Figure 4-17 Y-Strains (vertical or loading direction) along the line 1 in CTA1 for 5 images: #500, #680, #730, #740 and #770 (Figure 4-16).

In Figure 4-17, the sudden jump in strain values from image #730 to image #740 implies a sudden growth of damage passing through the line 1 in Figure 4-16. Image #730 was captured at POD=1.56 mm and Image #740 was captured at POD=1.62 mm just after the sudden load drop (at Image #734) shown in Figure 4-6. Consequently, this sudden load drop can be attributed to the sudden damage growth in the specimen. In Figure 4-17, the height of damage can also be estimated to be around 4-6 mm from the area with sudden jump in the strain values. These findings are confirmed later in this chapter.

After deriving surface strain values, using elastic properties of the composite laminate obtained previously, elastic stresses and nodal forces were calculated for each image. After detecting the damage zone by checking equilibrium equations, an average damage initiation strain was measured using strains on the boundary of the damage zone (Section 3.2.3.). As an example, strains of the elements on the boundary of the damaged area in CTA1 specimen are shown in Figure 4-18. From this graph, the average strain value on the boundary was measured to be 1.1% with a standard deviation of 0.17%. Damage zones in CTA1 specimen for image #730 and #740 based on this average strain value are shown in Figure 4-19 and Figure 4-20 respectively. These two figures confirm the previous finding of a sudden damage growth passing through Line 1 in Figure 4-16. In

fact, based on the size of the damage zone in these figures, it can be observed that between Image #730 and Image #740, damage suddenly extended about 7 mm.

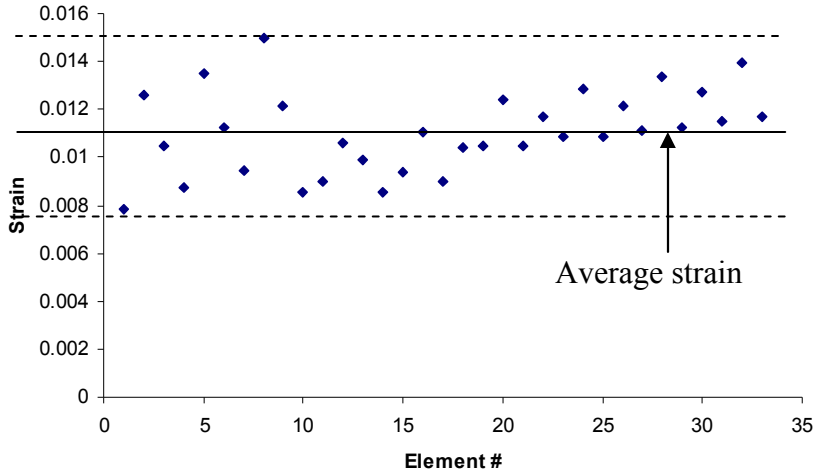


Figure 4-18 Finding the average damage initiation strain from the strains of the damage boundary elements in CTA1.

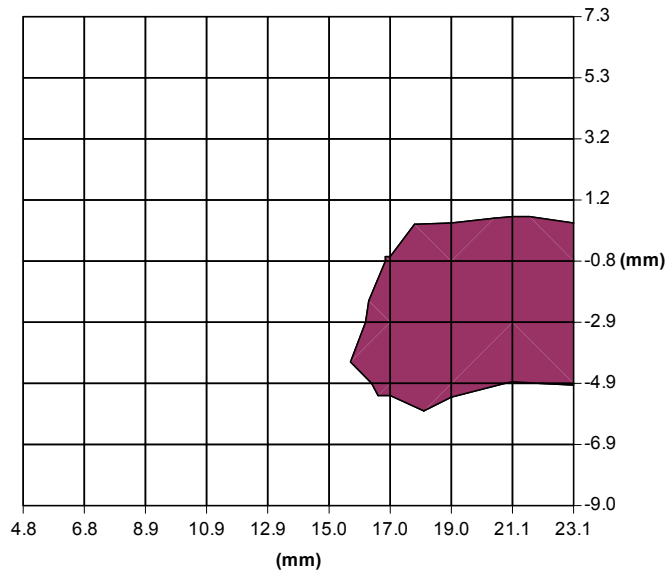


Figure 4-19 Damaged area for CTA1 specimen based on the mesh generated by DaVis (Figure 4-16), in Image #730 (Figure 4-6). Damage is identified as the zone in which strains are higher than the damage initiation strain equal to 1.1% in this study.

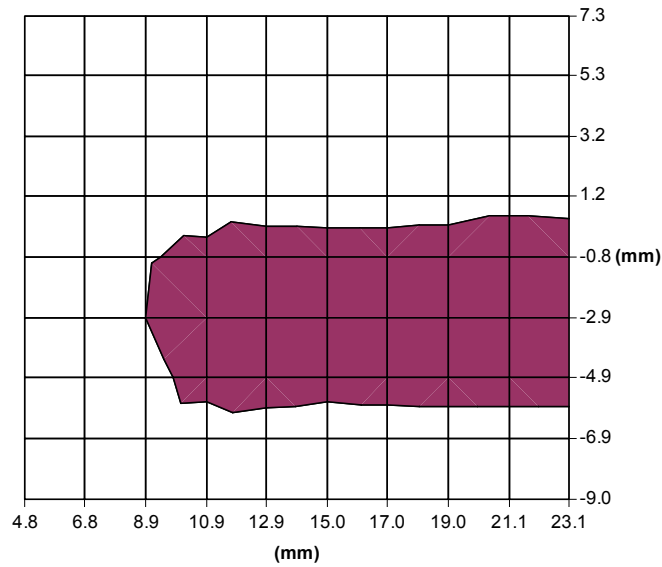


Figure 4-20 Damaged area for CTA1 specimen based on the mesh generated by DaVis (Figure 4-16), in Image #740 (Figure 4-6).

After establishing the extent of damage in each image, using the CrackPro code and based on the proposed method, approximate stress-strain responses of the composite laminate were obtained. As an example, the approximate stress-strain curve obtained for CTA1, for a strip of elements 6 mm ahead of the notch tip is shown in Figure 4-21. The family of curves obtained for CTA1 is also shown in Figure 4-22. The approximate stress-strain curve obtained for CTA2, for a strip of elements 5 mm ahead of the notch tip is shown in Figure 4-23 and the family of approximate curves obtained for CTA2 is shown in Figure 4-24.

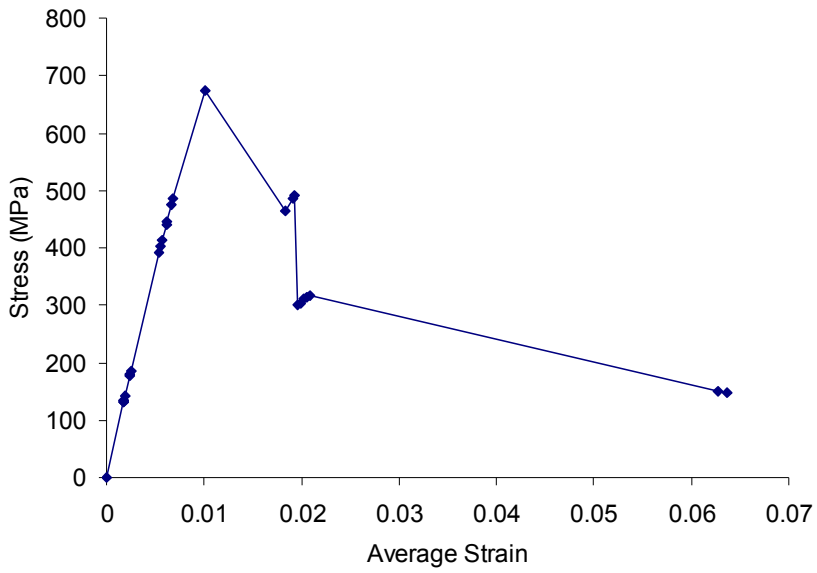


Figure 4-21 Approximate stress-strain response of the composite laminate extracted from CTA1 specimen, 6 mm ahead of the notch tip.

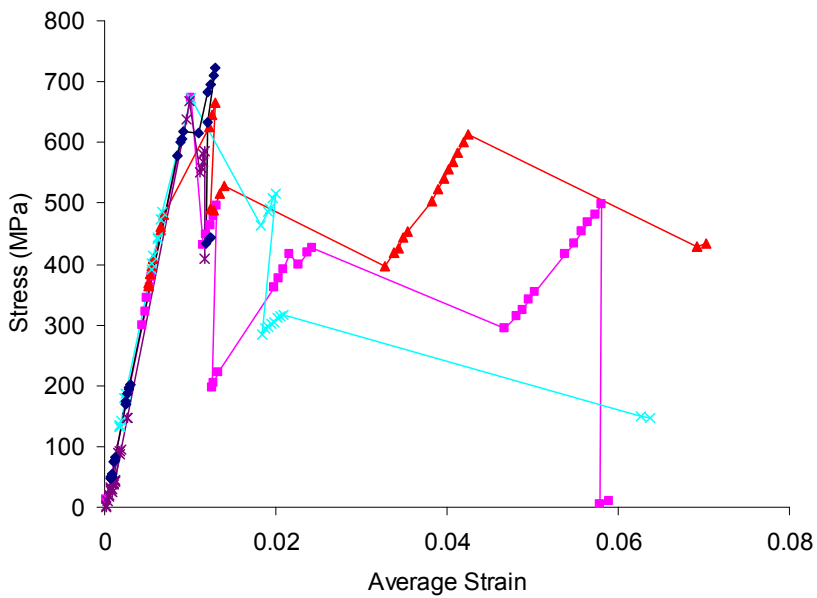


Figure 4-22 Approximate family of stress-strain responses of the composite laminate obtained from CTA1 specimen.

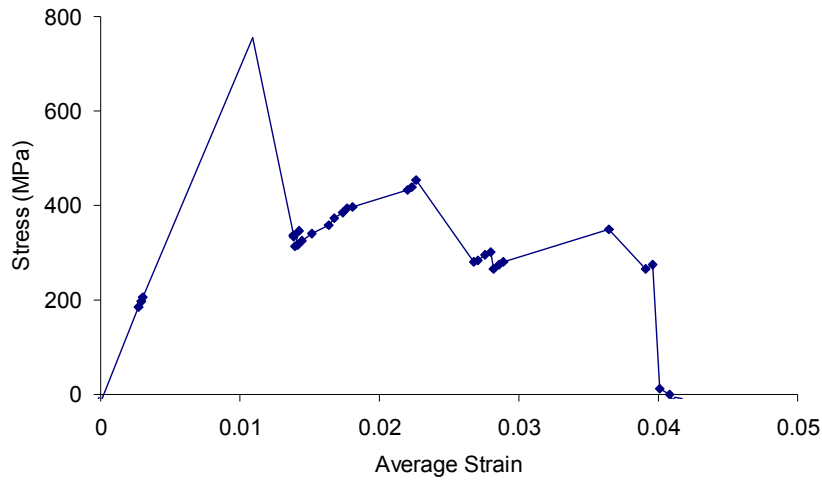


Figure 4-23 Approximate stress-strain response of composite laminate extracted from CTA2 specimen, 5 mm ahead of the notch tip.

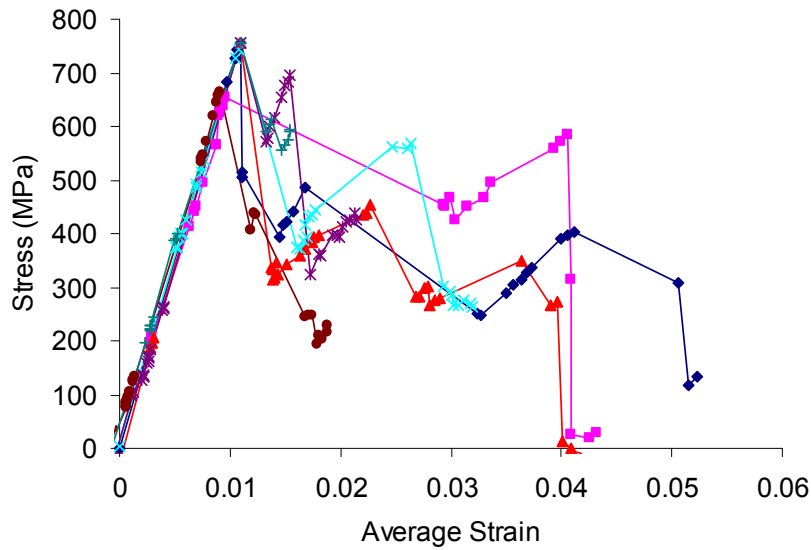


Figure 4-24 Approximate family of stress-strain responses of the composite laminate obtained from CTA2 specimen.

In these figures, it can be observed that all of the approximate constitutive responses, contain a series of sudden jumps which are usually followed by stiffening behaviour (sawtooth shapes). Although initially it may seem that these jumps are artificially generated in the approximation process, comparison of approximate curves and also further analyzing the load-POD response of the damaging specimen, shows a consistent behaviour. By correlating these jumps with the sudden damage extensions and

consequently sudden load drops in global load-POD curves, it can be observed that sawtooth shapes in approximate responses are the result of damaging behaviour of the material. In Figure 4-25, some of these load drops (A, B and C) are specified on the load-POD curve of the CTA2 specimen. During the test, each load drop was accompanied by a loud noise. These load drops were the result of the sudden crack extensions in the specimen which could be monitored on the surface of the specimen. Surface images obtained before and after specified load drops in Figure 4-25 (A, B and C), are shown in Figure 4-26. Using image numbers, corresponding jumps in the stress-strain curves can be identified. For example, load drop “A” in Figure 4-25, occurs between images #1276 (A^-) and #1277 (A^+). Stress-strain pairs obtained from these images result in sudden jumps in local stress-strain curves obtained using the proposed method. These jumps are identified in Figure 4-27 and Figure 4-28 for stress-strain responses obtained 5 mm and 7 mm ahead of the CTA2 initial notch tip, respectively.

We can also calculate the approximate damage length in each specimen using the current proposed method. By constructing the damage length-POD curve, we can identify the sudden damage extensions in each test. For example, the damage length-POD curve was constructed for the CTA2 specimen and is shown in Figure 4-29. Sudden damage extensions correspond to the load drops in Figure 4-25 are also identified in Figure 4-29. Damage extensions for load drops “A”, “B” and “C”, are approximately equal to 2.5, 1 and 2 mm respectively.

From these figures, it can be observed that, in these laminates, damage propagates in a stepwise manner. Sudden damage extensions of about 1-3 mm are followed by slow rate damage extensions. This behaviour could be due to the heterogeneous fibre failure in the laminate. As shown in other studies (Ilcewicz et al., 1993), the manufacturing process of a given laminate, such as tow placement, might introduce inhomogeneity in the material and therefore contribute to changes in its local softening behaviour. The IM7/8552 prepreg used in the current laminate, consists of 12000 (12K) filament count tows (Hexcel Composites Ltd). For a fibre diameter of 5.2 micron (Hexcel Composites Ltd) and lamina thickness of 0.125 mm, this results in an approximately 2.5 mm tow size in the current laminate (about 24 fibres through the thickness of each lamina and 500 fibres

in the plane of the lamina for each tow). This coincides with the size of the sudden damage extensions observed in OCT tests. Further investigation, however, is needed to verify the effect of tow size on the sudden damage extensions. Moreover, any voids or defects in the material acts as a stress concentration point and causes the damage to extend abruptly. These extensions result in instantaneous load drops in the global load-POD curve. Locally, this behaviour can be observed as jumps in the stress-strain curves. Therefore, it can be concluded that the approximate stress-strain responses obtained in this study (e.g. Figure 4-24), represent the real behaviour of the damaging material. To further validate this finding, sudden damage extensions are identified for the CTA1 specimen as well. In Figure 4-30, some of the load drops (D and E) are specified for the CTA1 specimen in the global load-POD curve. In Figure 4-31 and Figure 4-32, corresponding jumps are shown in stress-strain curves 4 mm and 6 mm ahead of the initial notch tip respectively. In Figure 4-33, calculated damage length-POD and corresponding sudden damage extensions are also shown. Again from these figures, it can be concluded that damage does not grow in a continuous manner and sudden damage extensions result in jumps in the global and local responses of the material.

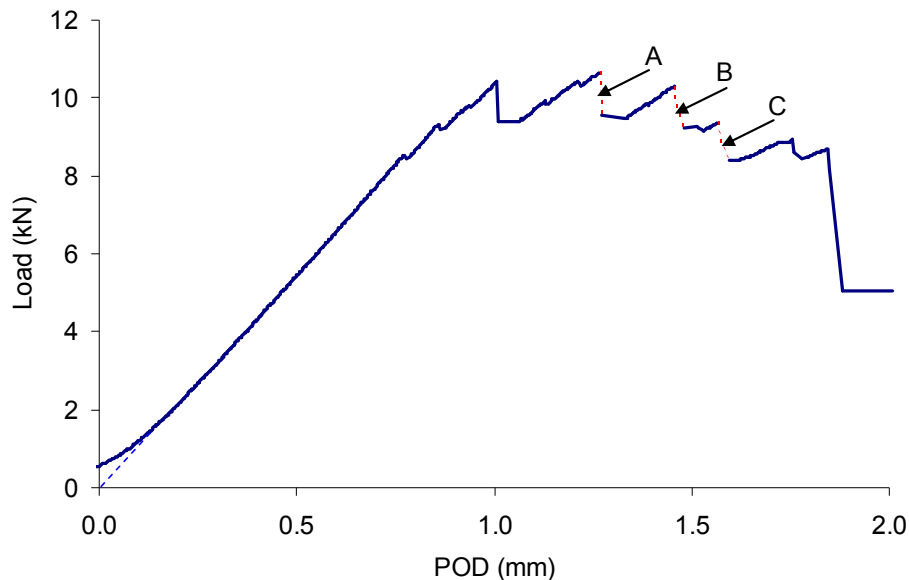


Figure 4-25 Specifying some of the load drops (A, B and C) in the load-POD curve of the CTA2 specimen.

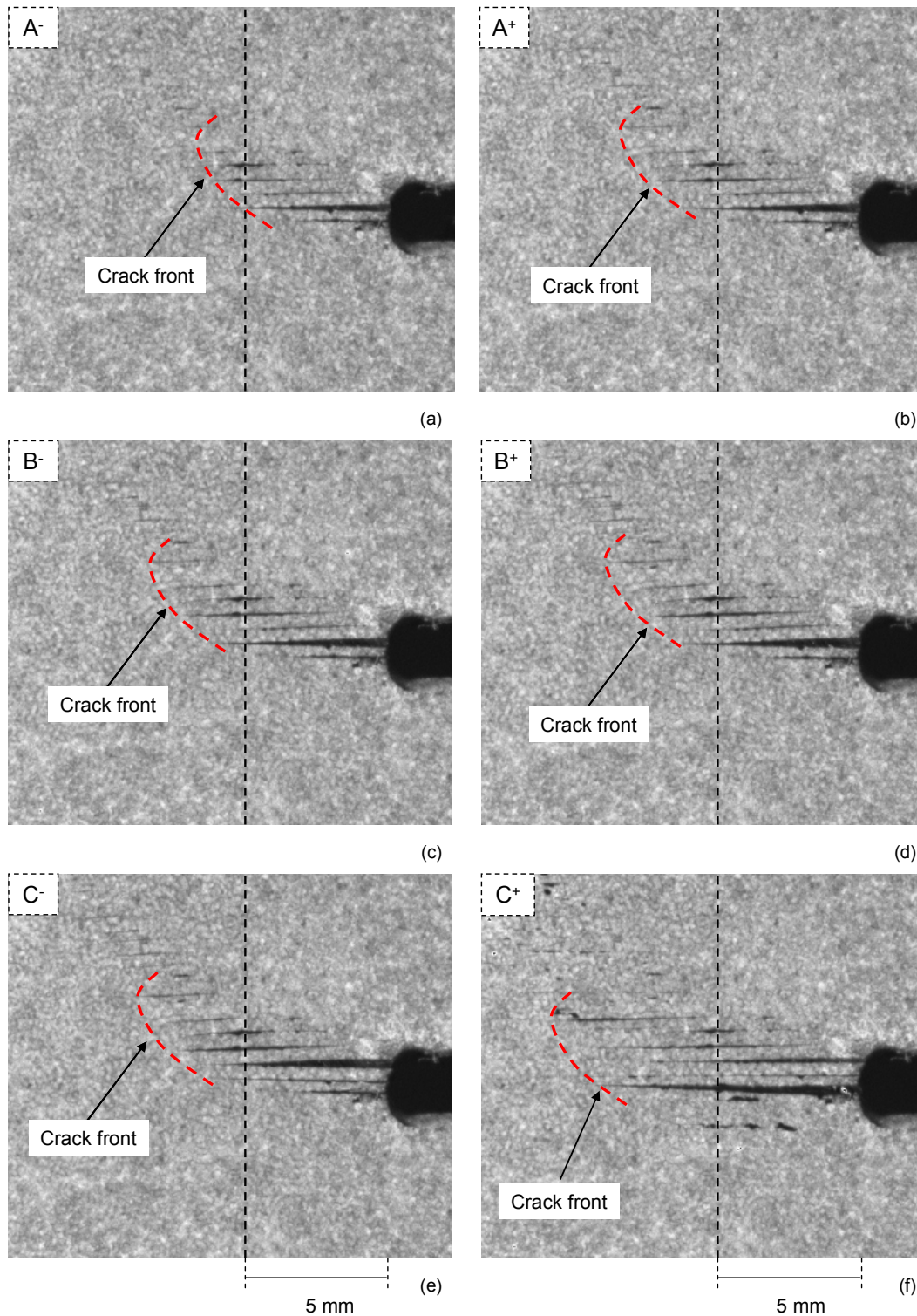


Figure 4-26 Surface images of the CTA2 specimen before and after the sudden load drops specified in Figure 4-25. (a) and (b) before and after the load drop "A". (c) and (d) before and after the load drop "B". (e) and (f) before and after the load drop "C".

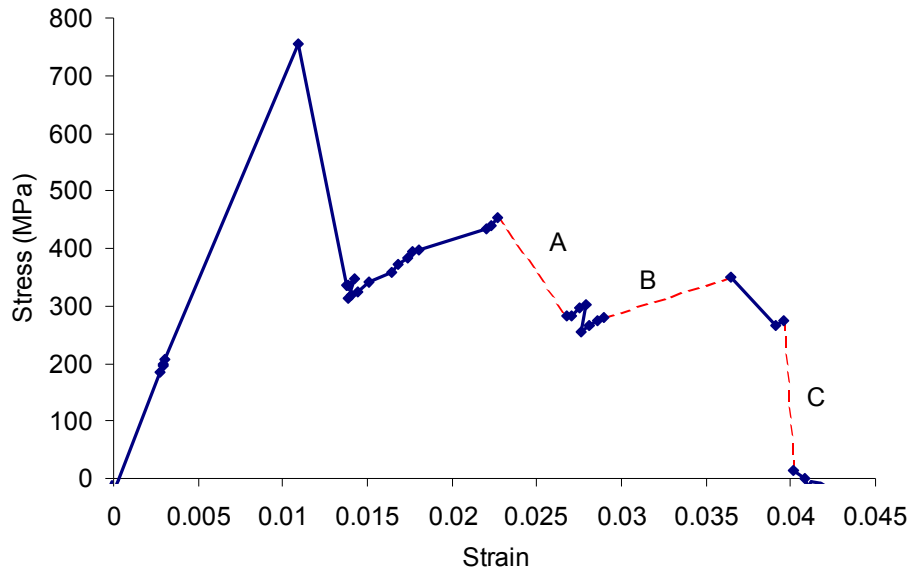


Figure 4-27 Stress-strain response, 5 mm ahead of the notch tip in the CTA2 specimen. Sudden jumps in the response curve (A, B and C) correlate to load drops in the global load-POD curve (Figure 4-25).

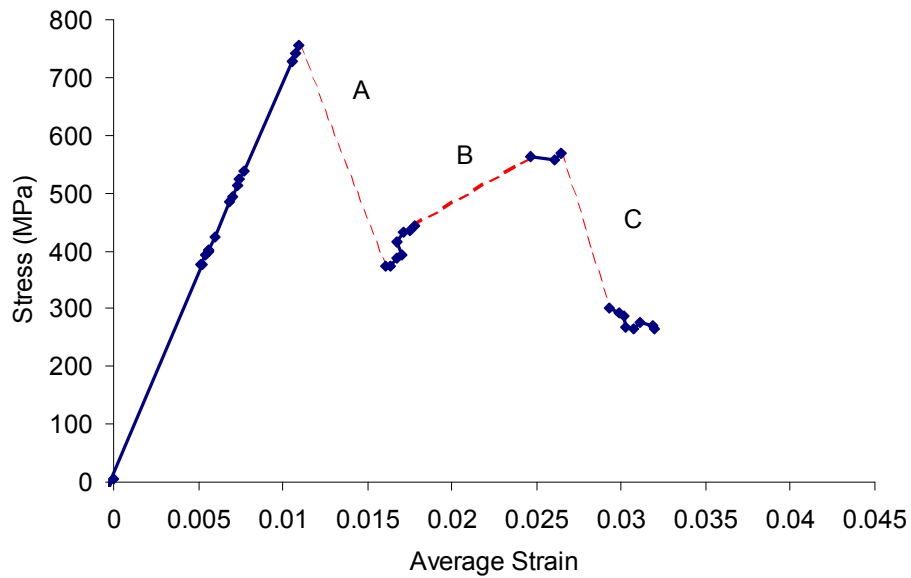


Figure 4-28 Stress-strain response, 7 mm ahead of the notch tip in the CTA2 specimen. Sudden jumps in the response curve (A, B and C) correlate to load drops in the global load-POD curve (Figure 4-25).

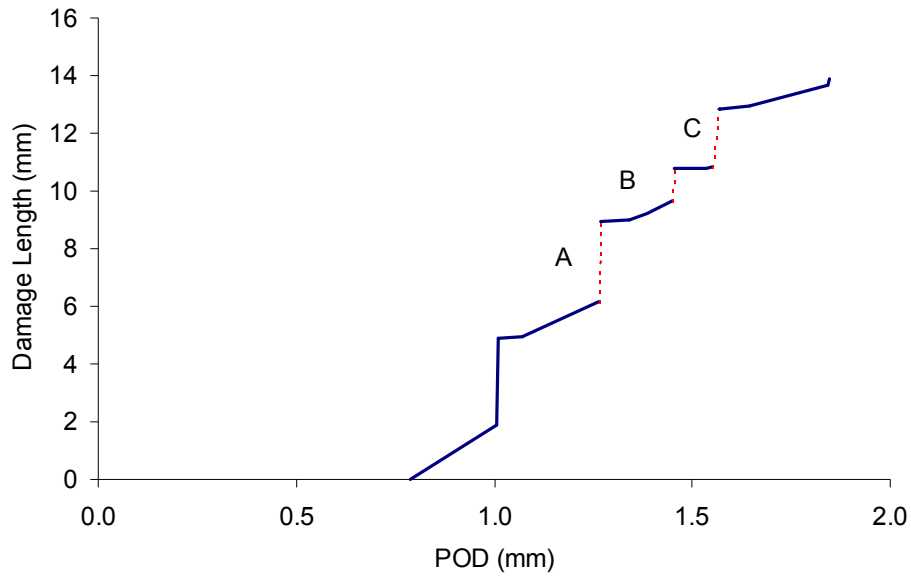


Figure 4-29 Calculated damage length-POD in the CTA2 specimen using the proposed method. Sudden damage growth (e.g. A, B and C) correlates to the load drops in the global load-POD curve (Figure 4-25).

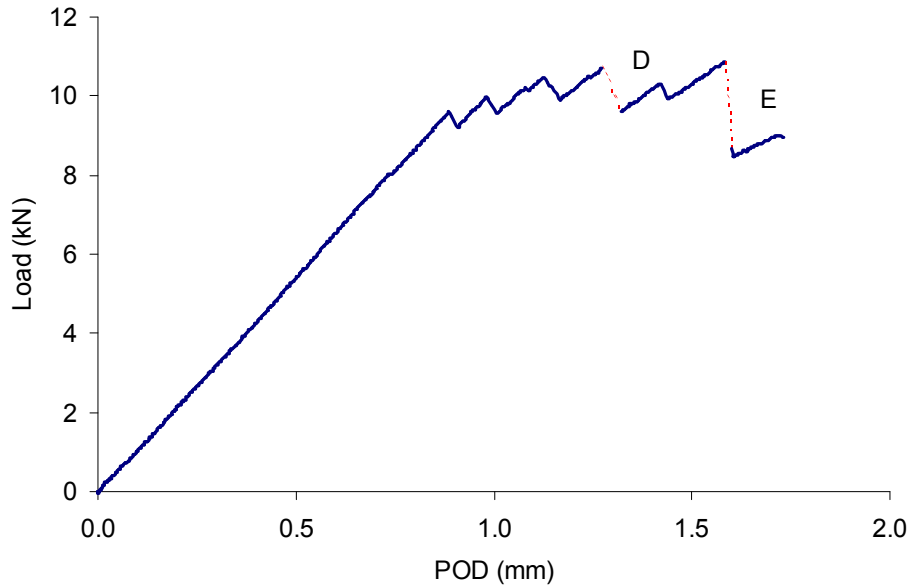


Figure 4-30 Specifying some of the load drops (D and E) in the load-POD curve of the CTA1 specimen.

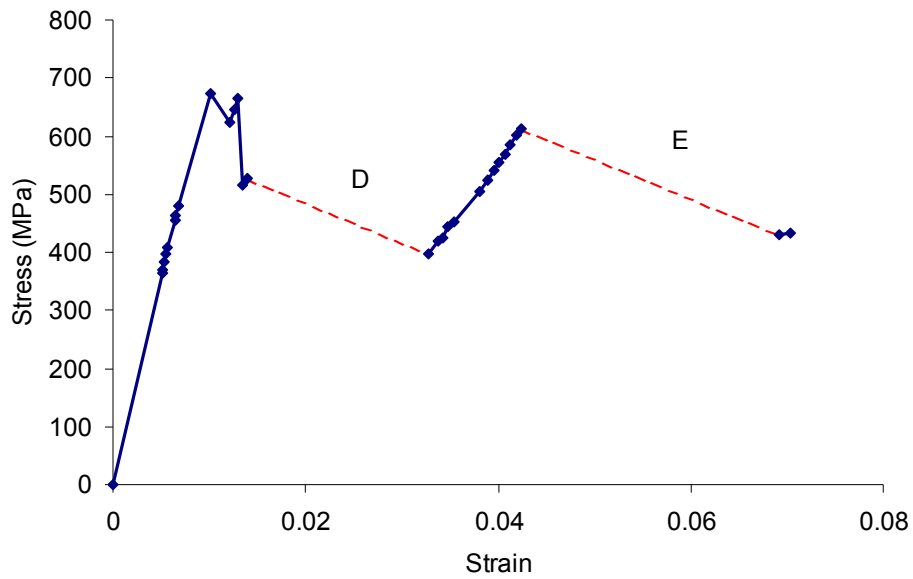


Figure 4-31 Stress-strain response, 4 mm ahead of the notch tip in the CTA1 specimen. Sudden jumps in the response curve (D and E) correlate to load drops in the global load-POD curve (Figure 4-30).

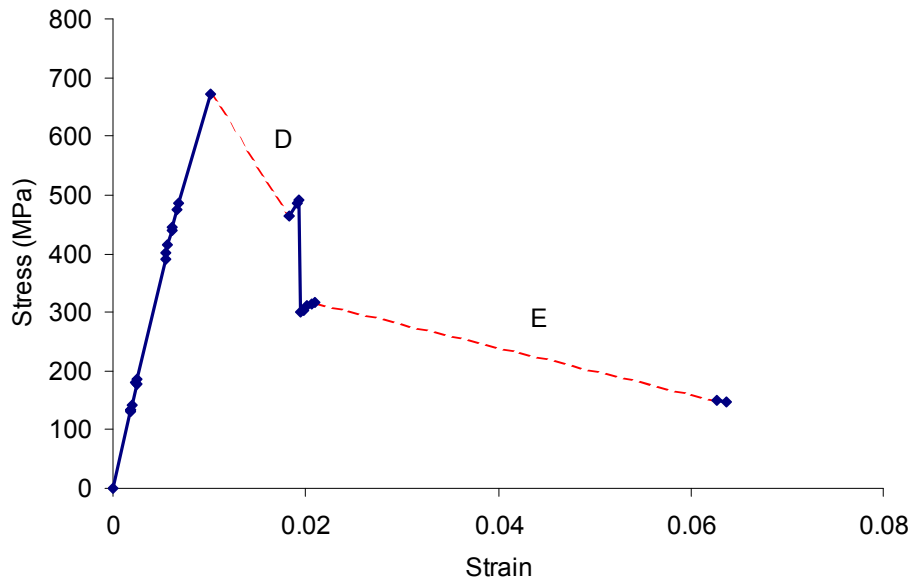


Figure 4-32 Stress-strain response, 6 mm ahead of the notch tip in the CTA1 specimen. Sudden jumps in the response curve (D and E) correlate to load drops in the global load-POD curve (Figure 4-30).

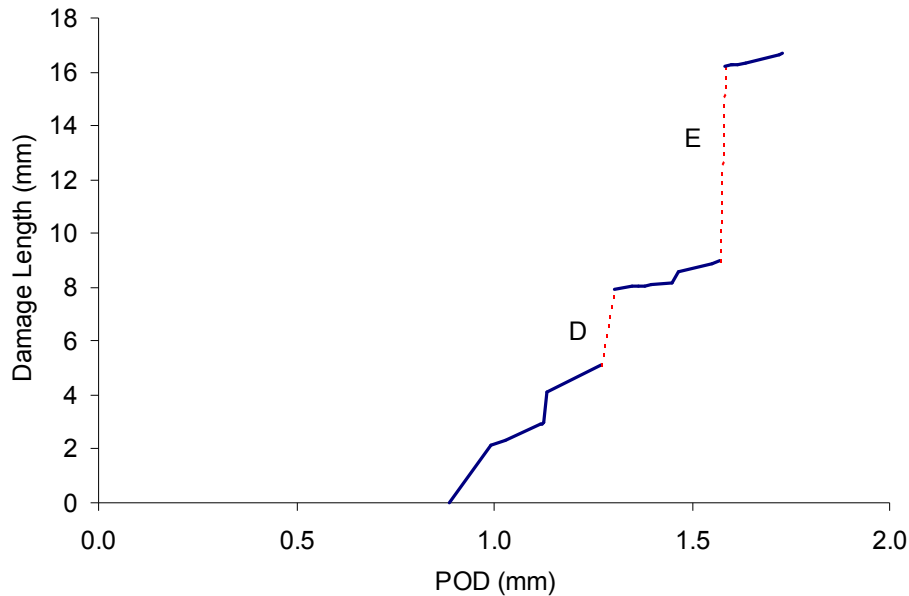


Figure 4-33 Calculated damage length-POD in the CTA1 specimen using the proposed method. Sudden damage growth (e.g. D and E) correlates to the load drops in the global load-POD curve (Figure 4-30)

After observing the damage length-POD curves in OCT tests (e.g. Figure 4-33), it may seem that due to the inhomogeneity of the material response, a smooth damage function (e.g. linear or exponential), would not be sufficient to simulate the damaging behaviour of composites. However, as mentioned before, the current approach of continuum damage mechanics is to smear the degradation of the material in the damage band using a smooth function. This is mainly due to the ease of implementation and also difficulties associated with characterizing a non-smooth function. By using a smooth damage function, continuous strain-softening curves and consequently continuous global responses are obtained. In small specimens where the size of the observed jumps in the damage length-POD curve (Figure 4-33) becomes comparable to the size of the specimen, the self-similar damage growth assumption will no longer be a valid assumption. Obviously in these cases, smearing approach will not be successful in simulating the response of the specimens. This approach, however, has been shown to be successful in capturing the global behaviour of OCT specimens (e.g. Floyd, 2004; McClennan, 2004) and also larger notched specimens (e.g. Walker et al., 1996).

Any continuous softening response shape chosen at this stage, should at least represent an average behaviour of the inhomogeneous local responses. Approximate stress-strain curves obtained in this study, provide an opportunity to observe the real damaging behaviour of the material and choose an appropriate softening response shape. In this study, three possible response shapes, linear, bilinear and trilinear, are chosen and analyzed. Although it may seem that a complicated multi-linear curve is needed to appropriately simulate the damaging behaviour of these laminates, it will be shown that a bilinear or trilinear softening curve is sufficient to adequately capture the global and local behaviour of the material.

Using the family of approximate curves (Figure 4-22 and Figure 4-24), upper bound and lower bound limit responses were identified and shown in Figure 4-34. Also in this Figure, analyzed softening response shapes are depicted.

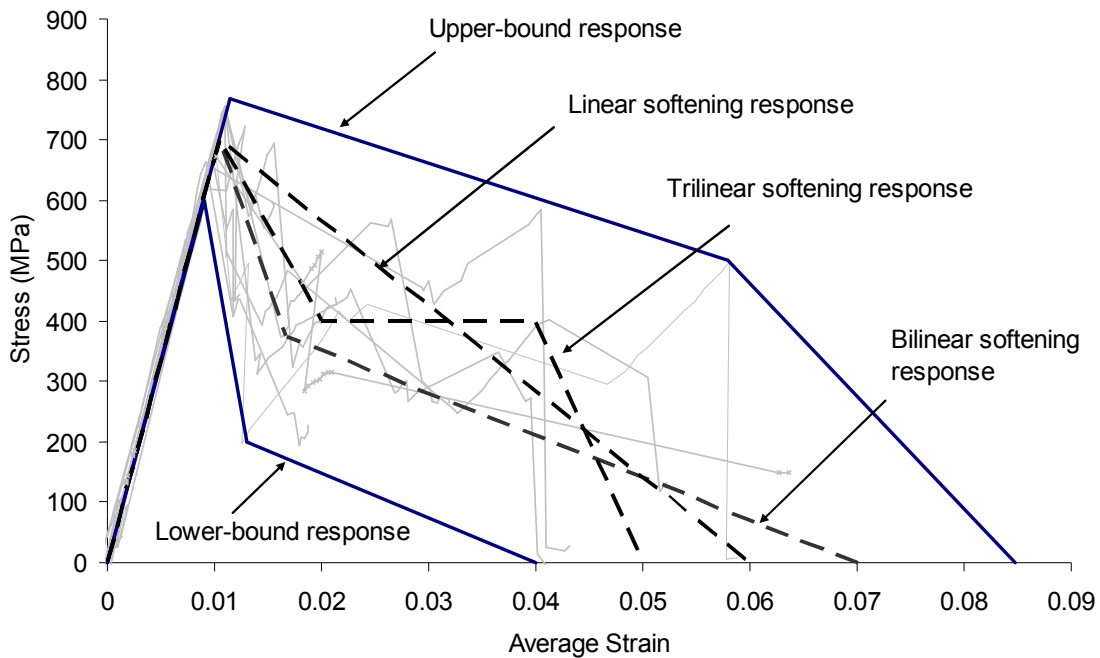


Figure 4-34 Upper-bound and lower-bound responses based on the family of approximate stress-strain curves. Linear, bilinear and trilinear softening responses considered for the optimization process are also shown here.

In the optimization process we need to measure the fracture energy of the material. In this study, the fracture energy was obtained from the area below the load-POD curve using Equation 3-27. For CTA1, three unloadings were performed after images #379, #535 and #771 as shown in Figure 4-35. For CTA2, four unloadings were performed after images #488, #1295, #1914 and #2913 as shown in Figure 4-36. In these tests, the unloading curves were extended linearly to zero load to obtain the area below the load-POD curves. From these seven unloadings, an average fracture energy value was obtained. The calculations for CTA1 and CTA2 are summarized in Table 4-5 and Table 4-6 respectively. The fracture energy as a function of damage length, a , is also shown in Figure 4-37. Based on these calculations, the average fracture energy is about 110 kJ/m² with a standard deviation equal to 13 kJ/m². In this study, tensile fracture energy is taken to be 110 kJ/m² for the IM7/8552 quasi-isotropic laminate.

Table 4-5 Calculating the fracture energy for CTA1 based on the area below the load-POD curve confined by the unloading path.

| Image # | Crack Length mm | Area below load-POD kN.mm | G_f kJ/m ² |
|---------|--------------------|------------------------------|----------------------------|
| 379 | 1.8 | 0.77 | 103.8 |
| 535 | 6.1 | 2.85 | 115.1 |
| 771 | 14.9 | 5.86 | 97.2 |

Table 4-6 Calculating the fracture energy for CTA2 based on the area below the load-POD curve and confined by the unloading path.

| Image # | Crack Length mm | Area below load-POD kN.mm | G_f kJ/m ² |
|---------|--------------------|------------------------------|----------------------------|
| 488 | 4.2 | 1.55 | 90.5 |
| 1295 | 6.6 | 3.31 | 123.6 |
| 1914 | 11.4 | 5.74 | 125.2 |
| 2913 | 24.0 | 10.37 | 106.7 |

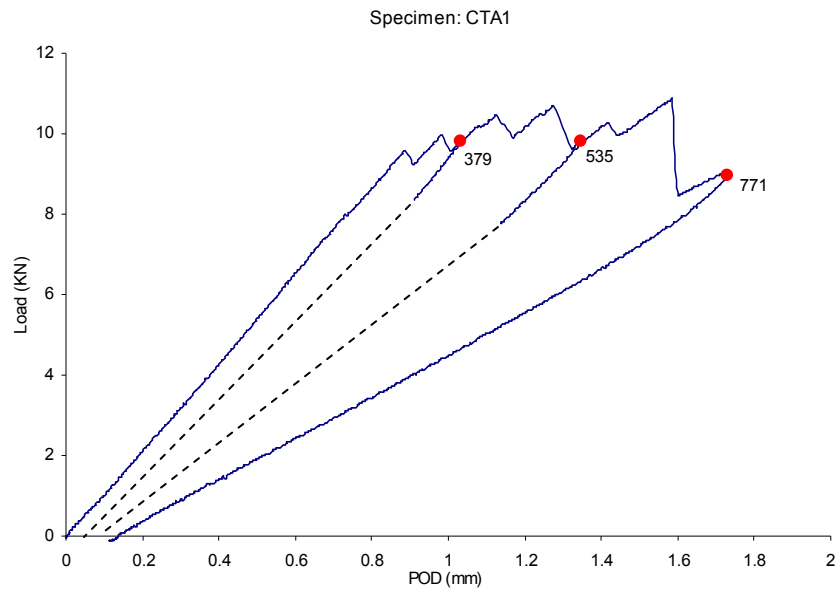


Figure 4-35 Measuring fracture energy for the area below the load-POD curve and limited to the unloading path for CTA1.

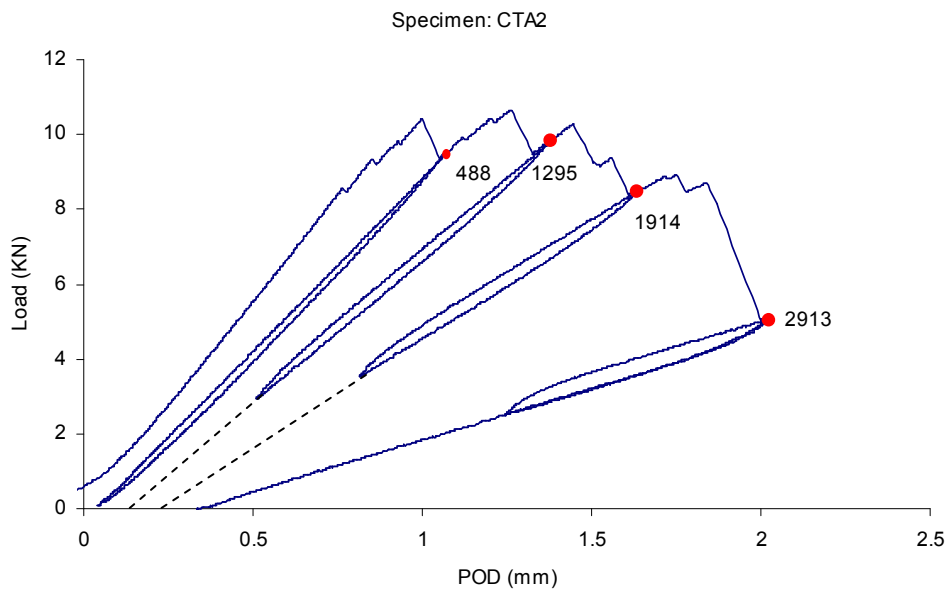


Figure 4-36 Measuring fracture energy for the area below the load-POD curve and limited to the unloading path for CTA2.

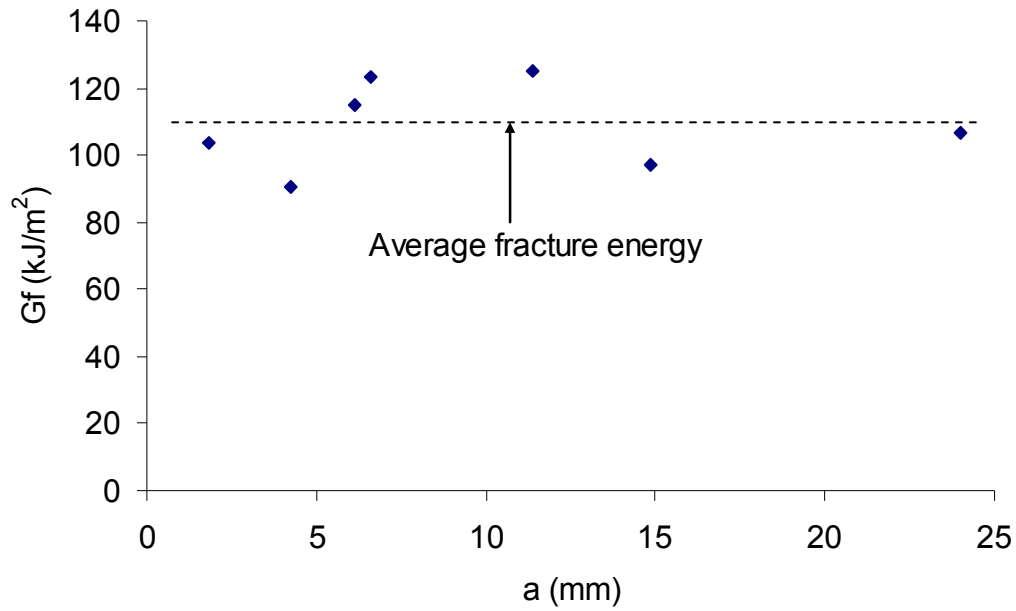


Figure 4-37 Finding the average fracture energy from OCT tests.

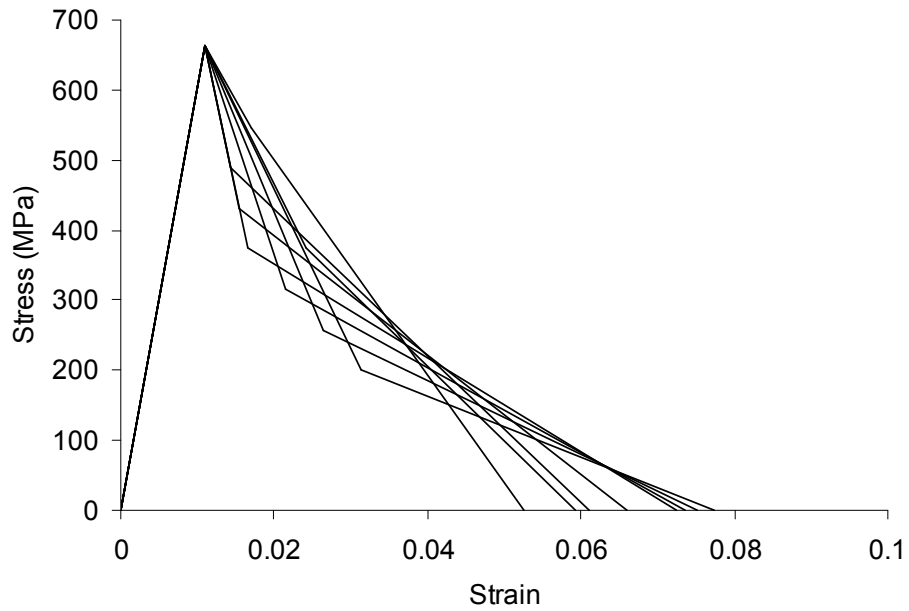


Figure 4-38 Stress-strain curves obtained from the satisfaction of global energy criterion based on a bilinear response shape.

The fracture energy value obtained in this section, along with the upper bound and lower bound limits were used in the first step of the optimization process. Using CrackPro, all the curves within these two bounds that could satisfy the global energy criterion were identified. As an example, some of the curves obtained based on a bilinear softening response shape are shown in Figure 4-38.

After this step, the local equilibrium criterion was enforced in CrackPro. In this step using linear, bilinear and trilinear softening shapes, optimized responses were obtained. These responses are shown in Figure 4-39. It can be observed that all of the curves have the same damage initiation strain value equal to 1.1%. Also the bilinear and trilinear softening curves, almost have the same slope after the peak. This shows that in the optimization process, by adding more complexity to the softening shape, initial features of simpler curves are kept constant. The other observation relates to the plateau stress in the trilinear softening curve. This plateau in fact represents the average behaviour of the sawtooth shapes previously observed in the approximate stress-strain curves (e.g. Figure 4-28). As explained previously, this is caused by the inhomogeneous fibre failure which results in sudden damage extensions followed by stiffening responses. This shows that the trilinear softening shape, is a better average representation of the real behaviour of the material compared to the other optimized curves. The effect of the plateau stress, however, may not be observed in the small size notched specimens. As explained previously, this is because in small specimens, failure occurs before the material goes through the complete strain-softening response. This also suggest that in larger structures, characterizing the end part of the softening response becomes more important. A summary of material properties and also optimized softening curves obtained using the proposed method are given in Table 4-7 and Table 4-8.

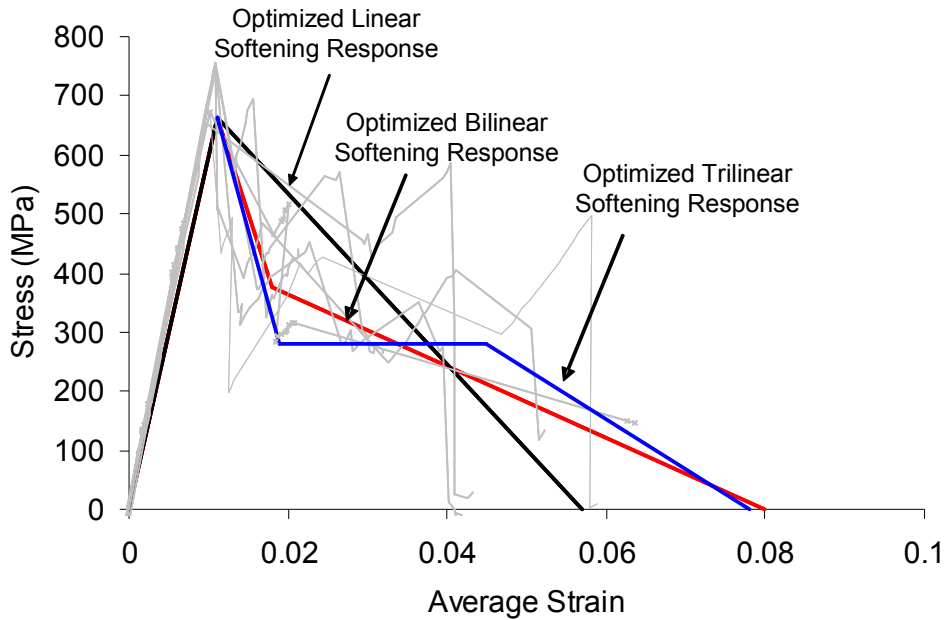


Figure 4-39 Optimized softening curves obtained using the proposed method.

Table 4-7 Summary of the properties obtained for the composite laminate.

| | | | | |
|--------------------------|-----------------|------|----------------------|------------------------------------|
| Elastic modulus | E_x | 60.2 | (GPa) | From FE analysis |
| | E_y | 60.2 | (GPa) | From FE analysis |
| Poisson's ratio | ν_{xy} | 0.32 | | From laminate plate theory |
| Shear modulus | G_{xy} | 22.8 | (GPa) | From elastic theory = $E/2(1+\nu)$ |
| Damage initiation strain | ε_i | 1.1% | | From CrackPro |
| Fracture energy | G_f | 110 | (kJ/m ²) | From area below load-POD |

Table 4-8 Coordinates of the optimized response curves obtained using the proposed method.

| Linear Softening Curve | | Bilinear Softening Curve | | Trilinear Softening Curve | |
|------------------------|--------------|--------------------------|--------------|---------------------------|--------------|
| Strain (%) | Stress (MPa) | Strain (%) | Stress (MPa) | Strain (%) | Stress (MPa) |
| 0 | 0 | 0 | 0 | 0 | 0 |
| 1.1 | 663 | 1.1 | 663 | 1.1 | 663 |
| 5.7 | 0 | 1.8 | 375 | 1.9 | 280 |
| | | 8 | 0 | 4.5 | 280 |
| | | | | 7.8 | 0 |

4.2.5. Finite Element Simulation

In this section, independent FE simulations of the OCT tests were carried out in LS-DYNA. Linear, bilinear and trilinear optimized softening responses were used as inputs for simulations using the built-in material model, MAT_081. Quasi-static simulations of the OCT test were carried out using a 0.25 mm mesh size and applying the Bazant's crack band scaling law (Bazant and Oh, 1983) to adjust the stress-strain curve and thus maintain the objectivity of the numerical results. Part of the FE mesh in LS-DYNA is shown in Figure 4-40.

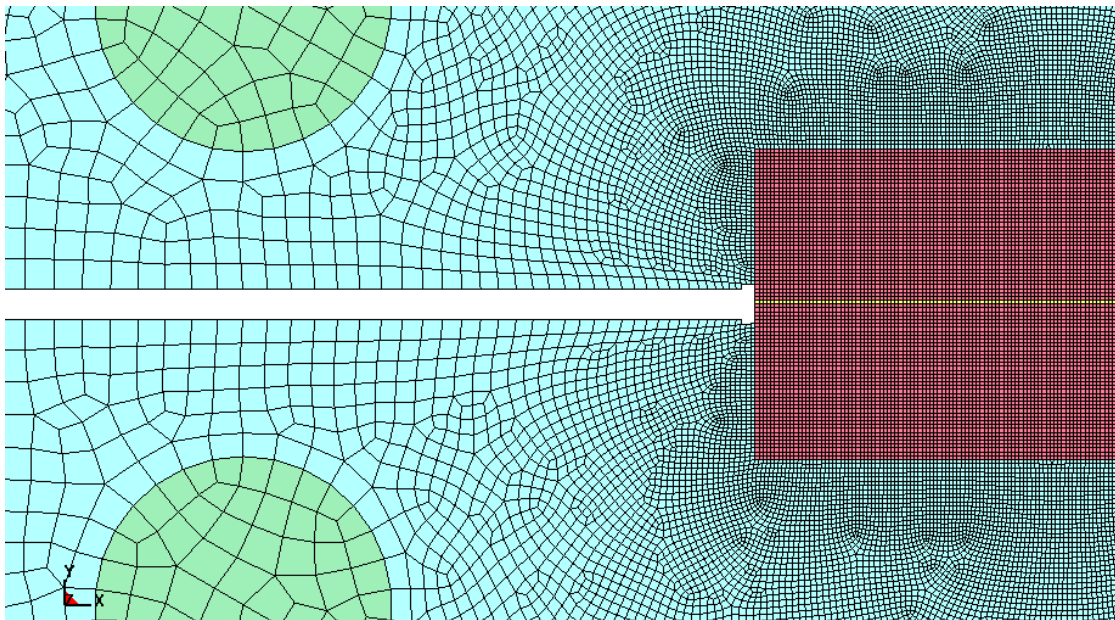


Figure 4-40 Part of the finite element mesh used to simulate the response of OCT specimens with 0.25 mm elements at the notch tip.

In Bazant's crack band scaling law, the area below the strain-softening response is scaled based on the element size. This is because in the local FE simulation, damage localizes in one row of elements and consequently smaller amount of energy is dissipated in smaller elements. Assume that the area below the material stress-strain curve is equal to γ and the fracture energy is equal to G_f . Based on Equation 3-28, for an element size (height) of h_e , we have:

$$G_f = h_e \gamma_s \quad (4-1)$$

In which γ_s is the scaled energy density of the element such that:

$$\gamma_s = n\gamma \quad (4-2)$$

Here, n is the scale factor in Bazant's scaling law calculated as follows:

$$n = \frac{G_f}{h_e \gamma} \quad (4-3)$$

Based on Equation 4-3, the smaller the element size, the larger the value of n . Using this factor, the area below the stress-strain curve is scaled (Figure 4-41) such that the dissipated energy remains constant (Bazant and Oh, 1983).

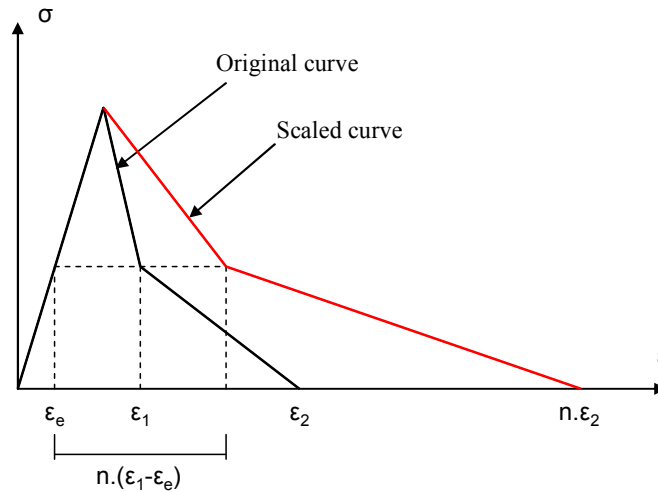


Figure 4-41 Applying the Bazant's crack band scaling law to adjust the energy density of elements (Bazant and Oh, 1983).

Using the above scaling process, a small element is likely to undergo large strains as damage in that element propagates. In LS-DYNA, strains that are computed in the elements are treated as true strains, ϵ_T . The relation between the true strains and nominal (engineering) strains, ϵ_E , is given by:

$$\epsilon_T = \ln(1 + \epsilon_E) \quad (4-4)$$

Assume that the damage saturation strain obtained using the proposed method is equal to ϵ_2 . The total displacement applied to the elements, δ_s , before complete failure is equal to the saturation strain times the element height. Using the true strain measure of ϵ_2 , however, this displacement is calculated as:

$$\delta_s = h_e [\exp(\varepsilon_2) - 1] \quad (4-5)$$

which is larger than the intended value. Consequently, this results in larger dissipation of energy (i.e. the product of stress and displacement) in the elements. To deal with this problem, one has to either disable the large deformation calculation in the FE code or use the equivalent true strain values as inputs (Figure 4-42c). Since the large deformation calculation cannot be disabled in LS-DYNA, the second approach has been adopted here. Therefore in this study, initially, the optimized stress-strain curves (Figure 4-42a) were scaled based on the Bazant's crack band scaling law (Equations 4-1 to 4-3) as shown in Figure 4-42b. These curves were then modified to include the effect of large deformation calculation in LS-DYNA (Equation 4-4) as shown in Figure 4-42c. This process insures the correct dissipation of energy in the FE simulation.

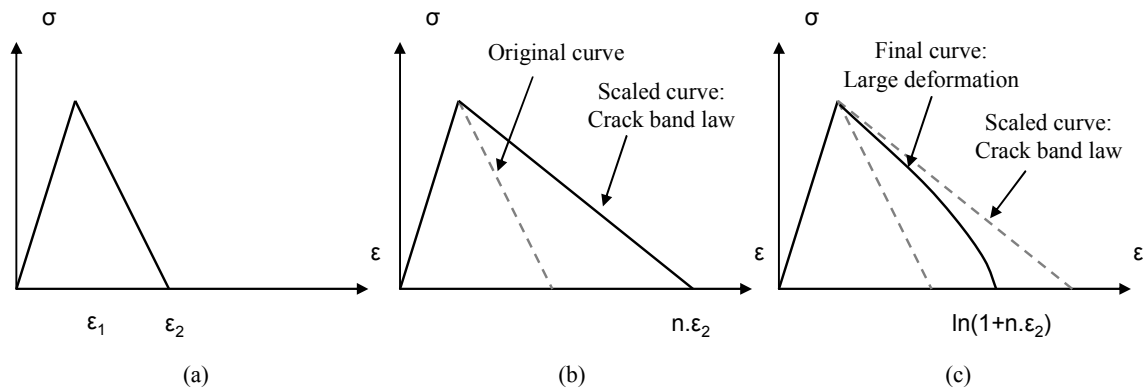


Figure 4-42 (a) Original stress-strain curve, (b) Scaling the original stress-strain curve based on the Bazant's crack band scaling law (Bazant and Oh, 1983), and (c) modifying the scaled stress-strain curve to consider the effect of large deformation calculation in FE codes.

Using LS-DYNA, for each optimized curve, the load-POD response was obtained and compared to experimental results. The predicted load-POD responses using all softening curves along with the experimental results are shown in Figure 4-43. It can be observed that, compared to the result of the linear softening curve, results of both bilinear and trilinear softening curves agree better with experiments. In fact, the accuracy of the peak load was improved by about 10% when using the bilinear or trilinear softening curve instead of the linear softening curve. The agreement between experimental and numerical

results also validates the current approach for extracting the softening response of composites for predicting the damaging behaviour of OCT specimens.

In addition to these global responses, the equivalent damage length-POD curves were also obtained. Equivalent damage length is obtained by replacing the zone that contains partially damaged elements (FPZ) with an equivalent fully damaged zone. In both simulation and experiment, this length was calculated by integrating the dissipated energy over the partially damaged elements. The constructed equivalent damage length-POD curves are compared in Figure 4-44. This comparison shows that, initially, the FE simulation underpredicts the damage length at lower values of POD. This may be explained using the R-curve effect in OCT tests. When damage starts to propagate in the material, initially, damage has not reached its characteristic height. This results in smaller energy dissipation and consequently smaller fracture energy values in the material. Compared to FE simulation in which the fracture energy is constant, smaller crack extensions can be predicted in the simulation at small PODs. At larger PODs, however, results obtained using all optimized curves are in good agreement with the experiments. Comparison between the global and local responses obtained from the experiments and FE simulations using optimized curves are listed in Table 4-9.

Although, as mentioned before, the trilinear softening curve is a better representation of the inhomogeneous behaviour of the material, in these simulations, both bilinear and trilinear curves performed equally well in capturing the global and local behaviour of the specimens.

Table 4-9 Comparison of the experimental results and FE results obtained using the optimized linear, bilinear and trilinear softening curves.

| | Peak load (kN) | Equivalent damage length (mm) at POD = | | |
|--|----------------|--|-----------|-----------|
| | | 1 mm | 1.5 mm | 1.7 mm |
| Average of Experiments | 10.75 | 1.1 | 7.8 | 13.1 |
| FE result (error) with trilinear curve | 10.87 (1%) | 0.8 (23%) | 6.9 (12%) | 12.0 (8%) |
| FE result (error) with bilinear curve | 10.82 (1%) | 0.6 (44%) | 6.8 (12%) | 12.0 (8%) |
| FE result (error) with linear curve | 11.96 (11%) | 0.3 (77%) | 7.6 (2%) | 12.8 (2%) |

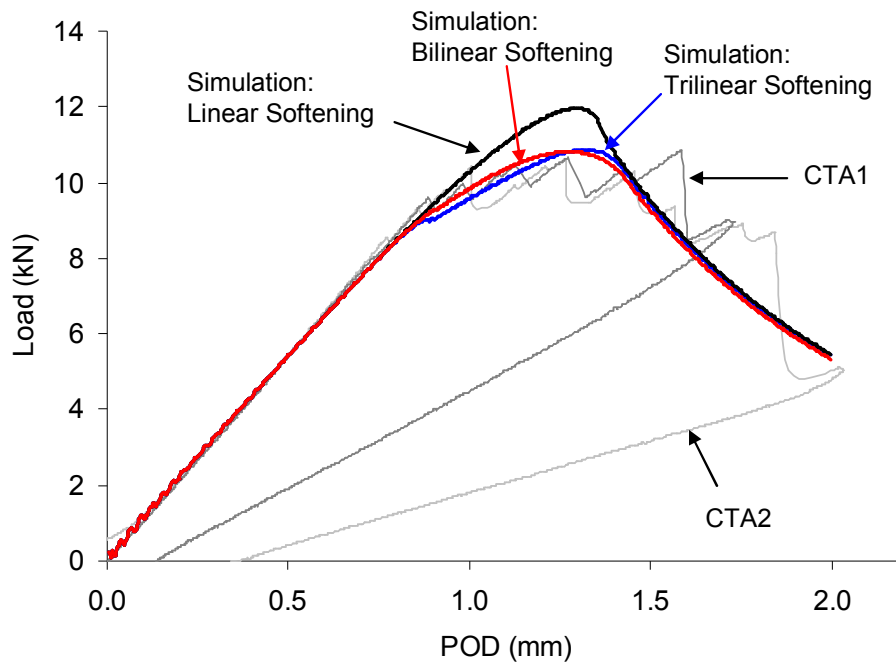


Figure 4-43 Comparison of load-POD curves obtained using optimized linear, bilinear and trilinear softening responses with experimental results.

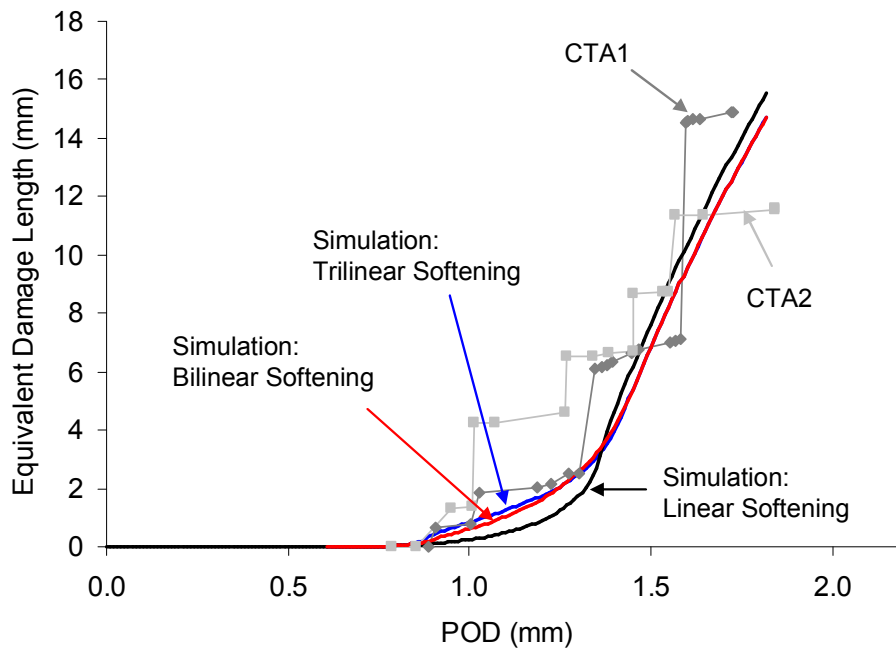


Figure 4-44 Equivalent damage length-POD curves for the CTA1 and CTA2 experiments and FE results obtained using the optimized softening curves.

4.2.6. Sensitivity Analysis of the Optimized Response

In this section, effects of changing the parameters of the optimized trilinear softening response on the damaging behaviour of OCT specimens are studied. FE simulations were carried out using various trilinear softening responses. Six parameters of the optimized trilinear curve were varied and their effects were studied: slopes after the peak, θ_1 , θ_2 and θ_3 (Figure 4-45), plateau stress, $\sigma_{plateau}$, damage initiation strain, ε_i , and fracture energy, G_f (for a given size element, this corresponds to the area under the stress-strain curve or γ). To study the effect of changing each parameter independently, the other 5 parameters were kept constant in each simulation. For example, as shown in Figure 4-46, in the optimized trilinear softening response, the first slope after the peak is varied to create other strain-softening responses. In doing so, the other two slopes, θ_2 and θ_3 , damage initiation strain, plateau stress and area below the curve are kept constant. The first slope of the optimized softening curve equal to 2×10^{-5} radians, was varied by 50% to create new softening curves (Figure 4-46). Results of FE simulations using these curves are shown in Figure 4-47. By increasing the first slope by 50%, the peak load increased from 10.87 kN to 11.05 kN and the POD at the peak load decreased from 1.32 mm to 1.31 mm.

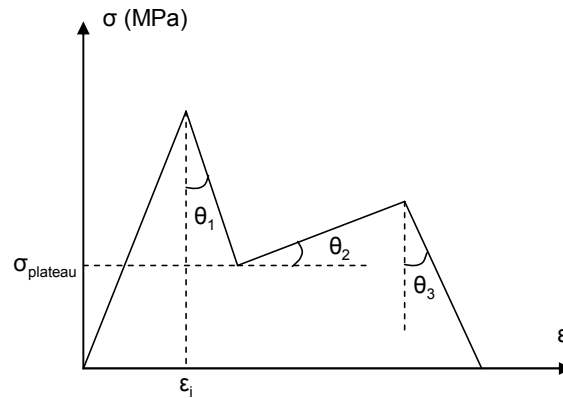


Figure 4-45 Sensitivity analysis of the various parameters of the trilinear softening curve.

The sensitivity of the response to the first slope, is defined using the following derivative:

$$S = \frac{\Delta P}{\Delta \theta_1} = \frac{P_1 - P_2}{(\theta_1)_1 - (\theta_1)_2} \quad (4-6)$$

In which S is the sensitivity and P is the peak load. In order to compare the sensitivity of various parameters, we have to normalize their sensitivity values. The usual approach is to multiply each derivative by the standard deviation of the changing parameter.

However, since in this case, we cannot define standard deviation of parameters, the normalized sensitivity is defined as follows:

$$S = \frac{\Delta P}{\Delta \theta_1 \%} = \frac{P_0 - P}{\frac{(\theta_1)_0 - (\theta_1)}{(\theta_1)_0}} \quad (4-7)$$

In which $(\theta_1)_0$ and P_0 are the slope and the peak load of the optimized curve. It should be noted that these derivatives should be derived for small perturbation of each parameter. Therefore, although the curves shown in this section were created by changing each parameter noticeably, in the calculation of derivatives, parameters were perturbed slightly.

Figure 4-48 shows softening curves constructed by changing the second slope after the peak, θ_2 , and their effect on the load-POD curve is shown in Figure 4-49. Just like the first slope, by increasing this slope, the peak load increases and the POD at the peak decreases.

Figure 4-50 shows softening curves constructed by changing the third slope after the peak, θ_3 , and their effect on the load-POD curve is shown in Figure 4-51. Unlike the other two slopes, by increasing this slope, the peak load decreases. But the POD at the peak still decreases. This slope also has a more noticeable effect on the peak load. For the case where θ_3 becomes zero (i.e. a sudden drop in stress), a small drop in the load-POD curve can be observed.

Figure 4-52 shows softening curves constructed by changing the damage initiation strain, ε_i , and their effect on the load-POD curve is shown in Figure 4-53. By increasing the damage initiation strain, the peak load increases and the POD at the peak decreases noticeably. Also the first nonlinearity in the load-POD curve, is delayed by increasing this parameter.

Figure 4-54 shows softening curves constructed by changing the plateau stress, $\sigma_{plateau}$, and their effect on the load-POD curve is shown in Figure 4-55. This parameter has a large effect on both the peak load and the POD at the peak. The nonlinear portion of the load-POD curve becomes flattened by decreasing the plateau stress. This effect, however,

is accompanied by an increase in the length of the plateau portion. The later is the result of keeping the fracture energy density constant. In the sensitivity analysis calculations, however, the derivatives have been derived by slightly perturbing the plateau stress (about 4% in this study) and not by large changes shown here (about 35%).

Figure 4-56 shows softening curves constructed by changing the fracture energy, G_f , and their effect on the load-POD curve is shown in Figure 4-57. We can change the fracture energy by changing the area below the stress-strain curve because the fracture energy is a linear function of the fracture energy density (Equation 3-28). By increasing the fracture energy, both the peak load and POD at the peak are increased noticeably.

Sensitivity of the peak load and also sensitivity of the POD at the peak to these six parameters were calculated and listed in Table 4-10. As expected, it can be concluded that the fracture energy has the largest effect on both the peak load and the POD at the peak. Other studies (e.g. McClennan, 2004) confirm this finding for the sharp notched OCT specimens. After the fracture energy, the damage initiation strain and plateau stress have the largest effect on the peak load. Compared to these three parameters, the slopes θ_1 , θ_2 , and θ_3 have negligible effects on the peak load. The fracture energy has the largest effect on the POD at the peak.

It should be noted that the current sensitivity results cannot be generalized to other optimized curves and other specimen geometries and sizes. For example, in Appendix B, it is shown that in small notched specimens, in which the damage height is comparable to the size of the specimen, the only parameter that affects the peak load is the damage initiation strain. In very large notched specimens, in which the damage height becomes negligible compared to the other dimensions of the specimen, only fracture energy affects the peak load. In other sizes, other parameters of the optimized curve such as the slopes after the peak stress also affect the peak load. For other optimized curves (e.g. linear and bilinear softening curves), the sensitivity results might also change. From this exercise it can be concluded that in optimizing the trilinear softening response for predicting the damaging behaviour of sharp-notched OCT specimens, fracture energy, damage initiation strain and plateau stress are more important parameters than the slopes θ_1 , θ_2 , and θ_3 . The

effect of individual parameters on the global load-POD curve can also be observed in these FE simulations.

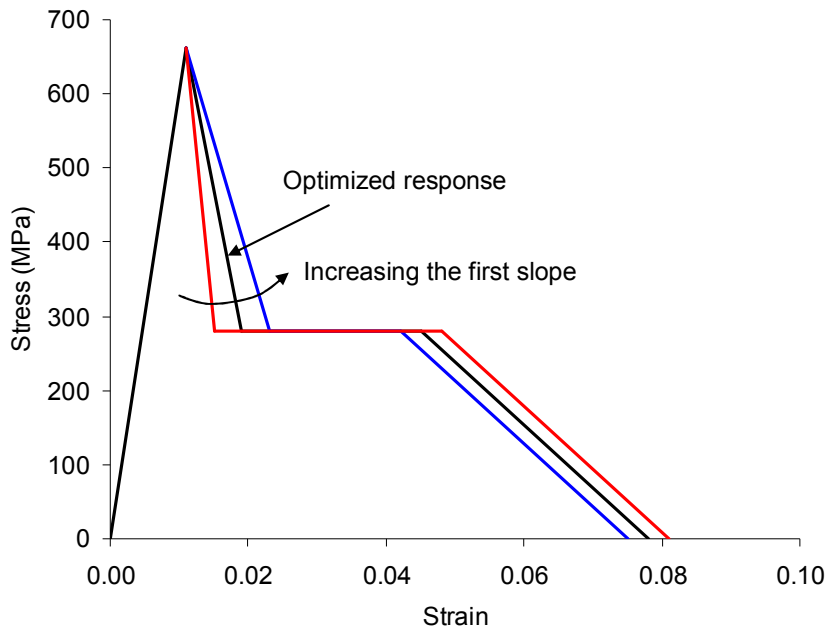


Figure 4-46 Changing the first slope after the peak of the optimized trilinear softening curve to study its effect on the load-POD response of OCT specimens.

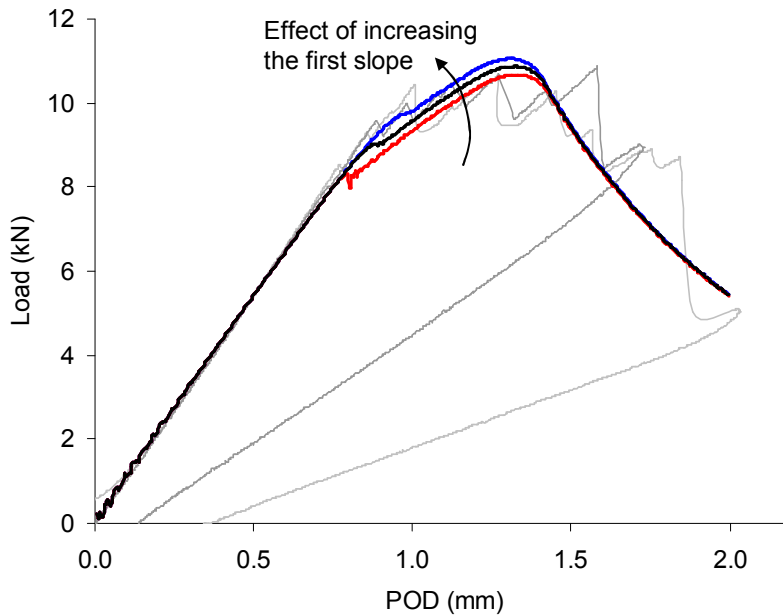


Figure 4-47 FE results for effect of increasing the first slope of the trilinear softening curve (Figure 4-46) on the load-POD response of the OCT test.

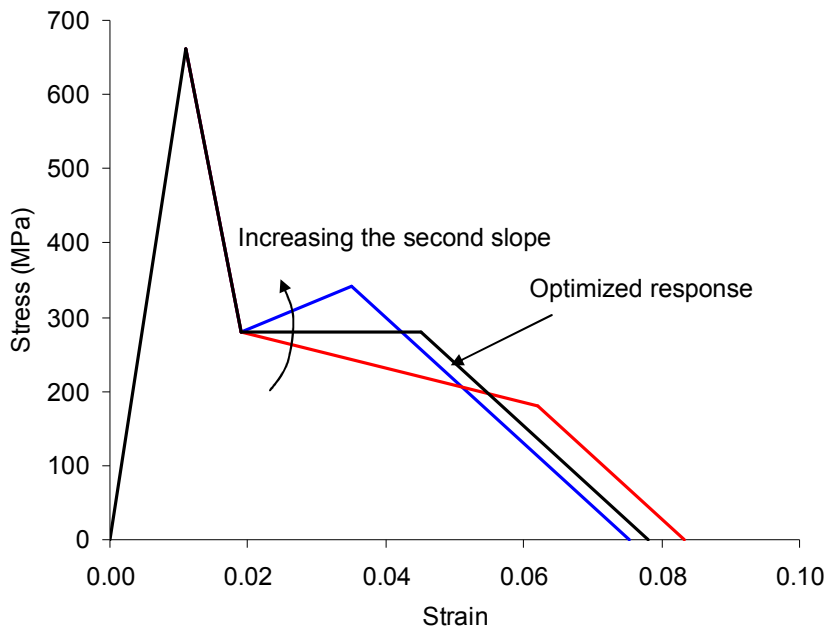


Figure 4-48 Changing the second slope of the optimized trilinear softening curve to study its effect on the load-POD response of OCT specimens.

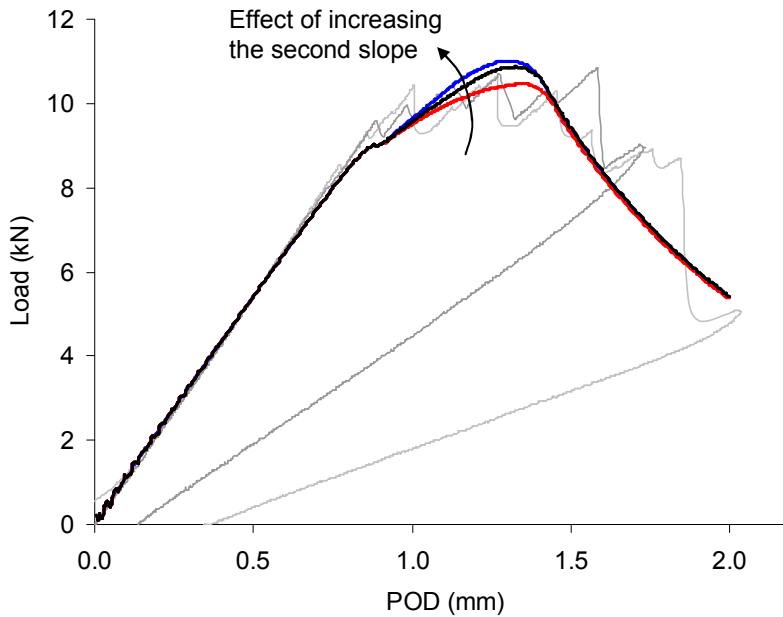


Figure 4-49 FE results for effect of increasing the second slope of the trilinear softening curve (Figure 4-48) on the load-POD response of the OCT test.

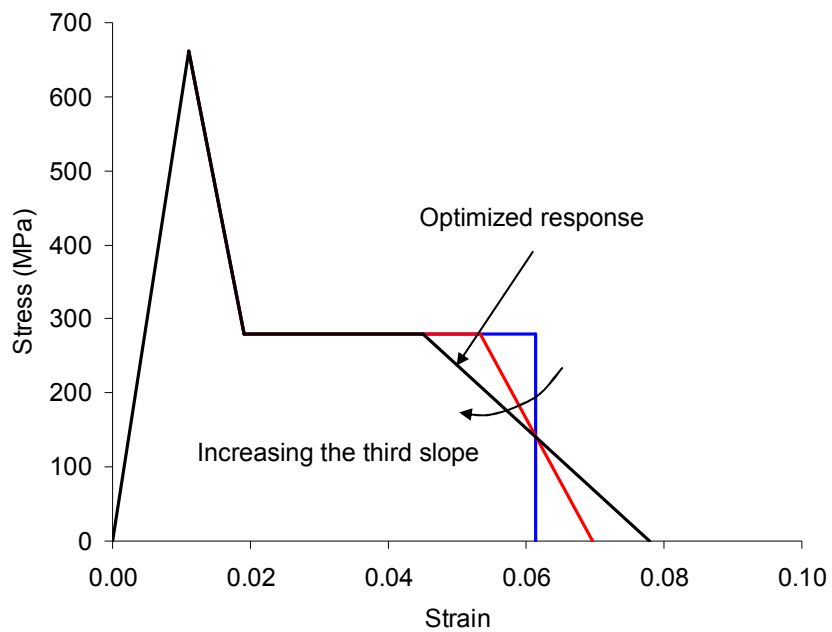


Figure 4-50 Changing the third slope of the optimized trilinear softening curve to study its effect on the load-POD response of OCT specimens.

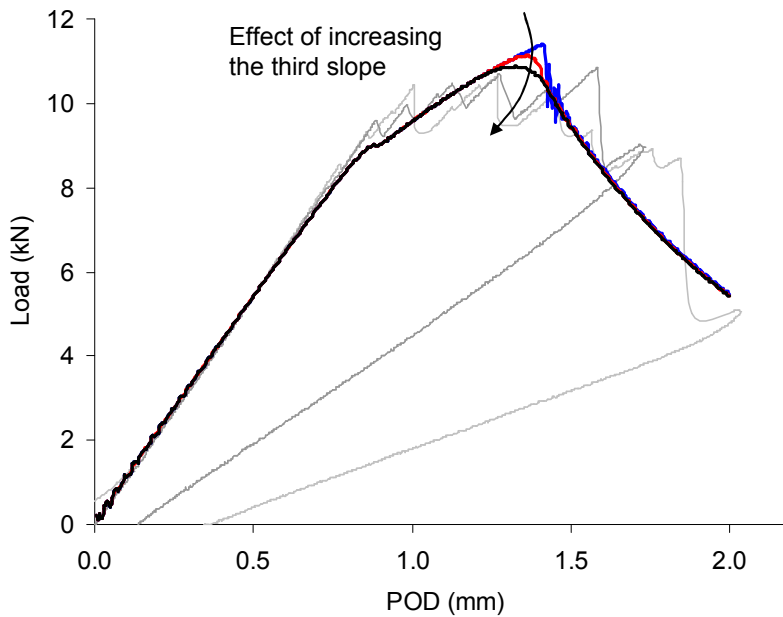


Figure 4-51 FE results for effect of increasing the third slope of the trilinear softening curve (Figure 4-50) on the load-POD response of the OCT test.

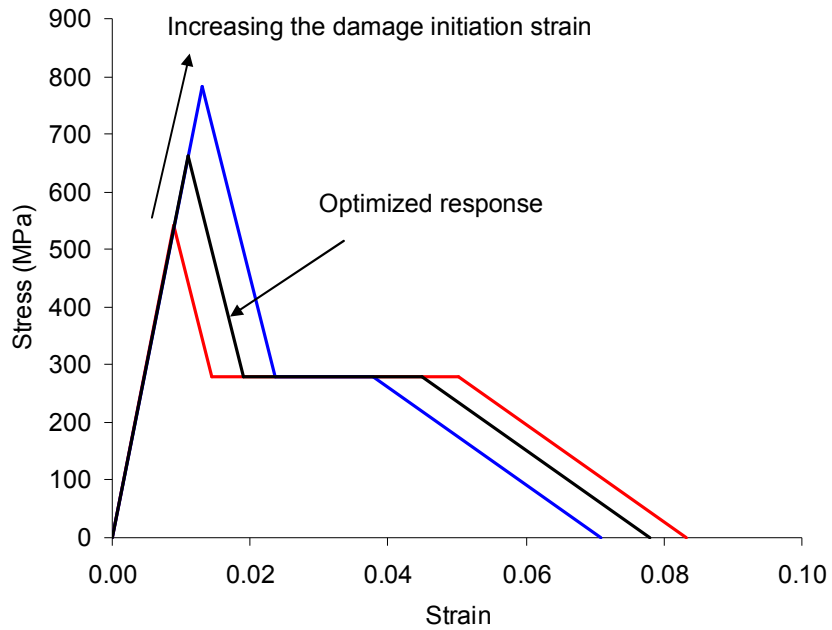


Figure 4-52 Changing the damage initiation strain of the optimized trilinear softening curve to study its effect on the load-POD response of OCT specimens.

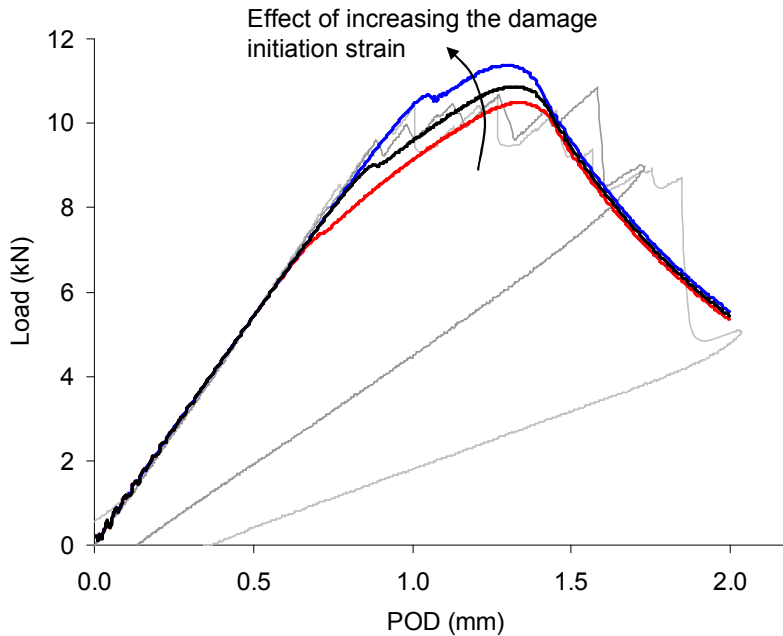


Figure 4-53 FE results for effect of increasing the damage initiation strain of the trilinear softening curve (Figure 4-52) on the load-POD response of the OCT test.

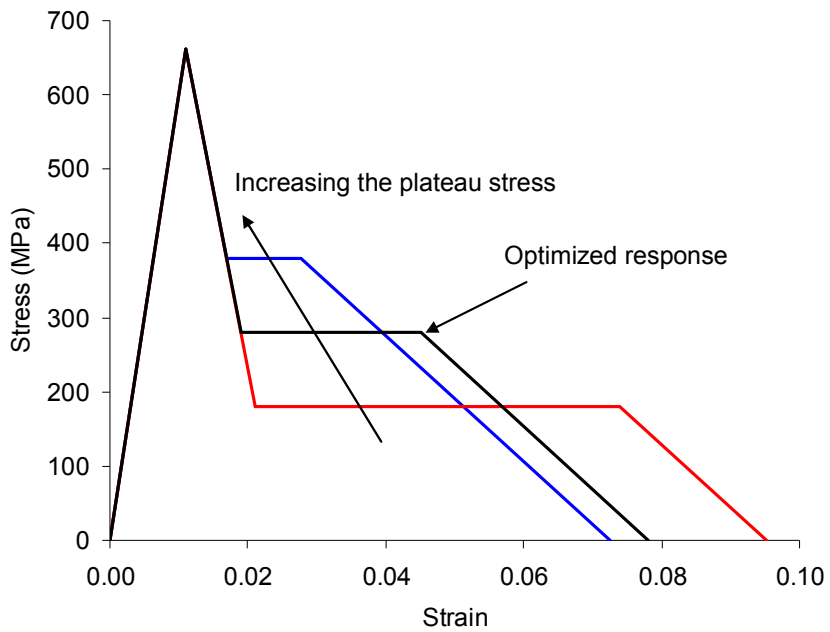


Figure 4-54 Changing the plateau stress of the optimized trilinear softening curve to study its effect on the load-POD response of OCT specimens.

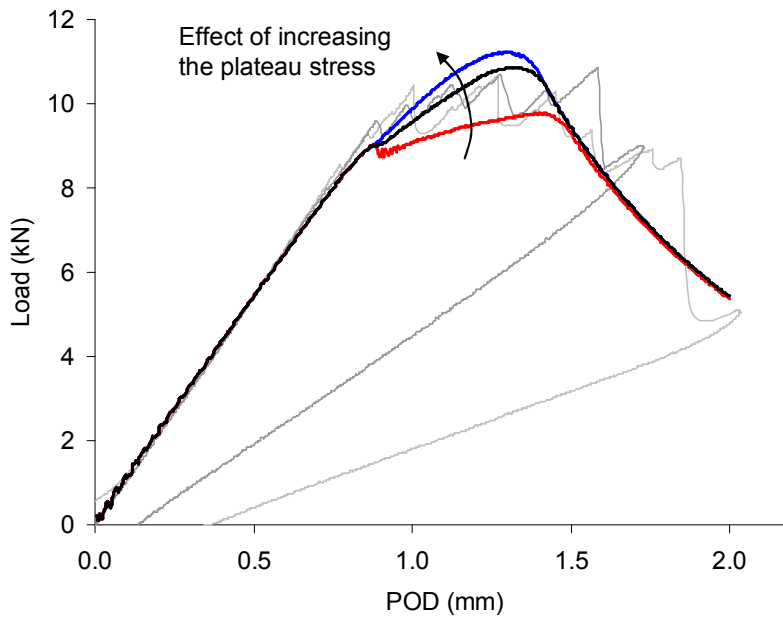


Figure 4-55 FE results for effect of increasing the plateau stress of the trilinear softening curve (Figure 4-54) on the load-POD response of the OCT test.

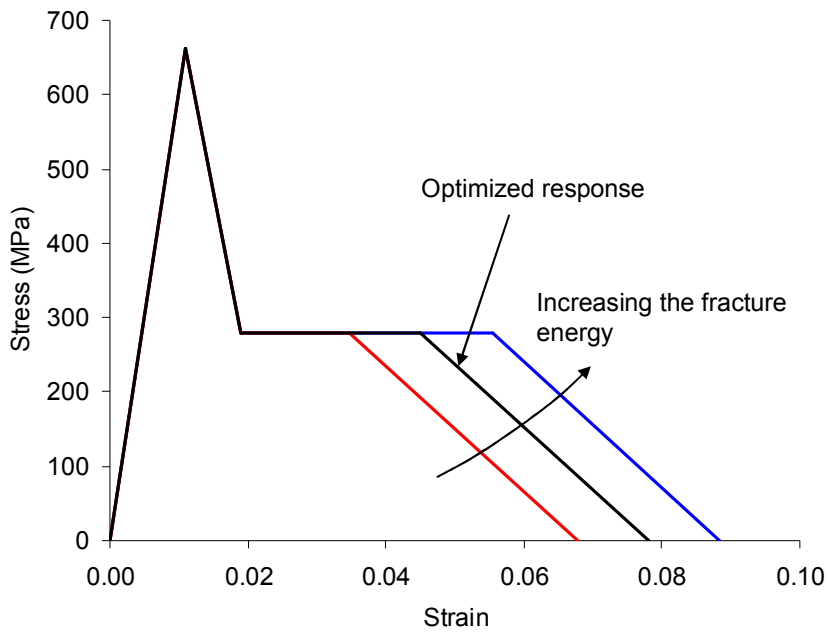


Figure 4-56 Changing the energy density of the optimized trilinear softening curve to study its effect on the load-POD response of OCT specimens.

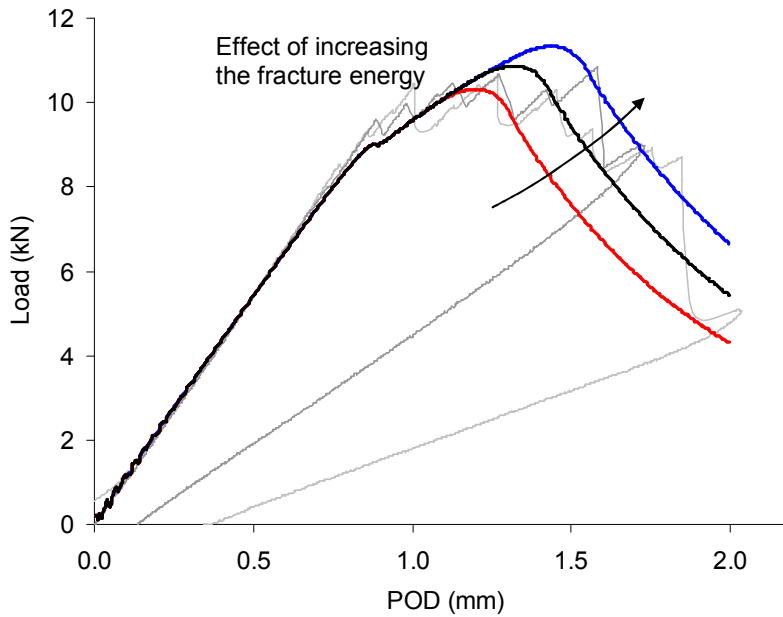


Figure 4-57 FE results for effect of increasing the energy density of the trilinear softening curve (Figure 4-56) on the load-POD response of the OCT test.

Table 4-10 Sensitivity analysis of various parameters of the optimized trilinear softening curve.

| | | Sensitivity to | | | |
|--------------------------------------|--------------------|-----------------|--------------------|-------------|-------------|
| | | Optimized Curve | Experimental Range | Peak Stress | POD at Peak |
| Fracture Energy (kJ/m ²) | G_f | 110 | 90 to 125 | 3.37 | 0.79 |
| Damage Initiation Strain | ε_i | 0.011 | 0.009 to 0.013 | 2.45 | -0.13 |
| Plateau Stress (MPa) | $\sigma_{plateau}$ | 280 | 250 to 400 | 1.82 | -0.11 |
| 3 rd Slope | $\tan(\theta_3)$ | 1.2E-04 | 0 to 1.5E-04 | -0.52 | -0.06 |
| 1 st Slope | $\tan(\theta_1)$ | 2E-05 | 1E-05 to 3E-05 | 0.38 | -0.02 |
| 2 nd Slope | $\tan(\theta_2)$ | 0 | -4000 to 2000 | 0.21 | -0.02 |

4.3. Non-destructive and Destructive Investigation of Damaged Specimens

In order to further validate the capability of the proposed methodology in identifying the damage properties of composite laminates, a series of non-destructive and also destructive tests (NDT and DT) were conducted on the damaged OCT specimens. The findings from these tests such as crack length or damage height were compared with those obtained using the proposed model. For NDT of OCT specimens, X-ray Computed Tomography (CT) Imaging was used. For destructive testing, two approaches were utilized. In one approach, cross-sections were cut from the damaged specimen. These cross-sections were analyzed using scanning electron microscopy (SEM). In another destructive testing approach, a deplying technique was used. By burning off the epoxy resin from the damaged area, damaged plies were analyzed individually to track fibre breakage in each layer. These tests are discussed here.

4.3.1. Non-destructive Tests using CT Scans

For non-destructive tests, CT scans were conducted at the UBC CT Imaging Center. This technique uses an X-ray beam to transmit energy into the specimen. This energy is used to construct slice-by-slice 2D images along the specimen length or width (Herman, 2009). Using these images, internal features and any inhomogeneity in the specimen density can be identified. These inhomogeneities can be attributed to damage growth such as delamination, matrix cracking or fibre breakage.

Unfortunately, due to the low spatial resolution of the CT machine at UBC (about 0.5 mm), little data was obtained using this technique. For CTA1, using CT scanning, density maps were obtained for cross-sections about 1 mm apart in front of the notch. As an example, the density map obtained for a cross-section 1 mm ahead of the notch tip is shown in Figure 4-58a. In the density map, a sudden reduction of density around the damaged area is observed. From this map, the damage height can be measured between 5 to 6 mm. Using the current method, the damage height was measured to be about 6 mm for the same cross-section (Figure 4-58b). This shows a good agreement between the experimental results and the damage height measured using the proposed method. No other data can be inferred from the density map due to the low resolution. Therefore, destructive testing techniques were used to examine the extent of damage in OCT specimens.

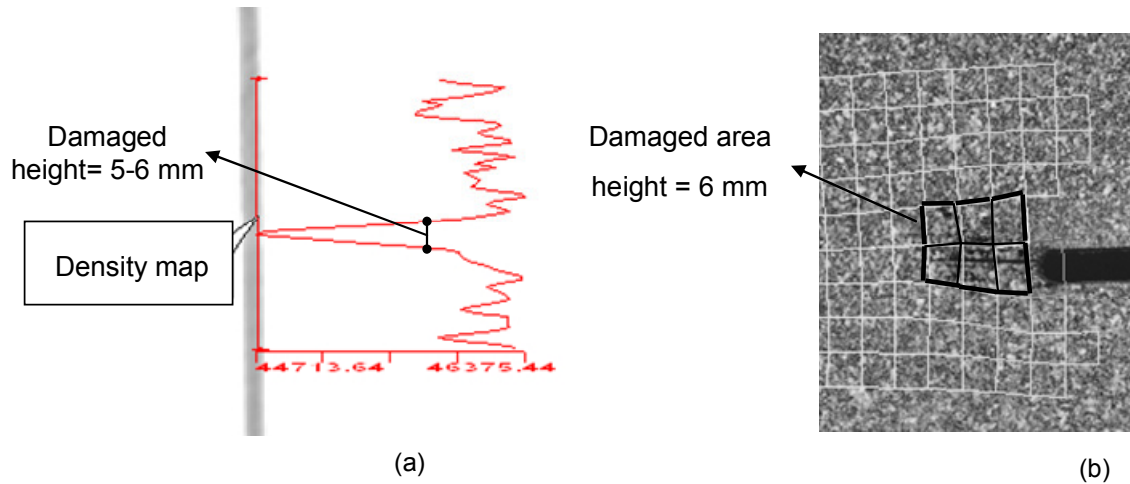


Figure 4-58 Damage height obtained using (a) CT scanning at a cross-section 1 mm ahead of the notch tip and (b) the proposed method.

4.3.2. Destructive Tests: Cross-sectional Cuts

For destructive tests, several cross-sections were cut perpendicular to the damage growth direction in OCT specimens. These sections were analyzed to construct a damage profile in front of the initial notch tip. A slow speed diamond cutting wheel with a 0.5 mm (0.02 in) thick blade was used to cut smooth sections from CTA1 specimen. A total of 16

sections were cut ahead of the notch tip each 1.9 mm (0.075 in) apart (as shown in Figure 4-59). After comparing polished and unpolished surfaces under the microscope, it was concluded that polishing was not necessary for these sections.

Various methods were examined to study and analyze the cross-sections of the damage zone in the CTA1 specimen. This included taking images using a high resolution scanner, high resolution digital camera, 10x microscope, optical microscope and scanning electron microscopy (SEM). Initial results obtained using the scanner and the digital camera were not satisfactory. The damaged area was not clearly visible in the images obtained using these two methods.

Although damage zone could be observed in images obtained using the 10x microscope and the optical microscope, details of the damage zone was not visible in these images. Examples of images taken from section #12 of CTA1 specimen are shown in Figure 4-60 and Figure 4-61 using the 10x microscope and the optical microscope respectively.

The final method examined to take images of the damaged area was scanning electron microscopy (SEM). SEM is a type of electron microscope that takes images of a specimen by scanning it with a high-energy beam of electrons (Goldstein et al., 1992). A Hitachi S-3000N scanning electron microscope was used to take high resolution images of the damaged area. Hitachi S-3000N is a PC controlled variable pressure SEM that has a resolution of 5 nm. For scanning the composite laminate cross-sections, a constant pressure of 20 Pa was used without coating the specimen.

An image taken by SEM from cross-section #12 of CTA1 specimen is shown in Figure 4-62. In this image, fibre breakage, matrix cracking and delamination failures are clearly visible. Damage appears in the form of fibre breakage in 0 degree layers. Delamination can be observed between the top -45 and 0 degree layers. Matrix cracking can also be observed in the 90, 45 and -45 degree layers. This shows that compared to other techniques explained here, SEM is a better approach for analyzing damage in these cross-sections. Images for cross-sections #12 and #13 compiled from several other images are

shown in Figure 4-63 and Figure 4-64. From these cross-sections, the extent of damage and also damage saturated areas can be identified.

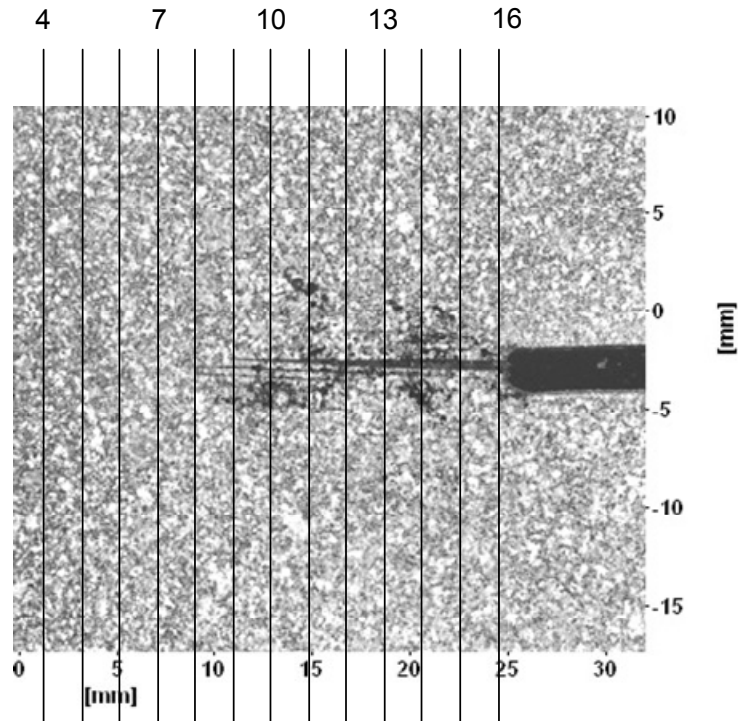


Figure 4-59 Sections cut from CTA1 specimen. Sections 4 to 16 are shown in this figure.



Figure 4-60 An image of section #12 obtained using a 10x microscope.

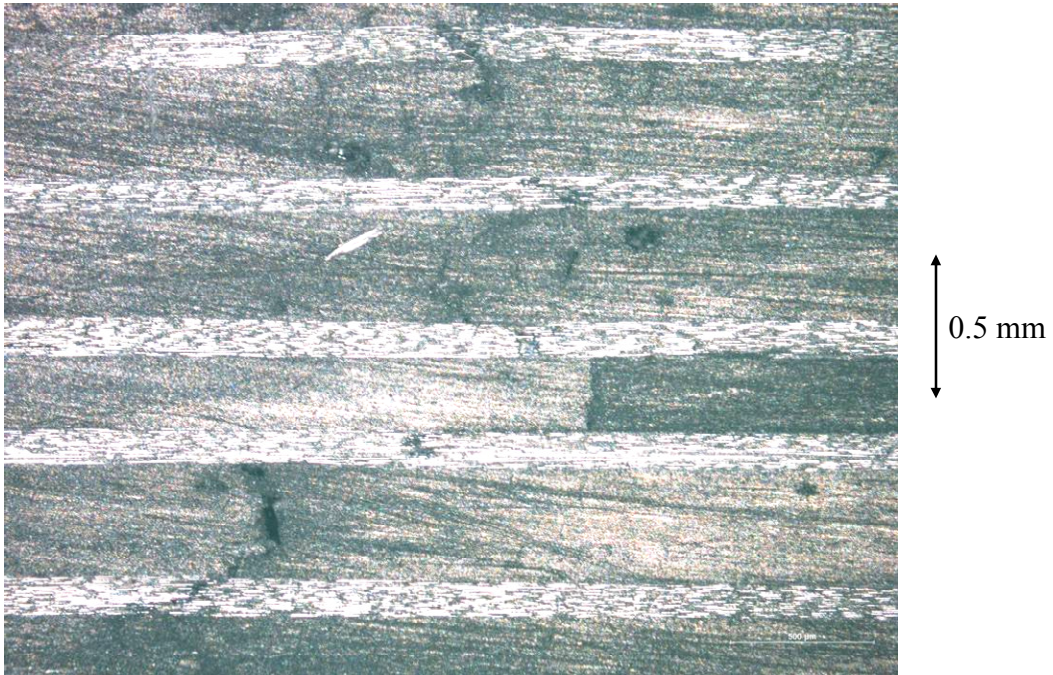


Figure 4-61 An image of section #12 obtained using an optical microscope.

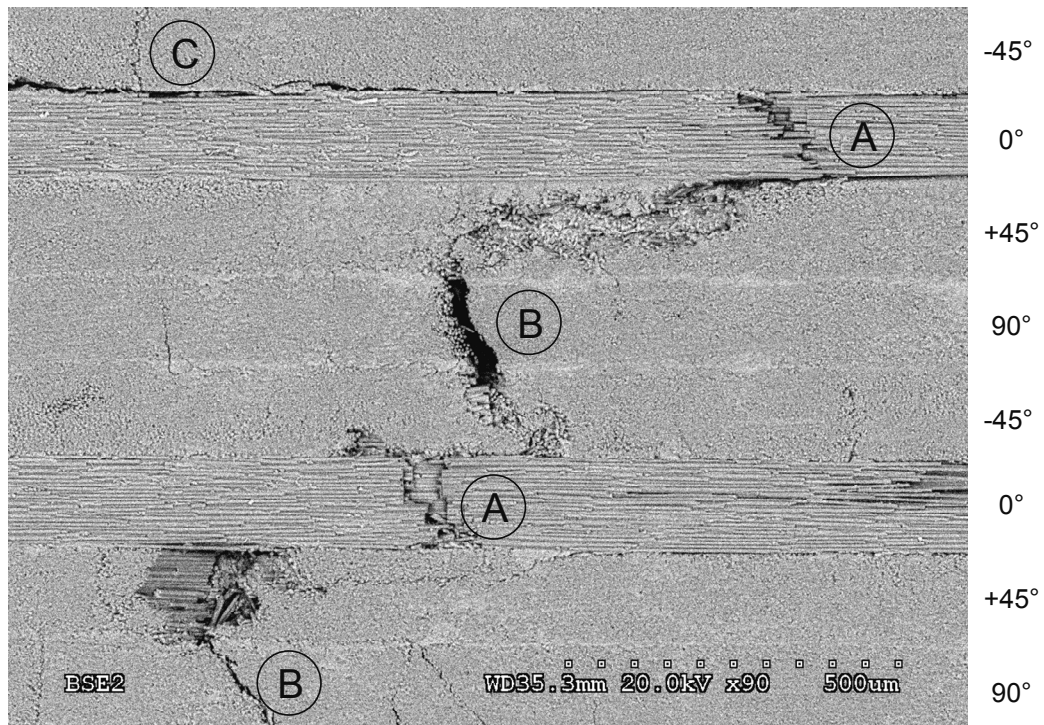


Figure 4-62 An image obtained for section #12 using SEM showing fibre breakage (A), matrix cracking (B) and delamination (C).

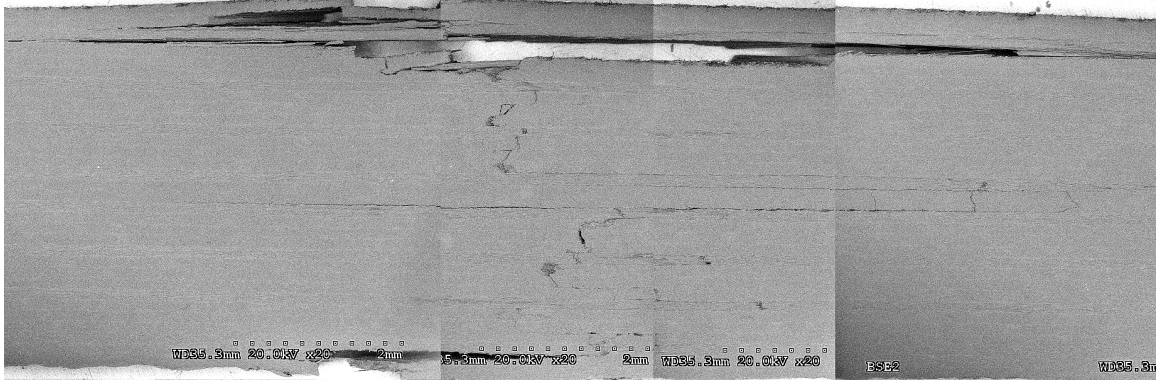


Figure 4-63 SEM image of cross-section #12 of CTA1 specimen.

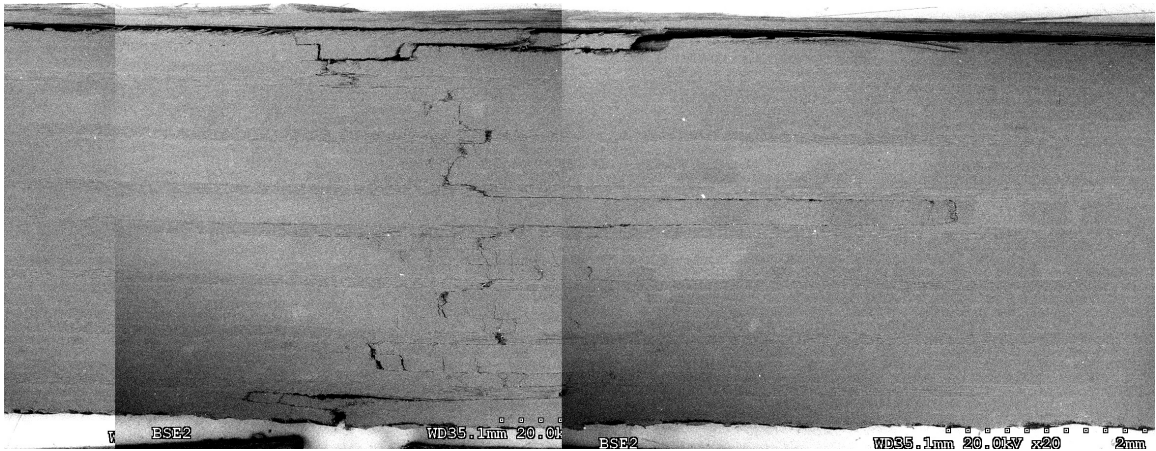


Figure 4-64 SEM image of cross-section #13 of CTA1 specimen.

SEM images of all the cross-sections were subsequently analyzed. Damage was detected in cross-sections #8 to #16 with a small amount of delamination in section #7. Schematic representation of damage in cross-section #7 to #16 are shown in Figure 4-65 and Figure 4-66. The 0 mm coordinate shown on the right side of these figures marks the vertical position of the notch tip.

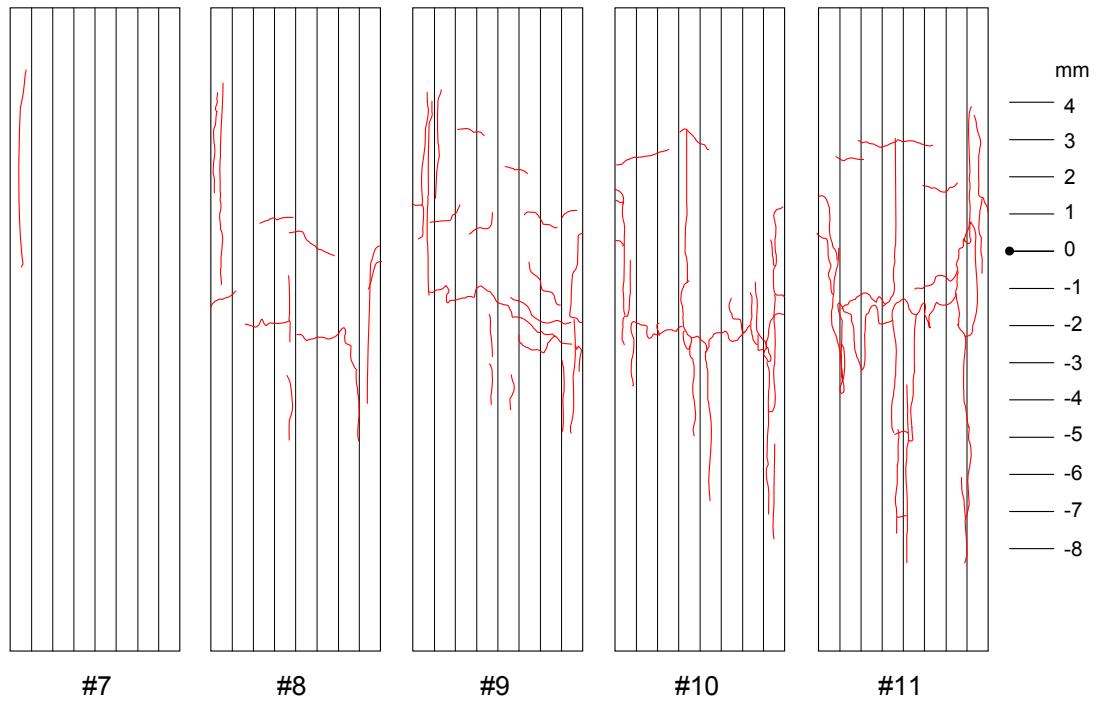


Figure 4-65 Schematic representation of damage in cross-sections #7 to #11 in CTA1. 0 mm indicates the notch tip vertical position.

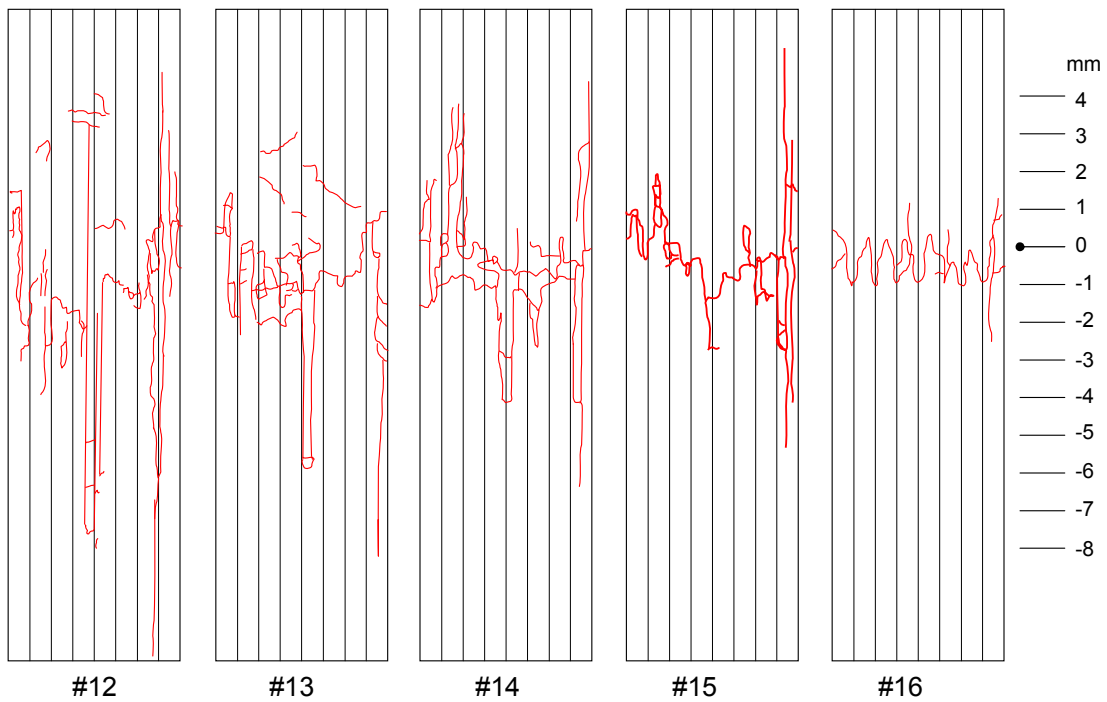


Figure 4-66 Schematic representation of damage in cross-sections #12 to #16 in CTA1. 0 mm is the notch tip vertical coordinate.

In Figure 4-65 and Figure 4-66, vertical damage lines represent delamination. Horizontal and inclined lines represent matrix cracking and fibre breakage. From these schematics, damage zones can be identified. However, it should be noted that, in these tests, the reduction of global load due to delamination growth were negligible. This is because the small delaminated areas observed in these cross-sections has a small effect on the surface strain and global behaviour of the specimens. Since in the current approach surface strain field is used to detect the damage zone, therefore, due to its negligible effect, delamination might not be detected in these tests. This deficiency, however, is not limited to the current approach and might affect any method that relies on the surface strain values to detect damage. As a result, damage area in this study is identified as the zone that contains fibre breakage or matrix cracking or noticeable delamination. Using this definition, we can examine the specimen cross-sections and identify the damage zone. For example in Figure 4-65 for cross-section #11, the damage is approximately limited to -3.5 to +3 mm zone. This finding can be used to measure the damage initiation strain value. Since the strain distribution for the surface is known, for each cross-section, we can identify this strain value and eventually calculate an average value of strain for damage initiation.

From the distribution of damage in the specimen cross-sections, the damage saturated zone can be identified. This zone represents the area for which the material has lost its load bearing capacity due to excessive fibre breakage and matrix cracking in all layers. Since no load cannot be transferred through the damage saturated zone, stress in this zone should be equal to zero. Therefore by identifying the boundaries of the saturated zone, the damage saturation strain can be extracted. This strain represents the threshold for losing load bearing capacity and creating stress free zones. For example, this area is indicated in Figure 4-67 for cross-section #12. In this cross-section, all the layers are damaged in the zone confined within the range $-1.5 \text{ mm} < y < 1 \text{ mm}$. Using the strain distribution of this cross-section, damage saturation strain was identified to be approximately equal to 6.2 %. In the same figure, damage initiation strain can be measured to be equal to 1.4% for the zone $-3 \text{ mm} < y < 3 \text{ mm}$. Repeating the same process for all the cross-sections, we can identify the damage zone and damage saturated zone for CTA1 specimen. The results of

these findings are listed in Table 4-11 and the constructed damage zone and damage saturated zone are shown in Figure 4-68.

Using the measured strain distribution on the surface of the specimen, average values of damage initiation and damage saturation strains were obtained for all the cross-sections. The results are as follows:

Average damage initiation strain = 1.3 % with StDv = 0.3%

Average damage saturation strain = 6.7 % with StDv = 1.4%

These results agree well with the strain values calculated using the proposed method. Previously, the damage initiation and damage saturation strains were determined equal to 1.1% and 7.8% respectively using the trilinear softening shape. The agreement between the results of these two methods can be better visualized by superimposing the areas determined using the sectioning method and the proposed method in one graph. This is shown in Figure 4-69. As shown in this figure, both the damage area and saturated area determined using the current approach matches very well with the areas measured using the sectioning method. This validates the capability of the proposed method to not only identify the damage zone, but also the damage initiation and saturation strains with an acceptable degree of accuracy.

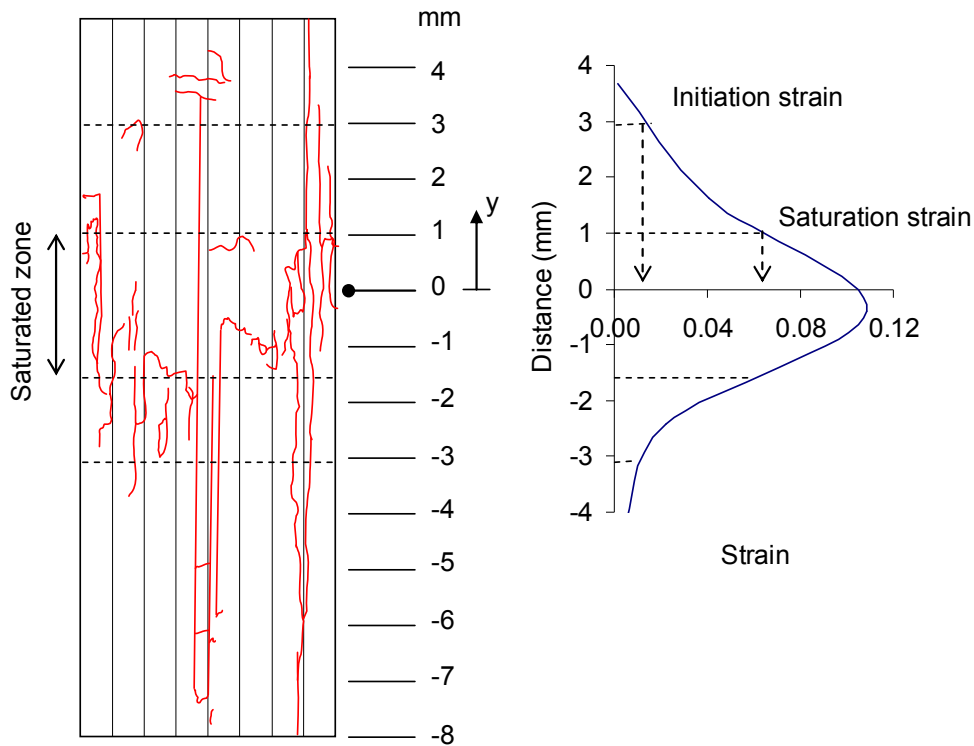


Figure 4-67 Identifying saturated damage zone and saturation strain from the schematic of damage and also strain distribution in cross-section #12.

Table 4-11 Damage zone and saturated zone identified from the schematics of damage in cross-sections.

| Cross-section | Damage initiation zone | Damage saturation zone |
|---------------|------------------------|------------------------|
| 16 | $-1 < y < 1$ mm | $-1 < y < 1$ mm |
| 15 | $-2.5 < y < 2.5$ mm | $-1.25 < y < 1.5$ mm |
| 14 | $-3 < y < 3$ mm | $-1.25 < y < 1.5$ mm |
| 13 | $-3 < y < 3$ mm | $-2 < y < 1.25$ mm |
| 12 | $-3 < y < 3$ mm | $-1.5 < y < 1$ mm |
| 11 | $-3.5 < y < 3$ mm | $-1.5 < y < 0$ mm |
| 10 | $-3 < y < 3$ mm | 0 |
| 9 | $-3 < y < 2$ mm | 0 |
| 8 | $-0.5 < y < 1$ mm | 0 |
| 7 | 0 | 0 |

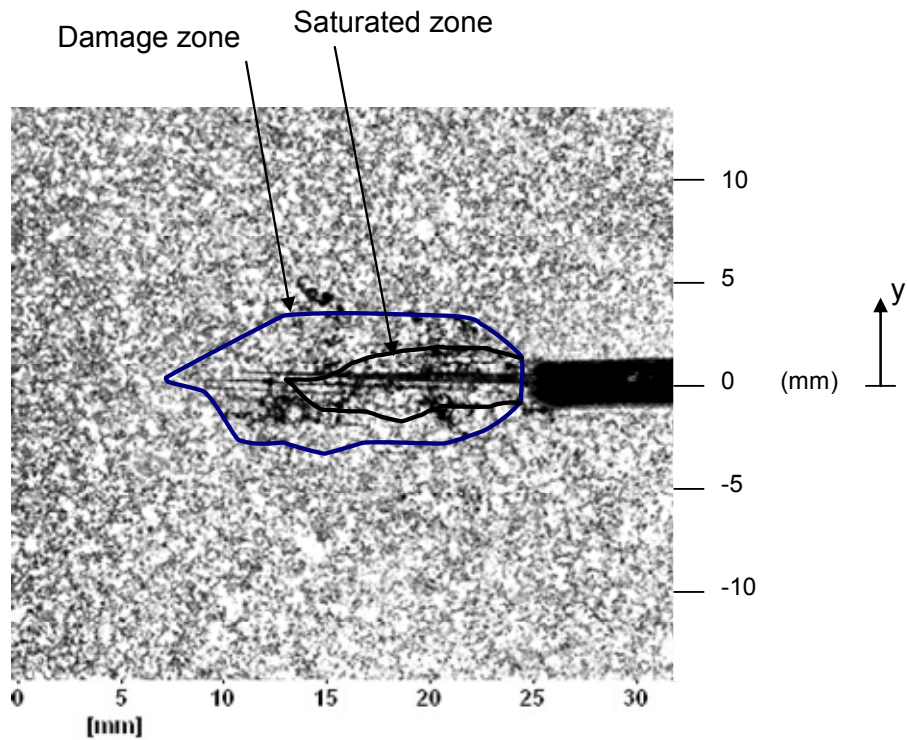


Figure 4-68 Identified damage zone and damage saturated zone from the cross-sections of the CTA1 specimen.

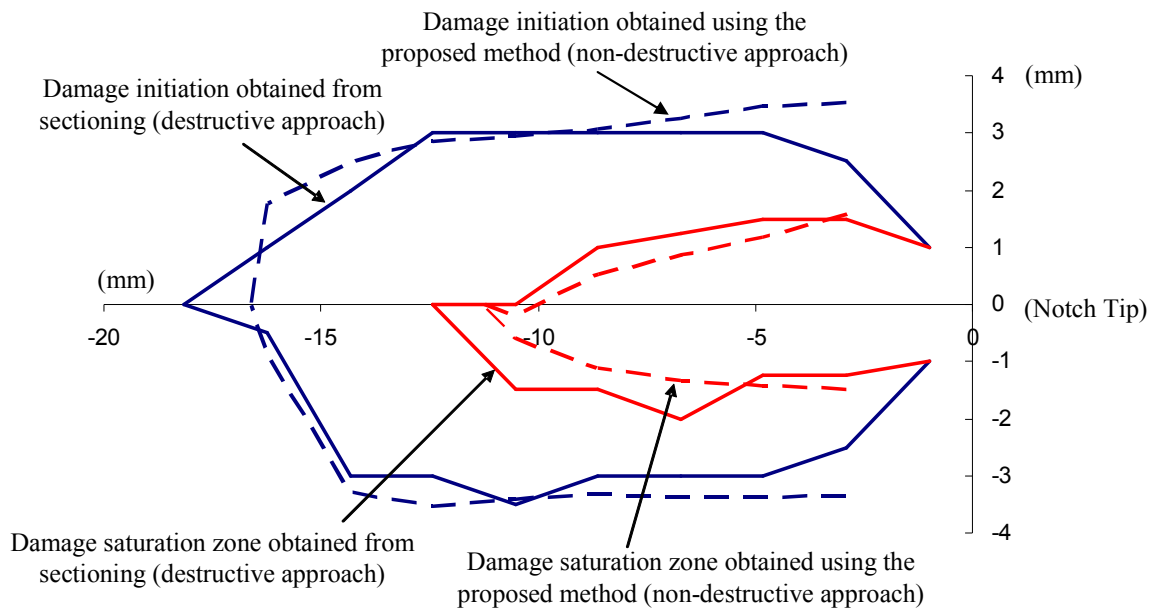


Figure 4-69 Comparison of damage zone and damage saturated zone measured using the sectioning method and calculated using the proposed methodology in CTA1.

4.3.3. Destructive Testing: Deploying

In another approach, to examine the fibre breakage in each layer, a deploying technique was utilized. This technique is based on oxidising the epoxy resin to expose fibres and examining the individual plies (Freeman, 1982).

For CTA2 experiment, a section containing the damage zone in front of the initial notch tip was cut out from the specimen. This 40x27 mm section is shown in Figure 4-70 on the specimen surface. To oxidise (burn off) the epoxy resin, the cut out part was placed in a furnace and heated to 420 °C for about 7 hours.

After removing the cut out part from the furnace, each ply was separated carefully. Then the plies were laid out and sealed on a thick sheet to preserve their sequence. For this layout, a total of 32 plies were separated. Examples of these plies are shown in Figure 4-71, Figure 4-72 and Figure 4-73.

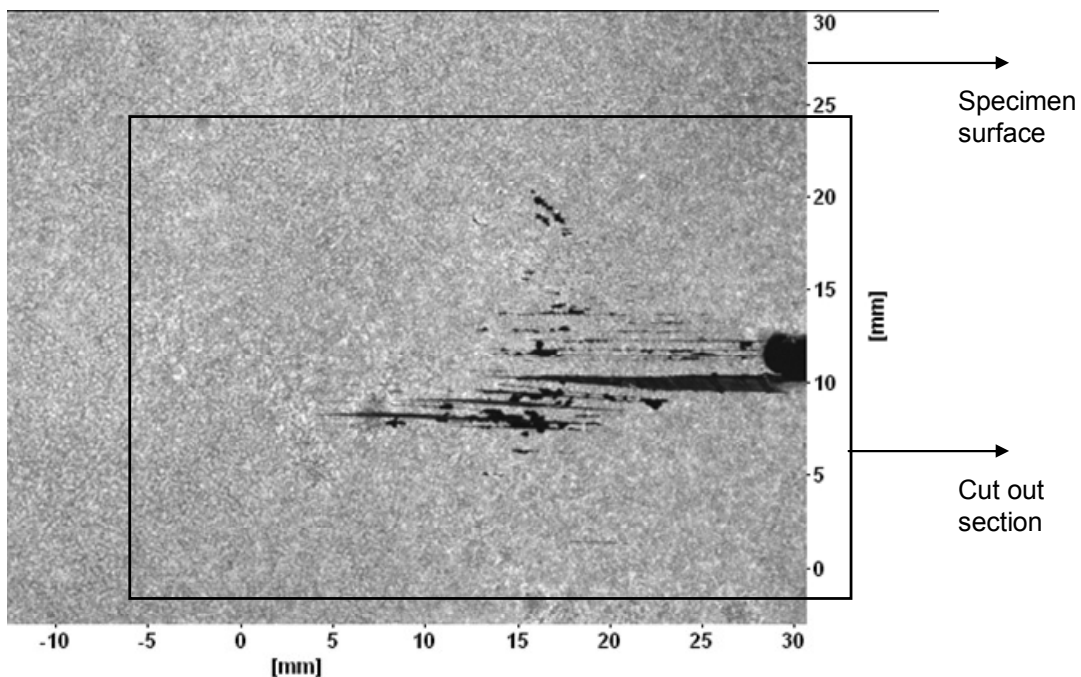


Figure 4-70 CTA2 specimen surface at the end of the experiment. An area of interest was cut out to be analyzed using the deploying technique.



Figure 4-71 Ply # 3 of CTA2 specimen with 0° fibre direction.

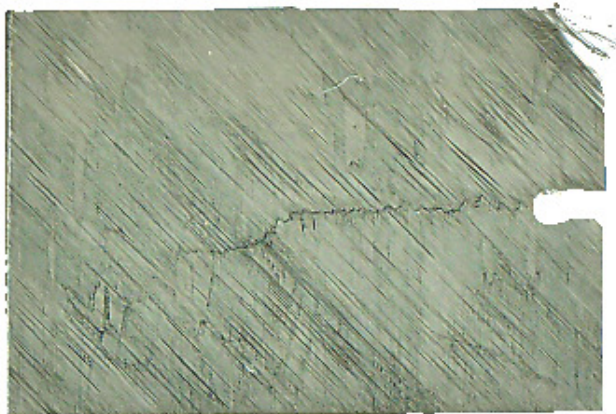


Figure 4-72 Ply # 10 of CTA2 specimen with +45° fibre direction.



Figure 4-73 Ply # 21 of CTA2 specimen with -45° fibre direction.

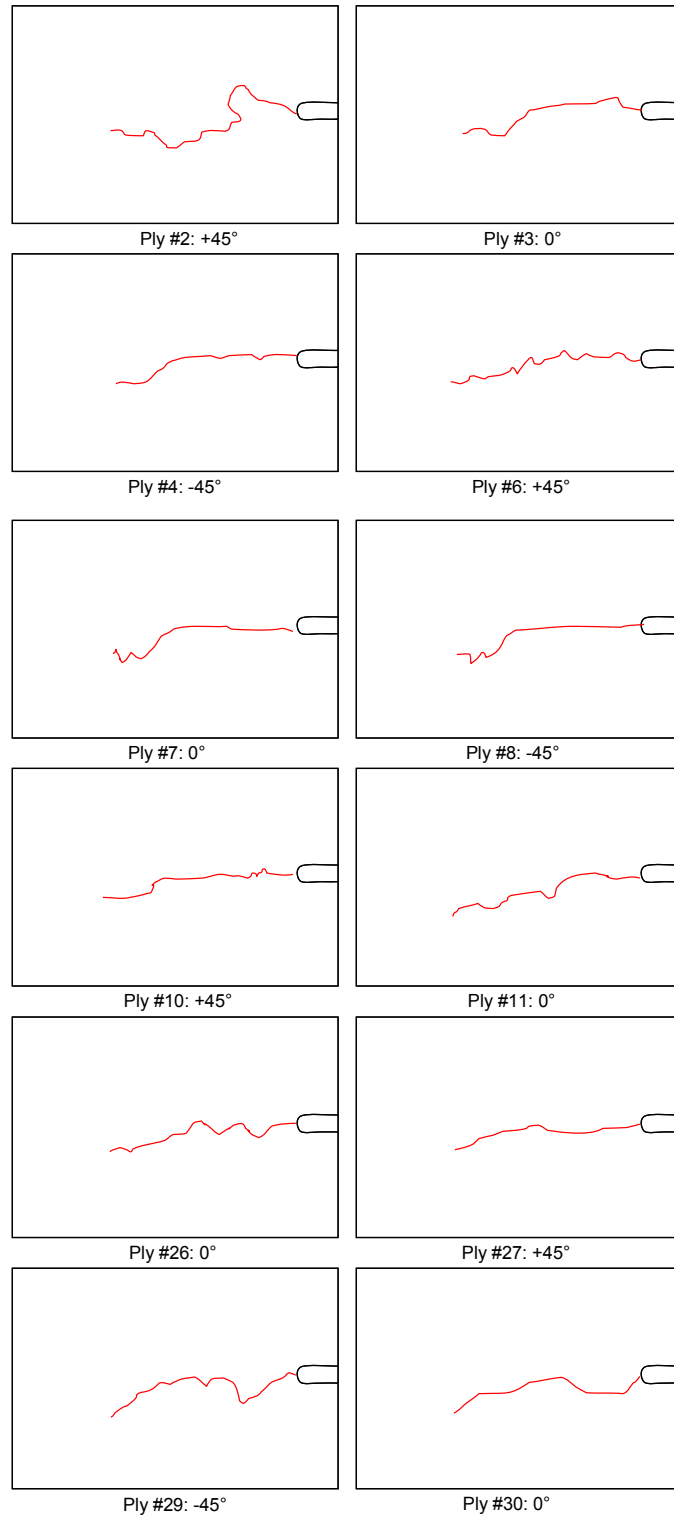


Figure 4-74 Fibre breakage traces in some of the plies of CTA2 specimen.

After separating the plies, each ply was scanned to provide soft copy images of them. Fibre breakage traces were then highlighted on these images. Schematics of these traces for some of the plies are shown in Figure 4-74. In Figure 4-75, both the calculated damage zone using the proposed methodology and fibre breakage traces obtained from the deplying technique are depicted. The calculated damage zone is based on the damage initiation strain value of 1.1% obtained previously. The comparison of these two areas shows good agreement and further validates the capability of the proposed method to identify the damage region.

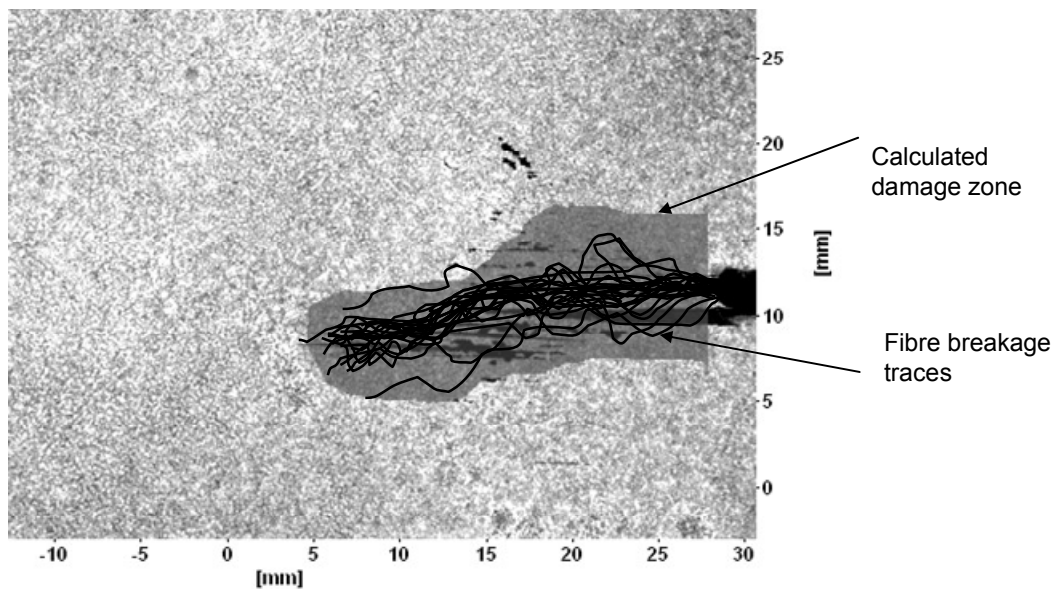


Figure 4-75 Comparing the calculated damage zone for CTA2 specimen using the proposed methodology and the fibre breakage zone obtained using the deplying technique.

4.4. Summary and Conclusions

To examine the capability of the proposed method to identify the constitutive response and damage properties of composite laminates, a series of OCT tests were conducted. For each OCT test, the load-POD curve and also images from the specimen surface were recorded during the test. Using these images and the DIC technique, displacement vector fields were obtained. Afterward, using the proposed methodology and the displacement fields, the approximate strain-softening responses of the composite laminate were obtained. By analyzing these approximate responses and also the global load-POD

response in each test, it was observed that damage does not grow in a smooth manner. Due to inhomogeneous fibre failures, sudden damage extensions occurred in each test resulting in instantaneous load drops and consequently jumps in the local stress-strain curves.

Although using these approximate curves, the real damaging behaviour of the material can be studied and characterized, it was suggested that for the FE simulation purposes, a continuous softening response can be used to represent the material damaging behaviour. Using approximate curves, optimized responses using linear, bilinear and trilinear softening shapes were obtained. Furthermore it was suggested that a trilinear softening response with a plateau stress was a better representation of the inhomogeneous behaviour of the material compared to linear and bilinear softening responses.

FE analyses of the OCT tests were performed using optimized strain-softening responses. Results obtained from the FE analyses using bilinear and trilinear softening responses agreed well with the experimental results. It was also proposed that in other notched specimen sizes, the end portion of the softening response might become important in effectively predicting their damaging behaviour (Appendix B).

To further validate the capability of the model to identify the damage region and damage parameters, a series of destructive tests such as sectioning and depleting were performed on the damaged specimen. From these tests, the damage zone in each specimen was identified and examined. The results obtained from these tests agreed well with the calculated results using the proposed methodology. This shows that using the proposed model, damage properties of composite laminates can be determined with sufficient degree of accuracy in OCT tests. Moreover, further comparison of this method with the other already established methods such as line analysis (Appendix C), shows a noticeable improvement in accuracy for determining the material damage properties. These successful validations instil confidence in exercising the proposed model for identifying the constitutive response of composites under tension and thus calibrating the existing numerical models based on strain-softening material behaviour.

Chapter 5: Application to CC Tests and Validation Using FE Simulation and Destructive Testing

5.1. Introduction

In this chapter, the proposed method has been utilized to determine the compressive damage properties and constitutive response of composite laminates using compact compression tests. To conduct compact compression tests, a compressive jig was designed and built in the course of this study. Using this jig, compressive experiments were conducted on the IM7/8552 quasi-isotropic laminate. A geometry similar to compact tension test geometry was considered for compact compression tests to produce a stable damage growth under compressive loads.

In this chapter, first, the development of the compressive jig will be presented. Then, the experimental results obtained from compact compression tests along with the results obtained using the current proposed method are presented and compared.

5.2. Compressive Testing Jig

Compared to well developed tensile experiments for composite materials, compression tests have received relatively little attention. The main issue that prevents the development of reliable and easy to reproduce compressive experiments is the buckling and instability of test specimens.

In recent years, few studies have been focused on developing tests for studying the progressive damage propagation of composites under compression. Similar to compact tension (CT), developing a compact compression test would allow us to study the damaging behaviour of composites under compression. The lack of availability of a standard test method for conducting compact compression tests has been the main reason for developing such a test in this study.

Soutis et al. (1993) investigated the compressive fracture properties of open-hole carbon fibre/epoxy laminates. In this study which was later followed by a similar study (Soutis et al., 2002), Soutis et al. were able to measure the compressive strength of multidirectional laminates. In their study, a self-similar crack growth as a result of progressive damage propagation was not observed. In these studies, however, stable growth of fibre microbuckling near the edges of the hole was observed.

Moran et al. (1995) presented their work on the progressive kink band propagation under compression for an edge-notched unidirectional laminate. Later on, Sivashanker (Sivashanker, 1998; Sivashanker, 2001; Sivashanker and Bag, 2001) investigated the progressive damage propagation of both unidirectional and multidirectional edge-notched laminates under compression. He applied compression through wedge grips and used anti-buckling devices to prevent out-of-plane movement of specimens. As a result, he was able to study damage behaviour of composites under compression.

Following the above attempts, in a few studies, sandwich panels have been used in order to prevent buckling of composite laminates (e.g. Bayldon et al., 2006) and produce progressive damage propagation. For example, Ratcliffe et al. (2004) studied the progressive damage propagation in composite laminates by applying eccentric compressive loads on composite sandwich panels.

Recently, in a study by Pinho et al. (Pinho, 2005; Pinho et al., 2006), compact compression tests on relatively small specimens were conducted. This study, however, does not provide details of the compression test fixture and how the buckling of specimens were prevented.

Considering the above attempts for studying compressive damage behaviour of composites, the following properties should be considered in designing a compact compression test fixture:

1. Ease of fabrication.
2. Insensitivity to misalignment of the specimen and load application points.

3. Stability of the specimen (i.e. buckling of the specimen should be prevented).
4. Ability to produce progressive damage propagation and self-similar crack growth under compression.

Based on these properties, a jig was built and utilized for compact compression test of composites. The current compressive jig is shown in Figure 5-1 and Figure 5-2. Load is applied through small balls on top and bottom of the jig and transferred to the specimen through the pins near the notch tip. The whole fixture moves inside railing guides around it to prevent buckling and bending of the specimen. The geometry of the compact compression test used in this study is also shown in Figure 5-3.

During the experiments on sample panels, strain fields were measured on the surface of the specimens using the current DIC technique. These strain fields were then compared with the strain fields obtained from an elastic analysis of the compact compression panels using LS-DYNA. Any misalignment or bending in the specimen, results in an asymmetric strain field or strains that are all larger (out-of-plane bending away from the camera) or smaller (out-of-plane bending toward the camera) than strains obtained using FE simulation. Comparison with FE results did not show any out-of-plane or in-plane bending of the specimen. As an example, comparison of experimental and numerical strains along a line approximately 1.25 mm ahead of the notch tip (Figure 5-4a) is shown in Figure 5-4b. Elastic strains were measured at $POD = -0.7$ mm on the specimen surface. Considering the maximum error in measured strains using DIC technique (about 0.3% in this study), this comparison shows an acceptable agreement between experimentally measured and numerically predicted strains.

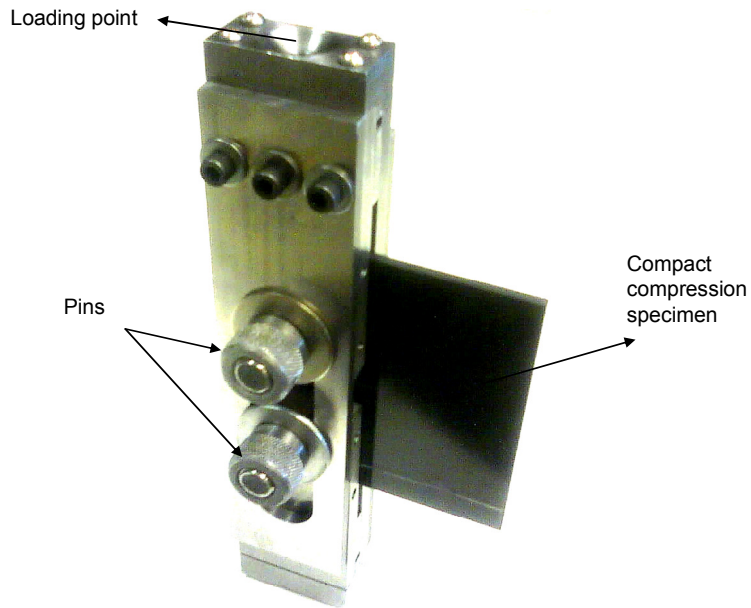


Figure 5-1 Compact compression test fixture.

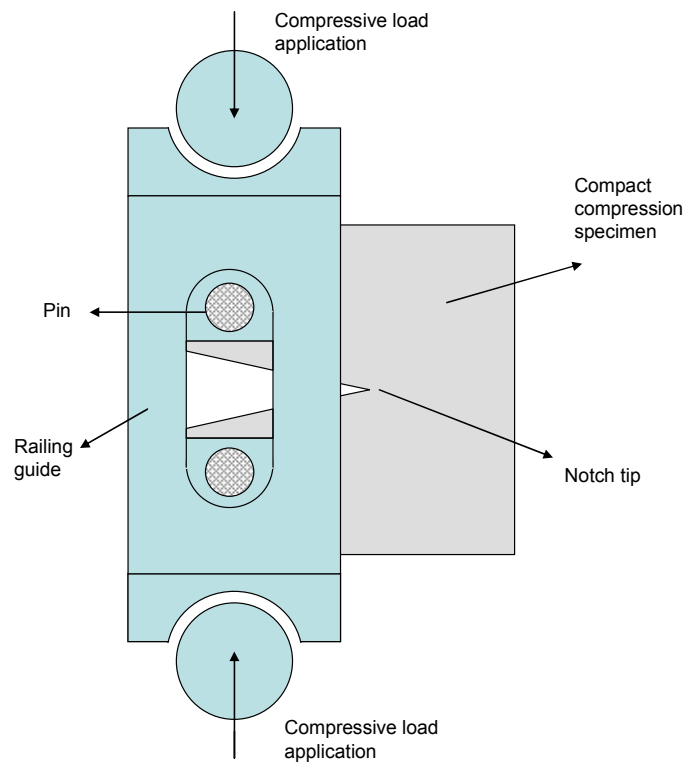


Figure 5-2 Schematic of compact compression test fixture.

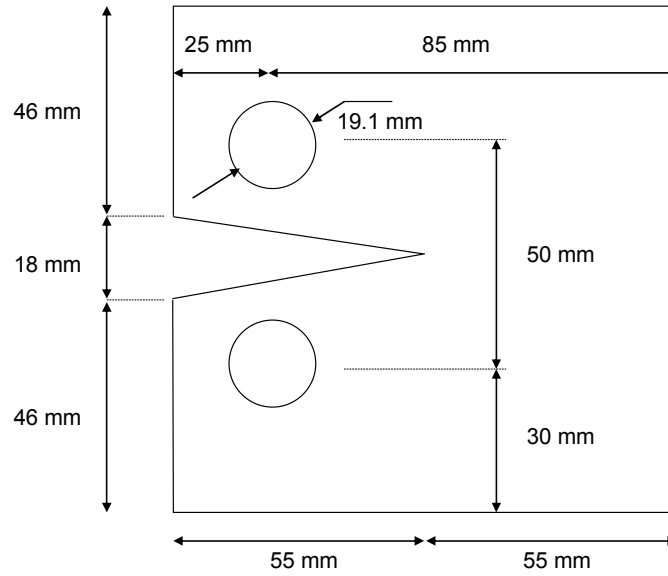


Figure 5-3 Compact compression specimen geometry.

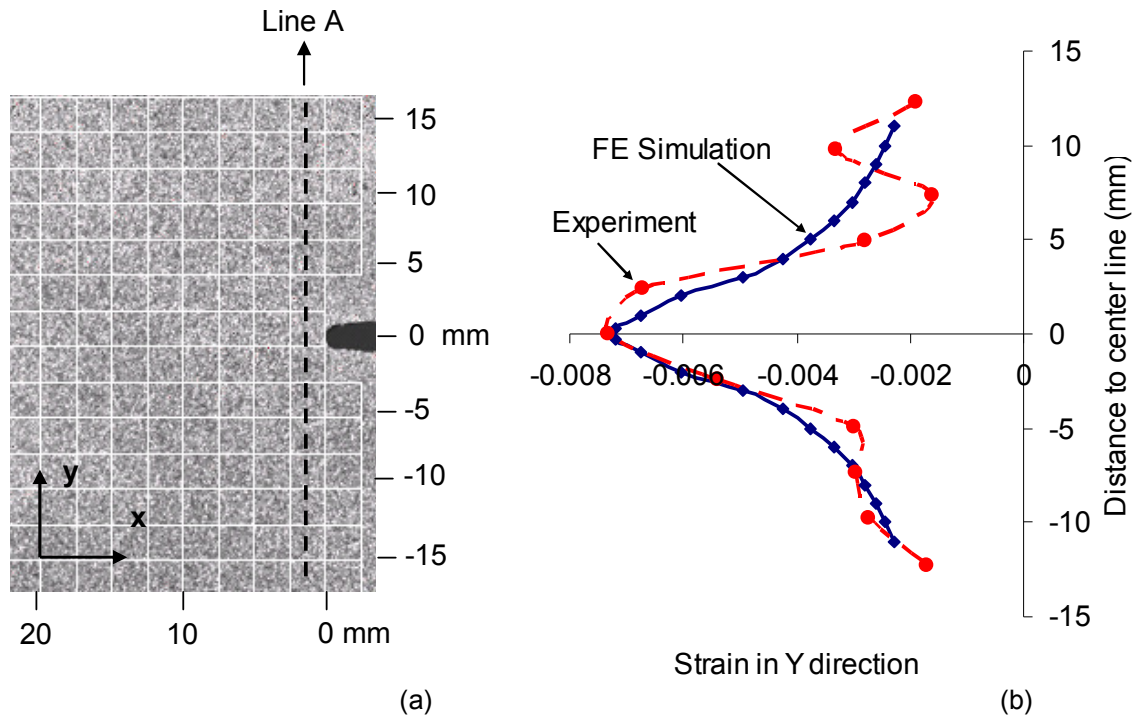


Figure 5-4 Comparing the elastic strains on the surface of a CC specimen with the strains obtained from FE simulation. (a) Location of comparison line and (b) Strains in Y direction along line A at POD = -0.7 mm.

5.3. Compact Compression Tests

The material used for compact compression (CC) tests was the same as that used for OCT tests. Quasi-isotropic IM7/8552 panels were cut based on the CC test geometry shown in Figure 5-3. The summary of the tests and analyses conducted in this section are presented below:

1. Three compact compression tests were conducted: CCA2, CCB1 and CCB2.
2. Using the DIC technique, displacement fields were obtained during each test.
3. Using the proposed methodology, damage related parameters and stress-strain response of the laminate under compression were obtained.
4. FE analyses of the CC tests were performed using LS-DYNA and the results were compared with the experimental results.
5. CCB1 test specimen were de-plyed and fibre breakage traces were analyzed in each ply. Experimental results were compared with the calculated results using the current proposed method.
6. CCA2 test specimen were sectioned and analyzed using the SEM technique. Experimental results were compared with the calculated results using the current proposed method.

5.3.1. Tests

Three CC tests were conducted in this study using specimens cut from two panels. CCA2 specimen was cut from panel A which was the same panel that OCT specimens were cut from. CCB1 and CCB2 were cut from panel B. Specifications for these specimens are listed in Table 5-1.

Table 5-1 Specification of CC specimens tested in this study.

| Specimen | Height (mm) | Width (mm) | Thickness (mm) | Notch (mm) | Lay-up |
|----------|-------------|------------|----------------|------------|-----------------------------|
| CCA2 | 109.11 | 110.53 | 4.07 | 54.2 | [90/45/0/-45] _{4s} |
| CCB1 | 109.39 | 110.13 | 4.03 | 54.61 | [90/45/0/-45] _{4s} |
| CCB2 | 109.1 | 109.08 | 4.04 | 55.34 | [90/45/0/-45] _{4s} |

Similar to tensile tests, for compression tests, a screw-driven Instron uniaxial testing machine and a MTS load cell were used. The same Instron extensometer (model 2620-825 with ±5 mm travel) was used to measure POD(s). Just like tensile tests, the specimens were loaded under displacement controlled condition with a loading rate of 0.25 mm/min. Full-field displacement vectors were obtained in each test.

For CCB1 specimen, multiple load-unload cycles were performed in order to measure the fracture energy more accurately. The load-POD curves of two of the tests are shown in Figure 5-5. For CCB1, 1555 images were recorded while for CCB2, 460 images were recorded during the test. The surface image of CCB1 specimen at the end of the test is shown in Figure 5-6.

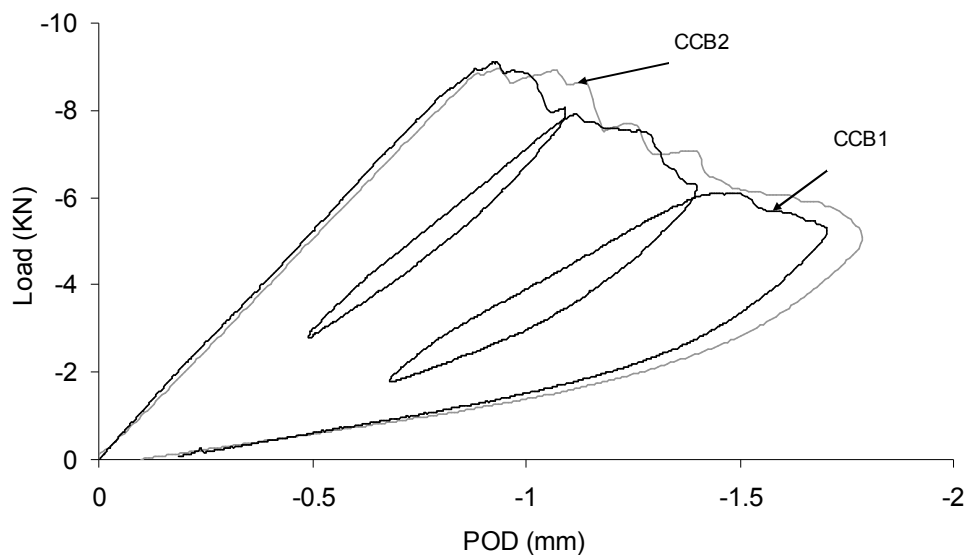


Figure 5-5 Load-POD curves for CC tests.

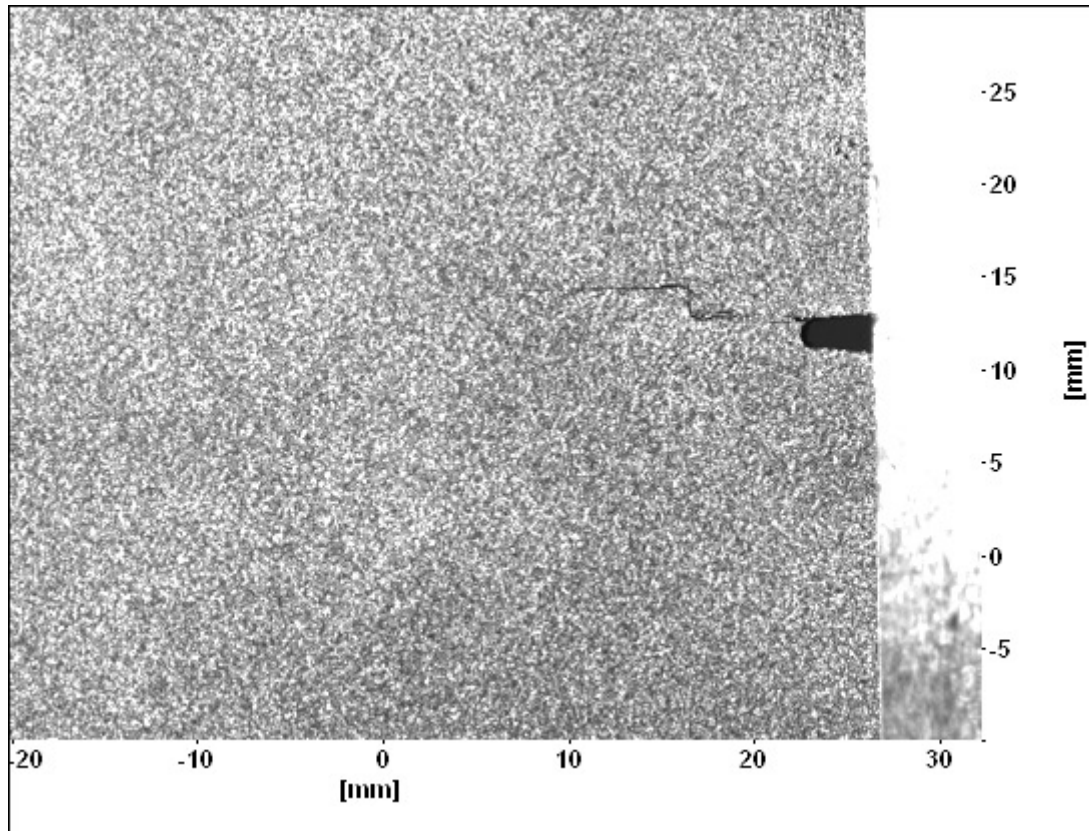


Figure 5-6 Surface image of CCB1 specimen at the end of the experiment.

5.3.2. Application of the Proposed Method

For CCA2 specimen, DaVis generated a mesh with element sizes equal to 2.801 mm. For CCB1, element sizes were 2.452 mm. Meshes generated by DaVis for CCB1 and CCA2 specimens are shown in Figure 5-7 and Figure 5-8 respectively.

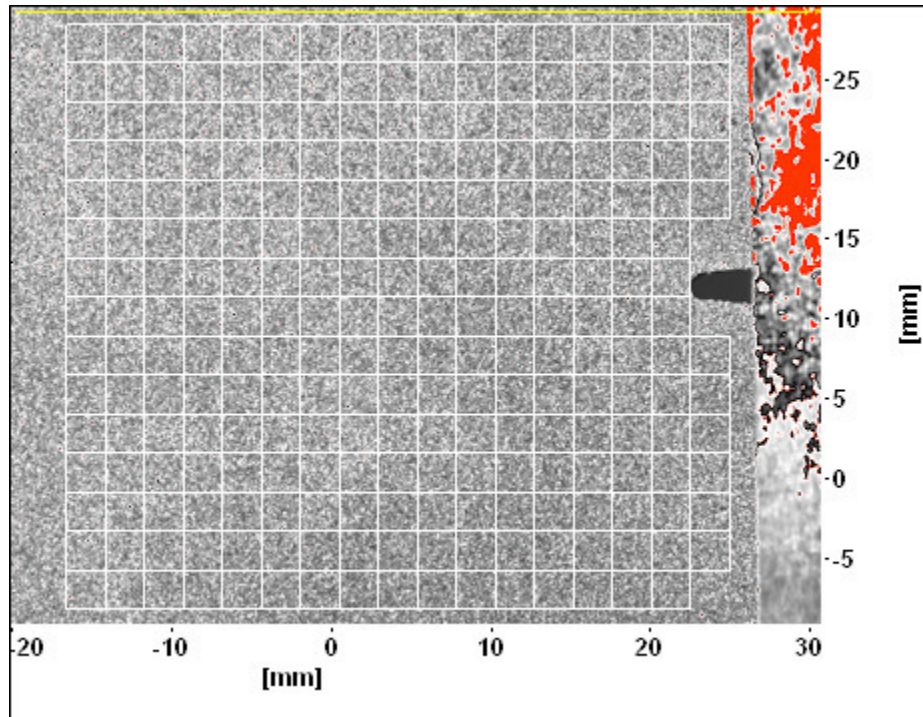


Figure 5-7 The mesh generated by DaVis on the surface of CCB1 specimen with element sizes equal to 2.452 mm.

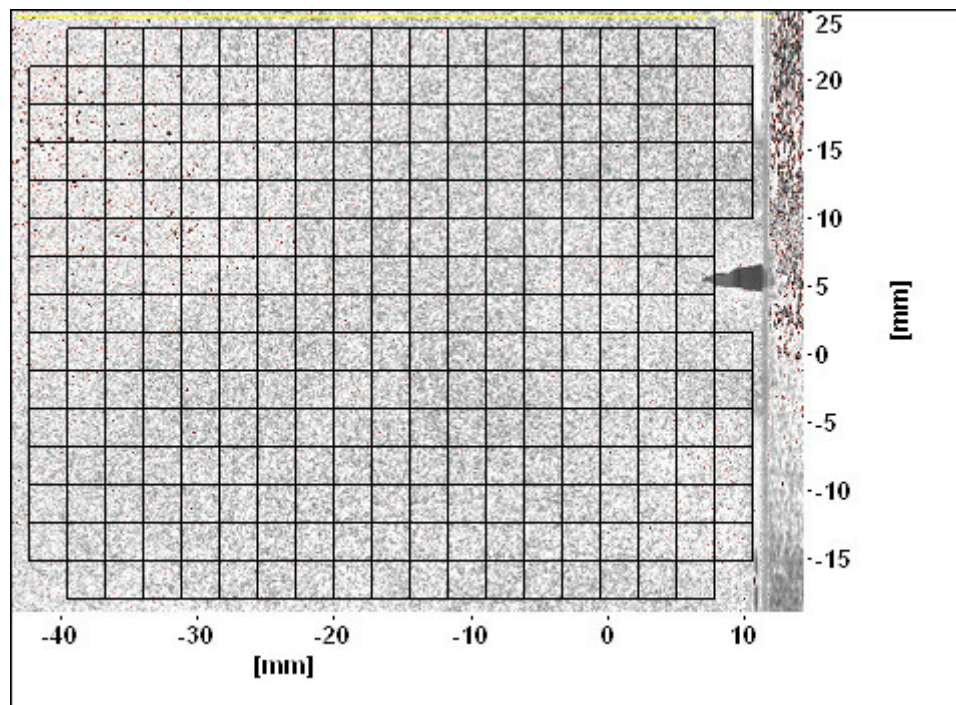


Figure 5-8 The mesh generated by DaVis on the surface of CCA2 specimen with element sizes equal to 2.801 mm.

Following the steps outlined in the previous chapters, the displacement data were imported into the CrackPro code. Equilibrium equations were used to identify the extent of damage in each test. Afterward, approximate stress-strain curves for the composite laminate were constructed by analyzing columns of damaged elements. Two examples of approximate stress-strain responses obtained from the above process are shown in Figure 5-9 and Figure 5-10 for columns of elements 1.2 mm and 11 mm ahead of the notch tip in CCB1 specimen, respectively. By overlaying all these curves, the shape of the optimized response can be constructed. For these tests, a trilinear softening response which consists of a stress drop followed by a plateau stress was chosen. This assumption for the response shape agrees with the findings of previous studies (Sivashanker, 2001; Zobeiry, 2004; McGregor et al., 2008; McGregor, 2005; Zobeiry et al., 2008). The trilinear softening response shape along with approximate responses are shown in Figure 5-11.

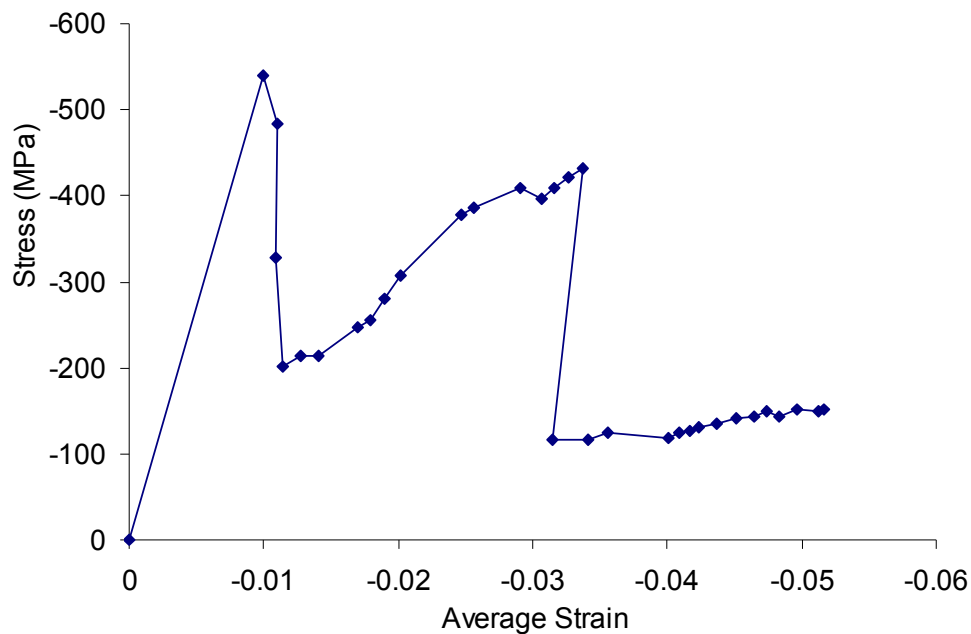


Figure 5-9 Approximate compressive stress-strain response obtained from CCB1, 1.2 mm ahead of the initial notch tip.

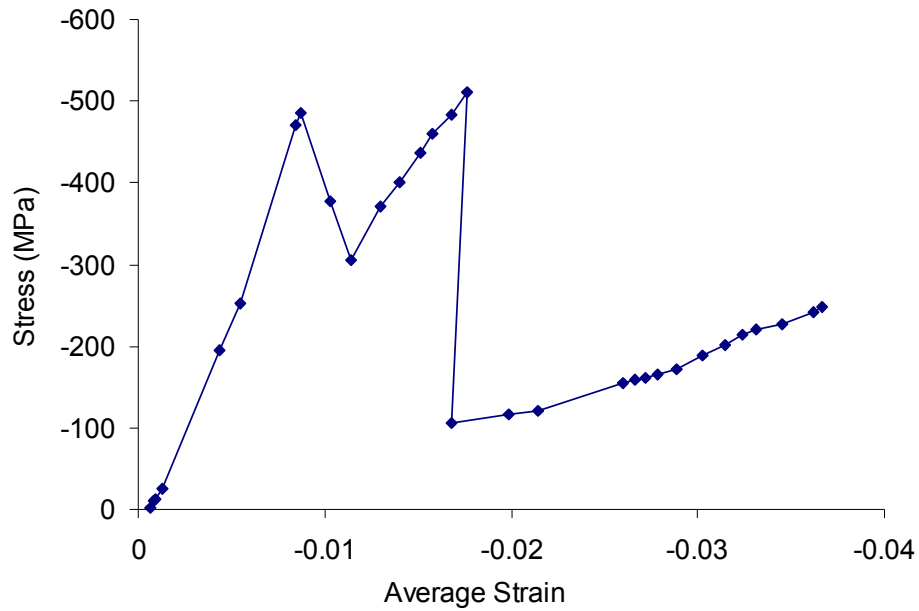


Figure 5-10 Approximate compressive stress-strain response obtained from CCB1, 11 mm ahead of the initial notch tip.

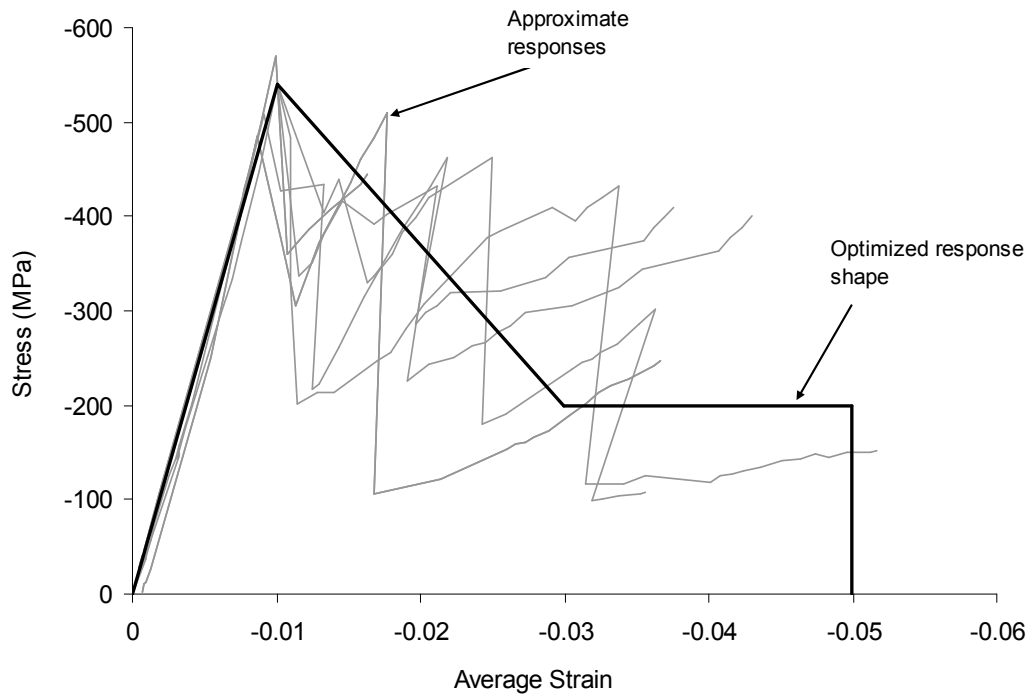


Figure 5-11 Approximate stress-strain responses along with the optimized response shape obtained from the optimization process.

In composites, one of the main differences between the tensile and compressive damage propagation is the damage band broadening. Under tensile loads, damage height is constant while damage is propagating. For example in OCT tests in this study, the damage height was measured to be approximately equal to 5 mm. However, Damage height under compressive loads increases as damage propagates. As shown in other studies (Zobeiry, 2004; McGregor, 2005) when damage zone forms under compression, by applying more compression, damage propagates into the undamaged material in the vicinity of the damage zone. This of course is not the case in tension and after the crack formation, no load can be transferred between the two edges of the crack. Under compression, load is transferred between the two damage edges and that causes the damage band broadening. In this study, it was observed that damage height was initially about 4-6 mm under compression. This initial height was broadened to a maximum height of 12 mm until no compression load could be transferred between the damage edges anymore.

The damage band broadening can be observed in Figure 5-13 on the surface of the CCB1 specimen. Following the steps in the optimization process, the optimized stress-strain response for the laminate under compression was obtained. This response is presented in Table 5-2 and Figure 5-12.

Table 5-2 Key values in the optimized constitutive response obtained using the proposed methodology applied to CC tests.

| | | | | |
|--------------------------|--------------------|-------|-----------------|------------------------------------|
| Elastic modulus | E_x | 54.2 | (GPa) | From FE analysis |
| | E_y | 54.2 | (GPa) | From FE analysis |
| Poisson's ratio | ν_{xy} | 0.32 | | From laminate plate theory |
| Shear modulus | G_{xy} | 20.5 | (GPa) | From elastic theory = $E/2(1+\nu)$ |
| Damage initiation strain | ϵ_i | -1.2% | | From CrackPro |
| Damage saturation strain | ϵ_s | -2.0% | | From CrackPro |
| Ultimate strain | ϵ_u | -4.5% | | From CrackPro |
| Plateau stress | $\sigma_{plateau}$ | -200 | (MPa) | From CrackPro |
| Total Fracture energy | G_f | 85 | kJ/m^2 | From area below load-POD |

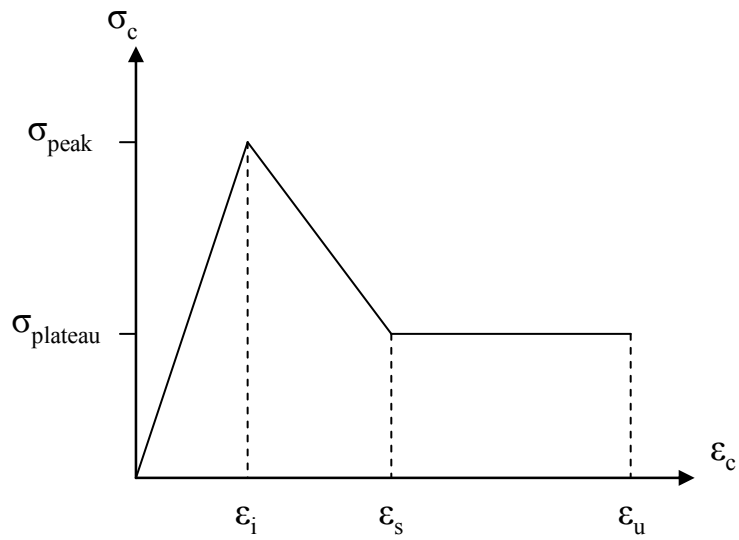


Figure 5-12 Optimized compressive response obtained using the proposed methodology.

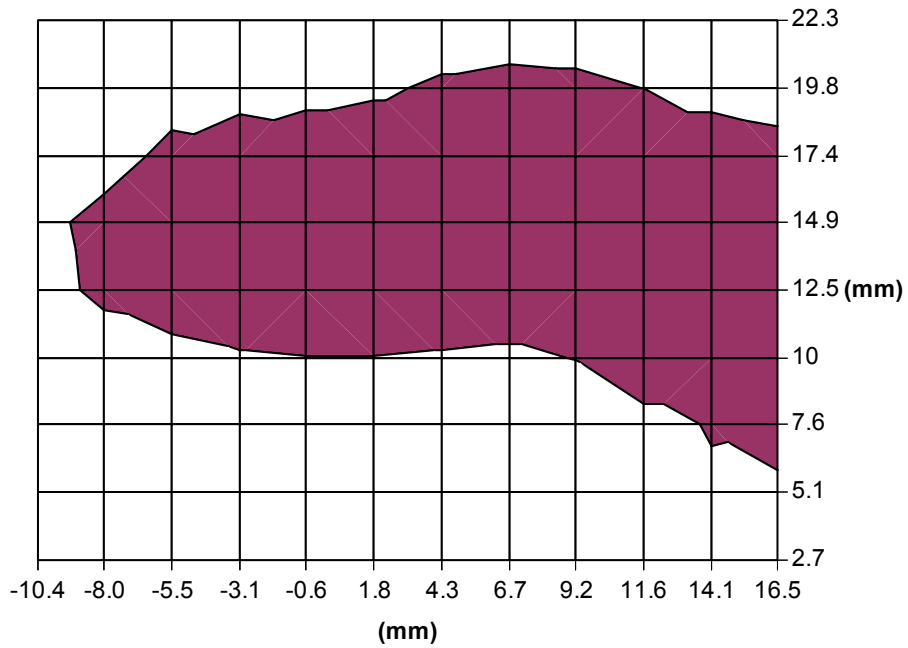


Figure 5-13 Damaged area in CCB1 specimen just before final unloading. Damage height grows to about 12 mm after band broadening stage.

5.3.3. Finite Element Simulation

To validate the optimized constitutive response obtained here, independent FE simulations of CC tests were carried out. Similar to the tensile loading case, LS-DYNA FE code and built-in material model, MAT_081, were used to simulate the CC tests. A quasi-static simulation of the CC test was carried out using a 0.5 mm mesh size and applying the Bazant's crack band scaling law (Bazant and Oh, 1983). Again, as explained in simulation of OCT tests, true strains were used as inputs for LS-DYNA due to calculation of large strains in the code. Part of the 0.5 mm mesh in LS-DYNA is shown in Figure 5-14. The load-POD curve obtained from LS-DYNA simulation is shown in Figure 5-15 along with the results obtained from experiments. This shows an acceptable agreement between the simulation results and experimental results. Comparison between the peak load and the POD at the peak load is shown in Table 5-3.

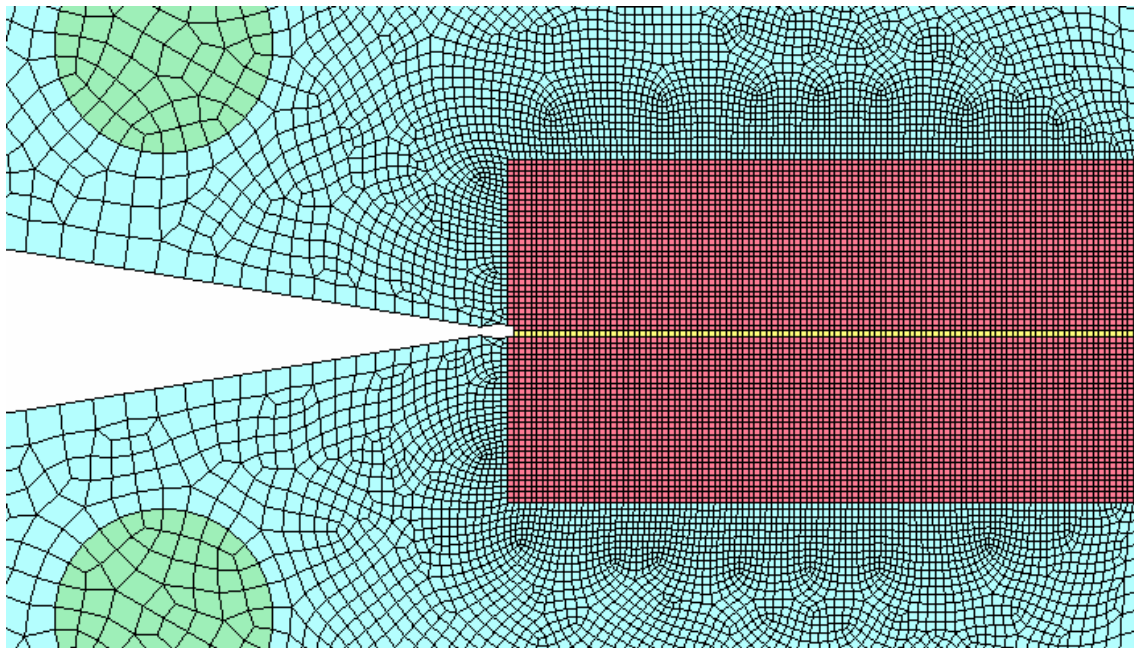


Figure 5-14 Part of the mesh used for simulating CC tests in LS-DYNA.

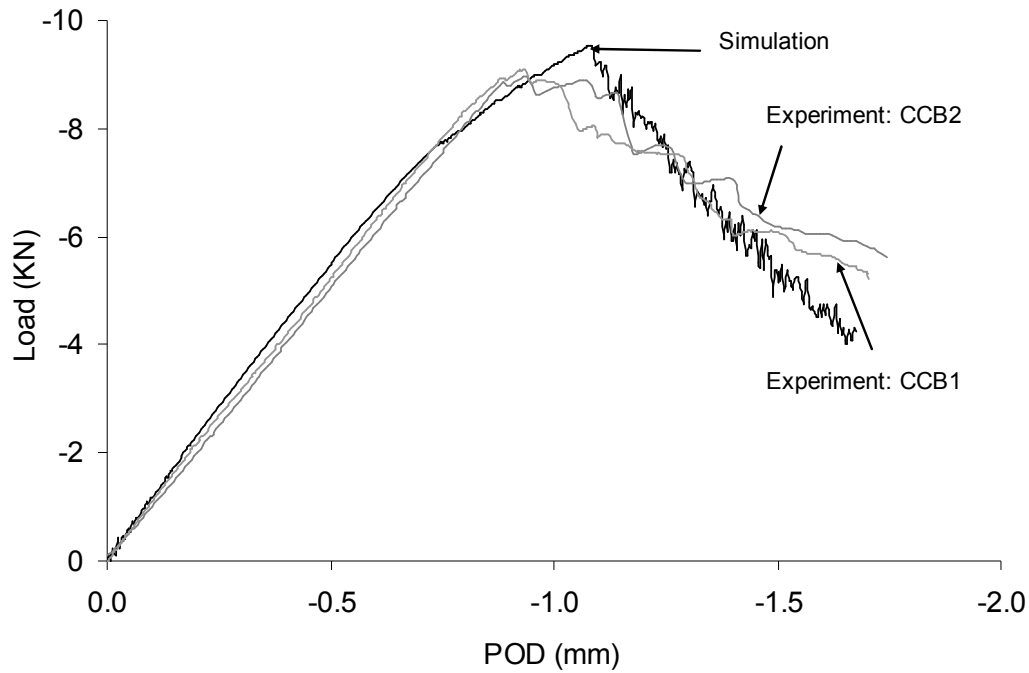


Figure 5-15 Comparison of load-POD curve obtained from LS-DYNA and experimental results.

Table 5-3 Comparison of experimental and numerical results for CC tests.

| | Peak load (kN) | POD (mm) at the peak load |
|--|----------------|---------------------------|
| Average of Experiments | -9.06 | -0.93 |
| FE result (error) with optimized curve | -9.54 (5%) | -1.08 (15%) |

5.3.4. Deploying

To further study the damage propagation under compression in composite laminates, the post-mortem CCB1 specimen was deploded. Following the same procedure for deploding as explained in the previous chapter, a section of interest (43x32 mm) in front of the notch was cut from CCB1 specimen using a slow-speed diamond saw. This section was left in the 420° C oven for about 6.5 hours. The individual plies were then separated and studied to identify fibre breakage/bending traces in each ply. These traces are shown for three plies in Figure 5-16, Figure 5-17 and Figure 5-18. Schematics of these traces are also shown in Figure 5-19 for various plies.

These traces were overlaid as shown in Figure 5-21. This figure shows a fibre breakage/bending zone of approximately 31 mm. This length is different from the damage length obtained using the proposed method equal to 26.5 mm. This implies that for 4-5 mm of the material that contains fibre breakage/bending, equilibrium can be satisfied within an acceptable error range.

However in tension, as shown previously, this was not the case and the calculated length of damage was approximately equal to the measured length of fibre breakage trace. The difference between compression and tension is that when fibres bend or break under compression, load can still be transferred through the damage zone via friction or other mechanisms until the two damage surfaces start to slide past each other. This means that at the tip of the fibre breakage/bending zone, the error in equilibrium is negligible due to this load transfer.

To further examine this conjecture, an optical microscope was used to analyze this zone. Figure 5-20 shows images obtained using an optical microscope for layer #22 (0°) of CCB1 specimen. From this image we can observe that for the area that equilibrium cannot be satisfied (Figure 5-20d), debris and rubble form due to sliding and crushing of fibres on each other. On the other hand, Figure 5-20c shows no sign of this rubble formation for the area that equilibrium can be satisfied within an acceptable error range. This 4-5 mm length associated with strains within range of -0.5% to -1.1%, was studied in more detail using sectioning technique and will be discussed next.

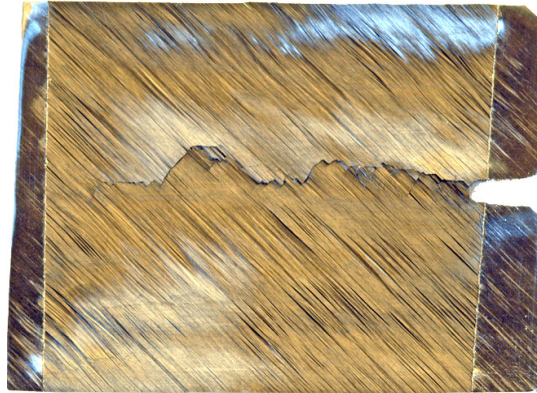


Figure 5-16 Fibre breakage/bending trace in ply #4 of CCB1 specimen with -45° fibre direction for a 43x32 mm cut.

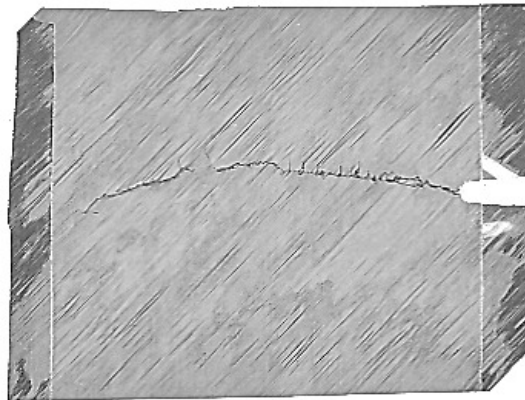


Figure 5-17 Fibre breakage/bending trace in ply #6 of CCB1 specimen with $+45^\circ$ fibre direction for a 43x32 mm cut.

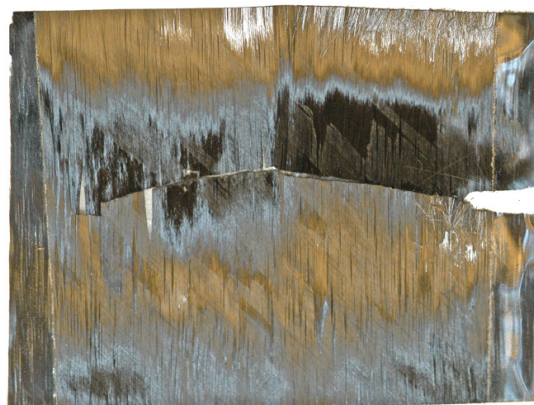


Figure 5-18 Fibre breakage/bending trace in ply #7 of CCB1 specimen with 0° fibre direction for a 43x32 mm cut.

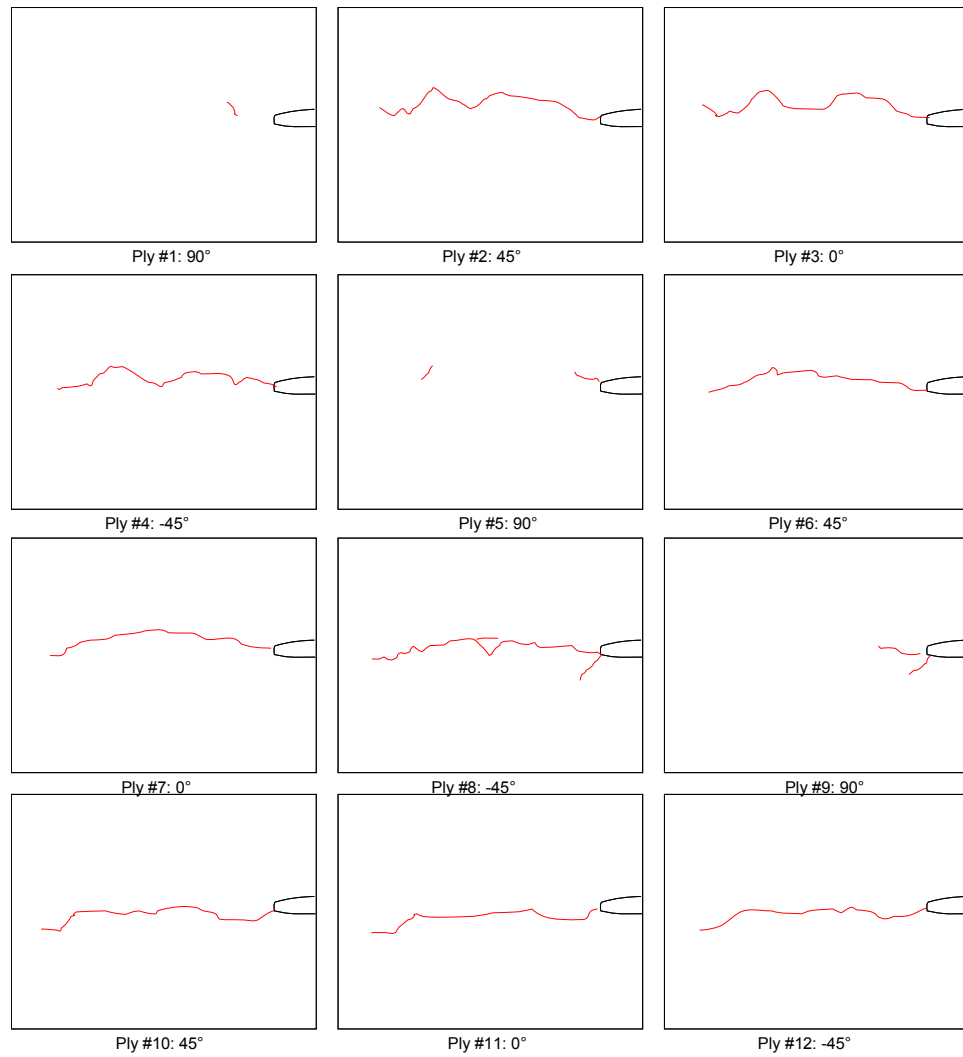


Figure 5-19 Fibre breakage/bending traces in various plies of CCB1 specimen. Each cut is 43x32 mm.

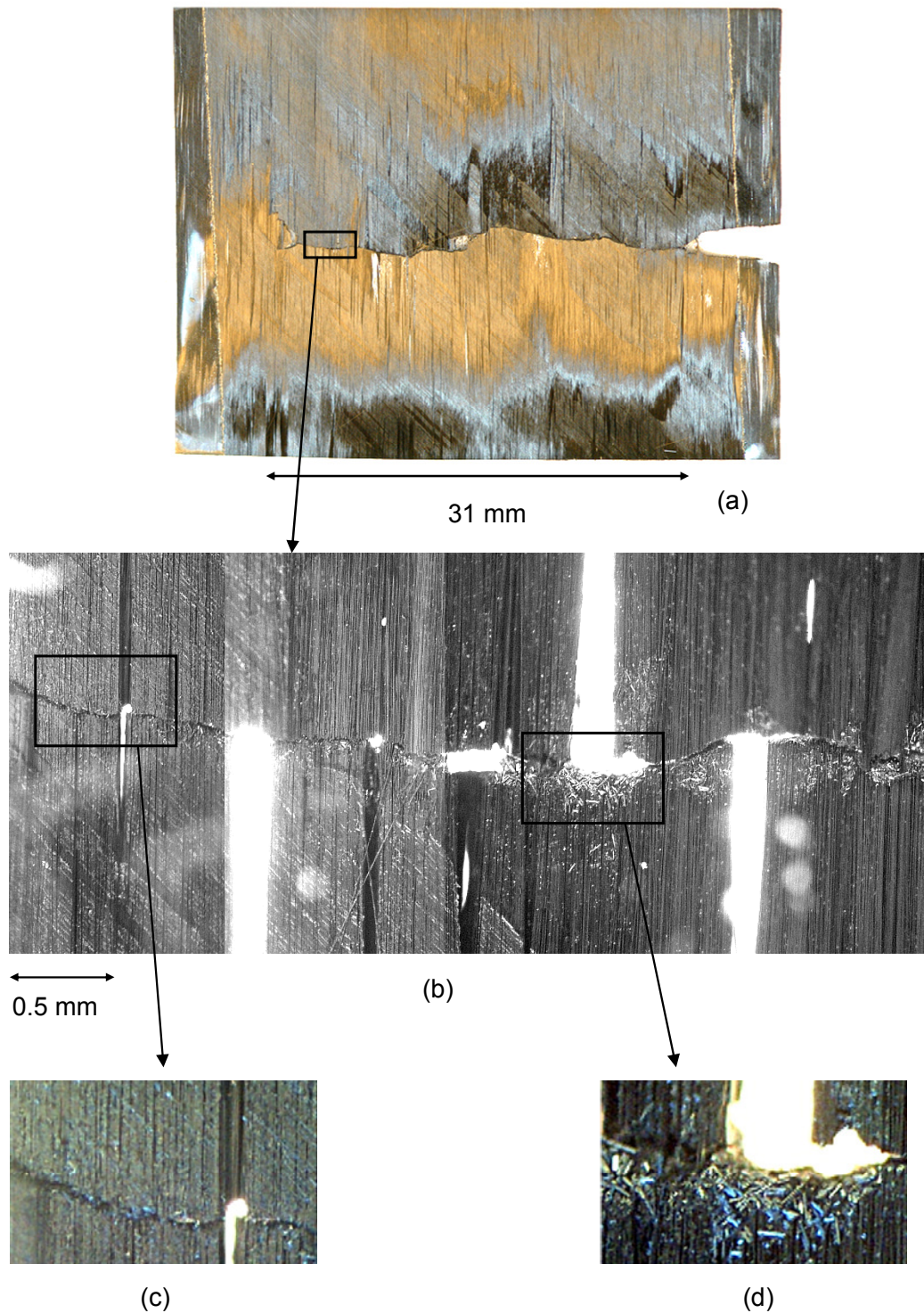


Figure 5-20 (a) Fibre breakage/bending traces in layer #22 of CCB1 specimen with 0° fibre direction, (b) showing part of the damage tip, (c) part of the damage zone that still can transfer load under compression and (d) rubble formation leading to loss of load bearing capacity.

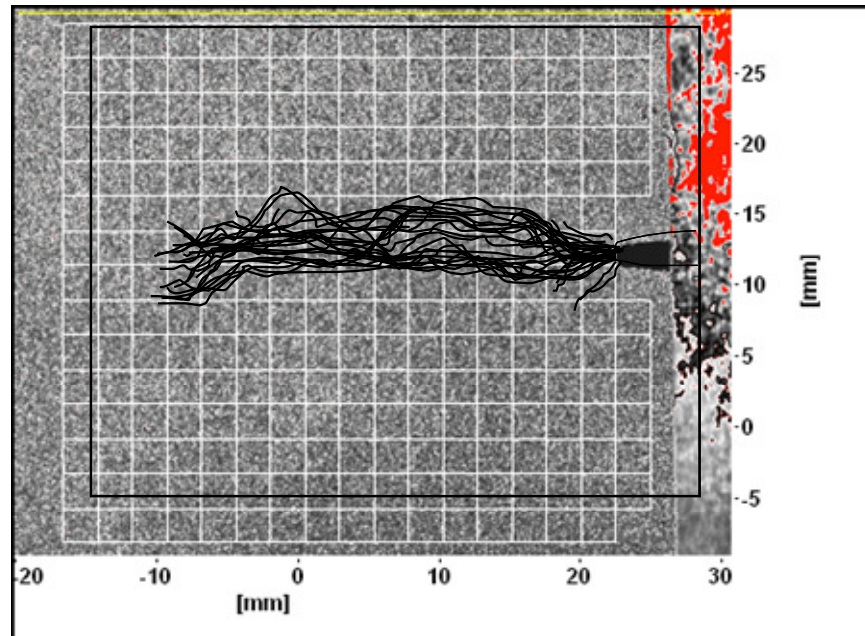


Figure 5-21 Overlaying fibre breakage/bending traces identified using deplying technique in all layers of CCB1 specimen.

5.3.5. Sectioning

To further study the damage zone in CC tests, the CCA2 specimen was sectioned. Following the same procedure as described for tensile specimens, 20 sections were cut from the CCA2 specimen each 1.9 mm apart in front of the initial notch tip. Table 5-4 summarizes the results obtained in these cuts.

Using the SEM technique, images of the damage zone in these cross-sections were obtained. In these images, kinking in 0 degree layers, off-axis matrix cracking, off axis fibre breakage/bending and delamination can be observed. An example of the SEM results for cross-section #10 is shown in Figure 5-22.

In Figure 5-23, three of these cuts along with the schematics of damage in these sections are shown. In these sections, we can observe formation of failure slip surfaces from section #6 to section #8. These surfaces consist of two large delamination surfaces merging with an inclined damage surface between them (Figure 5-24). These surfaces result in a mechanism that reduces the load-bearing capacity of the section noticeably. In

fact, before the formation of these slip surfaces, load can still be transferred between the two edges of the damage. Figure 5-25 shows the kink band saturation state after the formation of these slip surfaces in cross section #10.

Comparing the results obtained from sectioning with the results obtained from depleting, we can conclude that the formation of these slip surfaces and compressed rubble material around them, is the main reason for the loss of load bearing capacity in composite laminates under compression.

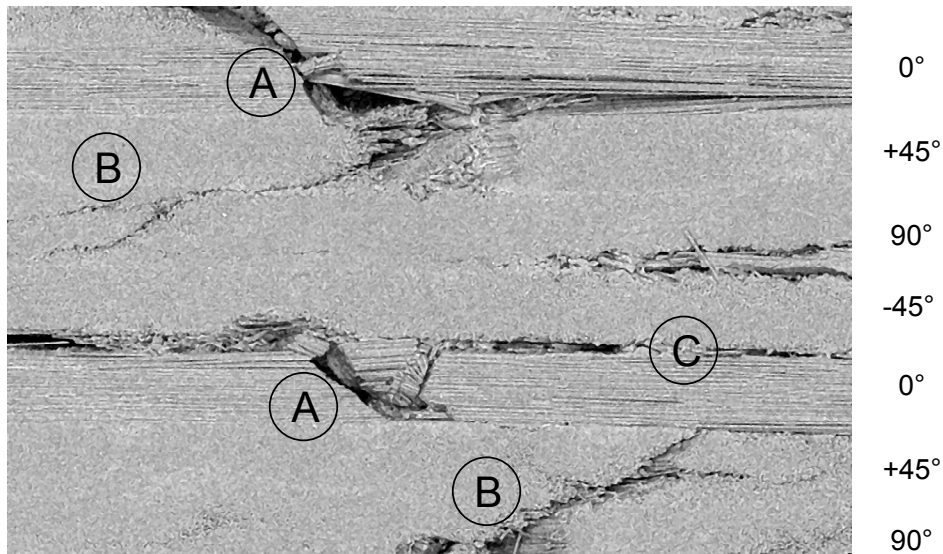


Figure 5-22 Overview of damage zone in the composite laminate under compression obtained from cross-section #10 using SEM technique. Failure mechanisms are kinking (A), off axis matrix cracking and fibre breakage/bending (B) and delamination (C).

Table 5-4 Section cuts in front of the notch tip for CCA2 specimen and the maximum strain in each section.

| Cross Section | Notch tip distance | Maximum strain |
|---------------|--------------------|----------------|
| 11 | 17.9 mm | -1.9 % |
| 10 | 19.9 mm | -1.7 % |
| 9 | 21.5 mm | -1.4 % |
| 8 | 23.5 mm | -1.2 % |
| 7 | 25.7 mm | -0.9 % |
| 6 | 27.4 mm | -0.7 % |
| 5 | 29.7 mm | -0.5 % |
| 4 | 31.2 mm | -0.4 % |

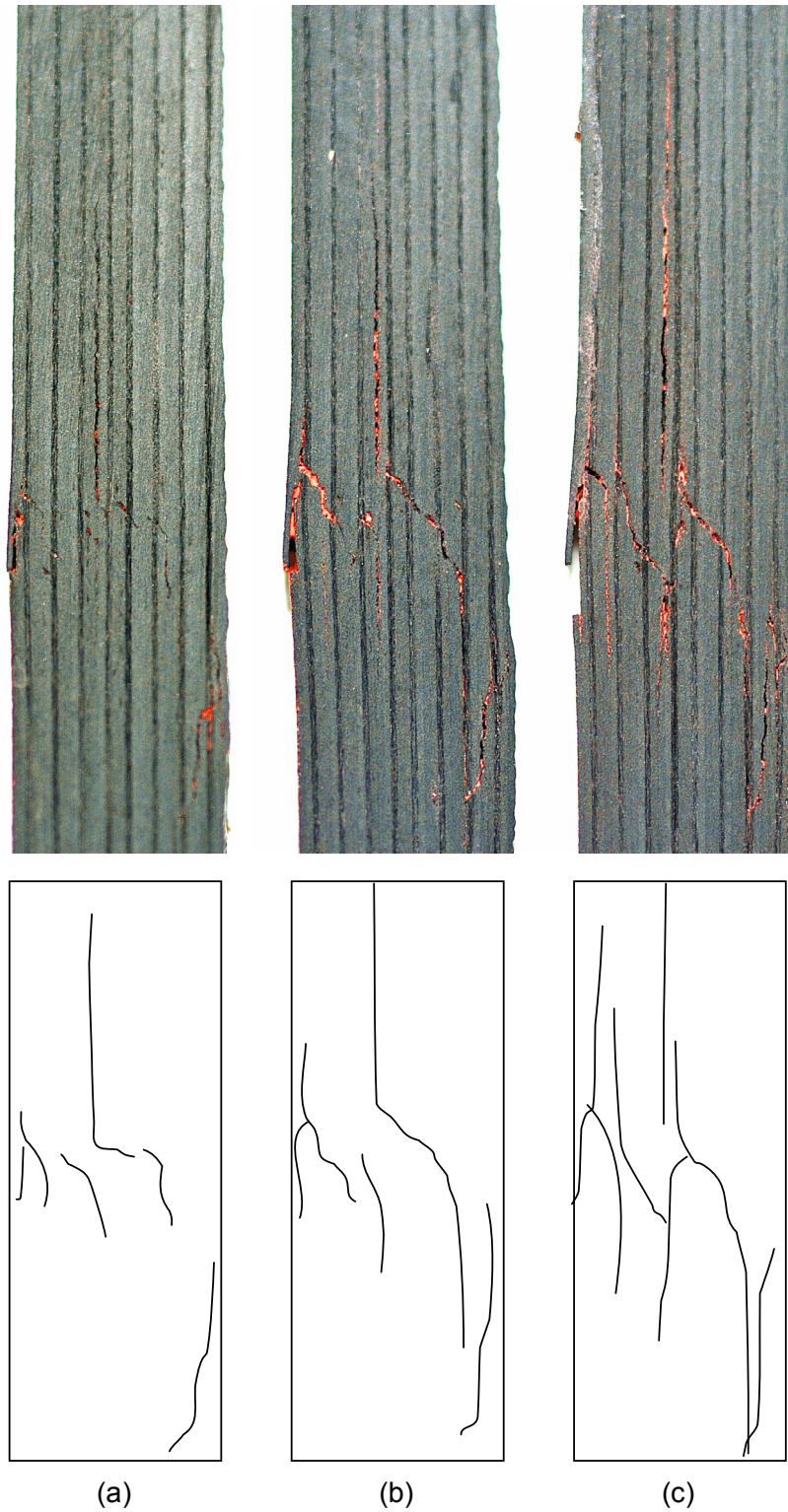


Figure 5-23 Formation of slip surfaces in sections of CCA2 specimen: (a) cross-section #6 with maximum strain equal to -0.7%, (b) cross-section #7 with maximum strain equal to -0.9%, (c) cross-section #8 with maximum strain equal to -1.2%

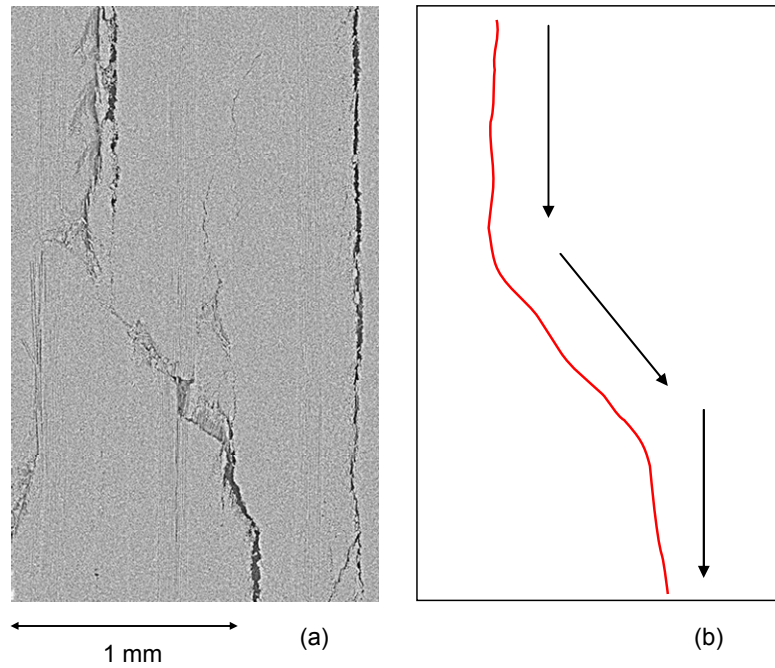


Figure 5-24 (a) and (b) Formation of slip surfaces in cross section # 8 of CCA2 specimen.

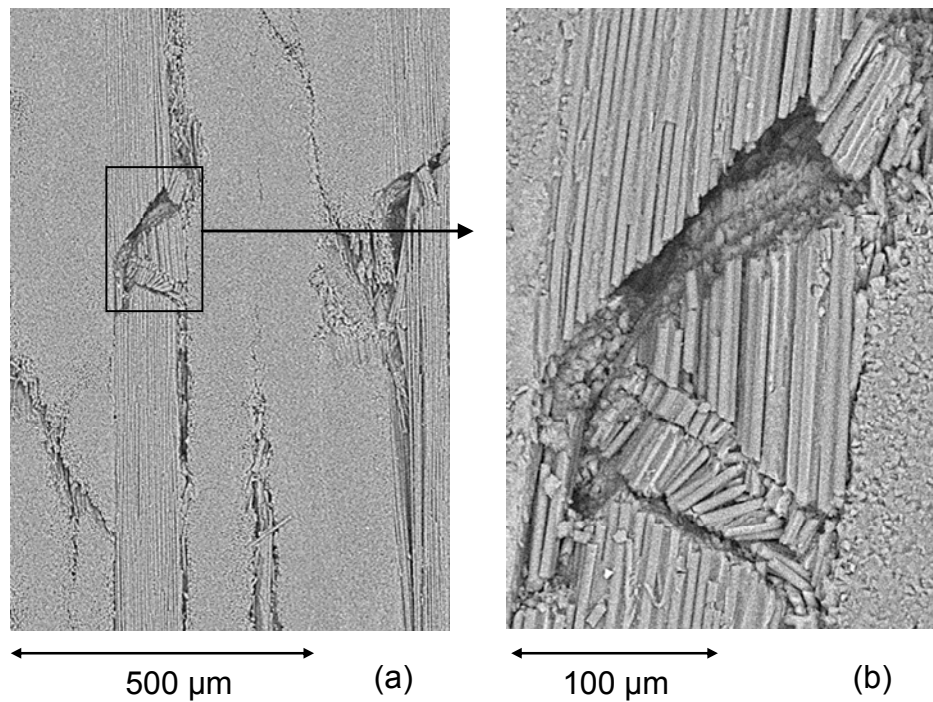


Figure 5-25 (a) Cross section #10 in CCA2 specimen and (b) Kink band formation.

5.4. Compressive Damage Length

For compressive tests, it was noted that the damage length measured using deplying technique, approximately equal to 31 mm, was different from the damage length calculated using the proposed method, approximately equal to 26.5 mm. However, it is noteworthy that the global dissipated energy and the global load-POD curve obtained using the proposed method, matched well with the experimental results. This is because in the global criterion of the optimization process, a response curve that satisfies the fracture energy criterion is chosen. The difference between the calculated and measured damage length is mainly due to fact that under compression, unlike tension, after the formation of the fibre bending/breakage zones, stress can still be transferred between the edges of the damage zone (zobeiry; 2004). To better study this issue, the compressive damage length has been divided into five zones as shown in Figure 5-26. These zones are described here:

- I. Undamaged elastic zone.
- II. Pre-peak nonlinear zone: Despite the fact that small fibre breakage/bending forms in this zone, stress is still transferred through this zone. Modulus loss is not significant and damage height is much smaller than the final characteristic damage height.
- III. Softening zone: In this zone, the damage height increases to a characteristic size, h_c (about 5 mm in this study). Due to formation of slip surfaces and excessive fibre breakage/bending, the material loses its load bearing capacity and the laminate modulus decreases significantly.
- IV. Broadening zone: Upon further compression of the damage zone, damage propagates into the neighbouring undamaged material. As a result, the damage height increases to a maximum height, h_u , approximately equal to 12 mm in this study. A constant stress, or plateau stress, is transferred through this zone.

- V. Zero stress zone: The two surfaces of the damage slide on each other and the material fails.

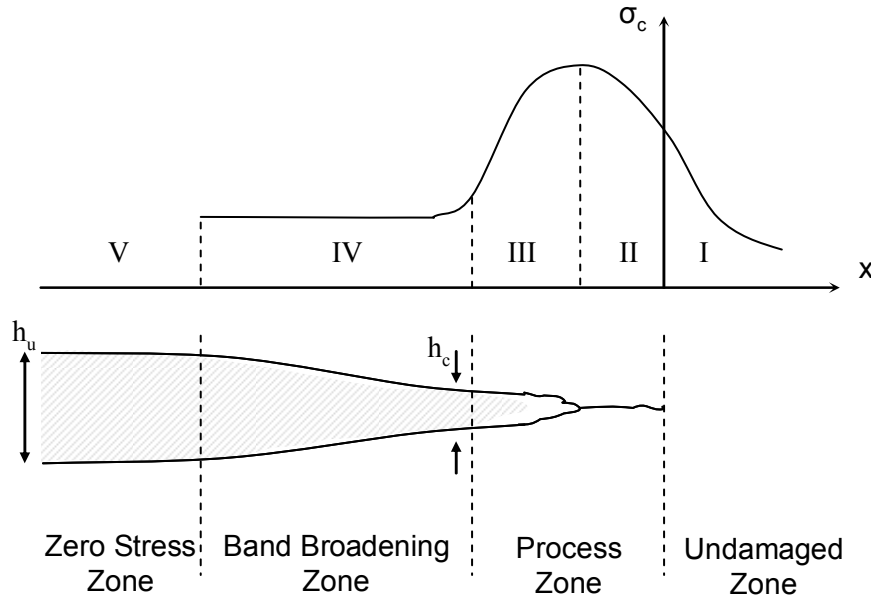


Figure 5-26 Formation of damage zones in composite laminates under compression.

The noticeable difference between the damage behaviour under tension and compression is that the process zone under compression (zones II and III), contains visible fibre breakage/bending. These damaged fibres can still transfer load under compression. Under tension, however, fibre breakage leads to complete loss of load bearing capacity and broken fibres cannot transfer load anymore.

It can be observed that the nonlinearity in the material response and also stiffness reduction in zone II is negligible compared to the nonlinearity and stiffness reduction in zone III. Since in the current study, the equilibrium forces are checked at each node, if the load drop due to damage growth doesn't exceed a certain threshold, it will not be detected as damage zone and this may result in a smaller damage length estimation. This has been the main reason for smaller damage length estimation in CC specimens using the current proposed method. However, it should be noted that based on the FE simulation results in this chapter, the global load-displacement response of the CC specimens can still be predicated successfully using the current approach.

Obviously under compression, calculation of fracture energy cannot be based on the total length of the fibre breakage/bending zone measured from the deplying technique. In fact, the energy dissipated in zone II is much smaller than dissipated energies in zones III and IV. To properly measure the crack length and consequently fracture energy, we have to calculate an equivalent damage length. Basically, the process zone is replaced with an equivalent damage zone. This zone should have a height equal to the characteristic height, h_c . The length of this zone should be calculated such that this zone dissipates the same amount of energy as the process zone (Zones II and III). To calculate this length, we use the full-field strain data and also a modified stress-strain response for the composite laminate as shown in Figure 5-27. This response has been constructed based on the calculation of the proposed method and also observations from deplying and sectioning techniques. For compressive strains between 0.5% and 1.2%, fibre breakage and bending appear with small modulus loss (Zone II). For compressive strains between 1.2% and 2%, based on equilibrium equations and sectioning results, slip surfaces appear and laminate loses its load bearing capacity. Afterward, band broadening occurs and ultimately the material fails.

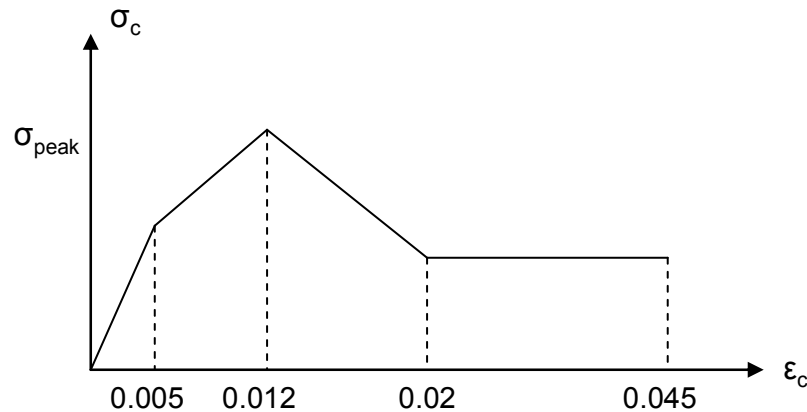


Figure 5-27 Modified stress-strain response of the composite laminate under compression with pre-peak nonlinearity.

The peak stress calculated previously from equilibrium equations was approximately equal to 650 MPa. However, due to the pre-peak nonlinearity, this value should be

reduced. This reduction also should be such that the peak stress satisfies the following equation:

$$|E \varepsilon_i| - |\sigma_{error}| \leq |\sigma_{peak}| \leq |E \varepsilon_i| \quad (5-1)$$

In the above equation, E is the laminate Young's modulus, ε_i is the strain at the peak stress equal to 1.2% in this study. σ_{error} is the error in the stress calculated based on the error and noise in the displacement field. In this study, the error in the strain field is about $\pm 0.3\%$. As a result, the error range for stress is within 150 MPa. The reasoning behind the above equation is that since in the optimization of a bilinear softening curve, maximum stress was determined to be equal to $E \cdot \varepsilon_i$, the actual peak stress for a laminate with pre-peak nonlinearity should be smaller than this value limited by the error in stress. In fact, any error larger than σ_{error} would have been detected in the optimization process. Therefore, we have:

$$500 \leq |\sigma_{peak}| \leq 650 \text{ MPa} \quad (5-2)$$

Now using this modified stress-strain response, we can calculate the equivalent damage length such that the dissipated energy in the process zone is equal to the dissipated energy in the equivalent zone.

As mentioned above, the equivalent damage zone has a height equal to h_c which is about 5 mm in this study. Using the modified stress-strain response, we can integrate over the elements in the process zone to calculate the dissipated fracture energy. From this calculation, an equivalent damage length was determined to be between 26 and 26.9 mm at the conclusion of the CCB1 experiment. This range corresponds to a range of peak stress between 500 and 650 MPa. The following provides a summary of the results for the CCB1 specimen:

- Length of the fibre breakage/bending zone measured using the depleting technique: 31 mm

- Equivalent damage length calculated by integrating energy over the damage zone: between 26 and 26.9 mm
- Calculated damage length using CrackPro: 26.5 mm

The acceptable match between the calculated and equivalent damage length is a result of the optimization process used in the proposed method. Since the optimization process is based on satisfying the fracture energy criterion, the damage length obtained using the proposed method is almost equal to the equivalent damage length. This means that by using the constitutive response obtained from the optimization process, not only we can simulate the global response, but also calculate an acceptable equivalent damage length. This further validates the capability of the proposed method for characterizing the constitutive response of composite laminates under compression.

5.5. Summary and Conclusions

In this chapter, experimental results obtained from CC tests along with the numerical results obtained using the proposed method are presented. Comparison of the results obtained in this section with the results obtained in the previous chapter for tensile specimens, highlights significant differences between the damage propagation in composite laminates under compression and tension. Under compression, while damage is propagating, load is still being transferred through the zone that contains fibre breakage/bending via friction and other mechanisms. Under tension, however, upon formation of fibre breakage, no load can be transferred through the damage zone.

Load transfer through the damage zone in compression results in a small nonlinearity in the stress-strain response of the material and subsequently a negligible error in elastic equilibrium equations. On the other hand, since in the damage tip area there is no significant loss of modulus, the global response obtained using the proposed method correlates well with the experimental results.

The current approach, based on the equilibrium equations, was able to determine the equivalent damage length. Using the optimized stress-strain response of the laminate,

both the global and local responses of the composite laminate were simulated successfully. These successful validations, confirm the applicability of the proposed method for identifying the constitutive response of composite laminates under compression.

Chapter 6: Conclusions and Contributions

In this study, a new methodology for extracting the strain-softening response of composite materials is introduced. This approach is based on the full-field measurement of surface displacements in notched specimens and use of fundamental mechanics (equilibrium and compatibility arguments) to infer the optimum strain-softening curve associated with the damage zone.

In the current approach simple equilibrium equations are applied to a virtual mesh generated on the surface of a specimen to detect the damage zone. Afterward, using some simplified assumptions, a family of approximate stress-strain responses for the composite laminate is obtained under Mode I loading configuration. These approximate responses are then used as the basis for an optimization algorithm used to arrive at the best curve that satisfies both locally and globally defined criteria.

To validate the capability of the proposed method to identify the constitutive response of composite materials, a series of over-height compact tension (OCT) and compact compression (CC) tests were conducted in this study. Using the proposed method, constitutive responses of composite laminates under tension and compression were obtained and used to simulate the behaviour of OCT and CC tests in LS-DYNA. The results obtained from FE simulations were successfully compared with the experimental results to validate the proposed method.

In order to further validate the capability of the method to detect the extent of damage and damage related parameters, a series of destructive tests such as depleting and sectioning were performed on damaged OCT and CC specimens. Results obtained from these tests were found to be in good agreement with the results obtained from the proposed method.

The methodology presented here is a promising method for identifying the constitutive response of composite laminates. So far, the favourable agreement between the experimental measurements and numerical simulations at both the global and local levels instils confidence in the optimized stress-strain response and the methodology used to obtain it.

The following presents the notable findings, limitations and applicability of this approach and also the main contributions of this study.

6.1. Notable Findings of Current Study

Some of the notable findings in this study are listed below:

- In this study it was confirmed that by checking equilibrium equations at virtual nodes on the surface of the specimen, damage region can be effectively identified. This finding was verified by comparing the results obtained using this non-destructive technique with the results obtained from sectioning and deplying of the damaged specimens.
- Due to the heterogeneous nature of fibre failure and also manufacturing process, inhomogeneous material behaviour at the local level was observed in this study. It was shown that this inhomogeneity results in inconsistent damage growth in the composite material leading to stress-strain responses that contain jumps. Jumps in the order of 2-3 mm in the damage length followed by slow-speed damage growth intervals was also observed as a result of this inhomogeneity.
- It was pointed out that when the size of the jumps in the damage length extensions become comparable to the size of the specimen, a smearing approach cannot be applied to simulate the damaging behaviour of the specimen since damage growth is no longer a self-similar event,. It can also be concluded that small specimen geometries should not be used to characterize the material damage properties.

- It was shown that in small specimens with sharp notches, only the damage initiation strain affects the global response of the specimen while in large notched specimens, only the fracture energy affects the global response. For other specimen geometries and sizes, other features of the strain-softening response play a role in determining the structural response.
- Under compressive loading, it was shown that the damage height broadens (band broadening) until it reaches its ultimate height at which point the two regions of the specimen on either side of the damage zone slip relative to each other. At this stage, no load can be transferred between the boundaries of the damage zone. In the process of forming these slip surfaces, two delaminated regions merge with an inclined kink band and matrix cracking region to reduce the material stiffness significantly.

6.2. Limitations and Applicability of Current Approach

As described in the previous chapters, the limitations and applicability of the proposed method can be summarized as follows:

- The proposed method can be applied to cases where the surface strains are equal to, or at least representing, the through-thickness strains. This is the case in plane strain and plane stress tests such as compact tension or compact compression.
- The methodology has been developed and validated for the Mode I failure. Although in theory it can also be utilized for Mode II failure, its applicability has not been validated in this study. The approximate estimation of the stress distribution inside the damage zone is based on the assumption that stresses in the damage zone can be obtained from stress distribution on the boundary of the damage zone. In tests such as OCT and CC where shear strain around the damage zone is negligible, this assumption can be justified. For the mixed Mode I/II failure, no approximate response can be obtained.

- As shown with the compression tests, any nonlinearity before the peak stress might not be detected using the current approach. Since the equilibrium condition is checked at each node, if the load drop due to damage growth doesn't exceed a certain threshold, then it will not be detected using the current approach. Consequently, a smaller damage length may be obtained.
- This method has been successfully applied for characterizing damage in notched composite laminates under tension and compression. Its capability has yet to be determined for other geometries and loading conditions.

6.3. Contributions

The notable contributions made by this study are listed below:

- A new methodology to identify directly the damage related parameters from full-field measurement of kinematic variables has been developed and successfully utilized in this study. This method has none of the main drawbacks associated with the current available approaches most notably the required a priori assumption for the shape of the strain-softening curve.
- Using the current approach, the stress and strain distributions in FPZ can be obtained while damage is propagating. This provides a great opportunity to observe the real softening behaviour of the material and characterize the material damage models accordingly. Using this approach, non-smooth softening response (jagged stress-strain curves with discontinuous slopes and sudden jumps) in composites due to heterogeneous fibre failure was observed. In this study, it was shown that a continuous trilinear strain-softening response is a sufficient representation of the inhomogeneous material damaging response and can effectively simulate the damaging behaviour of OCT and CC tests.
- The damage parameters and constitutive response of an IM7/8552 quasi-isotropic CFRP laminate has been obtained in this study under both compressive and tensile loading. These properties along with the size of the damaged area obtained

using the proposed method (and validated using destructive damage detection tests such as deplying and sectioning), provide a comprehensive set of data for simulating the inelastic damaging behaviour of this particular laminate.

References

- Abda, A.B., Ameer, H.B., Jaoua, M., (1999). "Identification of 2D cracks by elastic boundary measurements", *Inverse Problems*, vol. 15, pp. 67-77.
- ASTM D 3039/D 3039M-00, (2000). "Standard Test Method for Tensile Properties of Polymer Matrix Composite Materials", *ASTM International*.
- Avril, S., Ferrier, E., Vautrin, A., Hamelin, P., Surrel, Y., (2004). "A full-field optical method for the experimental analysis of reinforced concrete beams repaired with composites", *Composites Part A: Applied Science and Manufacturing*, vol. 35, pp. 873-884.
- Avril, S., Bonnet, M., Bretelle, A., Grediac, M., Hild, F., Ienny, P., Latourte, F., Lemosse, D., Pagano, S., Pagnacco, E., Pierron, F., (2008). "Overview of identification methods of mechanical parameters based on full-field measurements", *Exp. Mech.*, vol. 48, pp. 381-402.
- Bayldon, J., Bazant, Z.P., Daniel, I.M., Yu, Q. (2006). "Size effect on compressive strength of sandwich panels with fracture of woven laminate facesheet", *Transactions of the ASME. Journal of Engineering Materials and Technology*, vol. 128, pp. 169-174.
- Bazant, Z.P., Oh, B.H., (1983). "Crack Band Theory for Fracture of Concrete", *Materiaux Et Constructions*, vol. 16, pp. 155-177.
- Bazant, Z.P., Cedolin, L., (1991). "Stability of Structures: Elastic, Inelastic, Fracture and Damage Theories", Oxford University Press, New York.
- Bazant, Z.P. and Planas, J., (1998). "Fracture and Size Effect", CRC Press LLC.

-
- Chalal, H., Meraghni, F., Pierron, F., Grediac, M., (2004). "Direct identification of the damage behaviour of composite materials using the virtual fields method", *Composites Part A: Applied Science and Manufacturing*, vol. 35, pp. 841-848.
- Claire, D., Hild, F., Roux, S., (2007). "Identification of a damage law by using full-field displacement measurements", *Int. J. Damage Mech.*, vol. 16, pp. 179-197.
- Elices, M., Guinea, G.V., Gomez, J., Planas, J., (2002). "The cohesive zone model: Advantages, limitations and challenges", *Eng. Fract. Mech.*, vol. 69, pp. 137-163.
- Fleck, N.A., (1997). "Compressive failure of fibre composites", *Advances in Applied Mechanics*, Vol. 33, pp. 43-113.
- Floyd, A.M., (2004). "An engineering approach to the simulation of gross damage development in composites laminates", Ph.D. Thesis, Department of Civil Engineering, The University of British Columbia.
- Freeman, S.M., (1982). "Characterization of lamina and interlaminar damage in Graphite/Epoxy composites by the deply technique", *6th Conference of Composite Materials: Testing and Design*, pp. 50-62.
- Geymonat, G., Hild, F., Pagano, S., (2002). "Identification of elastic parameters by displacement field measurement", *Comptes Rendus Mecanique*, vol. 330(6), pp. 403-408.
- Geymonat, G., (2003). "Identification of mechanical properties by displacement field measurement: A variational approach", *Meccanica*, 38(5), pp. 535-545.
- Goldstein, J., Newbury, D.E., Echlin, P., Joy, D.C., Romig, A.D., Lyman, C.E., Fiori, C., Lifshin, E., (1992). "Scanning Electron Microscopy and X-Ray Microanalysis: A Text for Biologists, Materials Scientists, and Geologists", Springer.
- Grediac, M., Pierron, F., Avril, S., Toussaint, E., (2006). "The virtual fields method for extracting constitutive parameters from full-field measurements: A review", *Strain*, vol. 42, pp. 233-253.

Herman, G.T., (2009). “Fundamentals of Computerized Tomography: Image Reconstruction from Projections”, Springer.

Hexcel Composites Ltd, www.hexel.com

Ilcewicz, L.B., Walker, T.H., Murphy, D.P., Dopker, B., Cairns, D.S., Poe, C.C. Jr., (1993). “Tension Fracture of Laminates for Transport Fuselage - Part IV: Damage Tolerance Analysis”, *Fourth NASA/DoD Advanced Technology Conference*, NASA CP 3229, pp. 254-298.

Jirasek, M., Patzak, B., (2002). “Consistent tangent stiffness for nonlocal damage models”, *Computers and Structures*, vol. 80, pp. 1279-1293.

Kongshavn, I., Poursartip, A., (1999). “Experimental investigation of a strain-softening approach to predicting failure in notched fibre-reinforced composite laminates”, *Compos. Sci. Technol.*, vol. 59, pp. 29-40.

Latourte, F., Chrysochoos, A., Pagano, S., Wattrisse, B., (2008). “Elastoplastic behavior identification for heterogeneous loadings and materials”, *Experimental Mechanics*, vol. 48, pp. 435-449.

LaVision, (2007). “Davis Manual-LaVision StrainMaster Brochure”, www.lavision.de

Le Magorou., L. Bos, F. Rouger, F., (2002). “Identification of constitutive laws for wood-based panels by means of an inverse method”, *Composites science and technology*, 62(4), pp. 591-596.

Maimi, P., Camanho, P.P., Mayugo, J.A., Davila, C.G., (2007a). “A continuum damage model for composite laminates: Part I - Constitutive model”, *Mechanics of Materials*, vol. 39, pp. 897-908.

Maimi, P., Camanho, P.P., Mayugo, J.A., Davila, C.G., (2007b). “A continuum damage model for composite laminates: Part II - Computational implementation and validation”, *Mechanics of Materials*, vol. 39, pp. 909-919.

- McClennan, S.A., (2004). "Crack growth and damage modeling of fibre reinforced polymer composites", MSc. Thesis, Department of Materials Engineering, The University of British Columbia.
- McGregor, C., (2005). "Simulation of progressive damage development in braided composite tubes under axial compression", MSc. Thesis, Department of Civil Engineering, University of British Columbia, Vancouver.
- McGregor, C., Poursartip, A., Vaziri, R., (2005). "Over-height compact tension testing of IM7/8552 carbon fibre/epoxy material", Internal Report, The University of British Columbia.
- McGregor, C., Vaziri, R., Poursartip, A., (2007). "Investigation into the tensile behaviour of notched braided laminates: Experimental and numerical, report submitted to general motors corporation", The University of British Columbia, Vancouver, Canada, Tech. Rep. NSERC CRD File No: CRCPJ306287-04.
- McGregor, C., Zobeiry, N., Vaziri, R., Poursartip, A., (2008). "A Constitutive Model for Progressive Compressive Failure of Composites", *Journal of Composite Materials*, Vol. 42(25), pp. 2687-2716.
- Meuwissen, M.H.H., Oomens, C.W.J., Baaijens, F.P.T., Petterson, R., Janssen, J.D., (1998). "Determination of the elasto-plastic properties of aluminum using a mixed numerical-experimental method", *Journal of Materials Processing Technology*, vol. 75, pp. 204 -211.
- Mitchell, J. (2002). "Notched Behaviour of Stitched and Unstitched RFI CFRP Laminates", MSc. Thesis, Department of Materials Engineering, University of British Columbia, Vancouver.
- Mollenhauer, D., Iarve, E.V., Kim, R., Langley, B., (2006). "Examination of ply cracking in composite laminates with open holes: A moire interferometric and numerical study", *Composites Part A: Applied Science and Manufacturing*, vol. 37, pp. 282-294.

- Moran, P.M., Liu, X.H., Shih, C.F., (1995). “Kink band formation and band broadening in fibre composites under compressive loading”, *Acta Metallurgica et Materialia*, Vol. 43, No. 8, pp. 2943-2958.
- Pierron, F., Green, B., Wisnom, M. R., (2007a). “Full-field assessment of the damage process of laminated composite open-hole tensile specimens. Part I: Methodology”, *Composites Part A: Applied Science and Manufacturing*, vol. 38, pp. 2307-2320.
- Pierron, F., Green, B., Wisnom, M. R., Hallett, S. R., (2007b). “Full-field assessment of the damage process of laminated composite open-hole tensile specimens. Part II: Experimental results”, *Composites Part A: Applied Science and Manufacturing*, vol. 38, pp. 2321-2332, 2007.
- Pinho, S.T. (2005). “Modelling failure of laminated composites using physically-based failure models”, PhD Thesis, Department of Aeronautics, Imperial College, London.
- Pinho, S.T., Robinson, P., Iannucci, L., (2006). “Fracture toughness of the tensile and compressive fibre failure modes in laminated composites”, *Composites science and technology*, vol. 66, pp. 2069-2079.
- Planas, J., Guinea, G.V., Elices, M., (1999). “Size effect and inverse analysis in concrete fracture”, *International Journal of Fracture*, vol. 95, pp. 367-378.
- Ratcliffe, J., Jackson, W., Schaff, J., (2004). “Compression strength prediction of impact-damaged composite sandwich panels”, in *60th Annual Forum Proceedings - American Helicopter Society*, pp. 656-672.
- Sivashanker, S., Fleck, N.A., Sutcliffe, M.P.F., (1996). “Microbuckle propagation in a unidirectional carbon fibre-epoxy matrix composite”, *Acta Materialia*, Vol. 44, No. 7, pp. 2581-2590.

- Sivashanker, S., (1998). "Damage growth in carbon fibre-PEEK unidirectional composites under compression", Proceedings of the 1997 Symposium on Integrated Experimental-Computational Modeling of Advanced Materials, McNu'97, Vol. A249, No. 1-2, pp. 259-276.
- Sivashanker, S., (2001). "Damage propagation in multidirectional composites subjected to compressive loading", Metallurgical and Materials Transactions A: Physical Metallurgy and Materials Science Physical Metallurgy and Materials Science, Vol. 32, No. 1, pp. 171-182.
- Sivashanker, S., Bag, A., (2001). "Kink-band propagation in a multidirectional carbon fibre-polymer composite", Metallurgical and Materials Transactions A: Physical Metallurgy and Materials Science Physical, Vol. 32, No. 12, pp. 3157-3160.
- Soutis, C., Curtis, P.T., Fleck, N.A., (1993). "Compressive failure of notched carbon-fibre composites", Proceedings of the Royal Society of London, Series A: Mathematical, Physical and Engineering Sciences, Vol. 440, No. 1909, pp. 241-256.
- Soutis, C., Lee, J., Kong, C., (2002). "Size effect on compressive strength of T300/924C carbon fibre-epoxy laminates", *Plastics, Rubber and Composites*, Vol. 31, No. 8, pp. 364-370.
- Walker, T.H., Avery, W.B., Ilcewicz, L.I., Poe, C.C. Jr., Harris, C.E., (1991). "Tension Fracture of Laminates for Transport Fuselage - Part I: Material Screening", *Second NASA Advanced Technology Conference*, NASA CP 3154, pp. 197-238.
- Walker, T.H., Ilcewicz, L.B., Polland, D.R., Poe, C.C. Jr., (1992). "Tension Fracture of Laminates for Transport Fuselage - Part II: Large Notches", *Third NASA Advanced Technology Conference*, NASA CP 3178, pp. 727-758.
- Walker, T.H., Ilcewicz, L.B., Polland, D.R., Bodine, J.B, Poe, C.C. Jr., (1993). "Tension Fracture of Laminates for Transport Fuselage - Part III: Structural

- Configurations”, *Fourth NASA Advanced Technology Conference*, NASA CP 3229, pp. 243-264.
- Walker, T.H., Schloz, D., Flynn, B., Dopler, B, Bodine, J., Ilcewicz, L., Rouse, M., McGowan, D., Poe, C.C. Jr., (1996). “Damage Tolerance of Composite Fuselage Structure”, *Sixth NSAS/DOD/ARPA Advanced Composite Technology Conference*, NASA CP-3326.
- Williams, K.V., (1998). “A physically-based continuum damage mechanics model for numerical prediction of damage growth”, MAsc. Thesis, Department of Materials Engineering, University of British Columbia, Vancouver.
- Williams, K.V., Vaziri, R., Poursartip, A., (2003). “A physically based continuum damage mechanics model for thin laminated composite structures”, *Int. J. Solids Structures*, vol. 40, pp. 2267-300, 05.
- Zobeiry, N., (2004). “Progressive damage modelling of composite materials under compressive loads”, MAsc. Thesis, Department of Civil Engineering, University of British Columbia, Vancouver.
- Zobeiry, N., Forghani, A., McGregor, C., Vaziri, R., Poursartip, A., (2008). “Progressive damage modeling of composite materials under both tensile and compressive loading regimes”, *Mechanical Response of Composite*, Springer, vol. 10, pp. 179-195.

Appendix A: CrackPro Code

A.1. Step I: Importing

```
Public Sub Import()  
  
    Dim FName As Variant  
    Dim Sep As String  
    Dim i As Integer  
  
    On Error GoTo ErrHandler  
    File = 0  
    Sheets("Start").Select  
  
    FName = Application.GetOpenFilename(("Dat Files (*.dat)  
    ,*.dat"), MultiSelect:=True)  
  
    If IsArray(FName) Then  
        For i = LBound(FName) To UBound(FName)  
            File = File + 1  
            ImportFile CStr(FName(i))  
        Next i  
    End If  
  
    LogBox ("Data from " & File & " files was imported.")  
    Exit Sub  
  
    ErrHandler:  
        LogBox ("Error #" & Err.Number & Err.Description)  
        Err.Clear  
End Sub
```

```
Public Sub ImportFile(FName As String)
```

```
    Dim Column As Integer  
    Dim Row As Integer  
    Dim WholeLine As String
```

```
    Column = 1  
    Row = 1
```

'Writing Image # into Start Sheet

```
Cells(4 + File, 9).Value = Mid(FName, InStrRev(FName, "B0")
+ 2, InStr(FName, ".dat") - InStrRev(FName, "B0") - 2)
```

'Writing Headers in Raw Data Sheet

```
Sheets("Raw Data").Cells(1, File * 2 + 1).Value =
    "Vx_" & Cells(4 + File, 9).Value
Sheets("Raw Data").Cells(1, File * 2 + 2).Value =
    "Vy_" & Cells(4 + File, 9).Value
```

'Opening Files

```
Open FName For Input Access Read As #1
While Not EOF(1)
    Line Input #1, WholeLine
```

'Write # of Xpoints and Ypoints

```
If File = 1 And Row = 3 Then
    TempArr = Split(WholeLine, "I=")
    TempArr1 = Split(TempArr(1), ", J=")
    Cells(5, 6).Value = TempArr1(0)
    Cells(6, 6).Value = TempArr1(1)
End If
```

'Write Data into Raw Data Sheet

```
If Row > 3 Then
    LineArr = Split(WholeLine, " ")
    If File = 1 Then
        Sheets("Raw Data").Cells(Row - 2, 1).Value = LineArr(0)
        Sheets("Raw Data").Cells(Row - 2, 2).Value = LineArr(1)
    End If
    Sheets("Raw Data").Cells(Row - 2, File * 2 + 1).Value =
        LineArr(2)
    Sheets("Raw Data").Cells(Row - 2, File * 2 + 2).Value =
        LineArr(3)
End If
```

```
Row = Row + 1
```

'Writing Length of Elements and # of Files

```
Cells(7, 6).Value = Abs(Sheets("Raw Data").Cells(2, 1).Value
    - Sheets("Raw Data").Cells(3, 1).Value)
L = Cells(7, 6).Value
Cells(8, 6).Value = File
```

```
Wend
Close #1
```

```
End Sub
```

A.2. Step I: Assembling

Sub Numbering()

```
Dim i As Integer
Dim j As Integer
Dim k As Integer
Dim FE As Integer
```

```
FE = 40
Sheets("Start").Select
k = 0
```

'Node Numbering

```
For i = 2 To Cells(12, 6).Value - Cells(11, 6).Value + 2
    For j = 1 To Cells(10, 6).Value - Cells(9, 6).Value + 1
        k = k + 1
        Sheets("Numbering").Cells(k + 1, 1).Value = k
        Sheets("Numbering").Cells(k + 1, 2).Value = i
        Sheets("Numbering").Cells(k + 1, 3).Value = j
    Next j
Next i
```

'Element Numbering

```
For j = 1 To Ynumber - 1
    k = (j - 1) * (Xnumber - 1)
    For i = 1 To Xnumber - 1
        Sheets("Numbering").Cells(i + k + 1, 5).Value = i + k
        Sheets("Numbering").Cells(i + k + 1, 6).Value =
            Xnumber + i + (j - 1) * (Xnumber)
        Sheets("Numbering").Cells(i + k + 1, 7).Value =
            Xnumber + i + (j - 1) * (Xnumber) + 1
        Sheets("Numbering").Cells(i + k + 1, 8).Value =
            i + (j - 1) * (Xnumber) + 1
        Sheets("Numbering").Cells(i + k + 1, 9).Value =
            i + (j - 1) * (Xnumber)
    Next i
Next j
```

```
LogBox ("Mesh was generated.")
End Sub
```

A.3. Step I: Pre-processing

Sub Calculate()

```

Dim Ly As Integer
Dim i, j, k As Integer
Dim k1, k2 As Integer
Dim n1, n2, n3, n4, n0, n1x, n2x, n3x, n4x, n1y, n2y, n3y, n4y As Integer
Dim forceE As Integer
Dim KMat(1 To 8, 1 To 8) As Variant
Dim UMat(1 To 8) As Variant
Dim BMat(1 To 3, 1 To 8) As Variant
Dim DMat(1 To 3, 1 To 3) As Variant
Dim strain(1 To 3) As Variant
Dim force(1 To 8) As Variant
Dim temp, tempx, tempy As Variant
Dim tempS(1 To 3) As Variant
Dim TempF(1 To 3) As Variant
Dim Eff, EP1, EP2, EP3 As Variant

```

' Creating U Matrices

For j = 1 To File

```

Ly = (2 + (Cells(12, 6).Value - Cells(11, 6).Value)) * (j - 1) + 1
Sheets("U").Cells(1, j).Value = "U_" & Cells(4 + j, 9).Value
For i = 1 To ELEMnumber

```

' Reading node numbers and coordinates

```

n1 = Sheets("Numbering").Cells(i + 1, 6).Value
n2 = Sheets("Numbering").Cells(i + 1, 7).Value
n3 = Sheets("Numbering").Cells(i + 1, 8).Value
n4 = Sheets("Numbering").Cells(i + 1, 9).Value
n1x = Sheets("Numbering").Cells(n1 + 1, 2).Value + (Ly - 1)
n2x = Sheets("Numbering").Cells(n2 + 1, 2).Value + (Ly - 1)
n3x = Sheets("Numbering").Cells(n3 + 1, 2).Value + (Ly - 1)
n4x = Sheets("Numbering").Cells(n4 + 1, 2).Value + (Ly - 1)
n1y = Sheets("Numbering").Cells(n1 + 1, 3).Value
n2y = Sheets("Numbering").Cells(n2 + 1, 3).Value
n3y = Sheets("Numbering").Cells(n3 + 1, 3).Value
n4y = Sheets("Numbering").Cells(n4 + 1, 3).Value

```

' U Matrix

```

Sheets("U").Cells(8 * (i - 1) + 1 + 1, j).Value =
    Sheets("Vx").Cells(n1x, n1y).Value
Sheets("U").Cells(8 * (i - 1) + 2 + 1, j).Value =
    Sheets("Vy").Cells(n1x, n1y).Value

```

```

Sheets("U").Cells(8 * (i - 1) + 3 + 1, j).Value =
    Sheets("Vx").Cells(n2x, n2y).Value
Sheets("U").Cells(8 * (i - 1) + 4 + 1, j).Value =
    Sheets("Vy").Cells(n2x, n2y).Value
Sheets("U").Cells(8 * (i - 1) + 5 + 1, j).Value =
    Sheets("Vx").Cells(n3x, n3y).Value
Sheets("U").Cells(8 * (i - 1) + 6 + 1, j).Value =
    Sheets("Vy").Cells(n3x, n3y).Value
Sheets("U").Cells(8 * (i - 1) + 7 + 1, j).Value =
    Sheets("Vx").Cells(n4x, n4y).Value
Sheets("U").Cells(8 * (i - 1) + 8 + 1, j).Value =
    Sheets("Vy").Cells(n4x, n4y).Value
Next i
Next j
LogBox ("U matrices were created.")

'Reading K, B and D Matrices: Element stiffness, strain-disp. & material stiffness
For i = 1 To 8
    For j = 1 To 8
        KMat(i, j) = Sheets("Calculation").Cells(47 + i, 2 + j).Value
    Next j
Next i
For i = 1 To 3
    For j = 1 To 8
        BMat(i, j) = Sheets("Calculation").Cells(1 + i, 2 + j).Value
    Next j
Next i
For i = 1 To 3
    For j = 1 To 3
        DMat(i, j) = Sheets("Calculation").Cells(7 + i, 2 + j).Value
    Next j
Next i

'Calculating strains, nodal forces & stresses based on elastic properties
For k = 1 To File
    For i = 1 To ELEMnumber
        For j = 1 To 8
            UMat(j) = Sheets("U").Cells(8 * (i - 1) + j + 1, k).Value
        Next j
        For j = 1 To 8
            temp = 0
            For k1 = 1 To 8
                temp = temp + KMat(j, k1) * UMat(k1)
            Next k1
            Sheets("Force").Cells(8 * (i - 1) + j + 1, k).Value = temp
        Next j
    Next i

```

'Calculating strains

```

n1 = Sheets("Numbering").Cells(i + 1, 6).Value
n1x = Sheets("Numbering").Cells(n1 + 1, 2).Value + (Ly - 1) - 1
n1y = Sheets("Numbering").Cells(n1 + 1, 3).Value
For j = 1 To 3
For k1 = 1 To 8
    temp = temp + BMat(j, k1) * UMat(k1)
Next k1
Sheets("Strain").Cells(3 * (i - 1) + j + 1, k).Value = temp
If j = 1 Then
    Sheets("StrainX").Cells(n1x, n1y).Value = temp
End If
    If j = 2 Then
        Sheets("StrainY").Cells(n1x, n1y).Value = temp
    End If
If j = 3 Then
    Sheets("StrainXY").Cells(n1x, n1y).Value = temp
End If
tempS(j) = temp
Next j

```

'Calculating stresses

```

For j = 1 To 3
TempF(j) = 0
For k1 = 1 To 3
    TempF(j) = TempF(j) + tempS(k1) * DMat(j, k1)
Next k1
Sheets("Stress").Cells(3 * (i - 1) + j + 1, k).Value =
TempF(j)
If j = 1 Then
    Sheets("StressX").Cells(n1x, n1y).Value = TempF(j)
    End If
If j = 2 Then
    Sheets("StressY").Cells(n1x, n1y).Value = TempF(j)
    End If
    If j = 3 Then
        Sheets("StressXY").Cells(n1x, n1y).Value = TempF(j)
    End If
Next j
Next i
Next k
LogBox ("Nodal forces and strains were calculated.")

```

Calculating principal strains

```

For k = 1 To File
  Ly = (2 + (Cells(12, 6).Value - Cells(11, 6).Value)) * (k - 1) + 1
  For i = 1 To Ynumber - 1
    For j = 1 To Xnumber - 1
      tempx = Sheets("StrainX").Cells(Ly + i, j).Value
      tempy = Sheets("StrainY").Cells(Ly + i, j).Value
      temp = Sheets("StrainXY").Cells(Ly + i, j).Value
      EP1 = (tempx + tempy) / 2 +
            ((tempx / 2 - tempy / 2) ^ 2 + temp ^ 2) ^ 0.5
      EP2 = (tempx + tempy) / 2 -
            ((tempx / 2 - tempy / 2) ^ 2 + temp ^ 2) ^ 0.5
      If Abs(EP1) > Abs(EP2) Then
        Sheets("StrainMax").Cells(Ly + i, j).Value = EP1
      Else
        Sheets("StrainMax").Cells(Ly + i, j).Value = EP2
      End If
    Next j
  Next i
Next k
LogBox ("Principal strains were calculated.")

```

Calculating effective strains

```

For k = 1 To File
  Ly = (2 + (Cells(12, 6).Value - Cells(11, 6).Value)) * (k - 1) + 1
  For i = 1 To Ynumber - 1
    For j = 1 To Xnumber - 1
      tempx = Sheets("StrainX").Cells(Ly + i, j).Value
      tempy = Sheets("StrainY").Cells(Ly + i, j).Value
      temp = Sheets("StrainXY").Cells(Ly + i, j).Value
      Eff = (EFF1 * tempx ^ 2 +
            EFF2 * tempy ^ 2 + EFF3 * temp ^ 2) ^ 0.5
      Sheets("StrainEff").Cells(Ly + i, j).Value = Eff
    Next j
  Next i
Next k
LogBox ("Effective strains were calculated.")

```

Checking nodal equilibrium forces

```

For k = 1 To File
  Ly = (2 + (Cells(12, 6).Value - Cells(11, 6).Value)) * (k - 1) + 1
  For i = 2 To (Xnumber - 2) * (Ynumber - 2) + 1
    Node information
    n0 = Sheets("Numbering").Cells(i, 11).Value
    n1x = Sheets("Numbering").Cells(n0 + 1, 2).Value + (Ly - 1)
    n1y = Sheets("Numbering").Cells(n0 + 1, 3).Value

```

```

'Elements Attached to this node
n1 = Sheets("Numbering").Cells(i, 12).Value
n2 = Sheets("Numbering").Cells(i, 13).Value
n3 = Sheets("Numbering").Cells(i, 14).Value
n4 = Sheets("Numbering").Cells(i, 15).Value
'Equilibrium
tempx = Sheets("Force").Cells(8 * (n1 - 1) + 1 + 1, k).Value +
        Sheets("Force").Cells(8 * (n2 - 1) + 3 + 1, k).Value
tempx = Sheets("Force").Cells(8 * (n3 - 1) + 5 + 1, k).Value +
        Sheets("Force").Cells(8 * (n4 - 1) + 7 + 1, k).Value +tempx
tempy = Sheets("Force").Cells(8 * (n1 - 1) + 2 + 1, k).Value +
        Sheets("Force").Cells(8 * (n2 - 1) + 4 + 1, k).Value
tempy = Sheets("Force").Cells(8 * (n3 - 1) + 6 + 1, k).Value +
        Sheets("Force").Cells(8 * (n4 - 1) + 8 + 1, k).Value+tempy
tempx = Abs(tempx) / 1000
tempy = Abs(tempy) / 1000
Sheets("dFx").Cells(n1x, n1y).Value = tempx
Sheets("dFy").Cells(n1x, n1y).Value = tempy
        Next i
    Next k
    LogBox ("Equilibrium was checked.")

End Sub

```

A.4. Step I: Damage Detection

Sub CommCen()

'Detecting damaged elements

```

For k = 1 To File
    Ly = (2 + (Cells(12, 6).Value - Cells(11, 6).Value)) * (k - 1) + 1
    For i = 2 To Ynumber - 1
        For j = 2 To Xnumber - 1
            Sheets("Charts Data").Cells(nam + i - 1, 1 + j - 1).Value = 1
            Sheets("Charts Data").Cells(nam + i - 1, 1 + j).Value = 1
            Sheets("Charts Data").Cells(nam + i, 1 + j - 1).Value = 1
            Sheets("Charts Data").Cells(nam + i, 1 + j).Value = 1
            If Sheets("dFy").Cells(Ly + i, j).Value < r Then
                Sheets("Charts Data").Cells(nam + i - 1, 1 + j - 1).Value = 0
                Sheets("Charts Data").Cells(nam + i - 1, 1 + j).Value = 0
                Sheets("Charts Data").Cells(nam + i, 1 + j - 1).Value = 0
                Sheets("Charts Data").Cells(nam + i, 1 + j).Value = 0
            End If
        Next j
    Next i
    For i = 1 To Ynumber - 1
        For j = 1 To Xnumber - 1
            Sheets("dFy01").Cells(Ly + i, j).Value =
                Sheets("Charts Data").Cells(nam + i, 1 + j).Value
        Next j
    Next i
Next k

```

'Finding Ei for each image

```

For j = 1 To File
    LyN = (2 + (Cells(12, 6).Value - Cells(11, 6).Value)) * (j - 1) + 1

```

'Check boundary elements

```

For i = 1 To Ynumber - 1
    For jj = 1 To Xnumber - 1

```

'number of undamaged elements

```

k = 0

```

'number of damaged elements

```

L = 0
If Sheets("Crack").Cells(nam + i, 1 + jj).Value = 1 Then
    temp = Sheets("Crack").Cells(nam + i, 1 + jj - 1).Value

```

```

    If temp = 1 Then
        L = L + 1
    ElseIf temp <> "" Then
        k = k + 1
    End If

    temp = Sheets("Crack").Cells(nam + i, 1 + j jj + 1).Value
    If temp = 1 Then
        L = L + 1
    ElseIf temp <> "" Then
        k = k + 1
    End If
End If

'Writing boundary crack elements
If k > 1 And L > 2 Then
    temp = Sheets(CrackStrain).Cells(Ly + i, jj).Value
    Sheets("Crack").Cells(nam + i + 20, 1 + jj).Value = temp
    If temp < r2 And temp > r1 Then
        jj = jj + 1
    If Sheets("P-d").Cells(3, 3).Value < 0 Then
        Sheets("Crack").Cells(jj + 3, 1 + (File - 1) * 2 + 4).Value =
            -Abs(temp)

        tempAv = tempAv - Abs(temp)
    Else
        Sheets("Crack").Cells(jj + 3, 1 + (File - 1) * 2 + 4).Value =
            Abs(temp)

        tempAv = tempAv + Abs(temp)
    End If
    End If
    End If

Next jj
Next i
tempAv = tempAv / jj
Sheets("Crack").Cells(3, 1 + (File - 1) * 2 + 4).Value = tempAv
Sheets("Crack").Cells(File, 2).Value = tempAv
Sheets("Crack").Cells(File, 1).Value = jj
tempE = tempE + Sheets("Crack").Cells(j, 2).Value
Next j

'Finding Average Ei
tempE = Round(tempE / File, 4)
Sheets("Start").Cells(21, 3).Value = tempE
argument = argument & ", Ei=" & tempE
Sheets("Crack").Cells(File + 1, 2).Value = tempE
Sheets("Crack").Cells(File + 1, 1).Value = "Average"

```

```
Ei = Sheets("Start").Cells(21, 3).Value  
LogBox ("Damage initiation strain, Ei = " & tempE)  
End Sub
```

A.5. Step I: Response Construction

Sub Profile()

```
Dim image As String
Dim Stress As String
Dim Ly As Integer
Dim Cx, Cy As Variant
Dim i, j, k, r, b, n1, n2, n3, n4, n1x, n2x, n3x, n4x, n1y, n2y, n3y, n4y As Integer
Dim Sheet1, Sheet2, arg1, arg2 As String
Dim Sheet2 As String
Dim temp, temp1, temp2, temp5 As Integer
Dim temp3, temp4 As Variant
```

```
'On Error GoTo ErrHandler
```

```
Application.ScreenUpdating = False
Application.DisplayAlerts = False
```

```
Sheet1 = "StressY"
Sheet2 = "StrainY"
cArr = Split(command.ComboBox5.Value, " ")
```

```
If cArr(0) = 2 Then
    Sheet2 = "dFy01"
    Ei = 0.5
End If
```

```
Sheets("Start").Select
'calculating origin coordinates
Cx = Sheets("Raw Data").Cells(1 + Cells(5, 6).Value * (Cells(11, 6) - 1) +
    Cells(9, 6).Value, 1).Value
Cy = Sheets("Raw Data").Cells(1 + Cells(5, 6).Value * (Cells(11, 6) - 1) +
    Cells(9, 6).Value, 2).Value
```

```
'Color code the damaged area
```

```
Sheets("StressProfile").Select
For k = 1 To File
    Ly = (2 + (Sheets("Start").Cells(12, 6).Value -
        Sheets("Start").Cells(11, 6).Value)) * (k - 1) + 1
    For i = 1 To Ynumber - 1
    For j = 1 To Xnumber - 1
        If Abs(Sheets(Sheet2).Cells(Ly + i, j).Value) > Abs(Ei) Then
            Cells(Ly + i, j).Value = j + (i - 1) * (Xnumber - 1)
            Cells(Ly + i, j).Interior.ColorIndex = 6
```

```

Else
    Cells(Ly + i, j).Value = Sheets(Sheet1).Cells(Ly + i, j).Value
End If
Next j
Next i
Next k

```

'Identify elements on the damage boundary

```

For k = 1 To File
    Ly = (2 + (Sheets("Start").Cells(12, 6).Value -
                Sheets("Start").Cells(11, 6).Value)) * (k - 1) + 1
    For j = 1 To Xnumber - 1
        temp1 = 0
        temp2 = 0
        For i = 2 To Ynumber - 2
            If Cells(Ly + i, j).Interior.ColorIndex = 6 Then
                If temp1 = 0 Then
                    temp1 = i
                End If
                temp2 = i
            End If
        Next i
        If temp1 = 0 And temp2 = 0 Then
            temp1 = Cells(k * 3 - 2, 3 * Xnumber + 5 + j - 1).Value
        End If
        Cells(k * 3 - 2, 3 * Xnumber + 5 + j).Value = temp1
        Cells(k * 3 - 1, 3 * Xnumber + 5 + j).Value = temp2
    Next j
Next k

```

'Stress-Strain curve Construction

```

For j = 1 To Xnumber - 1
    For k = 1 To File
        Ly = (2 + (Sheets("Start").Cells(12, 6).Value -
                    Sheets("Start").Cells(11, 6).Value)) * (k - 1) + 1
        temp1 = Cells(k * 3 - 2, 3 * Xnumber + 5 + j).Value
        temp2 = Cells(k * 3 - 1, 3 * Xnumber + 5 + j).Value
    
```

'Reading node and element numbers

```

If temp2 <> 0 Then
    n1 = Sheets("Numbering").
        Cells(Cells(Ly + temp2, j).Value + 1, 6).Value
    n2 = Sheets("Numbering").
        Cells(Cells(Ly + temp2, j).Value + 1, 7).Value
    n3 = Sheets("Numbering").
        Cells(Cells(Ly + temp1, j).Value + 1, 8).Value

```

```

        n4 = Sheets("Numbering").
            Cells(Cells(Ly + temp1, j).Value + 1, 9).Value
        n1x = Sheets("Numbering").Cells(n1 + 1, 2).Value + (Ly - 1)
        n2x = Sheets("Numbering").Cells(n2 + 1, 2).Value + (Ly - 1)
        n3x = Sheets("Numbering").Cells(n3 + 1, 2).Value + (Ly - 1)
        n4x = Sheets("Numbering").Cells(n4 + 1, 2).Value + (Ly - 1)
        n1y = Sheets("Numbering").Cells(n1 + 1, 3).Value
        n2y = Sheets("Numbering").Cells(n2 + 1, 3).Value
        n3y = Sheets("Numbering").Cells(n3 + 1, 3).Value
        n4y = Sheets("Numbering").Cells(n4 + 1, 3).Value
        temp3 = Sheets("Vy").Cells(n3x, n3y).Value +
            Sheets("Vy").Cells(n4x, n4y).Value
        temp4 = Sheets("Vy").Cells(n1x, n1y).Value +
            Sheets("Vy").Cells(n2x, n2y).Value
        Cells(k, Xnumber + 1 + j * 2).Value =
            (temp3 - temp4) / (2 * L * (temp2 - temp1 + 1))
        Cells(k, Xnumber + 2 + j * 2).Value = (Cells(Ly + temp1 - 1, j)
            Value + Cells(Ly + temp2 + 1, j).Value) / 2
    Else
        Cells(k, Xnumber + 1 + j * 2).Value =
            Sheets("StrainY").Cells(Ly + temp1, j).Value
        Cells(k, Xnumber + 2 + j * 2).Value = Cells(Ly + temp1, j).Value
    End If
Next k
Next j

Application.ScreenUpdating = True
Application.DisplayAlerts = True

Exit Sub

ErrorHandler:
    MsgBox ("Error #" & Err.Number & Err.Description)
    Err.Clear

End Sub

```

A.6. Step II: Optimization

Sub Multi_Linear()

'Reading Input Variables

```
Height = Sheets("Start").Range("C5").Value
Ex = Sheets("Start").Range("C6").Value
Ey = Sheets("Start").Range("C7").Value
Gxy = Sheets("Start").Range("C8").Value
vxy = Sheets("Start").Range("C9").Value
vyx = Sheets("Start").Range("C10").Value
L = Sheets("Start").Range("F7").Value
File = Sheets("Start").Range("F8").Value
Err_energy = Sheets("Start").Range("G22").Value
Err_force = Sheets("Start").Range("G20").Value
ELEMnumber = (Xnumber - 1) * (Ynumber - 1)
NODEnumber = Xnumber * Ynumber
```

'Main Loop

```
For h = 2 To Inum + 1
    Gf_Total = 0
    Gf_Total_error = 0
    Ei = Cells(h, 4).Value
    Si = Cells(h, 5).Value
    E_1 = Cells(h, 6).Value
    S_1 = Cells(h, 7).Value
    E_2 = Cells(h, 8).Value
    S_2 = Cells(h, 9).Value
    E_3 = Cells(h, 10).Value
    S_3 = Cells(h, 11).Value
    Ey1 = Cells(h, 12).Value
    Ey2 = Cells(h, 13).Value
    Ey3 = Cells(h, 14).Value
    EE = Ey1 + Ey2 + Ey3
```

'Evaluating Reduction Factors, Rx and Ry

```
For k = 1 To File
    m = 0
    For i = 1 To Ynumber - 1
        For j = 1 To Xnumber - 1
            m = 1 + m
            temp = Sheets("StrainY").Cells(Ly + i, j).Value
            Ry = 1
```

```

        'Linear Softening Curve, Ry
    If Lnum = 1 Then
    If Abs(temp) > E_1 Then
        Ry = 0
    End If
    If Abs(temp) > Ei And Abs(temp) < E_1 Then
        Ry = (Ei / (E_1 - Ei)) * (E_1 - Abs(temp)) / Abs(temp)
    End If
    End If
        'Bi-Linear Softening Curve, Ry
    If Lnum = 2 Then
    If Abs(temp) > E_2 Then
        Ry = 0
    End If
    If Abs(temp) > E_1 And Abs(temp) < E_2 Then
        Ry = Ey2 / EE * (E_1 / (E_2 - E_1)) *
            (E_2 - Abs(temp)) / Abs(temp)
    End If
    If Abs(temp) > Ei And Abs(temp) < E_1 Then
        Ry = Ey2 / EE + Ey1 / EE *
            (Ei / (E_1 - Ei)) * (E_1 - Abs(temp)) / Abs(temp)
    End If
    End If
        'Tri-Linear Softening Curve, Ry
    If Lnum = 3 Then
    If Abs(temp) > E_3 Then
        Ry = 0
    End If
    If Abs(temp) > E_2 And Abs(temp) < E_3 Then
        Ry = Ey3 / EE * (E_2 / (E_3 - E_2)) *
            (E_3 - Abs(temp)) / Abs(temp)
    End If
    If Abs(temp) > E_1 And Abs(temp) < E_2 Then
        Ry = Ey3 / EE + Ey2 / EE * (E_1 / (E_2 - E_1)) *
            (E_2 - Abs(temp)) / Abs(temp)
    End If
    If Abs(temp) > Ei And Abs(temp) < E_1 Then
        Ry = Ey3 / EE + Ey2 / EE + Ey1 / EE *
            (Ei / (E_1 - Ei)) * (E_1 - Abs(temp)) / Abs(temp)
    End If
    End If
    Sheets("Ry").Cells(Ly + i, j).Value = Ry
    Sheets("Ry").Cells(m + 1, Xnumber + 5 + k).Value = Ry

```

```

temp = Sheets("StrainX").Cells(Ly + i, j).Value
Rx = 1
'Linear Softening Curve, Rx
If Lnum = 1 Then
If Abs(temp) > E_1 Then
Rx = 0
End If
If Abs(temp) > Ei And Abs(temp) < E_1 Then
Rx = (Ei / (E_1 - Ei)) * (E_1 - Abs(temp)) / Abs(temp)
End If
End If
'Bi-Linear Softening Curve, Rx
If Lnum = 2 Then
If Abs(temp) > E_2 Then
Rx = 0
End If
If Abs(temp) > E_1 And Abs(temp) < E_2 Then
Rx = Ey2 / EE * (E_1 / (E_2 - E_1)) *
(E_2 - Abs(temp)) / Abs(temp)
End If
If Abs(temp) > Ei And Abs(temp) < E_1 Then
Rx = Ey2 / EE + Ey1 / EE * (Ei / (E_1 - Ei)) *
(E_1 - Abs(temp)) / Abs(temp)
End If
End If
'Tri-Linear Softening Curve, Rx
If Lnum = 3 Then
If Abs(temp) > E_3 Then
Rx = 0
End If
If Abs(temp) > E_2 And Abs(temp) < E_3 Then
Rx = Ey3 / EE * (E_2 / (E_3 - E_2)) *
(E_3 - Abs(temp)) / Abs(temp)
End If
If Abs(temp) > E_1 And Abs(temp) < E_2 Then
Rx = Ey3 / EE + Ey2 / EE * (E_1 / (E_2 - E_1)) *
(E_2 - Abs(temp)) / Abs(temp)
End If
If Abs(temp) > Ei And Abs(temp) < E_1 Then
Rx = Ey3 / EE + Ey2 / EE + Ey1 / EE * (Ei / (E_1 - Ei)) *
(E_1 - Abs(temp)) / Abs(temp)
End If
End If
Sheets("Rx").Cells(Ly + i, j).Value = Rx
Sheets("Rx").Cells(m + 1, Xnumber + 5 + k).Value = Rx
Next j

```

```
Next i
Next k
```

'Calculating Stresses & Forces

```
For k = 1 To File
For i = 1 To ELEMnumber
For j = 1 To 3
EMat(j) = Sheets("Strain").Cells(3 * (i - 1) + j + 1, k).Value
Next j
Rx = Sheets("Rx").Cells(i + 1, Xnumber + 5 + k).Value
Ry = Sheets("Ry").Cells(i + 1, Xnumber + 5 + k).Value
Rxy = 1 - ((1 - Rx) ^ 2 + (1 - Ry) ^ 2 - (1 - Rx) * (1 - Ry)) ^ 0.5
```

```
Sheets("Softening").Cells(4, 3).Value = Rx * Ex
Sheets("Softening").Cells(5, 3).Value = Ry * Ey
Sheets("Softening").Cells(6, 3).Value = Rxy * Gxy
Sheets("Softening").Cells(7, 3).Value = Rx * vxy
```

```
For ii = 1 To 3
For jj = 1 To 3
DMat(ii, jj) = Sheets("Softening").Cells(2 + ii, 6 + jj).Value
Next jj
Next ii
```

'Calculating Stresses

```
For j = 1 To 3
temp = 0
For ii = 1 To 3
temp = temp + DMat(j, ii) * EMat(ii)
Next ii
Sheets("RStress").Cells(3 * (i - 1) + j + 1, k).Value = temp
SMat(j) = temp
Next j
```

'Linear Softening Curve, Energy

```
If Lnum = 1 Then
Gff = L ^ 2 * Height * (Ei * Ey1 * E_1 / 2)
If temp < Ei Then
Rt = 1
Gf = 0
End If
If Abs(temp) > E_1 Then
Rt = 0
Gf = Gff
End If
```

```

If Abs(temp) > Ei And Abs(temp) < E_1 Then
    Rt = (Ei / (E_1 - Ei)) * (E_1 - Abs(temp)) / Abs(temp)
    S_t = EE * temp * Rt
    Gf = Gff - L ^ 2 * Height * S_t * E_1 / 2
End If
End If

```

'Bi-Linear Softening Curve, Energy

```

If Lnum = 2 Then
    Gff = L ^ 2 * Height * (Ei * Ey1 * E_1 / 2 + E_1 * Ey2 * E_2 / 2)
    If temp < Ei Then
        Rt = 1
        Gf = 0
    End If
    If Abs(temp) > E_2 Then
        Rt = 0
        Gf = Gff
    End If
    If Abs(temp) > E_1 And Abs(temp) < E_2 Then
        Rt = Ey2 / EE * (E_1 / (E_2 - E_1)) *
            (E_2 - Abs(temp)) / Abs(temp)
        S_t = EE * temp * Rt
        Gf = Gff - L ^ 2 * Height * S_t * E_2 / 2
    End If
    If Abs(temp) > Ei And Abs(temp) < E_1 Then
        Rt = Ey2 / EE + Ey1 / EE * (Ei / (E_1 - Ei)) *
            (E_1 - Abs(temp)) / Abs(temp)
        S_t = EE * temp * Rt
        Gf = L ^ 2 * Height * (Ei * EE * Ei / 2 + (temp - Ei) *
            (Ei * EE + S_t) / 2 - S_t * temp / 2)
    End If
End If

```

'Tri-Linear Softening Curve, Energy

```

If Lnum = 3 Then
    Gff = L ^ 2 * Height * (Ei * Ey1 * E_1 / 2 + E_1 * Ey2 * E_2 / 2 +
        E_2 * Ey3 * E_3 / 2)
    If temp < Ei Then
        Rt = 1
        Gf = 0
    End If
    If Abs(temp) > E_3 Then
        Rt = 0
        Gf = Gff
    End If
    If Abs(temp) > E_2 And Abs(temp) < E_3 Then

```

```

Rt = Ey3 / EE * (E_2 / (E_3 - E_2)) *
      (E_3 - Abs(temp)) / Abs(temp)
S_t = EE * temp * Rt
Gf = Gff - L ^ 2 * Height * S_t * E_3 / 2
End If
If Abs(temp) > E_1 And Abs(temp) < E_2 Then
Rt = Ey3 / EE + Ey2 / EE * (E_1 / (E_2 - E_1)) *
      (E_2 - Abs(temp)) / Abs(temp)
S_t = EE * temp * Rt
Gf = L ^ 2 * Height * (Ei * EE * Ei / 2 + (E_1 - Ei) *
      (Ei * EE + S_1) / 2 + (temp - E_1) *
      (S_1 + S_t) / 2 - S_t * temp / 2)
End If
If Abs(temp) > Ei And Abs(temp) < E_1 Then
Rt = Ey3 / EE + Ey2 / EE + Ey1 / EE * (Ei / (E_1 - Ei)) *
      (E_1 - Abs(temp)) / Abs(temp)
S_t = EE * temp * Rt
Gf = L ^ 2 * Height * (Ei * EE * Ei / 2 + (temp - Ei) *
      (Ei * EE + S_t) / 2 - S_t * temp / 2)
End If
End If

Sheets("Gf").Cells(i + 1, k).Value = Gf
Gf_Total = Gf_Total + Gf

```

'Calculating Forces

```

Cells(8 * (i - 1) + 1 + 1, k).Value = -L * h * (SMat(1) + SMat(3)) / 2
Cells(8 * (i - 1) + 2 + 1, k).Value = -L * h * (SMat(2) + SMat(3)) / 2
Cells(8 * (i - 1) + 3 + 1, k).Value = L * h * (SMat(1) - SMat(3)) / 2
Cells(8 * (i - 1) + 4 + 1, k).Value = -L * h * (SMat(2) - SMat(3)) / 2
Cells(8 * (i - 1) + 5 + 1, k).Value = L * h * (SMat(1) + SMat(3)) / 2
Cells(8 * (i - 1) + 6 + 1, k).Value = L * h * (SMat(2) + SMat(3)) / 2
Cells(8 * (i - 1) + 7 + 1, k).Value = -L * h * (SMat(1) - SMat(3)) / 2
Cells(8 * (i - 1) + 8 + 1, k).Value = L * h * (SMat(2) - SMat(3)) / 2

Next i
Sheets("Gf").Cells(1, k).Value = Gf_Total
End If
Next k

```

'Equilibrium

```

For k = 1 To File
Ly = (2 + (Cells(12, 6).Value - Cells(11, 6).Value)) * (k - 1) + 1
temp = 0
For i = 2 To (Xnumber - 2) * (Ynumber - 2) + 1

```

'Where to write

```
n0 = Sheets("Numbering").Cells(i, 11).Value
n1x = Sheets("Numbering").Cells(n0 + 1, 2).Value + (Ly - 1)
n1y = Sheets("Numbering").Cells(n0 + 1, 3).Value
```

'Elements Attached to current node

```
n1 = Sheets("Numbering").Cells(i, 12).Value
n2 = Sheets("Numbering").Cells(i, 13).Value
n3 = Sheets("Numbering").Cells(i, 14).Value
n4 = Sheets("Numbering").Cells(i, 15).Value
```

'Equilibrium

```
tempy = Sheets("RForce").Cells(8 * (n1 - 1) + 2 + 1, k).Value +
        Sheets("RForce").Cells(8 * (n2 - 1) + 4 + 1, k).Value
tempy = tempy + Sheets("RForce").Cells(8 * (n3 - 1) + 6 + 1, k).Value +
        Sheets("RForce").Cells(8 * (n4 - 1) + 8 + 1, k).Value
tempy = Abs(tempy) / 1000
Sheets("RdFy").Cells(n1x, n1y).Value = tempy
temp = temp + tempy ^ 2
Next i
Cells(h, k).Value = Abs((Abs(Sheets("P-d").Cells(k + 1, 8).Value) -
        (Sheets("Gf").Cells(1, k).Value) / 1000)
Next k
```

'Calculating Total Error in each image

```
tempP = 0
For k = 1 To File
    'G value for this image
    tempG = Abs(Cells(h, 14 + k + File + 1).Value)
    tempP = tempP + (tempG) ^ 2
Next k
Cells(h, 30).Value = (tempP) ^ 0.5
```

```
Next h
End Sub
```

Appendix B: Sensitivity Analysis of the Center-Notched Specimen to Parameters of the Strain-Softening Curve

In this section, LS-DYNA is utilized to simulate the damaging behaviour of center-notched specimens (Figure B-1) of various sizes (Table B-1). Five different specimen sizes were considered in which $2a/W$ (notch length to width ratio) and $2a/H$ (notch length to height ratio) were kept constant, equal to 0.2 and 0.1, respectively. In these simulations, the optimized trilinear softening response obtained in this study (Figure 4-39) was used to model the damaging behaviour of the material. Simulation results for various specimen sizes are shown in Figure B-2. These results agree well with the Bazant's energetic size effect law (Bazant and Planas, 1998) in which for large notched specimens, the slope of the Log(strength)-Log(Size) approaches to $-1/2$. In small notched specimens, this slope approaches to zero and the specimen strength approaches to the material strength, σ_{peak} .

Effect of changing six parameters of the trilinear softening curve were studied here: slopes after the peak, θ_1 , θ_2 and θ_3 (Figure 4-45), plateau stress, $\sigma_{plateau}$, damage initiation strain, ε_i , and fracture energy, G_f . For each specimen size, LS-DYNA was used to obtain the sensitivity of specimen strength to various parameters of the softening curve.

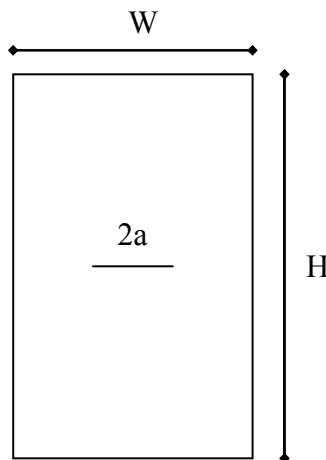


Figure B-1 Geometry of the center-notched specimen.

Table B-1 Specifications of center-notched specimens.

| Specimen # | 2a (mm) | W (mm) | H (mm) |
|------------|---------|--------|--------|
| 1 | 1 | 5 | 10 |
| 2 | 5 | 25 | 50 |
| 3 | 25 | 125 | 250 |
| 4 | 125 | 625 | 1250 |
| 5 | 375 | 1875 | 3750 |

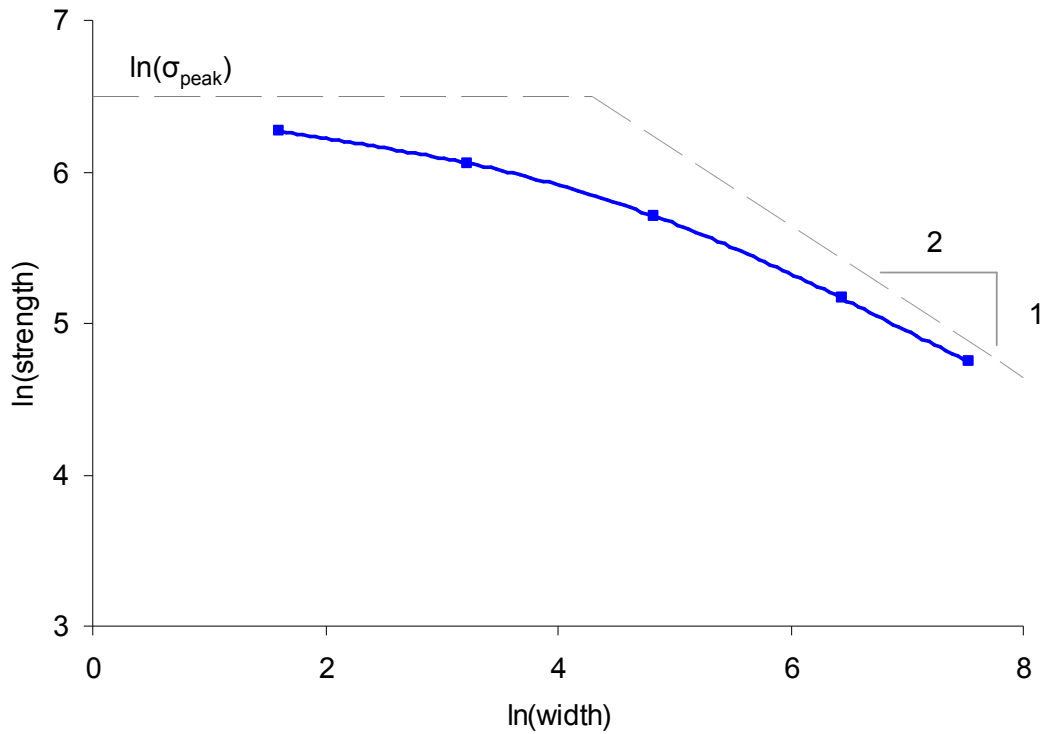


Figure B-2 Size effect observed in the center-notched specimens.

In this section, in order to compare the effect of parameters of the strain-softening response on the nominal stress of the notched specimens of various sizes, the previously defined sensitivity parameter (Equation 4-7) was modified as follows:

$$S = \frac{\Delta P\%}{\Delta \theta_1\%} = \frac{\frac{P_0 - P}{P_0}}{\frac{(\theta_1)_0 - (\theta_1)}{(\theta_1)_0}} \quad \text{(B-1)}$$

For each specimen size, each parameter is perturbed slightly and the peak nominal stress is obtained using LS-DYNA. For example, in Figure B-3a, Curve 2 is constructed by changing the damage initiation strain of the optimized trilinear softening curve (Curve 1) from 1.1% to 1.3%. In doing so, all the other 5 parameters of the softening response are kept constant. Simulation results obtained using these two curves for the specimen #2 (Table B-1) are shown in Figure B-3b.

The sensitivity results obtained for various specimen sizes are shown in Figure B-4 and Table B-2. It can be observed that for the smallest notched specimen, specimen #1, damage initiation strain has the largest effect on the specimen strength. On the other hand, in the largest specimen, specimen #5, only fracture energy has any effect on the specimen strength. In other specimen sizes, other parameters of the softening response also affect the specimen strength.

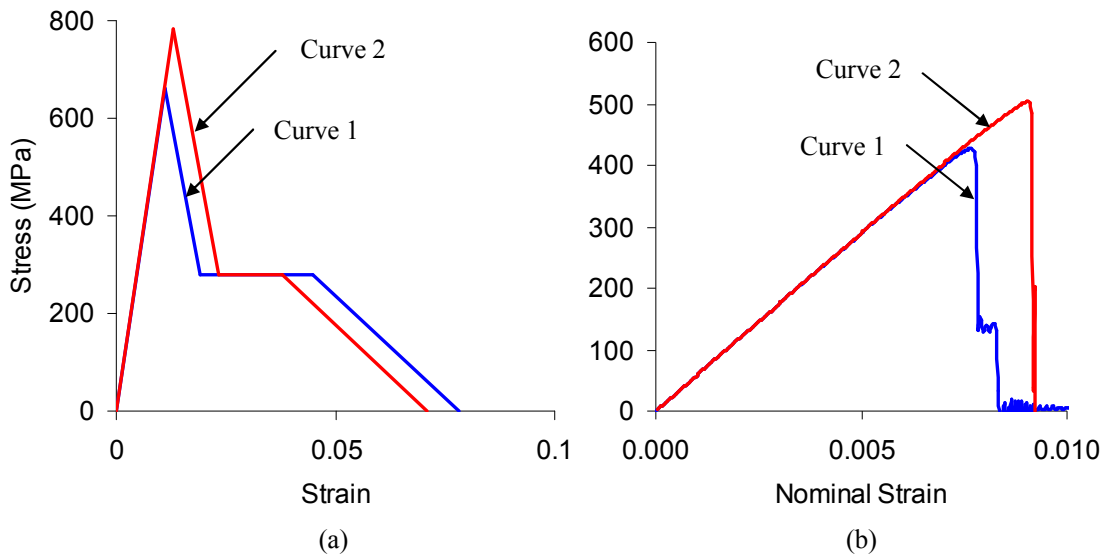


Figure B-3 (a) Stress-strain responses used to obtain the sensitivity of the center-notched specimens to the damage initiation value (curve 1: $\epsilon_i=1.1\%$ and curve 2: $\epsilon_i=1.3\%$) and (b) FE simulation results of the specimen #2 (Table B-1) using different damage initiation values.

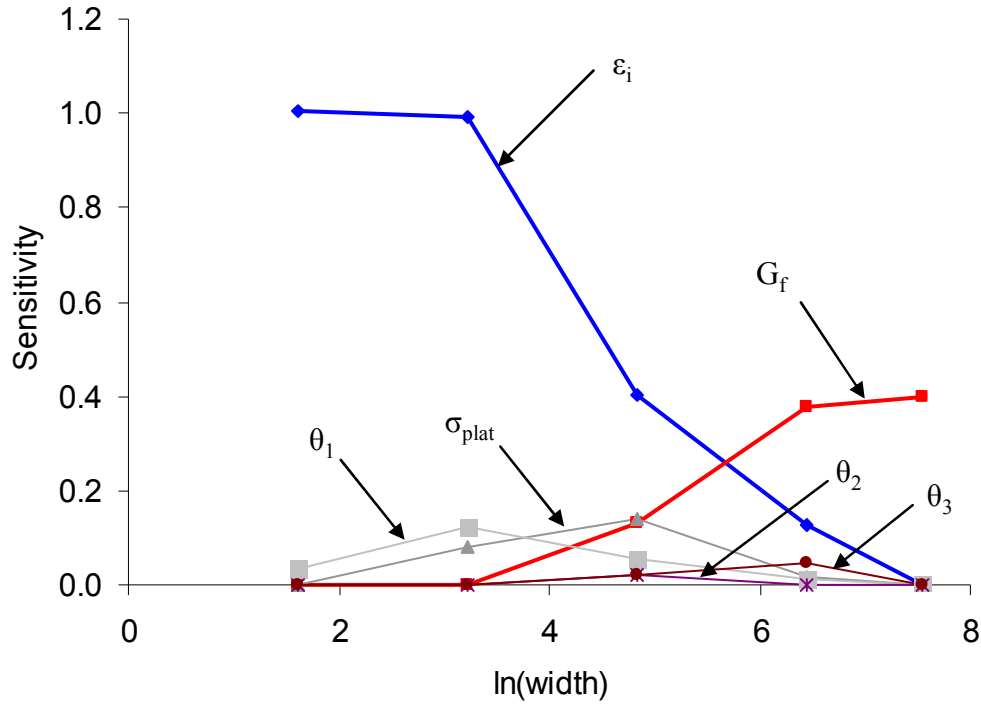


Figure B-4 Sensitivity of the strength to various parameters of the trilinear softening response for different sizes of the center-notched specimen (Table B-1).

Table B-2 Sensitivity of the strength to various parameters of the trilinear softening response for different sizes of the center-notched specimen (Table B-1).

| Specimen # | Normalized Sensitivity | | | | | |
|------------|------------------------|------------------------|------------------------|------------------------|-------------------|-------------------|
| 1 | ϵ_i (1.00) | θ_1 (0.03) | | | | |
| 2 | ϵ_i (0.99) | θ_1 (0.12) | σ_{plat} (0.08) | | | |
| 3 | ϵ_i (0.40) | σ_{plat} (0.14) | G_f (0.13) | θ_1 (0.05) | θ_2 (0.02) | θ_3 (0.02) |
| 4 | G_f (0.38) | ϵ_i (0.13) | θ_3 (0.05) | σ_{plat} (0.02) | | |
| 5 | G_f (0.40) | | | | | |

To better understand the effect of damage initiation strain, ϵ_i , and fracture energy, G_f , on the response of center-notched specimens, simulation results obtained using three different softening curves (Figure B-5) are shown in Figure B-6. In these softening curves, damage initiation strain and fracture energy values are varied. Curve 2, has the same fracture energy value as curve 1 (110 kJ/m²) but with a different damage initiation strain value (1.3%). Curve 3 on the other hand, has a different fracture energy value (50

kJ/m^2) but with the same damage initiation value (1.1%). As expected, in smaller specimen sizes, changing the fracture energy doesn't change the specimen peak stress (Figure B-6). On the other hand, changing the damage initiation strain, doesn't have any effect on the strength of large notched specimens.

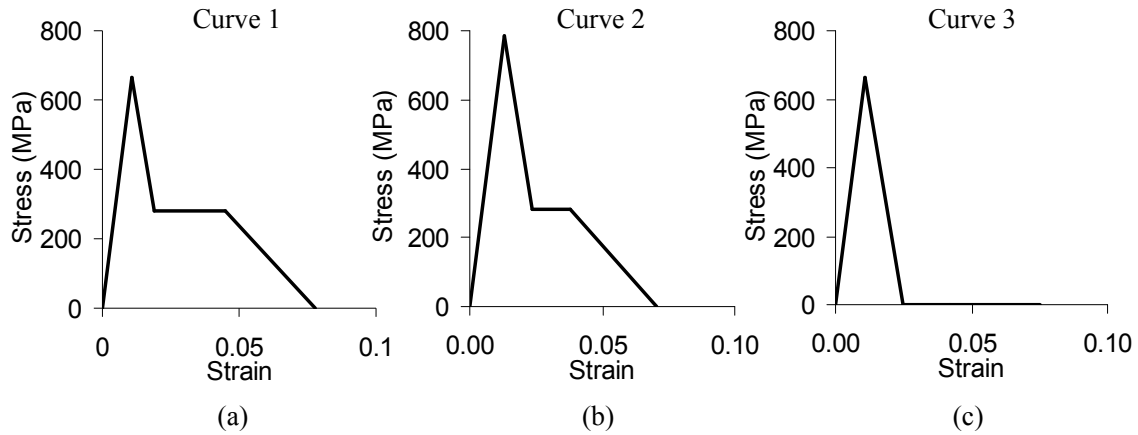


Figure B-5 (a) Curve 1: softening response with $\epsilon_i=1.1\%$ and $G_f=110 \text{ kJ/m}^2$, (b) Curve 2: softening response with $\epsilon_i=1.3\%$ and $G_f=110 \text{ kJ/m}^2$ and (c) Curve 3: softening response with $\epsilon_i=1.1\%$ and $G_f=50 \text{ kJ/m}^2$.

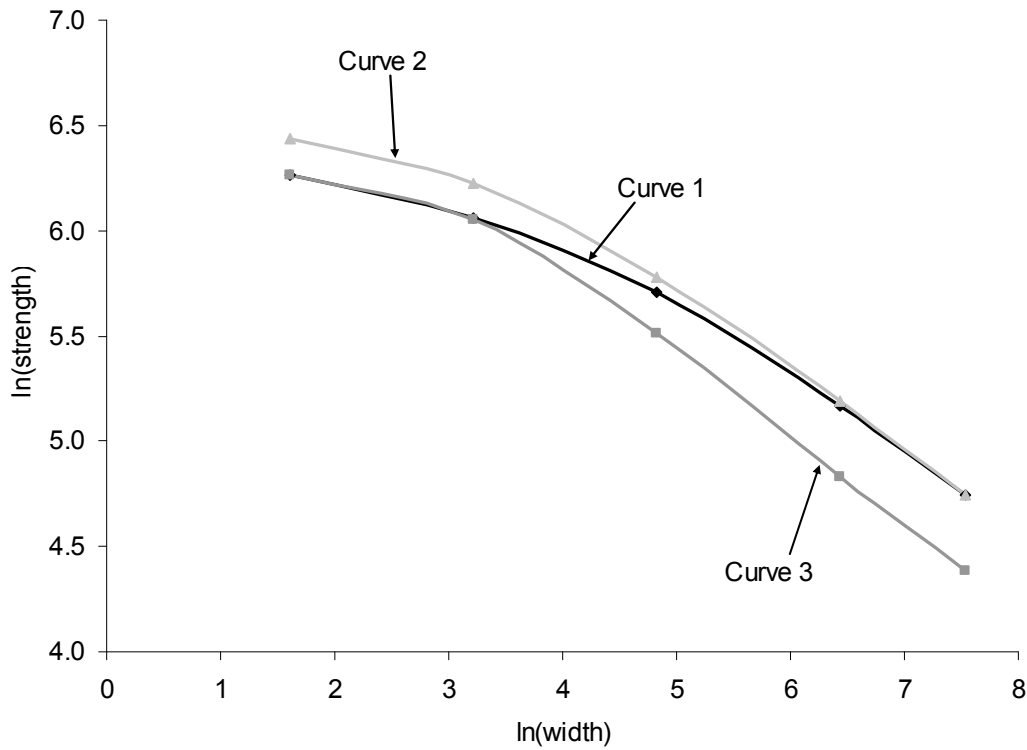


Figure B-6 Simulation results in center notched specimens using three different softening response (Figure B-5).

Appendix C: Comparison with Line Analysis

The line analysis method developed by Kongshvan and Poursartip (1999) is utilized here and its results are compared with the results obtained using the proposed method. Line analysis method has been used extensively in the past (Mitchell, 2002; McClennan, 2004) and its capability to extract material damage properties such as crack length has been confirmed. In this section, we compare results of this method for a CT test with the results of the current method to calculate damage length and damage initiation strain.

C.1. Compact Tension Test

A 90x90 mm compact tension specimen (Figure C-1) was tested to compare the capability of line analysis and current proposed method to identify the crack length and damage initiation strain. The same IM7/8552 quasi-isotropic laminate used for other tests in this study, was also used here. During the test, total of 170 images were recorded and Load-POD curve was obtained as shown in Figure C-2.

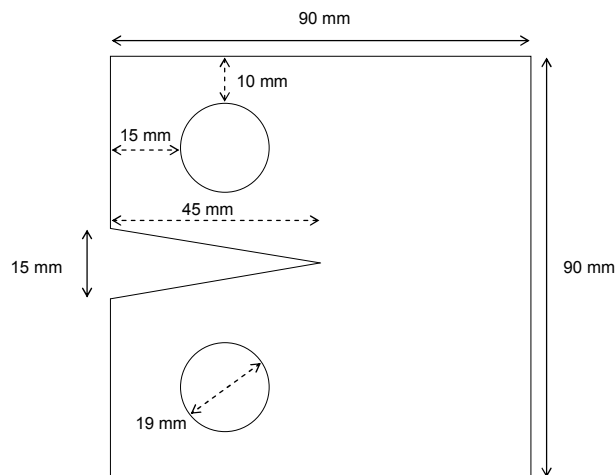


Figure C-1 Compact tension specimen specifications.

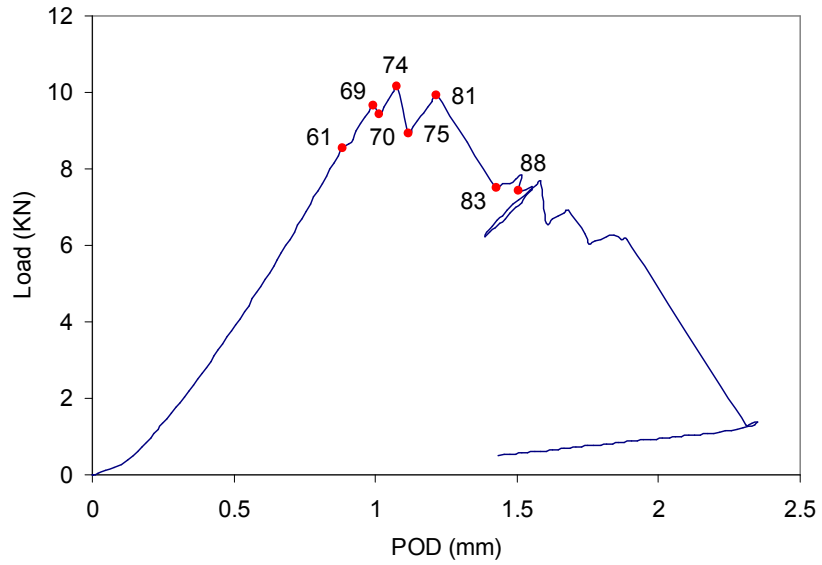


Figure C-2 Load-POD curve obtained for the CT test.

C.2. Application of the New Method

To obtain full-field displacement vectors for each image, all images were analysed using DaVis StarinMaster software. The mesh element size in this analysis was equal to 1.68 mm as shown in Figure C-3.

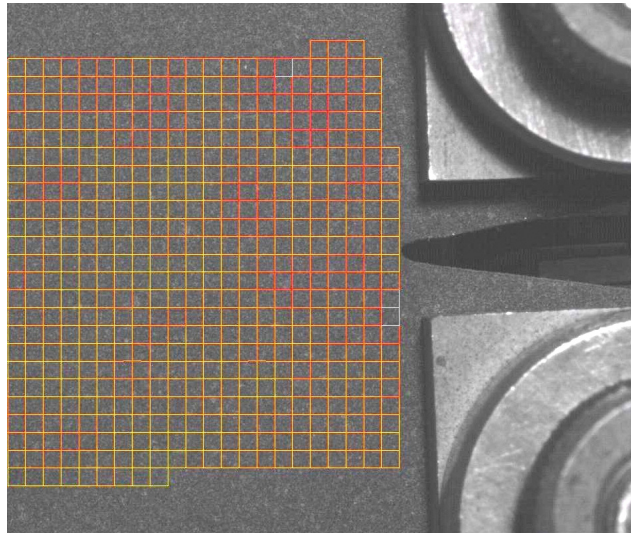


Figure C-3 Mesh generated by DaVis software for the CT specimen.

The displacement field data was imported into CrackPro code and the same steps as explained previously were taken to identify the damage region.

For 22 images, images #69-#90, which were taken at the nonlinear portion of the load-POD curve limited to the first unloading, analyses were carried out. Based on the CrackPro calculation, average damage initiation strain in all of these images were equal to 1.05% with standard deviation equal to 0.36%. This value were determined by taking average of the damage initiation strains in all images as shown in Figure C-4. This matches well with 1.1% strain value determined previously for OCT tests. The variation observed in the results is due to the presence of error in the raw displacement data.

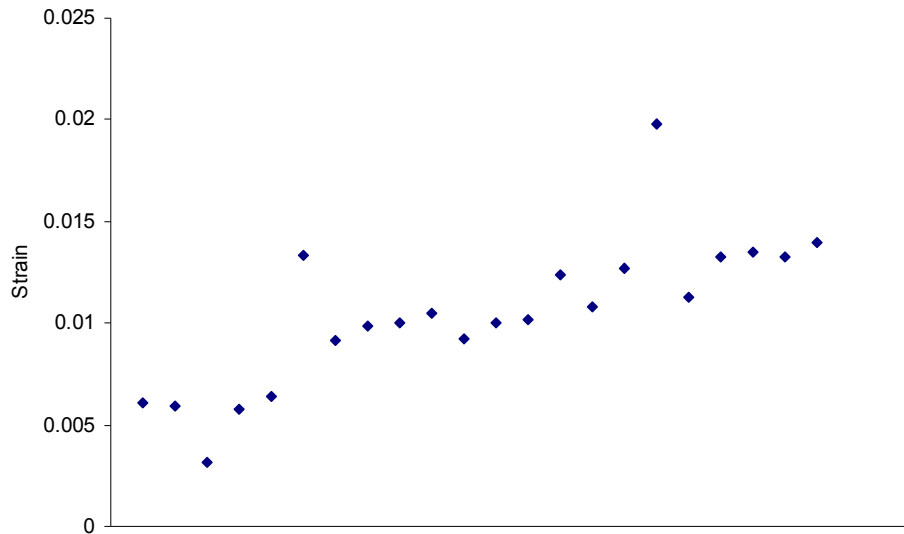


Figure C-4 Damage initiation strains for CT specimen obtained from various images.

C.3. Application of the Line Analysis Method

To use line analysis for compact tension test, virtual scribed lines on the surface of the specimen parallel to the damage growth direction were assumed. Total of 6 virtual lines were assumed on the surface of the specimen located at ± 3.3 mm, ± 4.9 mm and ± 8.2 mm distance from the center line. These lines are 2, 3 and 5 elements apart from the center line respectively. These lines are shown in Figure C-5.

In line analysis method, to determine the extent of crack, deformation of scribed lines are tracked. The damage or crack length is determined by monitoring the load-POD curve and also the specimen surface. At the instant when nonlinearity appears in the load-displacement curve, or the first crack appears on the surface of the specimen, the relative displacement of various lines are measured. This displacement is the threshold for onset of the crack. By monitoring the displacements of the scribed lines and comparing them to the value of this threshold, the crack length is determined. Since neither of images #61, #69 or #74 in Figure C-2 show noticeable crack growth during the experiment, we have to obtain the onset of the crack by monitoring the nonlinearity in the load-POD curve. Here, three analyses are performed using images #61, #69 and #74 (Figure C-2) as the threshold of the damage growth.

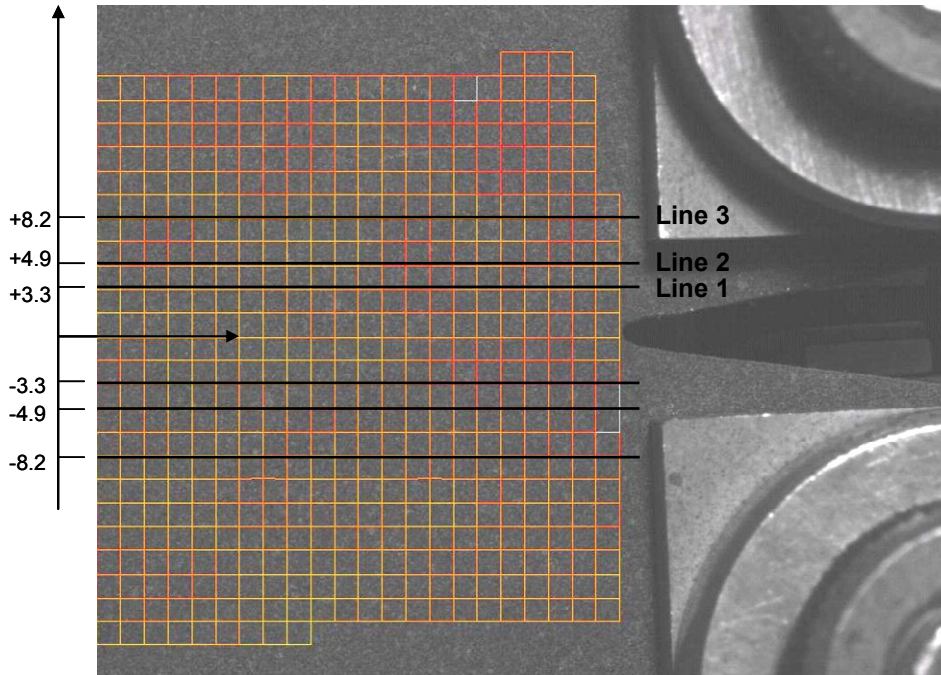


Figure C-5 Virtual scribed lines on the surface of the CT specimen.

The load drops from image 69-70, 74-75 and 81-83 in Figure C-2, result in big jumps in deformation of lines on the specimen surface (Figure C-6 and Figure C-7).

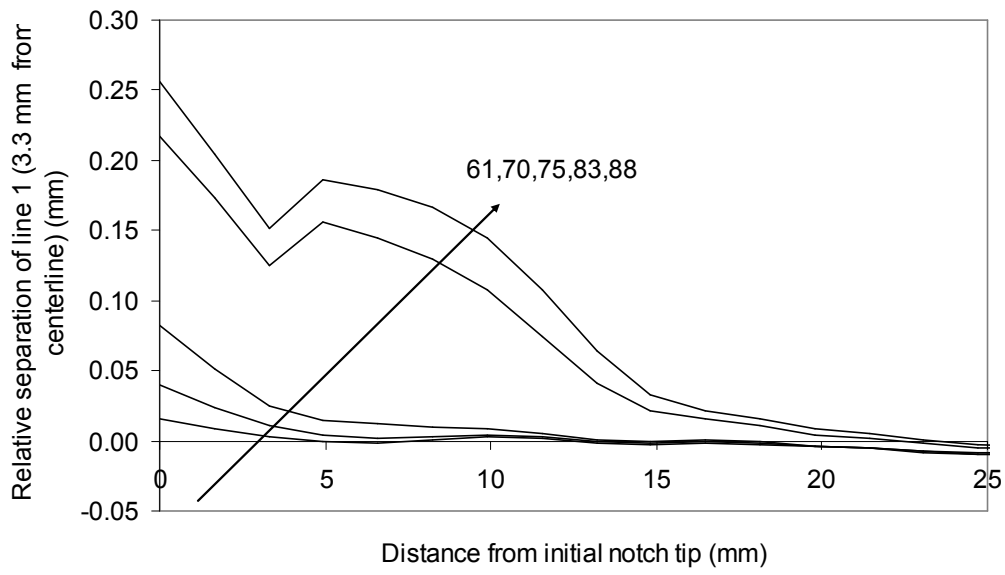


Figure C-6 Displacement of line 1 as a function of position in front of the notch tip. Each curve represents the position of line 1 in a specific image.

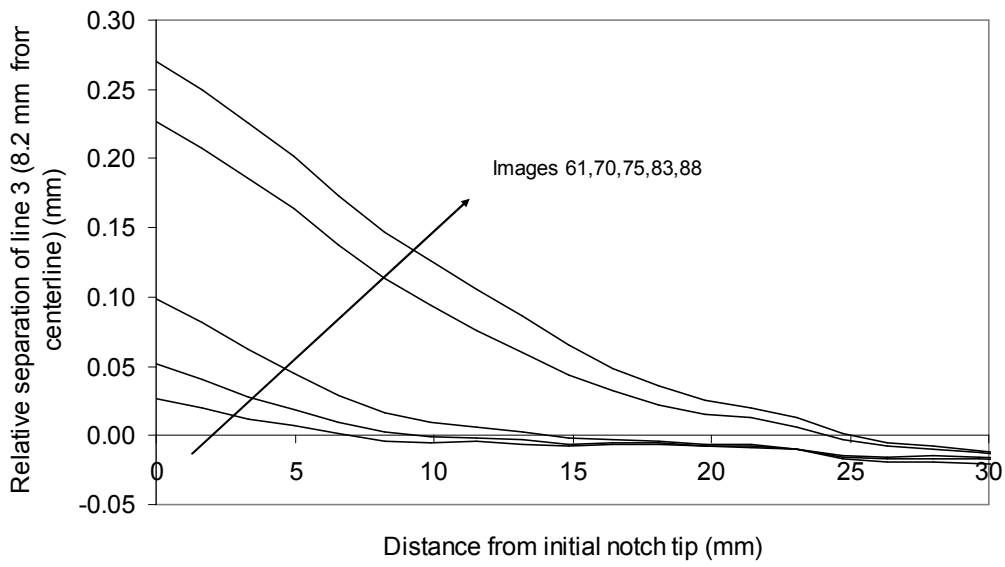


Figure C-7 Displacement of line 3 as a function of position in front of the notch tip. Each curve represents the position of line 3 in a specific image.

To complete the analyses, we have to find the damage threshold from each image. For example assuming that damage starts to grow in image #61, the threshold based on relative displacement of line 1 to the centerline is 0.015 mm or an average strain equal to 0.5%. Thresholds based on other criteria are determined and shown in Table C-1.

Table C-1 Finding damage initiation based on different criteria in line analysis.

| Image # | Line # | Critical displacement | Critical strain |
|---------|--------|-----------------------|-----------------|
| 61 | 1 | 0.015 mm | 0.50% |
| | 2 | 0.019 mm | |
| | 3 | 0.027 mm | |
| 69 | 1 | 0.038 mm | 1.10% |
| | 2 | 0.044 mm | |
| | 3 | 0.050 mm | |
| 74 | 1 | 0.081 mm | 2.50% |
| | 2 | 0.095 mm | |
| | 3 | 0.096 mm | |

As it is shown in Figure C-8, damage length can be determined using these threshold values and analysing the displacement of scribed lines. Based on various assumptions for damage initiation, however, we might end up with different results. For example assuming that the onset of the crack is at image #61 or #69 or # 74, critical displacement values are 0.015 mm, 0.038 mm and 0.081 mm respectively. Dividing these values to the original distance of the line 1 to the centerline, the damage initiation strain value is obtained equal to 0.5%, 1.1% and 2.5% based on each assumption. The damage length calculation based on these values are shown for line 1 in Figure C-9. As it is shown in this figure, there are big differences between crack length calculated using line analysis if one assumes a different threshold for crack growth. For example for POD equal to 1.4 mm, the crack is equal to 13 mm, 16 mm or 19 mm based on different assumptions. This big variation in crack length results in variation of fracture energy value. For example fracture energy calculated based on a 13 mm crack length is about 30% higher than that calculated using a 19 mm crack length.

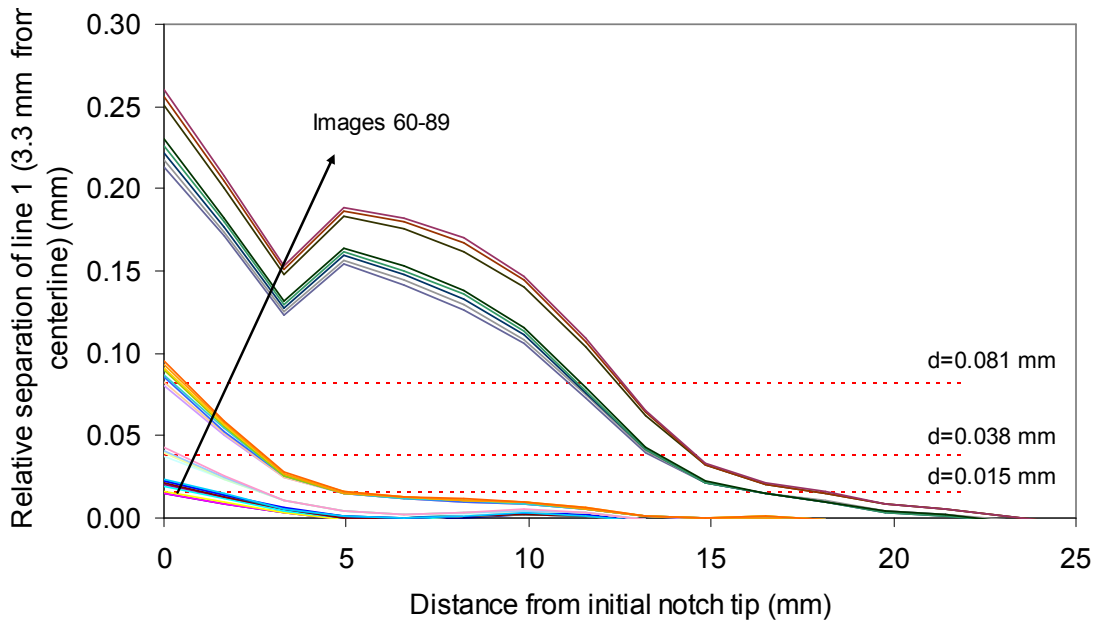


Figure C-8 Line analysis for Line 1 based on different thresholds.

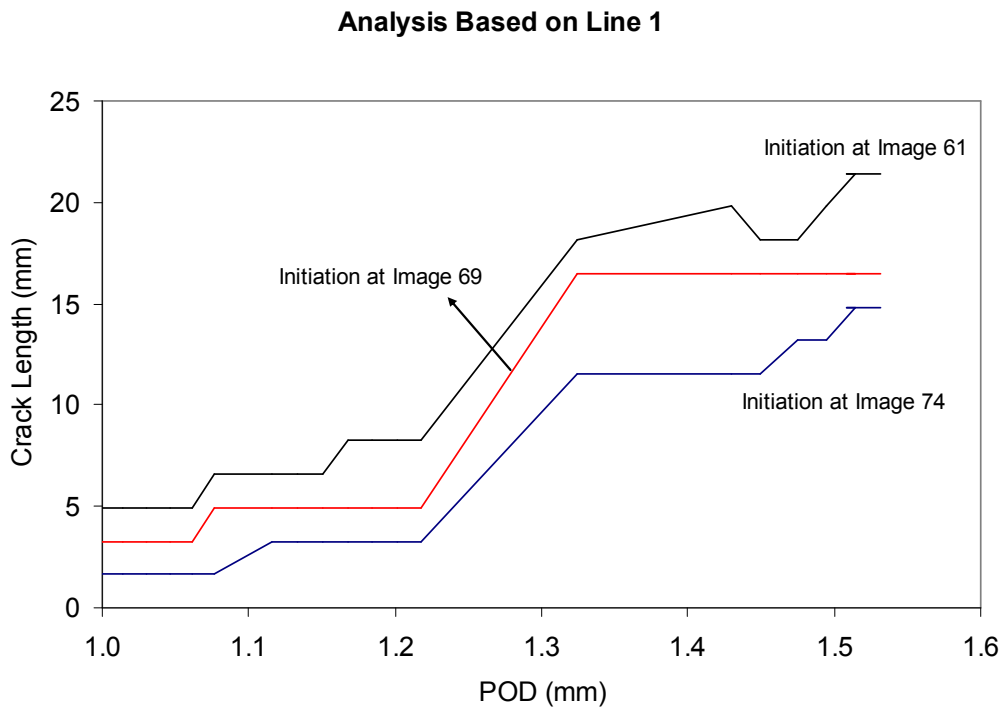


Figure C-9 Crack length obtained using line analysis and various assumptions for crack onset.

C.4. Comparison of the Two Methods

Comparing the results obtained from line analysis method with those of current proposed method, shows a higher degree of accuracy in the current method. The damage initiation strain obtained using the current proposed method was equal to 1.05% with standard deviation equal to 0.36%. This matches well with the experimental results obtained previously from OCT tests. On the other hand, using the line analysis method, based on different criteria for damage onset, we might end up with damage initiation strain value equal to 0.5%, 1.1% or 2.5%. This shows that the degree of uncertainty is much higher in the case of line analysis method.